NASA/TP-2000-209033

Results From F-18B Stability and Control Parameter Estimation Flight Tests at High Dynamic Pressures

Timothy R. Moes, Gregory K. Noffz, and Kenneth W. Iliff
NASA Dryden Flight Research Center
Edwards, California

November 2000

The NASA STI Program Office…in Profile

Since its founding, NASA has been dedicated to the advancement of aeronautics and space science. The NASA Scientific and Technical Information (STI) Program Office plays a key part in helping NASA maintain this important role.

The NASA STI Program Office is operated by Langley Research Center, the lead center for NASA's scientific and technical information. The NASA STI Program Office provides access to the NASA STI Database, the largest collection of aeronautical and space science STI in the world. The Program Office is also NASA's institutional mechanism for disseminating the results of its research and development activities. These results are published by NASA in the NASA STI Report Series, which includes the following report types:

- TECHNICAL PUBLICATION. Reports of completed research or a major significant phase of research that present the results of NASA programs and include extensive data or theoretical analysis. Includes compilations of significant scientific and technical data and information deemed to be of continuing reference value. NASA's counterpart of peer-reviewed formal professional papers but has less stringent limitations on manuscript length and extent of graphic presentations.

- TECHNICAL MEMORANDUM. Scientific and technical findings that are preliminary or of specialized interest, e.g., quick release reports, working papers, and bibliographies that contain minimal annotation. Does not contain extensive analysis.

- CONTRACTOR REPORT. Scientific and technical findings by NASA-sponsored contractors and grantees.

- CONFERENCE PUBLICATION. Collected papers from scientific and technical conferences, symposia, seminars, or other meetings sponsored or cosponsored by NASA.

- SPECIAL PUBLICATION. Scientific, technical, or historical information from NASA programs, projects, and mission, often concerned with subjects having substantial public interest.

- TECHNICAL TRANSLATION. English-language translations of foreign scientific and technical material pertinent to NASA's mission.

Specialized services that complement the STI Program Office's diverse offerings include creating custom thesauri, building customized databases, organizing and publishing research results…even providing videos.

For more information about the NASA STI Program Office, see the following:

- Access the NASA STI Program Home Page at ***http://www.sti.nasa.gov***

- E-mail your question via the Internet to help@sti.nasa.gov

- Fax your question to the NASA Access Help Desk at (301) 621-0134

- Telephone the NASA Access Help Desk at (301) 621-0390

- Write to:
  NASA Access Help Desk
  NASA Center for AeroSpace Information
  7121 Standard Drive
  Hanover, MD 21076-1320

NASA/TP-2000-209033

Results From F-18B Stability and Control Parameter Estimation Flight Tests at High Dynamic Pressures

Timothy R. Moes, Gregory K. Noffz, and Kenneth W. Iliff
NASA Dryden Flight Research Center
Edwards, California

National Aeronautics and
Space Administration

Dryden Flight Research Center
Edwards, California 93523-0273

November 2000

NOTICE

Use of trade names or names of manufacturers in this document does not constitute an official endorsement of such products or manufacturers, either expressed or implied, by the National Aeronautics and Space Administration.

Available from the following:

NASA Center for AeroSpace Information (CASI)
7121 Standard Drive
Hanover, MD 21076-1320
(301) 621-0390

National Technical Information Service (NTIS)
5285 Port Royal Road
Springfield, VA 22161-2171
(703) 487-4650

CONTENTS

Page

ABSTRACT 1

NOMENCLATURE 1

INTRODUCTION 6

VEHICLE DESCRIPTION 7
- Control Surfaces 8
- Software Configuration 10
- Mass Properties 10
- Instrumentation and Data Acquisition 11

METHODS OF ANALYSIS 12
- Parameter Identification Formulation 12
- Equations of Motion 13
- Aerodynamic Model Update 16

FLIGHT TEST APPROACH 17

RESULTS AND DISCUSSION 19
- Unexpected Leading-Edge Flap Deflections 19
  - Control-Surface Position Transducer and Rotary Variable Differential Transformer Deflection Measurements 19
  - Sonic Split 20
- Stability and Control Derivative Results Using Control-Surface Position Transducer Measurements 20
  - Longitudinal Stability and Control Results 20
  - Lateral-Directional Stability and Control Results 22
- Stability and Control Derivatives Results Using Rotary Variable Differential Transformer Surface Positions 23
- Aerodynamic Model Update 24
  - Symmetric Leading-Edge Flaps 25
  - Symmetric Trailing-Edge Flaps 25
  - Symmetric Ailerons 25
  - Differential Leading-Edge Flaps 25
  - Differential Trailing-Edge Flaps 26
  - Aileron 26
  - Differential Stabilator 26

CONCLUDING REMARKS 26

FIGURES 28
- Figure 1. F-18B Systems Research Aircraft (SRA). 28
- Figure 2. Three-view drawing of the F-18B SRA with major dimensions shown. 29
- Figure 3. AAW and SRA flight test point matrix. 30

Figure 4. Canopy mold line comparison between F-18 “A” and “B” models. 30
Figure 5. Asymmetries between left and right aileron surfaces and actuator fairings. 31
Figure 6. Basic F-18A/B symmetric LEF and TEF schedules (ref. 3). 32
Figure 7. Maximum-likelihood parameter estimation process. 32
Figure 8. Typical large longitudinal doublet SSI sequence (RVDT measurements). 33
Figure 9. Typical large lateral-directional doublet SSI sequence (RVDT measurements). 34
Figure 10. Symmetric aileron doublet time history. 35
Figure 11. Time history showing LEF split at supersonic Mach numbers. 36
Figure 12. Maximum doublet maneuver sizes used at the various test conditions. 37
Figure 13. Predicted and flight-determined longitudinal coefficient biases (pEst program analysis using CPT measurements). 38
Figure 14. Predicted and flight-determined angle-of-attack derivatives (pEst program analysis using CPT measurements). 39
Figure 15. Predicted and flight-determined pitch-rate derivatives (pEst program analysis using CPT measurements). 40
Figure 16. Predicted and flight-determined symmetric LEF derivatives (pEst program analysis using CPT measurements). 41
Figure 17. Predicted and flight-determined symmetric TEF derivatives (pEst program analysis using CPT measurements). 42
Figure 18. Predicted and flight-determined symmetric aileron derivatives (pEst program analysis using CPT measurements). 43
Figure 19. Predicted and flight-determined elevator (symmetric stabilator) derivatives (pEst program analysis using CPT measurements). 44
Figure 20. Predicted and flight-determined lateral-directional coefficient biases (pEst program analysis using CPT measurements). 45
Figure 21. Predicted and flight-determined angle-of-sideslip derivatives (pEst program analysis using CPT measurements). 46
Figure 22. Predicted and flight-determined roll rate derivatives (pEst program analysis using CPT measurements). 47
Figure 23. Predicted and flight-determined yaw rate derivatives (pEst program analysis using CPT measurements). 48
Figure 24. Predicted and flight-determined rudder derivatives (pEst program analysis using CPT measurements). 49
Figure 25. Predicted and flight-determined differential LEF derivatives (pEst program analysis using CPT measurements). 50
Figure 26. Predicted and flight-determined differential TEF derivatives (pEst program analysis using CPT measurements). 51
Figure 27. Predicted and flight-determined aileron derivatives (pEst program analysis using CPT measurements). 52
Figure 28. Predicted and flight-determined differential stabilator derivatives (pEst program analysis using CPT measurements). 53
Figure 29. Predicted and flight-determined longitudinal coefficient biases (pEst program analysis using RVDT measurements). 54
Figure 30. Predicted and flight-determined angle-of-attack derivatives (pEst program analysis using RVDT measurements). 55

Figure 31. Predicted and flight-determined pitch-rate derivatives (pEst program analysis using RVDT measurements). 56
Figure 32. Predicted and flight-determined symmetric LEF derivatives (pEst program analysis using RVDT measurements). 57
Figure 33. Predicted and flight-determined symmetric TEF derivatives (pEst program analysis using RVDT measurements). 58
Figure 34. Predicted and flight-determined symmetric aileron derivatives (pEst program analysis using RVDT measurements). 59
Figure 35. Predicted and flight-determined elevator (symmetric stabilator) derivatives (pEst program analysis using RVDT measurements). 60
Figure 36. Comparison of pitching-moment derivatives measured using CPTs and RVDTs. 61
Figure 37. Predicted and flight-determined lateral-directional coefficient biases (pEst program analysis using RVDT measurements). 62
Figure 38. Predicted and flight-determined angle of sideslip derivatives (pEst program analysis using RVDT measurements). 63
Figure 39. Predicted and flight-determined roll rate derivatives (pEst program analysis using RVDT measurements). 64
Figure 40. Predicted and flight-determined yaw rate derivatives (pEst program analysis using RVDT measurements). 65
Figure 41. Predicted and flight-determined rudder derivatives (pEst program analysis using RVDT measurements). 66
Figure 42. Predicted and flight-determined differential LEF derivatives (pEst program analysis using RVDT measurements). 67
Figure 43. Predicted and flight-determined differential TEF derivatives (pEst program analysis using RVDT measurements). 68
Figure 44. Predicted and flight-determined aileron derivatives (pEst program analysis using RVDT measurements). 69
Figure 45. Predicted and flight-determined differential stabilator derivatives (pEst program analysis using RVDT measurements). 70
Figure 46. Comparison of sideslip derivatives using CPT and RVDT measurements. 71
Figure 47. Comparison of control derivatives using CPT and RVDT measurements.. 72
Figure 48. Symmetric LEF SSI (Mach 1.2 at 25,000 ft). 73
Figure 49. Symmetric TEF SSI (Mach 1.2 at 25,000 ft). 74
Figure 50. Symmetric aileron doublet (Mach 0.85 at 15,000 ft). 75
Figure 51. Differential LEF doublet (Mach 1.2 at 15,000 ft). 76
Figure 52. Differential TEF doublet (Mach 1.2 at 15,000 ft). 77
Figure 53. Aileron doublet (Mach 1.2 at 15,000 ft).. 78
Figure 54. Differential stabilator doublet (Mach 1.2 at 15,000 ft). 79

APPENDIX A 80
Figure A-1. Large doublet sequence (Mach 0.85 at 15,000 ft). 81
Figure A-2. Small doublet sequence (Mach 0.85 at 10,000 ft). 82
Figure A-3. Small doublet sequence (Mach 0.85 at 5,000 ft). 83
Figure A-4. Medium doublet sequence (Mach 0.9 at 15,000 ft). 84

Figure A-5. Medium doublet sequence (Mach 0.9 at 10,000 ft). 85
Figure A-6. Small doublet sequence (Mach 0.9 at 5,000 ft). 86
Figure A-7. Large doublet sequence (Mach 0.95 at 15,000 ft). 87
Figure A-8. Large doublet sequence (Mach 0.95 at 10,000 ft). 88
Figure A-9. Medium doublet sequence (Mach 0.95 at 5,000 ft). 89
Figure A-10. Large doublet sequence (Mach 1.1 at 25,000 ft). 90
Figure A-11. Large doublet sequence (Mach 1.1 at 20,000 ft). 91
Figure A-12. Medium doublet sequence (Mach 1.1 at 15,000 ft). 92
Figure A-13. Small doublet sequence (Mach 1.1 at 10,000 ft). 93
Figure A-14. Large doublet sequence (Mach 1.2 at 25,000 ft). 94
Figure A-15. Medium doublet sequence (Mach 1.2 at 20,000 ft). 95
Figure A-16. Small doublet sequence (Mach 1.2 at 15,000 ft). 96
Figure A-17. Small doublet sequence (Mach 1.2 at 10,000 ft). 97
Figure A-18. Medium doublet sequence (Mach 1.3 at 25,000 ft). 98
Figure A-19. Small doublet sequence (Mach 1.3 at 20,000 ft). 99
Figure A-20. Small doublet sequence (Mach 1.3 at 15,000 ft). 100

APPENDIX B 101
Figure B-1. Large doublet sequence (Mach 0.85 at 15,000 ft). 102
Figure B-2. Large doublet sequence (Mach 0.85 at 10,000 ft). 103
Figure B-3. Large doublet sequence (Mach 0.85 at 5,000 ft). 104
Figure B-4. Large doublet sequence (Mach 0.9 at 15,000 ft). 105
Figure B-5. Large doublet sequence (Mach 0.9 at 10,000 ft). 106
Figure B-6. Large doublet sequence (Mach 0.9 at 5,000 ft). 107
Figure B-7. Large doublet sequence (Mach 0.95 at 15,000 ft). 108
Figure B-8. Large doublet sequence (Mach 0.95 at 10,000 ft). 109
Figure B-9. Medium doublet sequence (Mach 0.95 at 5,000 ft). 110
Figure B-10. Large doublet sequence (Mach 1.1 at 25,000 ft). 111
Figure B-11. Large doublet sequence (Mach 1.1 at 20,000 ft). 112
Figure B-12. Medium doublet sequence (Mach 1.1 at 15,000 ft). 113
Figure B-13. Small doublet sequence (Mach 1.1 at 10,000 ft). 114
Figure B-14. Large doublet sequence (Mach 1.2 at 25,000 ft). 115
Figure B-15. Medium doublet sequence (Mach 1.2 at 20,000 ft). 116
Figure B-16. Small doublet sequence (Mach 1.2 at 15,000 ft). 117
Figure B-17. Small doublet sequence (Mach 1.2 at 10,000 ft). 118
Figure B-18. Medium doublet sequence (Mach 1.3 at 25,000 ft). 119
Figure B-19. Small doublet sequence (Mach 1.3 at 20,000 ft). 120
Figure B-20. Small doublet sequence (Mach 1.3 at 15,000 ft). 121

APPENDIX C 122

APPENDIX D 128

REFERENCES 134

ABSTRACT

A maximum-likelihood output-error parameter estimation technique has been used to obtain stability and control derivatives for the NASA F-18B Systems Research Aircraft. This work has been performed to support flight testing of the active aeroelastic wing (AAW) F-18A project. The goal of this research is to obtain baseline F-18 stability and control derivatives that will form the foundation of the aerodynamic model for the AAW aircraft configuration. Flight data have been obtained at Mach numbers from 0.85 to 1.30 and at dynamic pressures ranging from 600 to 1500 lbf/ft^2. At each test condition, longitudinal and lateral-directional doublets have been performed using an automated onboard excitation system. The doublet maneuver consists of a series of single-surface inputs so that individual control-surface motions cannot be correlated with other control-surface motions. Flight test results have shown that several stability and control derivatives are significantly different than prescribed by the F-18B aerodynamic model. This report defines the parameter estimation technique used, presents stability and control derivative results, compares the results with predictions based on the current F-18B aerodynamic model, and shows improvements to the nonlinear simulation using updated derivatives from this research.

NOMENCLATURE

Acronyms

AAW	active aeroelastic wing
BL	butt line, in.
CG	center of gravity, percent *c*
CPT	control-surface position transducer
FADS	flush airdata sensing
FCS	flight control system
FS	fuselage station, in.
HM	hinge moment, in-lbf
LEF	leading-edge flap
OBES	onboard excitation system
PID	parameter identification
RFCS	research flight control system
RVDT	rotary variable differential transformer
SRA	Systems Research Aircraft
SSI	single-surface input
TEF	trailing-edge flap
WL	water line, in.

Symbols

a_n	normal acceleration (positive up), ft/sec^2
a_x	longitudinal acceleration (positive forward), ft/sec^2
a_y	lateral acceleration (positive toward the right), ft/sec^2
b	wing span, 37.42 ft
bias	measurement bias
c	mean aerodynamic chord, 11.52 ft
C_l	rolling-moment coefficient
C_{l_b}	rolling-moment coefficient bias, linear extrapolation to $\beta = 0°$
C_{l_p}	rolling-moment coefficient due to nondimensional roll rate, $\partial C_l/\partial(pb/2VR)$, rad^{-1}
C_{l_r}	rolling-moment coefficient due to nondimensional yaw rate, $\partial C_l/\partial(rb/2VR)$, rad^{-1}
C_{l_β}	rolling-moment coefficient due to sideslip, $\partial C_l/\partial\beta$, deg^{-1}
$C_{l_{\delta_a}}$	rolling-moment coefficient due to aileron deflection, $\partial C_l/\partial\delta_a$, deg^{-1}
$C_{l_{\delta_{dh}}}$	rolling-moment coefficient due to differential stabilator deflection, $\partial C_l/\partial\delta_{dh}$, deg^{-1}
$C_{l_{\delta_{dLEF}}}$	rolling-moment coefficient due to differential LEF deflection, $\partial C_l/\partial\delta_{dLEF}$, deg^{-1}
$C_{l_{\delta_{dTEF}}}$	rolling-moment coefficient due to differential TEF deflection, $\partial C_l/\partial\delta_{dTEF}$, deg^{-1}
$C_{l_{\delta_r}}$	rolling-moment coefficient due to rudder deflection, $\partial C_l/\partial\delta_{dr}$, deg^{-1}
C_m	pitching-moment coefficient
C_{m_b}	pitching-moment coefficient bias, linear extrapolation to $\alpha = 0°$
C_{m_q}	pitching-moment coefficient due to nondimensional pitch rate, $\partial C_m/\partial(qc/2VR)$, rad^{-1}
C_{m_α}	pitching-moment coefficient due to angle of attack, $\partial C_m/\partial\alpha$, deg^{-1}
$C_{m_{\delta_e}}$	pitching-moment coefficient due to elevator deflection, $\partial C_m/\partial\delta_e$, deg^{-1}
$C_{m_{\delta_{LEF}}}$	pitching-moment coefficient due to symmetric LEF deflection, $\partial C_m/\partial\delta_{LEF}$, deg^{-1}
$C_{m_{\delta_{sa}}}$	pitching-moment coefficient due to symmetric aileron deflection, $\partial C_m/\partial\delta_{sa}$, deg^{-1}
$C_{m_{\delta_{TEF}}}$	pitching-moment coefficient due to symmetric TEF deflection, $\partial C_m/\partial\delta_{TEF}$, deg^{-1}
C_N	normal-force coefficient
C_{N_b}	normal-force coefficient bias, linear extrapolation to $\alpha = 0°$
C_{N_q}	normal-force coefficient due to nondimensional pitch rate, $\partial C_N/\partial(qc/2VR)$, rad^{-1}

C_{N_α}	normal-force coefficient due to angle of attack, $\partial C_N/\partial\alpha$, deg^{-1}
$C_{N_{\delta_e}}$	normal-force coefficient due to elevator deflection, $\partial C_N/\partial\delta_e$, deg^{-1}
$C_{N_{\delta_{LEF}}}$	normal-force coefficient due to symmetric LEF deflection, $\partial C_N/\partial\delta_{LEF}$, deg^{-1}
$C_{N_{\delta_{sa}}}$	normal-force coefficient due to symmetric aileron deflection, $\partial C_N/\partial\delta_{sa}$, deg^{-1}
$C_{N_{\delta_{TEF}}}$	normal-force coefficient due to symmetric TEF deflection, $\partial C_N/\partial\delta_{TEF}$, deg^{-1}
C_n	yawing-moment coefficient
C_{n_b}	yawing-moment coefficient bias, linear extrapolation to $\beta = 0°$
C_{n_p}	yawing-moment coefficient due to nondimensional roll rate, $\partial C_n/\partial(pb/2VR)$, rad^{-1}
C_{n_r}	yawing-moment coefficient due to nondimensional yaw rate, $\partial C_n/\partial(rb/2VR)$, rad^{-1}
C_{n_β}	yawing-moment coefficient due to sideslip, $\partial C_n/\partial\beta$, deg^{-1}
$C_{n_{\delta_a}}$	yawing-moment coefficient due to aileron deflection, $\partial C_n/\partial\delta_a$, deg^{-1}
$C_{n_{\delta_{dh}}}$	yawing-moment coefficient due to differential stabilator deflection, $\partial C_n/\partial\delta_{dh}$, deg^{-1}
$C_{N_{\delta_{dLEF}}}$	yawing-moment coefficient due to differential LEF deflection, $\partial C_n/\partial\delta_{dLEF}$, deg^{-1}
$C_{N_{\delta_{dTEF}}}$	yawing-moment coefficient due to differential TEF deflection, $\partial C_n/\partial\delta_{dTEF}$, deg^{-1}
$C_{n_{\delta_r}}$	yawing-moment coefficient due to rudder deflection, $\partial C_n/\partial\delta_r$, deg^{-1}
C_Y	side-force coefficient
C_{Y_b}	side-force coefficient bias, linear extrapolation to $\beta = 0°$
C_{Y_p}	side-force coefficient due to nondimensional roll rate, $\partial C_Y/\partial(pb/2VR)$, rad^{-1}
C_{Y_r}	side-force coefficient due to nondimensional yaw rate, $\partial C_Y/\partial(rb/2VR)$ rad^{-1}
C_{Y_β}	side-force coefficient due to sideslip, $\partial C_Y/\partial\beta$, deg^{-1}
$C_{Y_{\delta_a}}$	side-force coefficient due to aileron deflection, $\partial C_Y/\partial\delta_a$, deg^{-1}
$C_{Y_{\delta_{dh}}}$	side-force coefficient due to differential stabilator deflection, $\partial C_Y/\partial\delta_{dh}$, deg^{-1}
$C_{Y_{\delta_{dLEF}}}$	side-force coefficient due to differential LEF deflection, $\partial C_Y/\partial\delta_{dLEF}$, deg^{-1}
$C_{Y_{\delta_{dTEF}}}$	side-force coefficient due to differential TEF deflection, $\partial C_Y/\partial\delta_{dTEF}$, deg^{-1}
$C_{Y_{\delta_r}}$	side-force coefficient due to rudder deflection, $\partial C_Y/\partial\delta_r$, deg^{-1}
F	state derivative function
G	response function

g	acceleration of gravity, 32.174 ft/sec^2
I_x	roll moment of inertia, slug-ft^2
I_y	pitch moment of inertia, slug-ft^2
I_z	yaw moment of inertia, slug-ft^2
I_{xz}	cross product of inertia, slug-ft^2
$\mathrm{J}(\xi)$	cost function
Left	left wing control surface
LI	left wing inboard control surface
LO	left wing outboard control surface
M	Mach number
m	aircraft mass, slug
n_t	number of time history points used in the pEst analysis
n_z	number of response variables used in the pEst analysis
p	roll rate, deg/sec
$\dot{p}$	roll acceleration, deg/sec^2
q	pitch rate, deg/sec
$\bar{q}$	dynamic pressure, lbf/ft^2
$\dot{q}$	pitch acceleration, deg/sec^2
R	conversion factor, 57.2958 deg/rad
Right	right wing control surface
RI	right wing inboard control surface
RO	left wing outboard control surface
r	yaw rate, deg/sec
$\dot{r}$	yaw acceleration, deg/sec^2
S	wing area, 400 ft^2
t	time, sec
t_i	discrete time point at i^{th} data point
t_0	initial time
$\mathbf{u}$	control input vector
V	true airspeed, ft/sec

W	response weighting matrix used in the cost function
x	longitudinal body axis (positive forward)
$\mathbf{x}$	state vector
$\dot{\mathbf{x}}$	time derivative of state vector
$x_{a_n},\ y_{a_n},\ z_{a_n}$	normal accelerometer position aft, right, and above the *CG*, ft
$x_{a_y},\ y_{a_y},\ z_{a_y}$	lateral accelerometer position aft, right, and above the *CG*, ft
x_α	angle-of-attack sensor position aft of the *CG*, ft
$x_\beta,\ z_\beta$	angle-of-sideslip sensor position aft and above the *CG*, ft
y	lateral body axis (positive right)
z	vertical body axis (positive down)
$\mathbf{z}$	response vector (measurement vector)
$\tilde{\mathbf{z}}$	computed response vector
α	angle of attack, deg
$\dot{\alpha}$	time derivative of angle of attack, deg/sec
β	angle of sideslip, deg
$\dot{\beta}$	time derivative of angle of sideslip, deg/sec
Δ	increment
δ	control-surface deflection, deg
δ_a	aileron deflection, deg
δ_{dh}	differential horizontal stabilator deflection, deg
δ_{dLEF}	differential leading-edge flap deflection, deg
δ_{dTEF}	differential trailing-edge flap deflection, deg
δ_e	elevator (symmetric stabilator) deflection, deg
δ_{LEF}	symmetric leading-edge flap deflection, deg
δ_r	rudder deflection, deg
δ_{sa}	symmetric aileron deflection, deg
δ_{TEF}	symmetric trailing-edge flap deflection, deg
ξ	stability and control derivative parameter vector
θ	pitch angle, deg
$\dot{\theta}$	time derivative of pitch angle, deg/sec

ϕ	roll angle, deg
$\dot{\phi}$	time derivative of roll angle, deg/sec
*	transpose
~	denotes estimated response parameter

INTRODUCTION

The NASA Dryden Flight Research Center (Edwards, California) is currently preparing for the active aeroelastic wing (AAW) flight project. The AAW technology integrates vehicle aerodynamics, active controls, and structural aeroelastic behavior to maximize vehicle performance. In particular, a goal of the project is to maximize the contribution of a reduced-stiffness wing to roll-rate performance. To demonstrate this technology, changes to flight control laws are required to take full advantage of the more flexible wing. A good understanding of the basic F-18 individual control-surface effectivenesses is considered essential for developing the AAW control laws.

Two primary reasons exist for uncertainty as to whether or not the basic F-18 aerodynamic model is accurate enough for AAW control-law development. First, the existing F-18 aerodynamic database* is not a product of extensive parameter identification (PID) flight testing in the high–dynamic pressure flight envelope of interest. Second, the AAW control laws require deflecting the control surfaces in ways never before done on the F-18 airplane. For example, the existing database does not include data from symmetric leading-edge flap (LEF) and symmetric trailing-edge flap (TEF) deflections at high speeds and low angles of attack because symmetric flap deflections currently are not used at these flight conditions by the standard flight control system (FCS). In the AAW control laws, some symmetric flap deflection is anticipated to be required at high speeds to meet structural load constraints. For these two reasons, a flight research program was desired to obtain individual control-surface effectiveness values at high-speed test conditions using surface deflections that often are outside of the normal F-18 usage.

The NASA Dryden F-18B Systems Research Aircraft (SRA) (figs. 1–2) has been used to obtain basic F-18 stability and control derivatives at the high–dynamic pressure test conditions of the AAW program (fig. 3) to improve the fidelity of the basic aircraft aerodynamic model. The AAW project will use a single-place F-18A airplane, whereas the SRA is a two-place F-18B airplane. The difference in outer mold line between the “A” and “B” models is the canopy extension required to accommodate the second cockpit position in the “B” model (fig. 4). The aerodynamic model contains separate aerodynamic coefficient data tables for the “A” and “B” models. Small differences exist in the basic “A” and “B” aerodynamic models. Typically, these differences consist of small constant biases across the Mach range in the stability and control derivatives that were determined by linearizing the aerodynamic models.

The use of the F-18B aircraft is considered acceptable for this work because the outer mold line only differs at the canopy section of the fuselage, and this research is to find increments between the flight-estimated stability and control derivatives and the aerodynamic model derivatives. These increments can be applied to either the F-18A or F-18B aerodynamic model because the control surfaces are identical and the fuselage differences are included in the baseline aerodynamic models.

*Naval Air Warfare Center (Patuxent River, Maryland) Common Database, version 3.1, May 22, 1997.

The AAW vehicle aerodynamic model will use the improved aerodynamic model from the SRA PID tests as a starting point. Aerodynamic model increments caused by wing flexibility can be obtained from analytical techniques and then added to the model for the AAW vehicle control-law development, which will result in improved AAW flight simulations and more efficient and safer AAW flight testing than is possible using current aerodynamic models.

Flight data presented in this report have been obtained at Mach numbers from 0.85 to 1.30 and at dynamic pressures ranging from 600 to 1500 lbf/ft^2. At each test condition, both longitudinal and lateral-directional doublets were performed using an automated onboard excitation system (OBES). The doublet maneuver consisted of a series of single-surface inputs (SSIs) so that individual control-surface motions would have low correlation with other control-surface motions. This report defines the maximum-likelihood output-error parameter estimation technique used (refs. 1–2), describes the flight test approach, presents stability and control derivative results, compares the results with predictions based on the current F-18B aerodynamic model, and compares aircraft responses obtained from flight data with responses obtained from the nonlinear simulation using updated derivatives from this research.

VEHICLE DESCRIPTION

The test aircraft is the first full-scale development, or preproduction, F-18B built by the McDonnell Douglas Corporation (St. Louis, Missouri), which since has been acquired by The Boeing Corporation, and Northrop Grumman Corporation (Los Angeles, California). This two-place aircraft is powered by two General Electric (Lynn, Massachusetts) F404-GE-400 afterburning engines, rated at approximately 16,000-lbf static thrust at sea level. The aircraft features a midwing configuration with a wing-root leading-edge extension that extends from the forward portion of the fuselage and blends into the wing. Flown by NASA Dryden, this particular F-18B airplane is known as the SRA and is highly instrumented for research purposes. Figure 2 shows a three-view drawing of the SRA and its major physical characteristics. Table 1 shows the reference area and lengths used in nondimensionalizing forces and moments.

Table 1. F-18B reference dimensions.

Wing area	400.00 ft^2
Mean aerodynamic chord (*c*)	11.52 ft
Wing span	37.42 ft
Moment reference at 0.25 *c*	*FS* 458.56 *WL* 100.00 *BL* 0.00
Leading edge of *c*	*FS* 423.99

Control Surfaces

Although the SRA is a preproduction F-18B airplane, the left outboard wing panel was changed in a previous program to a production wing panel. The major difference between the production and preproduction outboard wing panel is that the production aileron has approximately 1.7-percent more surface area than the preproduction aileron. The aileron actuator fairing on the lower surface of the outboard wing panel also was modified for a previous SRA project. The aileron actuators on both wings are identical; however, the fairings are different (fig. 5).

The SRA has five pairs of control surfaces (fig. 2): stabilators, rudders, ailerons, LEFs, and TEFs. Twin vertical tails, each with trailing-edge rudders, are canted outboard approximately 20° from the vertical axis. Conventional pitch control is provided by the symmetric deflection of the all-movable horizontal stabilators, symmetric LEFs, and symmetric TEFs. The LEF consists of separate inboard and outboard LEF surfaces that are controlled by the same actuator and are therefore considered to be a single surface in this report. This feature is different than the future AAW aircraft, which will be able to independently actuate inboard and outboard LEF surfaces. Roll control uses aileron deflection (δ_a), differential horizontal stabilator deflection (δ_{dh}), differential LEF deflection (δ_{dLEF}), and differential TEF deflection (δ_{dTEF}). Directional control is provided by rudder deflection (δ_r) and a rudder-to-aileron interconnect. In addition, the FCS augments lateral-directional control with an aileron-to-rudder interconnect. Symmetric aileron droop and rudder toe-in are employed only in the power-approach configuration. A speed brake is located on the upper aft fuselage, between the vertical stabilizers, but was not used in this research program. Table 2 shows the maximum control-surface position and rate limits for the SRA, which are identical for both the SRA and the basic F-18A or F-18B aircraft.

Table 2. F-18 aerodynamic control-surface position and rate limits.

Surface	Position limit, deg	Rate limit, deg/sec
Stabilator:		
Trailing edge up	24.0	40
Trailing edge down	10.5	40
Aileron:		
Trailing edge up	24.0	100
Trailing edge down	45.0	100
Rudder:		
Trailing edge left	30.0	82
Trailing edge right	30.0	82
TEF:		
Up	8.0	18
Down	45.0	18
LEF:		
Up	3.0	15
Down	33.0	15
Speed brake:		
Trailing edge up	60.0	20–30

Note that although the inboard and outboard LEFs are controlled by the same actuator, they experience different deflections because of twisting and bending of the wing structure under aerodynamic loading. Given the constraint of a single actuator, independently deflecting inboard and outboard surfaces to thereby obtain individual control-surface effectiveness values was not possible.

Consequently, an approach was developed to combine the inboard and outboard measurements into one effective LEF deflection. This approach used flap surface area ratios for obtaining an effective symmetric deflection. Each inboard LEF contributed 36.5 percent of the total LEF area, and each outboard LEF contributed 13.5 percent of the total LEF area. A similar but more complex approach was used to obtain an effective differential LEF deflection between left and right wings. This approach included taking the ratio of the product of wing panel areas and moment arms for the inboard and outboard wing panels, which resulted in defining an effective differential LEF deflection that included 28.6 percent of the outboard LEF deflection values and 71.4 percent of the inboard LEF deflection values.

The definitions of control-surface deflections are shown in the following equations:

Symmetric deflections:

$$\delta_{LEF} = 0.135(\delta_{LEF_{LO}} + \delta_{LEF_{RO}}) + 0.365(\delta_{LEF_{LI}} + \delta_{LEF_{RI}})$$
$$\delta_{TEF} = 0.5(\delta_{TEF_{Left}} + \delta_{TEF_{Right}})$$
$$\delta_{sa} = 0.5(\delta_{a_{Left}} + \delta_{a_{Right}})$$
$$\delta_{e} = 0.5(\delta_{e_{Left}} + \delta_{e_{Right}})$$

Differential deflections:

$$\delta_{r} = 0.5(\delta_{r_{Left}} + \delta_{r_{Right}})$$
$$\delta_{dLEF} = 0.286(\delta_{LEF_{RO}} - \delta_{LEF_{LO}}) + 0.714(\delta_{LEF_{RI}} - \delta_{LEF_{LI}})$$
$$\delta_{dTEF} = \delta_{TEF_{Left}} - \delta_{TEF_{Right}}$$
$$\delta_{a} = \delta_{a_{Left}} - \delta_{a_{Right}}$$
$$\delta_{dh} = \delta_{e_{Left}} - \delta_{e_{Right}}$$

Figure 6 (ref. 3) shows the symmetric LEF and TEF deflections used by the basic F-18 FCS. For the majority of the high-speed and low-angle-of-attack flight conditions investigated in this report, the basic FCS commanded 0° symmetric LEF and TEF deflection. Similarly, for all test conditions investigated in this report, the basic FCS commanded 0° symmetric aileron because symmetric aileron is only used in the low-speed power-approach configuration. For the research presented in this report, symmetrically deflecting the LEF, TEF, and ailerons at flight speeds faster than the basic FCS will allow was desired. Thus, the installation and use of a research flight control system (RFCS), described in the next section, was required.

Software Configuration

The FCS for the basic F-18 aircraft consists of quadruply-redundant 701E (General Electric, Lynn, Massachusetts) flight control computers running the standard F-18 version 10.1 flight control law, which is a digitally mechanized fly-by-wire control augmentation system. The SRA is equipped with a production support flight control computer built by Lockheed Martin Corporation (Bethesda, Maryland) that incorporates both the 701E flight control computer and a RFCS computer (ref. 4). The RFCS computer is used to operate an OBES that adds doublet inputs onto the command from the standard F-18 flight control laws, which results in the excitation of individual control surfaces without pilot stick and rudder inputs. The RFCS does not deactivate any inner-loop feedback, nor does it override any position or rate limits of the basic FCS.

The aircraft was under RFCS control only during the up-and-away research portions of a test flight. Software in the OBES contained preprogrammed PID maneuvers. The pilot selected the desired maneuver by a series of six key punches on the cockpit digital display indicator. The pilot then armed the maneuver with an additional key punch. After receiving clearance from the control room to proceed, the pilot engaged the maneuver using the existing nosewheel steering switch on the control stick. The pilot could disengage the RFCS at any time using a control-stick paddle switch.

Mass Properties

Accurate estimates of weight, center of gravity (*CG*), and inertias were required for each PID maneuver. A weight-and-balance ground test was performed to determine the unfueled aircraft weight and *CG*. Fuel data were obtained by the pilot prior to and after the test points and radioed to the ground control room. The pilot read fuel values from the four fuselage tanks. The wing fuel tanks were always empty by the time the aircraft was on station for research test points. For each test point, the fuel readings were used in a computer program to obtain aircraft *CG* and moments of inertia. Table 3 shows weight, *CG*, and inertias for an approximately 66-percent–fueled configuration. This configuration is one of many from the flight program and includes both aircrew members, support equipment, and a “clean” (that is, no ordnance or drop tanks), landing-gear-up flight configuration.

Table 3. SRA mass properties for an approximately 66-percent–fueled configuration.

Weight, lb	32,167
CG:	
c, percent	22.70
FS, in.	455.32
WL, in.	103.45
Roll inertia, slug-ft^2	16,179
Pitch inertia, slug-ft^2	119,353
Yaw inertia, slug-ft^2	131,500
Product of inertia, slug-ft^2	–2,120

Instrumentation and Data Acquisition

The SRA is equipped with a complete set of airdata, inertial, and control-surface position instrumentation. Some measurements were obtained from standard F-18 instrumentation; other measurements were obtained by installing additional instrumentation to meet research objectives. Data measurements were telemetered to the ground control room for real-time monitoring and were recorded for postflight analysis. Data were also recorded by an onboard digital recorder.

Measurements from standard F-18 instrumentation included Mach number, altitude, dynamic pressure, true airspeed, angle of attack, pitch and roll attitudes, and control-surface positions. “Pitot-static” information was obtained from production probes mounted on both sides of the fuselage. Flight data from airdata calibration maneuvers were obtained to calibrate the side probes because a previous SRA program required the removal of the upstream electronic countermeasure blisters and thus invalidated the basic aircraft static-pressure error calibration. Angle-of-attack data were obtained from standard F-18 fuselage side-mounted cones. Aircraft pitch- and roll-attitude data were obtained from the F-18 inertial navigation system (INS). Rotary variable differential transformers (RVDTs) were used by the FCS for control-surface position information. The RVDTs were installed on the surface actuator or transmission and thus were unable to measure total surface deflections, which include the effects of surface bending or twisting caused by aerodynamic loads.

The measurements from the standard F-18 instrumentation data were obtained from the F-18 military standard 1553 multiplex data bus. Data on the bus were lagged in time by a variable (but nearly constant) amount of time. This lag was a function of the amount of bus activity. The 1553 data parameters used for the PID analysis (angle of attack, pitch and roll attitudes, and RVDT measurements) were time-skewed by 0.1 sec to account for the lag. The 0.1-sec lag was determined by cross correlation of bus parameters with similar parameters that were not obtained from the bus (for example, INS-measured angular rates were obtained from the bus and cross correlated with angular rates obtained by independent measurements that were not time-lagged by the bus). Making these lag corrections was critical to accurately estimating stability and control derivatives.

Additional research instrumentation was added to the SRA to provide angle of sideslip, three-axes linear acceleration and angular rates, and control-surface positions. These data did not have the time-lag problem associated with data from the 1553 bus. Angle of sideslip was obtained from a nosetip-mounted flush airdata sensing (FADS) system that was developed in a previous SRA program (ref. 5). Sideslip data were also time-skewed by 0.1 sec to account for pneumatic lag in the FADS pressure lines. This lag was determined during the parameter estimation analysis by comparing measured and estimated angles of sideslip. A package of three-axes linear accelerometers and rate gyros was installed specifically for this research project to give inertial data completely independent of standard F-18 signal conditioning and 1553 data bus latencies. Control-surface position transducers (CPTs) were installed on each control surface to measure surface deflections. The CPTs provided a direct measurement of the surface deflection and thus recorded uncommanded motions caused by aerodynamic loads.

Data from the 1553 data bus were recorded at 25 samples/sec. The CPT and FADS angle-of-sideslip data were recorded at 50 samples/sec. Angular rates and linear accelerations from the research instrumentation package were recorded at 100 samples/sec. Signal conditioning included presample antialiasing filters for all measurements. Data were either thinned or interpolated to create a

50 samples/sec data set for PID analysis. Measurements of angles of attack and sideslip and linear accelerations were corrected for *CG* offset in the parameter estimation program. Angle of attack was measured at fuselage station (*FS*) 165.00; angle of sideslip was measured at *FS* 60.00 and water line (*WL)* 92.00; and the linear accelerations were measured at *FS* 298.50, butt line (*BL)* –14.00, and *WL* 92.15.

METHODS OF ANALYSIS

The formulation of the output-error parameter estimation technique used to analyze the flight data is described. The nonlinear equations of motion used in the analysis are defined. The approach used to update the aerodynamic model in the simulation based on parameter estimation results is also described.

Parameter Identification Formulation

The primary objective of this research is to estimate from flight test the control effectiveness of each control surface of the F-18 at high dynamic pressures. The actual vehicle system was modeled as a vector set of dynamic equations of motion that are defined in the next section. The form of these equations was assumed to be known, but the aerodynamic stability and control parameters in these equations were assumed to be unknown. The PID flight test maneuvers were flown to measure the response of the aircraft to predefined control-surface inputs. The parameter estimation program called pEst (ref. 1) was then used to adjust the unknown parameter values in the aerodynamic model until the estimated aircraft response agreed with the measured response.

The pEst program defines a cost function that can be used to quantitatively measure the agreement between the flight-measured response of the aircraft and the computed response based on the pEst program–determined aerodynamic model. The pEst program also mechanizes the process of searching for the unknown parameter values.

To obtain the cost function, the pEst program must solve a vector set of time-varying, ordinary differential equations of motion. The equations of motion are separated into a continuous-time–state equation and a discrete-time–response equation.

$$\dot{\mathbf{x}}(t) = \mathrm{F}[\mathbf{x}(t), \mathbf{u}(t), \xi] \tag{1}$$

$$\mathbf{z}(t_i) = \mathrm{G}[\mathbf{x}(t_i), \mathbf{u}(t_i), \xi] \tag{2}$$

where F is the state derivative function, G is the response function, $\mathbf{x}$ is the state vector, $\mathbf{z}$ is the response or measurement vector, $\mathbf{u}$ is the control input vector, ξ is the stability and control derivative parameter vector, and t is time. For this application of stability and control derivative estimation, state noise was assumed to not exist.

The output-error cost function, $J(\xi)$, used by the pEst program was as follows:

$$J(\xi) = \frac{1}{2n_z n_t} \sum_{i=1}^{n_t} [\mathbf{z}(t_i) - \tilde{\mathbf{z}}(t_i)]^* W [\mathbf{z}(t_i) - \tilde{\mathbf{z}}(t_i)] \tag{3}$$

where n_t is the number of time history points used, n_z is the number of response variables, $\tilde{\mathbf{z}}$ is the computed response vector, and W is the response weighting matrix. The superscript asterisk denotes transpose.

For each possible estimate of the unknown stability and control parameters, a probability that the aircraft response time histories attain values near the observed values can be defined. The maximum-likelihood estimates are defined as those estimates that maximize this probability. Minimizing the cost function gives the maximum-likelihood estimate of the stability and control parameters. Figure 7 shows the maximum-likelihood estimation process. The measured response is compared with the estimated response, and the difference between these is called the response error and is included in the cost function. The minimization algorithm is used to find the parameter values that minimize the cost function. Each iteration of this algorithm provides a new estimate of the unknown parameters on the basis of the response error. Updating of the mathematical model with the new parameters continues iteratively until a convergence criterion is satisfied (in this case, the ratio of the change in total cost to the total cost, $\Delta J(\xi)/J(\xi)$, must be less than 0.000001). The stability and control parameter estimates resulting from this procedure are the maximum-likelihood estimates.

The estimator also provides a measure of the reliability of each estimate based on the information obtained from each dynamic maneuver. This measure of reliability is called the Cramér-Rao bound (ref. 6). In practice, the Cramér-Rao bound is used as a measure of relative, not absolute, accuracy. A large Cramér-Rao bound indicates poor information content for the derivative estimate.

Equations of Motion

The aircraft equations of motion used in the PID analysis are derived from the more general system of nine coupled, nonlinear differential equations that describe the aircraft motion (ref. 2). These equations assume a rigid vehicle and a flat, nonrotating Earth. The time-rate of change of mass and inertia is assumed negligible. The SRA configuration studied here, like most aircraft, is nearly symmetric about the x-z plane. This symmetry is used, along with small angle approximations, to separate the equations of motion into two largely independent sets describing the longitudinal and lateral-directional motions of the aircraft. The nonsymmetries shown in figure 5 are not considered large enough to invalidate this approach. The equations of motion are written in body axes referenced to the *CG* and include both state and response equations. The applicable equations of motion are as follows for the longitudinal and lateral-directional axes:

Longitudinal state equations:

$$\dot{\alpha} = -\frac{\bar{q}SR}{mV\cos\beta} C_N \cos\alpha + q - \tan\beta(p \cos\alpha + r \sin\alpha) + \frac{gR}{V\cos\beta}(\cos\phi\cos\theta\cos\alpha + \sin\theta\sin\alpha) \tag{4}$$

$$\dot{q}\, I_y = \bar{q}ScC_m R + [rp(I_z - I_x) + (r^2 - p^2)I_{xz}]/R \tag{5}$$

$$\dot{\theta} = q \cos\phi - r \sin\phi \tag{6}$$

Longitudinal response equations:

$$\tilde{\alpha} = \alpha + x_\alpha \frac{q}{V} \tag{7}$$

$$\tilde{q} = q + q_{bias} \tag{8}$$

$$\tilde{\theta} = \theta \tag{9}$$

$$\tilde{a}_n = \frac{\bar{q}S}{mg} C_N - \frac{1}{gR}[x_{a_n}\dot{q} + y_{a_n}\dot{p}] - \frac{1}{gR^2} z_{a_n}(q^2 + p^2) + a_{n_{bias}} \tag{10}$$

where q_{bias} and $a_{n_{bias}}$ are estimates of instrumentation biases.

Lateral-directional state equations:

$$\dot{\beta} = \frac{\bar{q}SR}{mV} C_Y + p \sin\alpha - r \cos\alpha + \frac{gR}{V}[\sin\phi\cos\theta\cos\beta - \sin\beta(\cos\theta\cos\phi\sin\alpha - \sin\theta\cos\alpha)] \tag{11}$$

$$\dot{p}I_x - \dot{r}I_{xz} = \bar{q}SbC_l R + [qr(I_y - I_z) + pqI_{xz}]/R \tag{12}$$

$$\dot{r}I_z - \dot{p}I_{xz} = \bar{q}SbC_n R + [pq(I_x - I_y) - qrI_{xz}]/R \tag{13}$$

$$\dot{\phi} = p + q\tan\theta \sin\phi + r \tan\theta \cos\phi \tag{14}$$

Lateral-directional response equations:

$$\tilde{\beta} = \beta + \left[z_\beta \frac{p}{V} - x_\beta \frac{r}{V}\right] + \beta_{bias} \tag{15}$$

$$\tilde{p} = p + p_{bias} \tag{16}$$

$$\tilde{r} = r + r_{bias} \tag{17}$$

$$\tilde{\phi} = \phi \tag{18}$$

$$\tilde{a}_y = \frac{\bar{q}S}{mg}C_Y - \frac{1}{gR}[-x_{a_y}\dot{r} + z_{a_y}\dot{p}] - \frac{1}{gR^2}y_{a_y}(p^2 + r^2) \tag{19}$$

where β_{bias}, p_{bias}, and r_{bias} are estimates of instrumentation biases.

Equations 4–19 contain locally linear approximations of the aerodynamic coefficients. The longitudinal aerodynamic coefficients are expanded as follows:

$$C_N = C_{N_b} + C_{N_\alpha}\alpha + \frac{c}{2VR}C_{N_q}q + C_{N_{\delta_{LEF}}}\delta_{LEF} + C_{N_{\delta_{TEF}}}\delta_{TEF} + C_{N_{\delta_{sa}}}\delta_{sa} + C_{N_{\delta_e}}\delta_e \tag{20}$$

$$C_m = C_{m_b} + C_{m_\alpha}\alpha + \frac{c}{2VR}C_{m_q}q + C_{m_{\delta_{LEF}}}\delta_{LEF} + C_{m_{\delta_{TEF}}}\delta_{TEF} + C_{m_{\delta_{sa}}}\delta_{sa} + C_{m_{\delta_e}}\delta_e \tag{21}$$

The coefficients are based on a reference area of 400 ft^2 and c = 11.52 ft. The moment reference is at 0.25 c, which is at *FS* 458.56. The coefficient with the subscript "*b*" is a linear extrapolation of the angle-of-attack derivative from the average angle of attack of the maneuver to 0° angle of attack (ref. 2). Axial-force coefficients were not used in this analysis because the axial-force derivatives were not expected to affect flying qualities, and getting good estimates of axial-force derivatives without thrust measurements is generally difficult. All the longitudinal derivatives in equations (20)–(21) were estimated in the analysis.

The lateral-directional aerodynamic coefficients are expanded as follows:

$$\begin{aligned} C_Y = {} & C_{Y_b} + C_{Y_\beta}\beta + \frac{b}{2VR}(C_{Y_p}p + C_{Y_r}r) + C_{Y_{\delta_a}}\delta_a \\ & + C_{Y_{\delta r}}\delta_r + C_{Y_{\delta_{dLEF}}}\delta_{dLEF} + C_{Y_{\delta_{dTEF}}}\delta_{dTEF} + C_{Y_{\delta_{dh}}}\delta_{dh} \end{aligned} \tag{22}$$

$$\begin{aligned} C_l = {} & C_{l_b} + C_{l_\beta}\beta + \frac{b}{2VR}(C_{l_p}p + C_{l_r}r) + C_{l_{\delta a}}\delta_a \\ & + C_{l_{\delta r}}\delta r + C_{l_{\delta_{dLEF}}}\delta_{dLEF} + C_{l_{\delta_{dTEF}}}\delta_{dTEF} + C_{l_{\delta_{dh}}}\delta_{dh} \end{aligned} \tag{23}$$

$$\begin{aligned} C_n = {} & C_{n_b} + C_{n_\beta}\beta + \frac{b}{2VR}(C_{n_p}p + C_{n_r}r) + C_{n_{\delta a}}\delta_a \\ & + C_{n_{\delta r}}\delta_r + C_{n_{\delta_{dLEF}}}\delta_{dLEF} + C_{n_{\delta_{dTEF}}}\delta_{dTEF} + C_{n_{\delta_{dh}}}\delta_{dh} \end{aligned} \tag{24}$$

The reference wing span, *b*, is 37.42 ft. The coefficient with the subscript "*b*" is a linear extrapolation of the angle-of-sideslip derivative from the average angle of sideslip of the maneuver to 0° angle of sideslip. All the lateral-directional derivatives in equations (22)–(24) were estimated in the analysis.

Aerodynamic Model Update

The PID flight tests have been used to identify the force and moment derivatives in equations (20)–(24). The ground-based simulations contain an aerodynamic model that includes both aerodynamic coefficients (as a function of flow angles, Mach number, and altitude) and aerodynamic derivatives. A linearizer can be run on the ground-based simulation to obtain locally linear stability and control derivatives as a function of Mach and altitude. To update the aerodynamic model, derivative increments were obtained between the flight-determined derivatives and the simulation aerodynamic model derivatives obtained from the linearizer. The derivative increments were combined with aerodynamic state and control surface measurements to define total force and moment coefficient increments as shown in equations (25)–(29).

$$\begin{aligned}\Delta C_N = {} & \Delta C_{N_b} + \Delta C_{N_\alpha}\alpha + \Delta C_{N_q}\frac{qc}{2VR} + \Delta C_{N_{\delta_{LEF}}}\delta_{LEF} \\ & + \Delta C_{N_{\delta_{TEF}}}\delta_{TEF} + \Delta C_{N_{\delta_{sa}}}\delta_{sa} + \Delta C_{N_{\delta_e}}\delta_e\end{aligned} \tag{25}$$

$$\begin{aligned}\Delta C_m = {} & \Delta C_{m_b} + \Delta C_{m_\alpha}\alpha + \Delta C_{m_q}\frac{qc}{2VR} + \Delta C_{m_{\delta_{LEF}}}\delta_{LEF} \\ & + \Delta C_{m_{\delta_{TEF}}}\delta_{TEF} + \Delta C_{m_{\delta_{sa}}}\delta_{sa} + \Delta C_{m_{\delta_e}}\delta_e\end{aligned} \tag{26}$$

$$\begin{aligned}\Delta C_Y = {} & \Delta C_{Y_b} + \Delta C_{Y_\beta}\beta + \Delta C_{Y_p}\frac{pb}{2VR} + \Delta C_{Y_r}\frac{rb}{2VR} + \Delta C_{Y_{\delta_{dLEF}}}\delta_{dLEF} \\ & + \Delta C_{Y_{\delta_{dTEF}}}\delta_{dTEF} + \Delta C_{Y_{\delta_a}}\delta_a + \Delta C_{Y_{\delta_{dh}}}\delta_{dh} + \Delta C_{Y_{\delta_r}}\delta_r\end{aligned} \tag{27}$$

$$\begin{aligned}\Delta C_l = {} & \Delta C_{l_b} + \Delta C_{l_\beta}\beta + \Delta C_{l_p}\frac{pb}{2VR} + \Delta C_{l_r}\frac{rb}{2VR} + \Delta C_{l_{\delta_{dLEF}}}\delta_{dLEF} \\ & + \Delta C_{l_{\delta_{dTEF}}}\delta_{dTEF} + \Delta C_{l_{\delta_a}}\delta_a + \Delta C_{l_{\delta_{dh}}}\delta_{dh} + \Delta C_{l_{\delta_r}}\delta_r\end{aligned} \tag{28}$$

$$\begin{aligned}\Delta C_n = {} & \Delta C_{n_b} + \Delta C_{n_\beta}\beta + \Delta C_{n_p}\frac{pb}{2VR} + \Delta C_{n_r}\frac{rb}{2VR} + \Delta C_{n_{\delta_{dLEF}}}\delta_{dLEF} \\ & + \Delta C_{n_{\delta_{dTEF}}}\delta_{dTEF} + \Delta C_{n_{\delta_a}}\delta_a + \Delta C_{n_{\delta_{dh}}}\delta_{dh} + \Delta C_{n_{\delta_r}}\delta_r\end{aligned} \tag{29}$$

These increments have been added to the original aerodynamic model coefficients to obtain the updated aerodynamic model.

FLIGHT TEST APPROACH

The objective of this work is to obtain baseline F-18 control-surface effectiveness values for the initial control-law development for the AAW project. Consequently, PID data were obtained at the AAW test points shown in figure 3. A complete set of stability and control derivatives was obtained at each test point. As is typical, PID maneuvers were performed to separately obtain longitudinal and lateral-directional derivatives. Each longitudinal PID maneuver was composed of a sequence of SSI doublets in the following order: symmetric LEF, symmetric TEF, symmetric aileron, and symmetric stabilator. Each lateral-directional PID maneuver was composed of SSI doublets in the following order: rudder, differential LEF, differential TEF, aileron, and differential stabilator.

The term “single-surface input” refers to the ability of the OBES to independently excite each pair of control surfaces while making no input commands to the other surfaces. Note that even under OBES control, the feedback control system of the aircraft is still active. The initial OBES SSI caused a perturbation from trim. The feedback control system responded to the perturbation with additional control-surface deflection commands to several of the control-surface pairs. The control-surface excitation for each PID maneuver then was the sum of the SSIs for each pair of control surfaces plus the additional control-surface motions caused by the control system feedback.

The OBES is capable of obtaining control-surface deflections that are not highly correlated with (that is, independent of) the motion of the other control-surface pairs. The active feedback control system did result in some correlation of the control-surface motions; however, enough motion that was not correlated existed to get good identification of the individual control-surface effectivenesses.

The PID maneuvers were designed to accommodate two research objectives: stability and control derivative extraction (the purpose of this paper), and structural component loads modeling. The latter objective often led to the size of the doublet maneuvers being larger than necessary for stability and control derivative extraction. However, all maneuvers presented in this report have been deemed acceptable for PID analysis. The amplitudes of the control-surface deflections were varied for different test conditions because high–dynamic pressure flight conditions generally required small inputs because of structural load constraints. Table 4 shows the definition of large, medium, and small longitudinal and lateral-directional SSI sequences.

Each SSI doublet consisted of a 1-sec deflection in the positive direction followed by a 1-sec deflection in the negative direction. The deflections were done from a trimmed surface position. A 5-sec delay was programmed between each SSI. Minimal pilot stick and rudder inputs were requested during the maneuver sequence. However, the pilot was requested to make adjustments to bring the aircraft to wings level and maintain Mach number and altitude conditions during the 5-sec delays between SSIs. The thrust of the SRA was not sufficient to maintain altitude for some high–dynamic pressure test points. For these points, the pilot maintained the desired Mach number while commanding a slight dive through the target altitude with full engine afterburner.

Table 4. PID maneuver doublet sizes.

Doublets	SSI sequence		
	Large amplitude, deg	Medium amplitude, deg	Small amplitude, deg
Longitudinal:			
δ_{LEF} [a]	±3	±2	±1
δ_{TEF} [a]	±5	±4	±3
δ_{sa}	±6	±5	±4
δ_{e}	±1	±1	±1
Lateral-directional:			
δ_{r}	±4	±4	±4
δ_{dLEF}	±6	±4	±2
δ_{dTEF}	±10	±8	±6
δ_{a}	±12	±10	±8
δ_{dh}	±6	±6	±6

[a] Negative symmetric LEF and TEF deflections were not possible because of limitations in the flight control computer.

Figure 8 shows a typical large, longitudinal SSI doublet sequence time history using the RVDT outputs of the commanded surface deflections. Figure 8(a) shows the four LEF RVDT outputs. As can be seen, the negative portion of the OBES-commanded LEF doublet was completely eliminated because the trimmed position was near 0°. Similarly, as figure 8(b) shows, the negative portion of the TEF doublet was truncated at 0° deflection. The difference between right and left surface positions for the aileron and stabilator (figs. 8(c) and 8(d), respectively) was required to trim out the known right roll tendency of the aircraft. The effect of FCS feedback on the OBES input is clearly seen in the stabilator deflections. Figure 8(d) shows FCS-commanded stabilator response to LEF, TEF, and aileron inputs. Figure 8(d) also shows that the stabilator doublet inputs are quickly “taken out” by the feedback of the primary FCS. The FCS feedback response did not significantly degrade the maneuver quality because the aircraft had time to respond to the sharp doublet inputs.

Figure 9 shows a typical large, lateral-directional SSI doublet sequence time history. In this case, approximately –1° of rudder trim is required to trim out the known left yaw tendency of the aircraft as shown in figure 9(a). Also, the rudder SSI can be seen to be quickly “taken out” by the FCS. Again, the FCS feedback response did not significantly degrade the quality of the PID maneuver.

Before and after each doublet sequence, the pilot radioed fuel readings from the four fuselage tanks. In postflight analysis, fuel readings were used to compute aircraft *CG* and inertias. Mach number, altitude, and mass properties were input into a batch simulation of the aircraft, and a linearizer was used to obtain simulation predictions of the stability and control derivatives. The baseline F-18B aerodynamic model used by the simulation was obtained from the Naval Air Warfare Center (Patuxent River, Maryland) Common Database version 3.1.

RESULTS AND DISCUSSION

This section contains results from analyzing 112 PID flight test maneuvers. Unexpected deflections of the LEFs during the maneuvers are discussed first. Stability and control derivative results from the longitudinal and lateral-directional maneuvers are then presented for analyses using CPT-measured and RVDT-measured surface positions. Finally, a comparison is made between measured aircraft responses obtained from flight data and responses obtained from the nonlinear simulation using updated stability and control derivatives from this research.

All moment coefficients and derivatives were obtained at the flight *CG* and then translated (ref. 7) to a standard moment-reference location for plotting. The moment-reference location on the SRA is at *FS* 458.56 (0.25 *c*), *BL* 0.00, and *WL* 100.00. Trim angle of attack was between –1 and 2° for all test points and therefore was not used as a variable for plotting derivatives. Each derivative is plotted as a function of Mach number and altitude and with its corresponding scaled Cramér-Rao uncertainty level (ref. 8). The Cramér-Rao uncertainly levels obtained from the pEst program were multiplied by a factor of 5 for plotting to improve the ability to discern the estimate quality. The simulation prediction of the derivatives using the basic F-18B aerodynamic model also will be shown.

Unexpected Leading-Edge Flap Deflections

Control-surface instrumentation enabled the discovery of significant LEF control-surface motion, not commanded, during some of the PID maneuvers and during the transition between subsonic and supersonic flight. These results are presented in this section.

Control-Surface Position Transducer and Rotary Variable Differential Transformer Deflection Measurements

Figure 10 shows a time history of the symmetric aileron SSI portion of a subsonic, large, longitudinal doublet sequence. Figure 10(a) shows the aileron deflection commanded by the OBES. Although no LEF deflection was being commanded by the OBES, the FCS commanded a small amount of LEF deflection at the end of the doublet (fig. 10(b)) to respond to this somewhat dynamic maneuver in which a maximum normal acceleration of 3 *g* was obtained (fig. 10(d)). Figure 10(b) shows the RVDT measurements of the LEF deflections. Figure 10(c) shows the CPT measurements of the LEF deflections. As can be seen, much more motion was measured using the CPTs (which give a direct measurement of the surface position) than was measured using the RVDTs (which measure actuator and transmission positions). Also, the outboard surface CPTs showed more deflection than the inboard surface CPTs, resulting in a small split between inboard and outboard surfaces. These CPT measurements were considered suspect during the initial flight tests. Fortuitously, however, the right outboard LEF was instrumented for hinge-moment (*HM*) measurements. The *HM* measurements (fig. 10(e)) correlated well with the CPT measurements (fig. 10(c)) and not with the RVDT measurements (fig. 10(b)). Therefore, the CPTs were concluded to be a better indicator of actual surface motion.

Sonic Split

The inboard and outboard LEF surfaces were observed from CPT measurements to track well together during subsonic nonmaneuvering flight and to split by as much as 2° for supersonic flight. The surfaces then tracked well again as the aircraft returned to subsonic speeds. Figure 11 shows this repeatable effect, which is not measured by the RVDTs. This effect does not adversely affect the PID analysis because PID information comes from small perturbations about a trim point. The split only affects the trim configuration.

Stability and Control Derivative Results Using Control-Surface Position Transducer Measurements

This section presents stability and control derivatives obtained from PID flight maneuvers using CPT measurements in the analysis. The sizes of the doublet SSIs varied depending on flight condition. Figure 12 shows the maximum-sized maneuver used at each test condition for longitudinal doublets (fig. 12(a)) and lateral-directional doublets (fig. 12(b)). At some flight conditions, smaller-sized SSI doublets were also used. Figures 13–19 show the longitudinal derivatives and figures 20–28 show the lateral-directional derivatives obtained from the PID analysis. The derivatives are plotted as a function of freestream Mach number and altitude. All moment derivatives were obtained about the aircraft flight *CG* and then translated (ref. 7) to the moment reference (table 1) for plotting. The symbols represent the pEst program estimates of the derivative, and the lines represent the simulation prediction of the derivative at the same flight condition.

The scaled Cramér-Rao uncertainty bound is also shown for each pEst program estimate. The results are grouped by altitude because the data were obtained at approximately 5,000-ft intervals at altitudes between 5,000 and 25,000 ft. Appendices A and B show time history comparisons of the flight-measured and computed responses resulting from the PID analysis for each test condition for typical longitudinal and lateral-directional maneuvers, respectively.

Longitudinal Stability and Control Results

Figure 13 shows normal-force and pitching-moment coefficient biases. These bias values are not the traditional normal-force and pitching-moment coefficients at 0° angle of attack and no control-surface deflections. The predicted bias values come from the simulation linearizer. The linearizer provided a linear representation of the coefficient about the trim condition. The bias is simply the extrapolation of the linear fit to 0° angle of attack. Similarly, the flight data are obtained from the pEst program. The coefficient bias obtained in the pEst program is also the extrapolation of the linear fit to 0° angle of attack. For the data points presented, the trim angle of attack varied between –1° and 2°.

The simulator angle of attack typically trimmed approximately 0.5°–1.0°, higher than the flight-measured angle of attack. Airdata reconstruction techniques confirmed that the flight-measured trim angle of attack had a bias error that caused it to read low. This error was not a problem for the pEst program derivative extraction because the angle-of-attack measurement, while biased, still had the correct variation during the maneuver. However, the biased trim angle-of-attack value does affect the bias coefficient.

Figure 13(a) shows the normal-force coefficient bias results. The flight-determined values are consistently higher than the predictions, which is consistent with the simulator trimming at a higher angle of attack. Figure 13(b) shows the moment coefficient bias results. The flight-determined results are lower than the bias prediction, which also is consistent with the simulator trimming at a higher angle of attack.

Figure 14 shows the angle-of-attack derivatives. The flight-determined normal-force coefficient derivative results (fig. 14(a)) are 10–20-percent lower than the simulation prediction and show no significant trend with altitude. The flight-determined longitudinal stability derivative, however, is considerably less stable (that is, less negative) than the simulation prediction at all Mach numbers (fig. 14(b)). As altitude is decreased subsonically, a more stable derivative is observed because of aircraft flexibility effects.

Figure 15 shows the dynamic derivatives. A significant amount of scatter exists in the results with no strong altitude effect. The simulation predictions offer a reasonable fairing of the flight results for the normal-force coefficient due to nondimensional pitch rate, C_{N_q}. The flight-determined damping derivative (the pitching-moment coefficient due to nondimensional pitch rate, C_{m_q}), shows a definite trend at transonic Mach numbers. The C_{m_q} derivative becomes more negative than predictions at high subsonic Mach numbers and less negative at low supersonic Mach numbers.

Figure 16 shows the symmetric LEF derivatives. The normal-force derivative results (fig. 16(a)) agree well with the predictions except at approximately Mach 0.85 and Mach 0.95, where the flight data are more negative. The pitching-moment derivative results (fig. 16(b)) show reasonably good agreement subsonically between flight and predictions. Supersonic flight results show a trend toward zero pitching-moment effectiveness of the LEFs as Mach number increases to 1.3. This trend is in sharp contrast to the predictions that showed increasing nosedown effectiveness of the LEFs as Mach number increased.

Figure 17 shows the symmetric TEF derivatives. The flight-determined normal-force derivative results are significantly lower than the predictions (fig. 17(a)). Figure 17(b) shows the pitching-moment derivative. The simulation predicted a slight increase in the pitching-moment coefficient caused by symmetric TEF deflection, $C_{m_{\delta_{TEF}}}$, as altitude increased. This trend was not apparent from the flight results. The flight data are somewhat scattered but show agreement with the prediction of the derivative decreasing as Mach number increased. In general, the flight results showed less nosedown effectiveness than predicted.

Figure 18 shows the symmetric aileron derivatives. The normal-force derivative (fig. 18(a)) shows reasonable agreement between flight and predicted results. Figure 18(b) shows the pitching-moment derivative. The flight-determined derivative values indicate that the symmetric ailerons are significantly more effective than predicted, especially at subsonic speeds. The predicted trend of increasing nosedown effectiveness with increasing altitude was seen in the flight data.

Figure 19 shows the elevator (symmetric stabilator) derivatives. The flight values of the normal-force derivative agree well with predictions (fig. 19(a)). The pitching-moment effectiveness is slightly less than predicted (fig. 19(b)).

Lateral-Directional Stability and Control Results

Figure 20 shows the lateral-directional, zero-sideslip, trimmed coefficients. As previously stated in the "Vehicle Description" section, the SRA is not completely symmetrical about the x-z plane. The left outboard wing panel is a production panel, whereas the right outboard panel is a preproduction one. Also, and more significantly, a large aileron actuator fairing exists under the left outboard wing panel. The result of these (and other smaller, undocumented) asymmetries is that the SRA exhibits right roll and left yaw tendencies that are nominally trimmed out for straight-and-level flight. A large part of the left yaw tendency is suspected to be caused by the added drag associated with the large actuator fairing under the left wing. The pEst program analysis clearly identified a positive rolling moment (fig. 20(b)) and a negative yawing moment (fig. 20(c)) at 0° sideslip. A slight, positive side force (fig. 20(a)) was also identified that could be caused in part by the outboard bulging of the left aileron actuator fairing. The large Cramér-Rao bounds at Mach 0.95 and Mach 1.2 (fig. 20) were a result of poor sideslip information. At these test points, the FADS measurement of angle of sideslip did not work. Consequently, the sideslip response was weighted very low in the PID analysis, which resulted in very large Cramér-Rao bounds for these coefficient bias parameters. The actual value of the estimates agrees well with other estimates because of accurate lateral-acceleration measurements.

Figure 21 shows the angle-of-sideslip derivatives. The flight-determined side-force derivative (fig. 21(a)) is slightly smaller in magnitude than the prediction. Figure 21(b) shows the dihedral effect. With the exception of data at Mach 0.95, the flight-determined data show more negative values of the rolling-moment coefficient due to sideslip, C_{l_β}, than existed in the predictions. The predictions showed the C_{l_β} becoming more negative with increasing altitude. Flight results did not show this trend, but generally showed a nearly constant value throughout the Mach number and altitude range. The lateral-directional static stability derivative (the yawing-moment coefficient due to sideslip, C_{n_β}) showed stability levels noticeably lower (that is, less positive) than predicted throughout the Mach number range. For supersonic conditions, the flight data does show the predicted altitude effects caused by aircraft flexibility.

Figures 22 and 23 show the dynamic derivatives caused by roll and yaw rates, respectively. The rolling-moment coefficient due to nondimensional roll rate, C_{l_p}, shows slightly less damping than predictions (fig. 22(b)), whereas the yawing-moment coefficient due to nondimensional yaw rate, C_{n_r}, shows slightly more damping than predicted (fig. 23(c)).

Figure 24 shows the rudder derivatives. The side-force derivative obtained in flight agrees with predictions for subsonic conditions and is lower than predictions for supersonic conditions (fig. 24(a)). The flight-determined rolling moment caused by the rudders tends towards zero as the Mach number becomes supersonic (fig. 24(b)). For supersonic conditions, a more positive rolling moment caused by rudders was predicted. Figure 24(c) shows the yawing moment caused by rudder deflection. For subsonic conditions, the flight-determined and predicted values agree reasonably well. For supersonic conditions,

the flight-determined values show less effectiveness than the predictions. The small altitude effect seen in the predictions was also seen in the flight data.

Figure 25 shows the differential LEF derivatives. The simulation predicted zero side force caused by differential LEF deflections. Flight data show near-zero side force caused by differential LEF (fig. 25(a)). The flight-determined rolling-moment derivative values are generally lower than the simulation predicted (fig. 25(b)). The flight data do show a slight decrease in rolling-moment effectiveness with increasing altitude, but not to the extent predicted by the simulation. The yawing moment obtained from differential deflection of the LEFs was not modeled in the simulation. Figure 25(c) shows flight data.

Figure 26 shows the differential TEF derivatives. Figure 26(a) shows the side-force derivative. Flight data show more negative side force than predicted, especially at supersonic Mach numbers. Figure 26(b) shows the rolling-moment derivative caused by differential TEF. The flight-determined and predicted values agree very well. Trailing-edge flap "reversal" is seen for the Mach 0.95 data at altitudes below 10,000 ft. For supersonic conditions, the flight data show negative derivative values that agree reasonably well with the predictions. Figure 26(c) shows the yawing-moment derivative obtained from flight. At supersonic Mach numbers, the derivative is significantly larger than the simulation prediction and the effects of altitude are not as pronounced.

Figure 27 shows the aileron derivatives. The flight-determined side-force derivative values agree well with the predictions (fig. 27(a)). Figure 27(b) shows the flight-determined aileron rolling-moment effectiveness compared with predictions. The simulation predicted aileron reversal at Mach 0.95 and an altitude of 5000 ft. The flight data do not show aileron reversal, but do show the trend toward zero aileron roll effectiveness as the Mach number increased for subsonic speeds. The flight data also clearly show the predicted trend of reduced roll effectiveness with reduced altitude. The yawing-moment derivative (fig. 27(c)) agrees reasonably well with predictions of near-zero effectiveness.

Figure 28 shows the differential horizontal stabilator derivatives. The simulation predicted a slightly negative side-force derivative, whereas the flight data show values closer to zero and slightly positive at high supersonic Mach numbers (fig. 28(a)). The rolling moment caused by the horizontal stabilator was predicted well (fig. 28(b)). The yawing-moment derivative was predicted well for subsonic conditions, but diverged from predictions and became negative as the Mach number increased supersonically (fig. 28(c)).

Stability and Control Derivatives Results Using Rotary Variable Differential Transformer Surface Positions

As stated previously, obtaining the stability and control derivative results using the RVDT surface-position data instead of the CPT data was of interest. The RVDT instrumentation does not measure the control-surface deflections caused by bending or twisting under aerodynamic loading. For example, during this flight test program, significant LEF control-surface motion caused by aerodynamic effects was measured by the CPTs but not by the RVDTs (fig. 9). However, the stability and control derivatives obtained from RVDT surface-position data are useful for updating ground-based piloted simulations. These simulations do not include aerodynamic effects on the control surfaces and therefore do not take into consideration how the control-surface position are being modified by aerodynamic effects. Therefore, the derivatives obtained using RVDT information can provide accurate vehicle response

simulations without actually considering the total contribution of aerodynamic effects on the control-surface position.

Figures 29–35 show the longitudinal stability and control derivatives obtained using RVDT surface-position inputs into the pEst program. For the most part, these results agree well with the data presented in figures 13–19. Figure 36 shows a comparison of the pitching-moment derivative results. As expected, good agreement is seen in the static stability derivative (fig. 36(a)). The control derivatives show some differences (figs. 36(b)–(e)).

Figures 37–45 show the lateral-directional stability and control derivatives obtained using RVDT surface-position inputs into the pEst program. Figure 46 shows a comparison of analyses using CPT and RVDT data for the estimation of the static-directional stability and dihedral effect derivatives. The directional stability results (fig. 46(a)) show good agreement. Results obtained using RVDT data show more negative dihedral effect (fig. 46(b)) at supersonic Mach numbers. Figure 47 shows control derivatives with reasonably good agreement. Using the RVDT data did result in higher differential LEF derivative values.

Aerodynamic Model Update

Typically, the end result of PID analysis is an update of the aerodynamic model of the vehicle. An updated aerodynamic model can be used to improve ground-based flight simulations and, in the case of the AAW project, to improve the fidelity of the initial control-law design. Figures 13–35 and 37–45 show the stability and control derivatives obtained from PID flight test. Derivative increments were obtained from these figures by subtracting the simulation-predicted derivative from the flight-determined derivative. These increments were computed as a function of both Mach number and altitude. The force and moment coefficient increments defined in equations (25)–(29) were added to the original aerodynamic model force and moment coefficients to obtain an updated aerodynamic model. This new aerodynamic model was then used in the nonlinear simulation and compared to flight data to validate the PID results. Appendix C contains a complete set of the stability and control derivative increments as a function of Mach number and altitude for results obtained using CPT measurements in the PID analysis. Appendix D contains a set for results obtained using RVDT surface position measurements in the PID analysis.

This section compares flight data with simulation. Three simulation runs were done for each test condition. The nonlinear, piloted, real-time simulation was used to obtain the aircraft response resulting from the original aerodynamic model. The nonlinear batch simulation was used to obtain aircraft responses using the updated aerodynamic models. Two updated aerodynamic models were tested, one using appendix C increments and the other using appendix D increments. Simulations using the updated aerodynamic models were run with the appropriate (either CPT or RVDT) control-surface position measurements obtained in flight. These control-surface position measurements, however, were biased to match the control-surface positions predicted by the trimmed simulation. In all cases, the simulator was trimmed at flight Mach number and altitude conditions and flight mass properties. The bias increments (ΔC_{N_b}, ΔC_{m_b}, ΔC_{Y_b}, ΔC_{l_b}, and ΔC_{n_b}) were set to zero in the updated simulations to simplify the analysis because these parameters did not affect the dynamic response of the simulation. Seven SSI cases are analyzed in this section.

Symmetric Leading-Edge Flaps

Figures 16(b) and 32(b) show that the pitching-moment effectiveness of the symmetric LEF deflection was modeled well for subsonic speeds. At supersonic speeds, however, the symmetric LEFs were much less effective in generating pitching moment than predicted. Figure 48 shows the comparison between flight and simulation for a maneuver at Mach 1.2 and an altitude of 25,000 ft. As figure 48 shows, the simulation based on the original aerodynamic model predicted more variation in normal acceleration and pitch rate than what was actually measured in flight. The simulated responses obtained using the updated aerodynamic models better agree with the flight-measured normal acceleration and pitch rate than do the simulated responses using the original aerodynamic model.

Symmetric Trailing-Edge Flaps

Figures 17(a) and 33(a) show from flight data that the TEF deflections produce less normal force than predicted at all Mach numbers. Figure 33(b) shows a significantly more negative TEF pitching-moment derivative for flight at an altitude of 25,000 ft than predicted when using the RVDT surface positions in the PID analysis. Figure 49 shows the comparison between flight and simulation for a symmetric TEF deflection at Mach 1.2 and an altitude of 25,000 ft. The normal acceleration plot (fig. 49) shows that the updated simulations better agree with flight data than the original simulation. This agreement is consistent with using the smaller-than-predicted normal-force derivatives obtained from the pEst program. The pitch-rate plot also shows an improved match with flight data for the updated simulations as compared to the original simulation.

Symmetric Ailerons

Figures 18(b) and 34(b) show that the symmetric aileron deflection at subsonic speeds was much more effective than predicted. Figure 50 shows the comparison between flight and simulation for a maneuver at Mach 0.85 and an altitude of 15,000 ft. Figure 50 shows the original simulation predicted a ±0.5-*g* increment in the normal acceleration response caused by the symmetric aileron doublet; however, flight data show a much more dynamic maneuver in which normal acceleration ranges between –0.3 and 3.0-*g*. Both of the updated aerodynamic models show better agreement with the flight data than the original simulation.

Differential Leading-Edge Flaps

Figures 25(b) and 42(b) show that rolling-moment effectiveness of the differential TEFs was overpredicted by the original aerodynamic model for a maneuver at Mach 1.2 and an altitude of 15,000 ft. Figure 51 shows the comparison between flight and simulation for a maneuver at Mach 1.2 and an altitude of 15,000 ft. As figure 51 shows, the simulation based on the original aerodynamic model predicted 50-percent more roll rate and bank angle than that measured in flight. The updated simulations show better agreement with flight data than the original simulation, which is consistent with the reduced rolling-moment effectiveness determined by the PID analysis.

Differential Trailing-Edge Flaps

Figures 26 and 43 show that the PID flight analyses indicate increased side-force and yawing-moment effectiveness caused by differential TEF deflections. Figure 52 shows the comparison between flight and simulation for a differential TEF doublet maneuver at Mach 1.2 and an altitude of 15,000 ft. The flight data clearly demonstrate significant yaw rate and sideslip that the original simulation did not at all show. The differential TEFs were so effective in generating a yawing moment that the primary FCS commanded rudder deflection to counter the yawing moment (fig. 52(c)). The updated simulations agree much better with the flight data than did the original simulation.

Aileron

Figures 27 and 44 show the aileron derivatives obtained from the PID analysis and from the original aerodynamic model. For flight at Mach 1.2 and an altitude of 15,000 ft, the PID analysis estimated slightly more positive rolling moment and slightly more negative yawing moment caused by the aileron deflection than predicted. Figure 53 shows the comparison between flight and simulation for an aileron doublet maneuver at Mach 1.2 and an altitude of 15,000 ft. For the small angular rates and sideslip generated by the aileron doublet, the updated simulations do a better job of matching the flight data than did the original simulation. The original simulation showed some aileron reversal that was not seen in the flight data.

Differential Stabilator

Figures 28 and 45 show the differential stabilator derivatives obtained from the PID analysis and from the original aerodynamic model. For the test condition of Mach 1.2 and an altitude of 15,000 ft, the PID analysis shows approximately zero side force caused by the differential stabilator deflection; whereas the original aerodynamic model showed a negative side-force derivative. More significantly, the PID analysis shows a negative yawing-moment derivative, whereas the original aerodynamic model predicted a positive yawing-moment derivative of approximately the same magnitude. Figure 54 shows the comparison between flight and simulation for a differential stabilator doublet maneuver at Mach 1.2 and an altitude of 15,000 ft. For the small yaw rate and angle of sideslip generated by the differential stabilator, the updated simulations show better agreement with the flight data than the original simulation. Although the derivative for rolling moment caused by differential stabilator was only slightly modified, the updated simulations also show better agreement with the measured roll rate than the original simulation (fig. 54(c)).

CONCLUDING REMARKS

The full set of longitudinal and lateral-directional stability and control derivatives has been obtained for the F-18B aircraft at the high dynamic pressures of interest to the active aeroelastic wing program. A maximum-likelihood output-error parameter estimation technique was used to analyze maneuvers initiated by an onboard excitation system that provided single-surface doublet inputs. A total of 112 maneuvers was analyzed at flight conditions ranging in Mach number from 0.85 to 1.30 and dynamic pressure from 600 to 1500 lbf/ft^2. Comparisons were made with simulation predictions.

Longitudinal flight data analysis showed less static stability than predicted throughout the Mach region tested. Pitching-moment effectiveness of the symmetric leading-edge flaps agreed well with predictions for subsonic conditions but showed much less effectiveness for supersonic conditions than predicted. The normal force generated by symmetric trailing-edge flap deflection was significantly less than predicted. The symmetric ailerons were much more effective in pitch than predicted, especially for subsonic conditions.

Lateral-directional flight data analysis confirmed the known right roll and nose-left tendencies of the Systems Research Aircraft. The directional static stability was moderately less than predicted. The rolling-moment effectiveness of the leading-edge flaps was generally less than predicted and did not vary as significantly with altitude as predicted. At supersonic Mach numbers, the differential trailing-edge flap deflection generated significantly more yawing moment than predicted. The rolling-moment effectiveness of the trailing-edge flaps agreed well with the predictions, including the "trailing-edge flap reversal" at Mach 0.95 at low altitudes. "Aileron reversal" was never obtained as predicted, but the aileron effectiveness did approach zero as altitude decreased at Mach 0.95. At speeds faster than Mach 1.15, the differential stabilator generated a negative yawing moment rather than the predicted positive yawing moment.

Comparisons were also shown of results from analyzing the maneuvers using surface position from direct control-surface position transducer (CPT) measurements rather than surface position assumed from rotary variable differential transformer (RVDT) measurements at the surface actuator or transmission. This comparison was important because the RVDTs did not measure surface deflections caused by bending and twisting under aerodynamic loading. Flight data showed significant uncommanded leading-edge flap motion caused by aerodynamic loads during the dynamic parameter-identification maneuvers. Some differences in control-surface effectiveness values were attributed to whether CPT or RVDT data were used in the analysis.

Selected single-surface input (SSI) maneuvers were analyzed to show the effect of updating the nonlinear simulation with improved stability and control derivatives obtained from this series of flights. Increments to the stability and control derivatives from the original aerodynamic model to the updated aerodynamic model were a function of both Mach number and altitude. These increments were input into the nonlinear batch simulation, and the aircraft response time histories were obtained using the control-surface inputs from flight maneuvers. Time histories were obtained for symmetric leading-edge flap, symmetric trailing-edge flap, symmetric aileron, differential leading-edge flap, differential trailing-edge flap, aileron, and differential stabilator SSI doublet maneuvers. Two updated aerodynamic models were run in the simulator. One updated simulation included increments obtained using CPT values in the parameter estimation program analysis; the other updated simulation included increments obtained from using RVDT surface position values in the parameter estimation program analysis. In all cases, the aircraft responses from both of the updated simulations agreed more closely with the flight-measured responses than the original simulation-predicted responses.

Dryden Flight Research Center
National Aeronautics and Space Administration
Edwards, California, June 30, 2000

FIGURES

EC95 42988-04

Figure 1. F-18B Systems Research Aircraft (SRA).

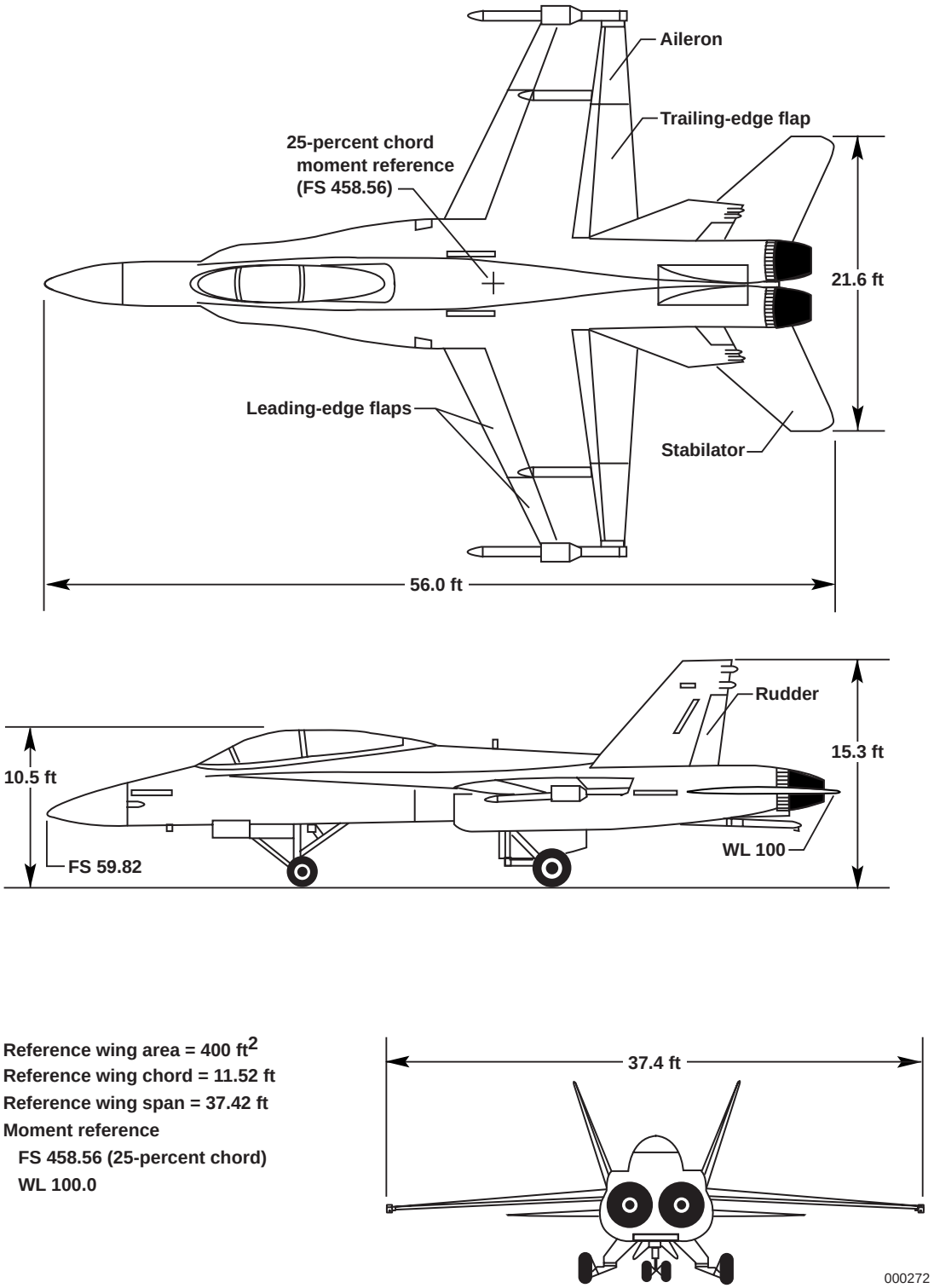

Figure 2. Three-view drawing of the F-18B SRA with major dimensions shown.

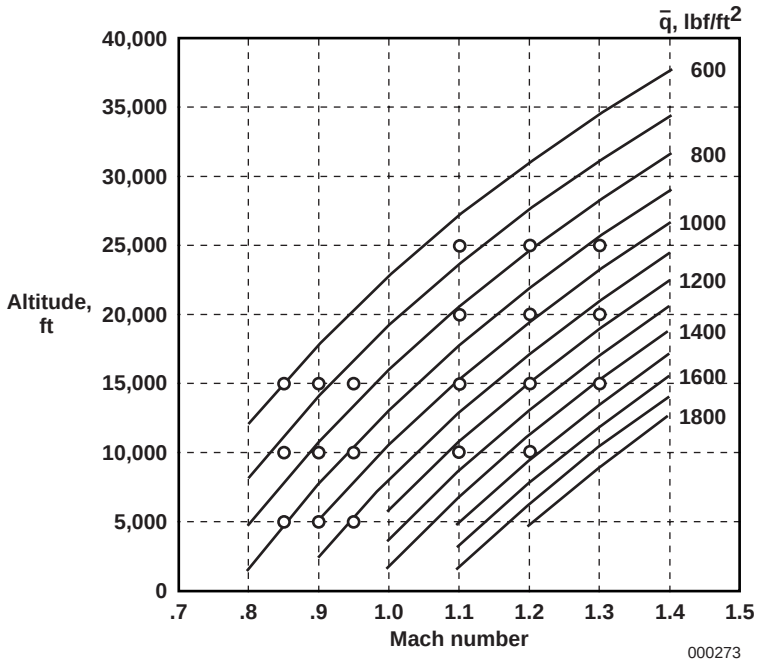

Figure 3. AAW and SRA flight test point matrix.

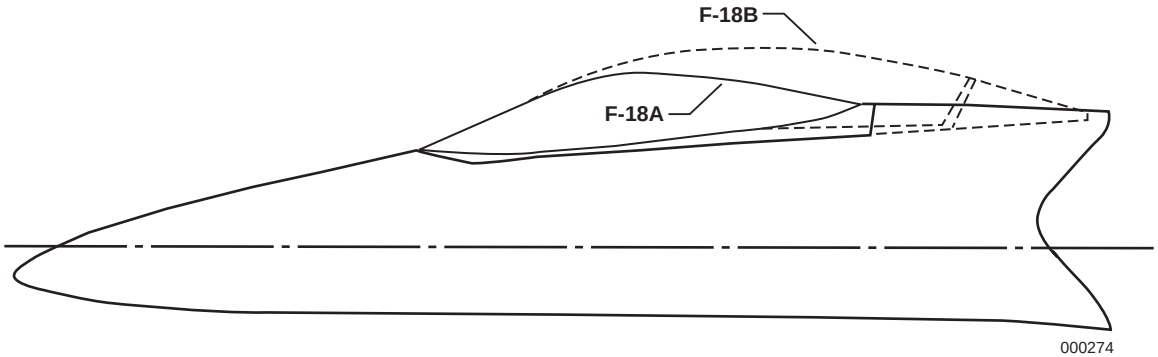

Figure 4. Canopy mold line comparison between F-18 “A” and “B” models.

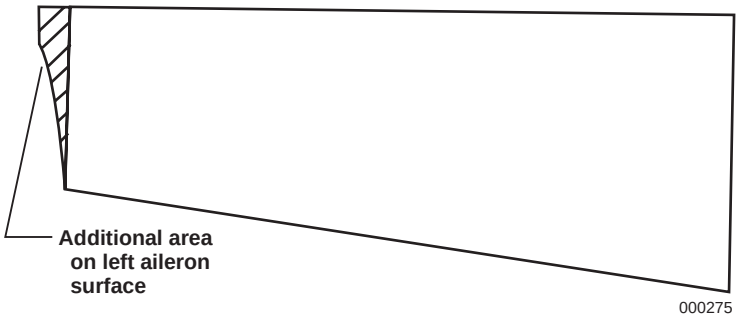

(a) Planform of the left “production” aileron showing the additional 1.7-percent more surface area that is not included on the right “preproduction” aileron.

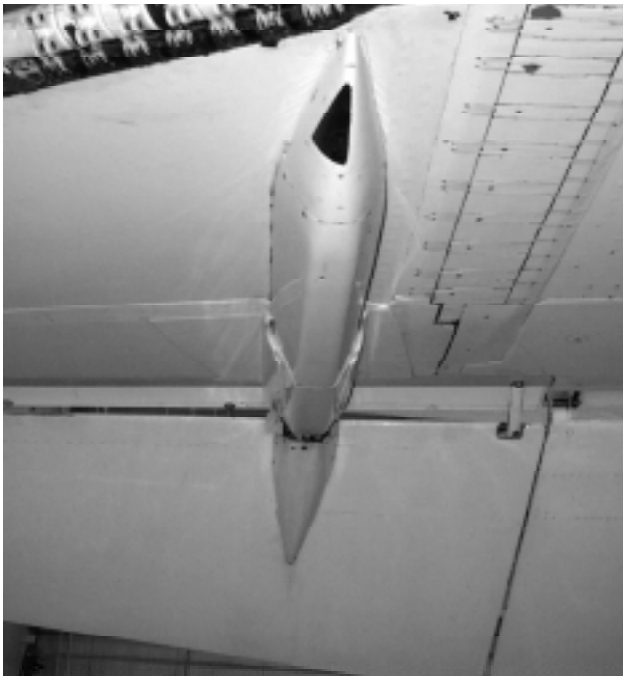

ED00 0331-01

(b) Right aileron actuator fairing.

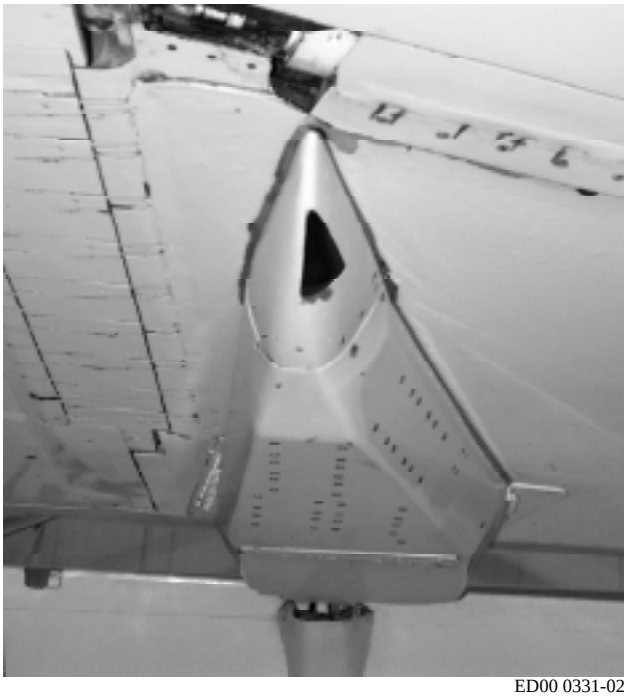

ED00 0331-02

(c) Left aileron actuator fairing.

Figure 5. Asymmetries between left and right aileron surfaces and actuator fairings.

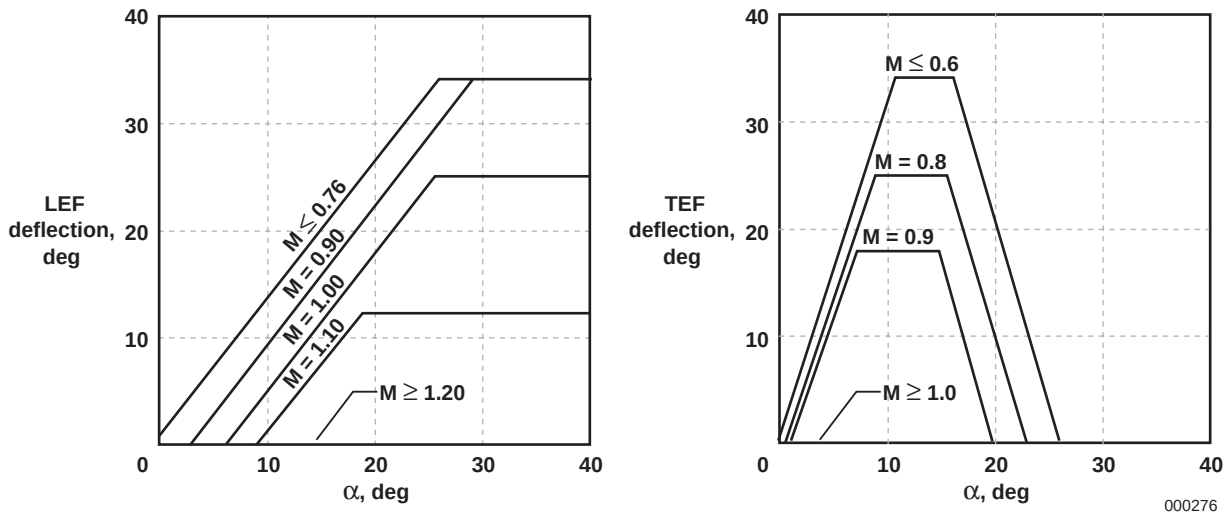

Figure 6. Basic F-18A/B symmetric LEF and TEF schedules (ref. 3).

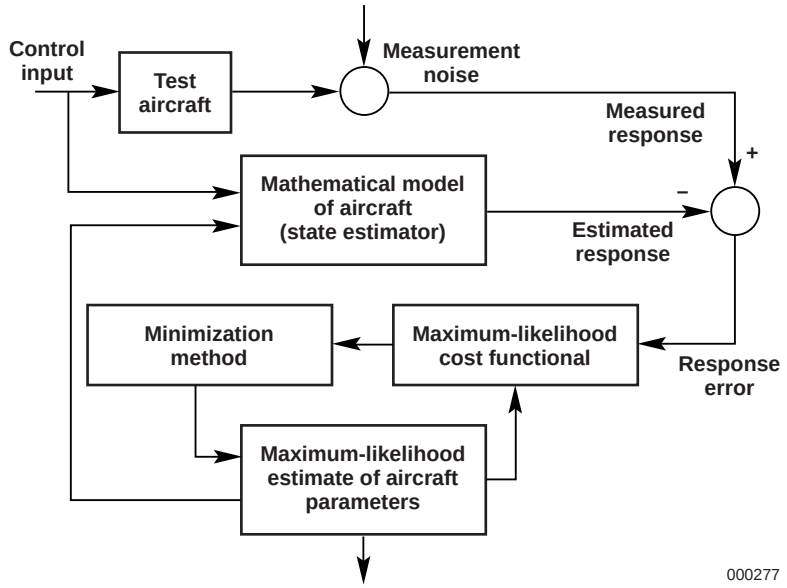

Figure 7. Maximum-likelihood parameter estimation process.

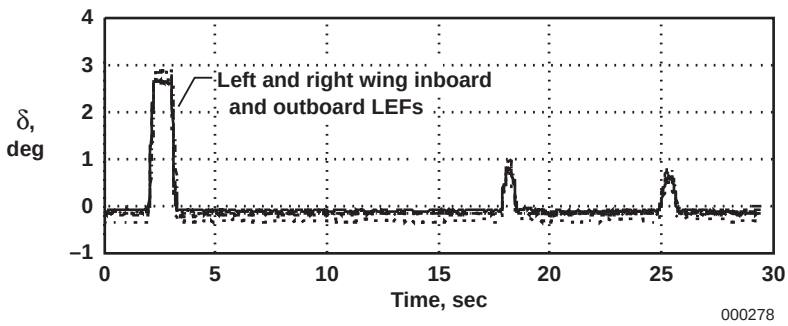

(a) LEF surface deflections (OBES LEF command at *t* = 2–3 sec).

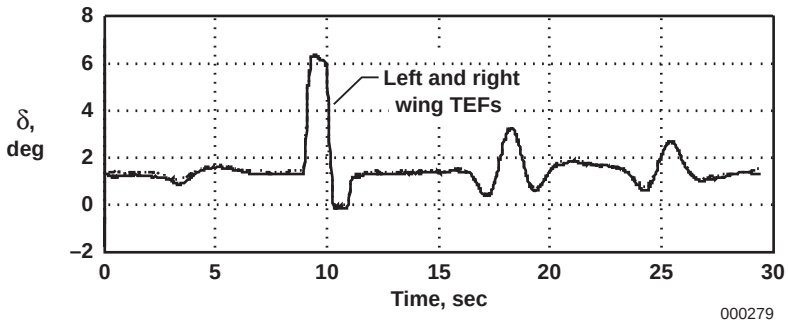

(b) TEF surface deflections (OBES TEF command at *t* = 9–11 sec).

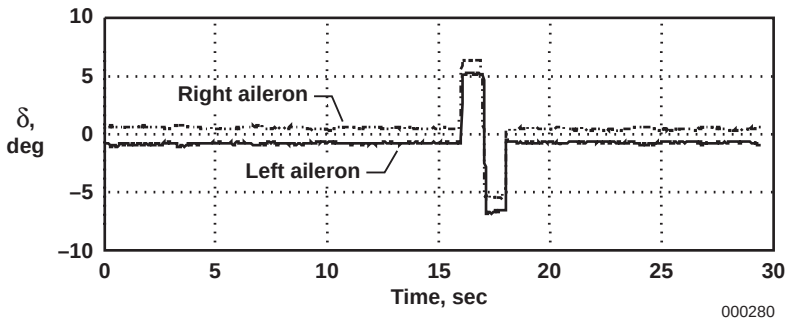

(c) Aileron surface deflections (OBES aileron command at *t* = 16–18 sec).

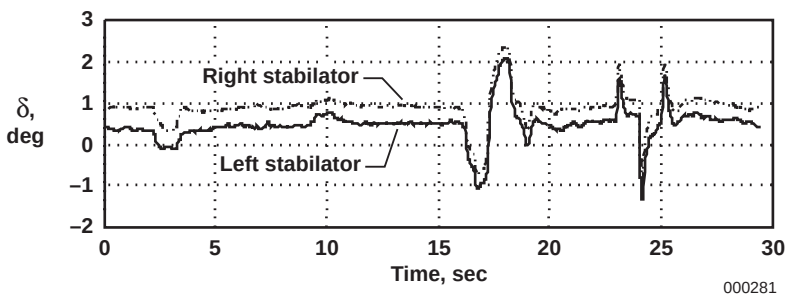

(d) Horizontal stabilator surface deflections (OBES stabilator command at *t* = 23–25 sec).

Figure 8. Typical large longitudinal doublet SSI sequence (RVDT measurements).

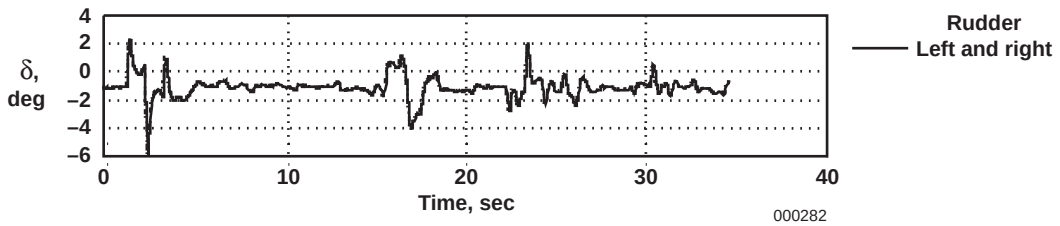

(a) Rudder surface deflections (OBES rudder command at t = 1–3 sec).

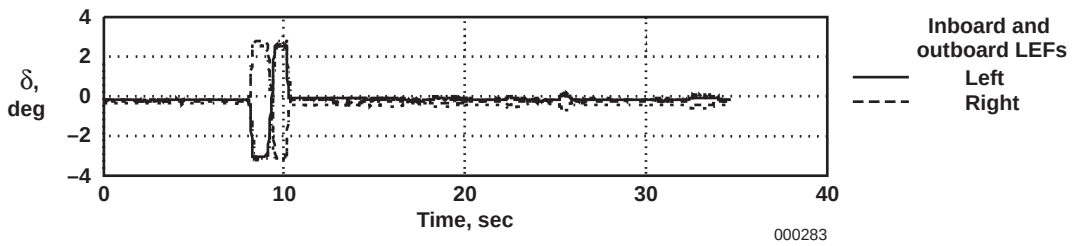

(b) LEF surface deflections (OBES LEF command at t = 8–10 sec).

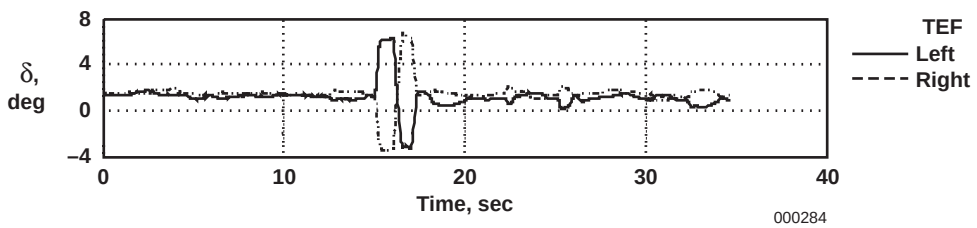

(c) TEF surface deflections (OBES TEF command at t = 15–17 sec).

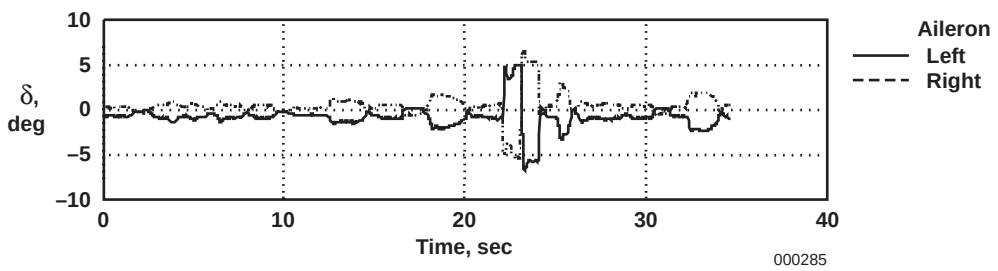

(d) Aileron surface deflections (OBES TEF command at t = 22–24 sec).

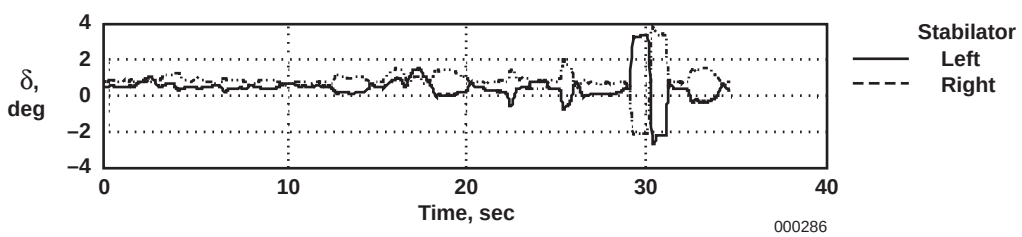

(e) Stabilator surface deflections (OBES stabilator command at t = 29–31 sec).

Figure 9. Typical large lateral-directional doublet SSI sequence (RVDT measurements).

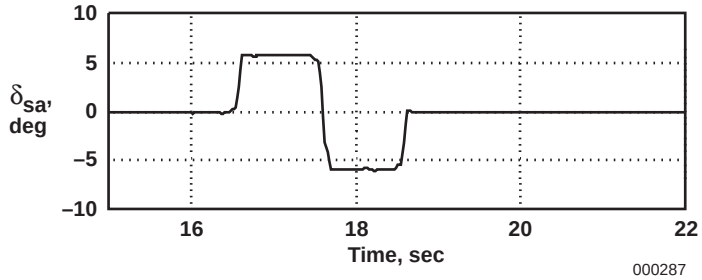

(a) Symmetric aileron deflection.

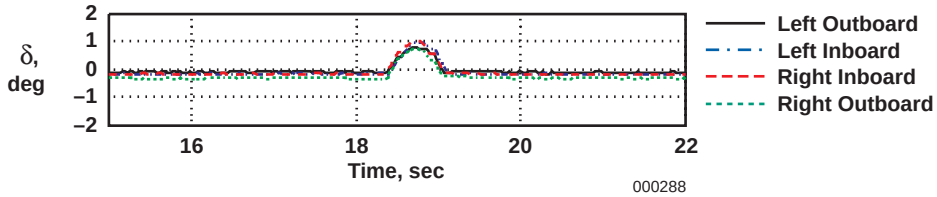

(b) LEF surface deflections from RVDT measurements.

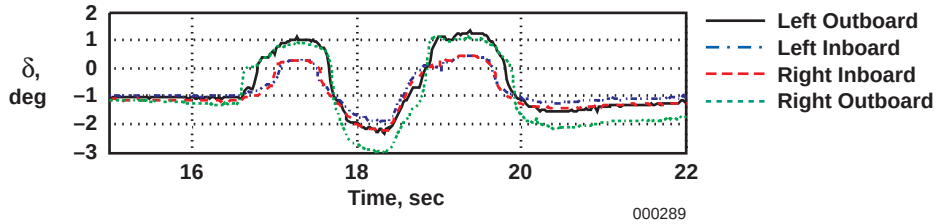

(c) LEF surface deflections from CPT measurements.

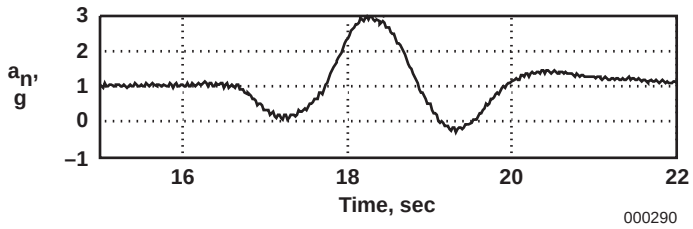

(d) Normal acceleration.

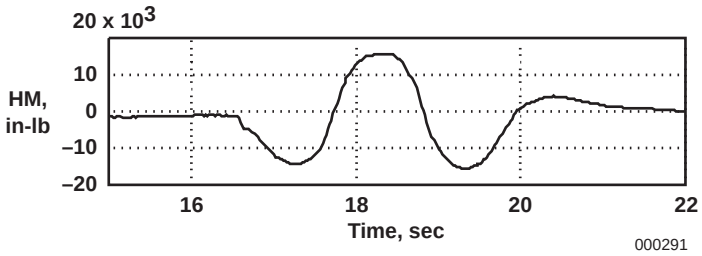

(e) Right outboard LEF hinge moment.

Figure 10. Symmetric aileron doublet time history.

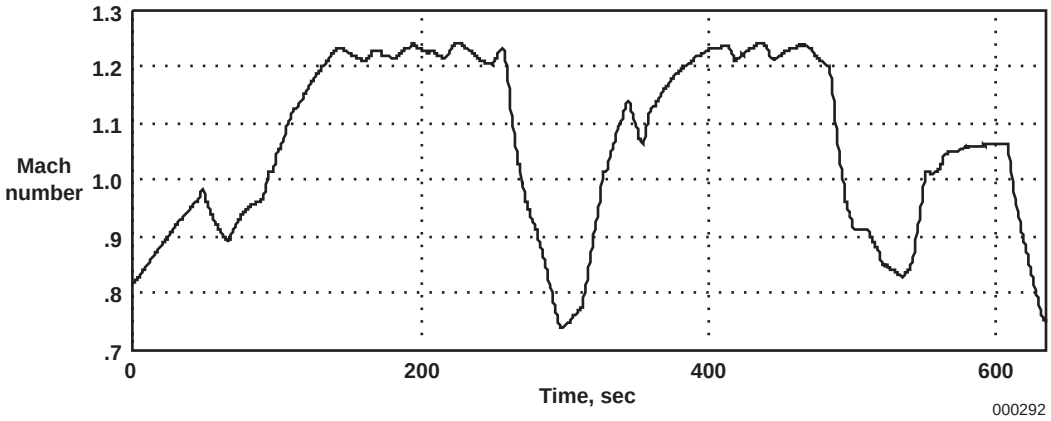

(a) Mach number.

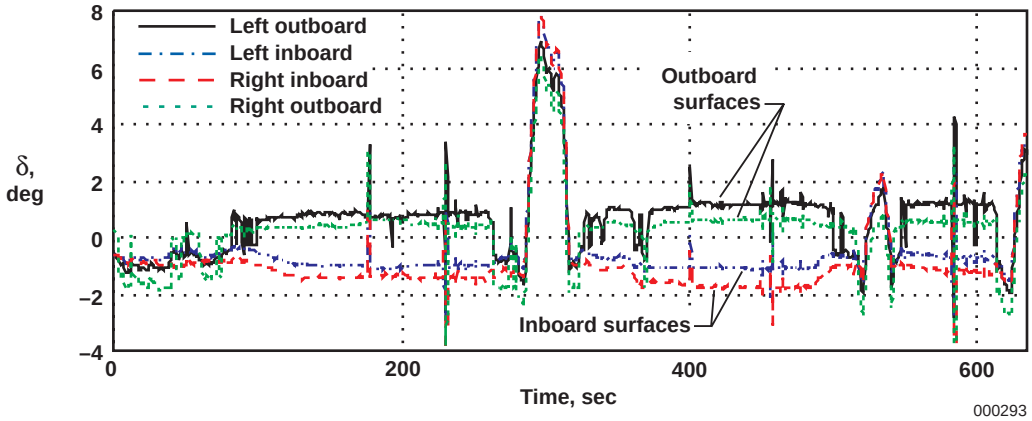

(b) LEF surface deflections using CPT measurements.

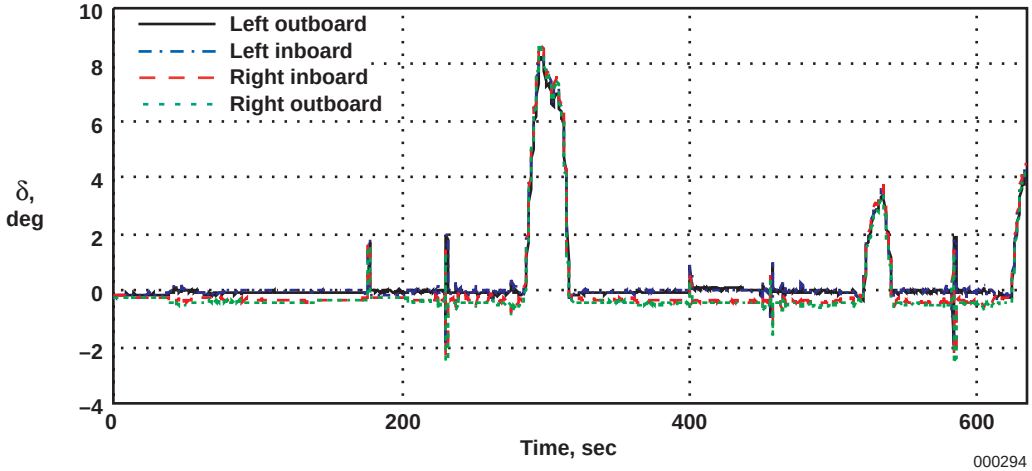

(c) LEF surface deflections using RVDT measurements.

Figure 11. Time history showing LEF split at supersonic Mach numbers.

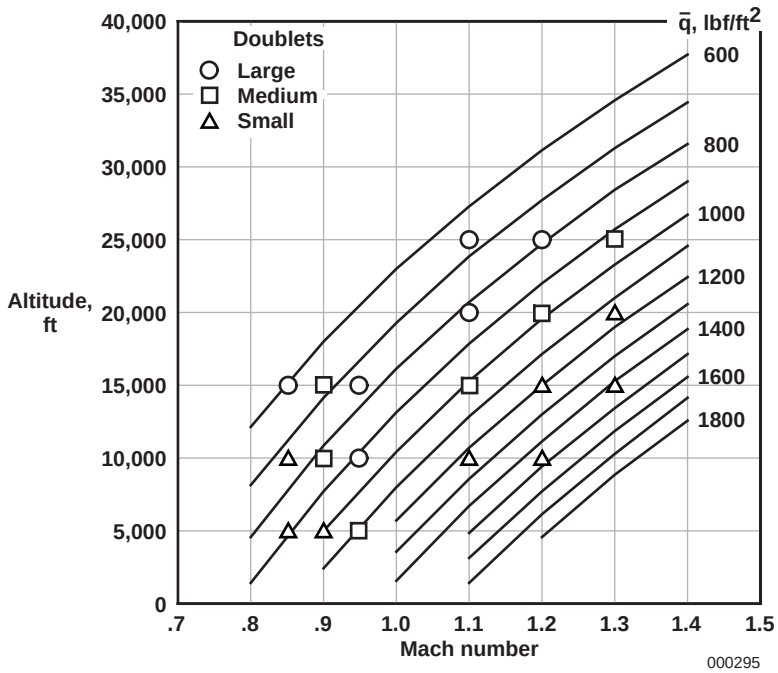

(a) Maximum longitudinal doublet sizes.

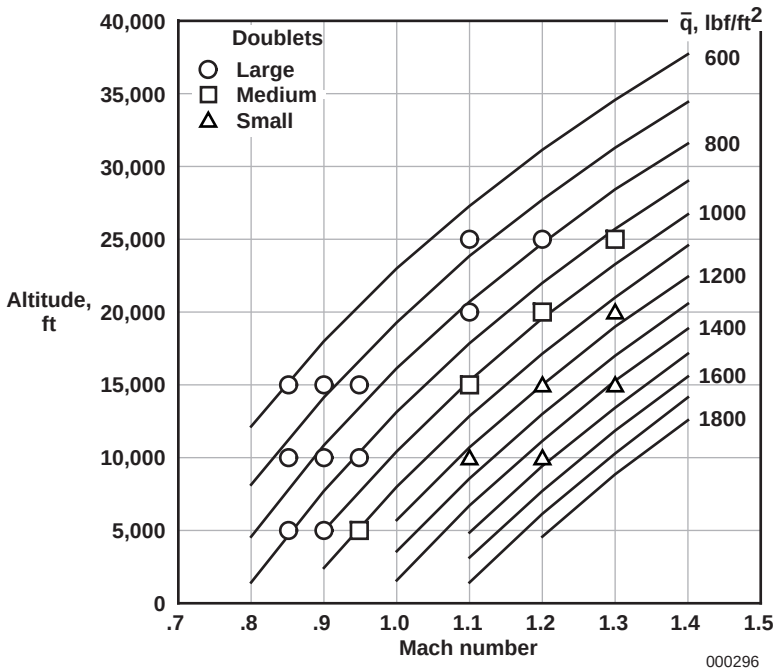

(b) Maximum lateral-directional doublet sizes.

Figure 12. Maximum doublet maneuver sizes used at the various test conditions.

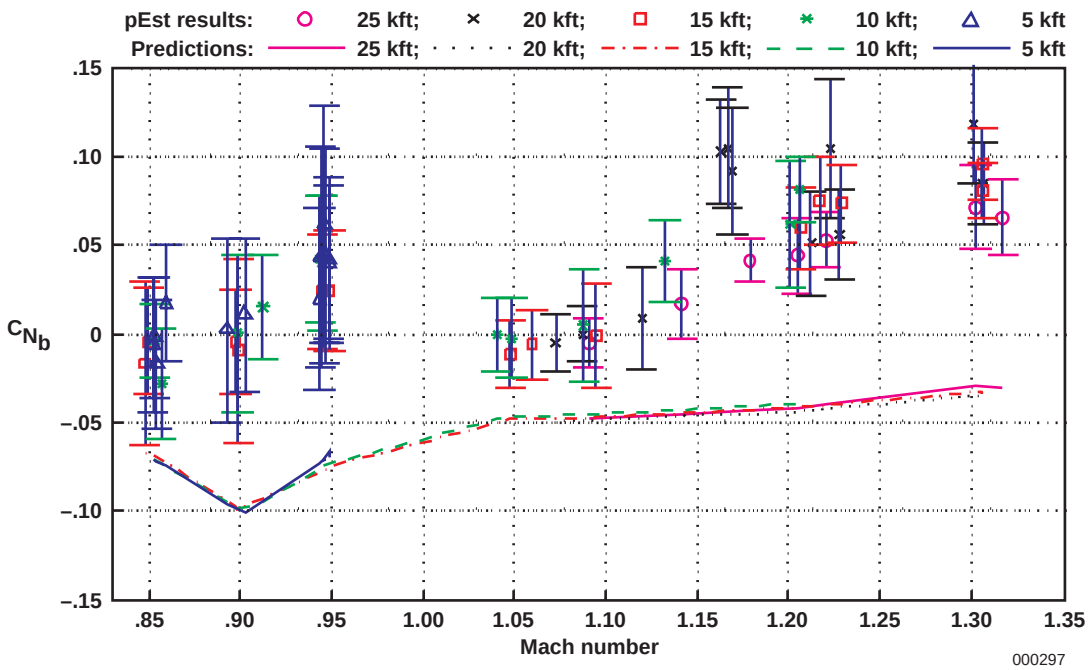

(a) C_{N_b}.

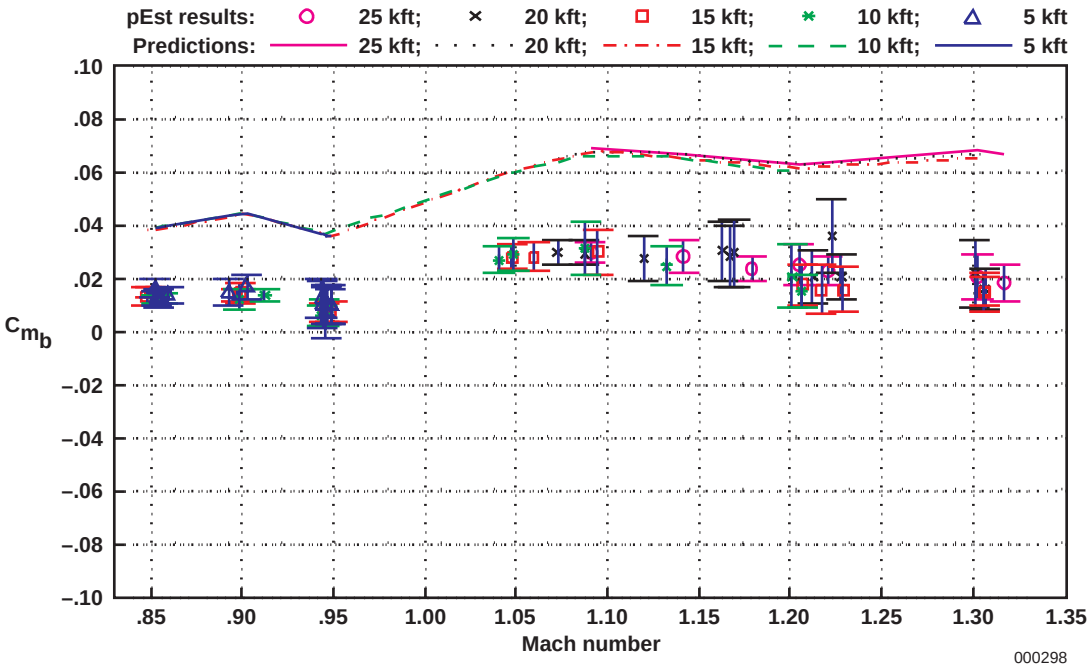

(b) C_{m_b}.

Figure 13. Predicted and flight-determined longitudinal coefficient biases (pEst program analysis using CPT measurements).

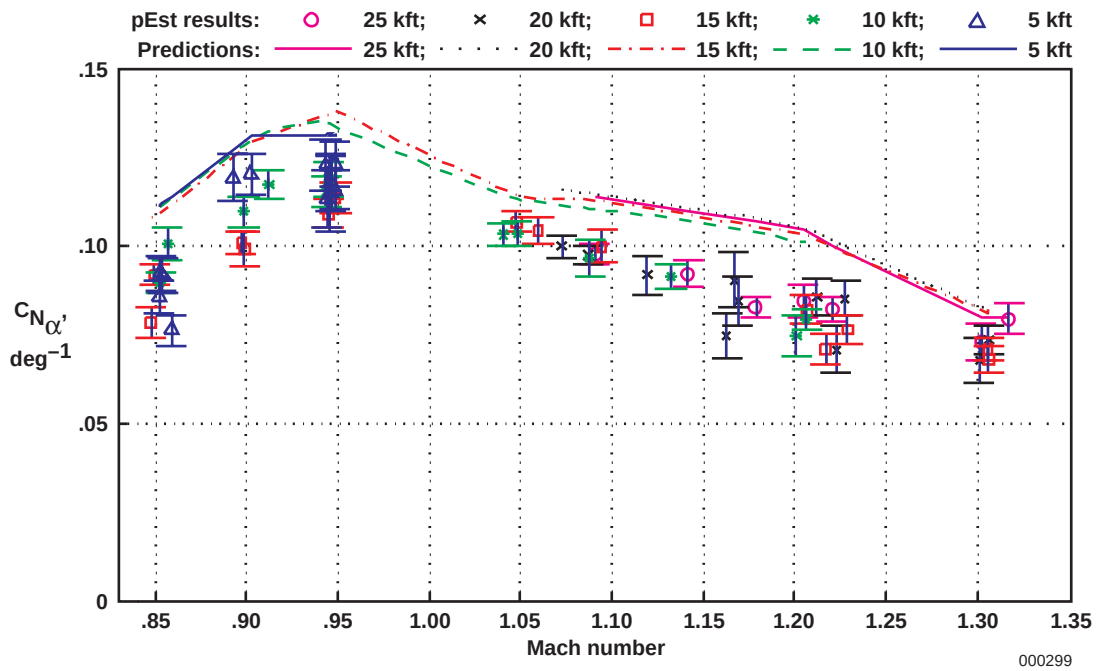

(a) C_{N_α}.

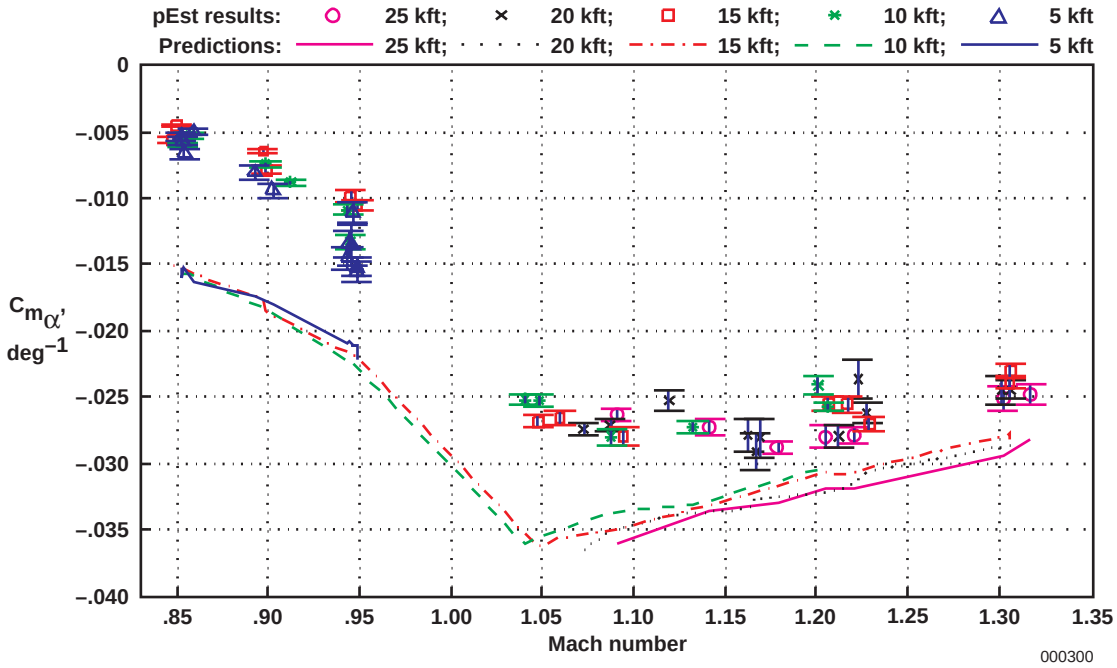

(b) C_{m_α} (moment reference at 0.25 c).

Figure 14. Predicted and flight-determined angle-of-attack derivatives (pEst program analysis using CPT measurements).

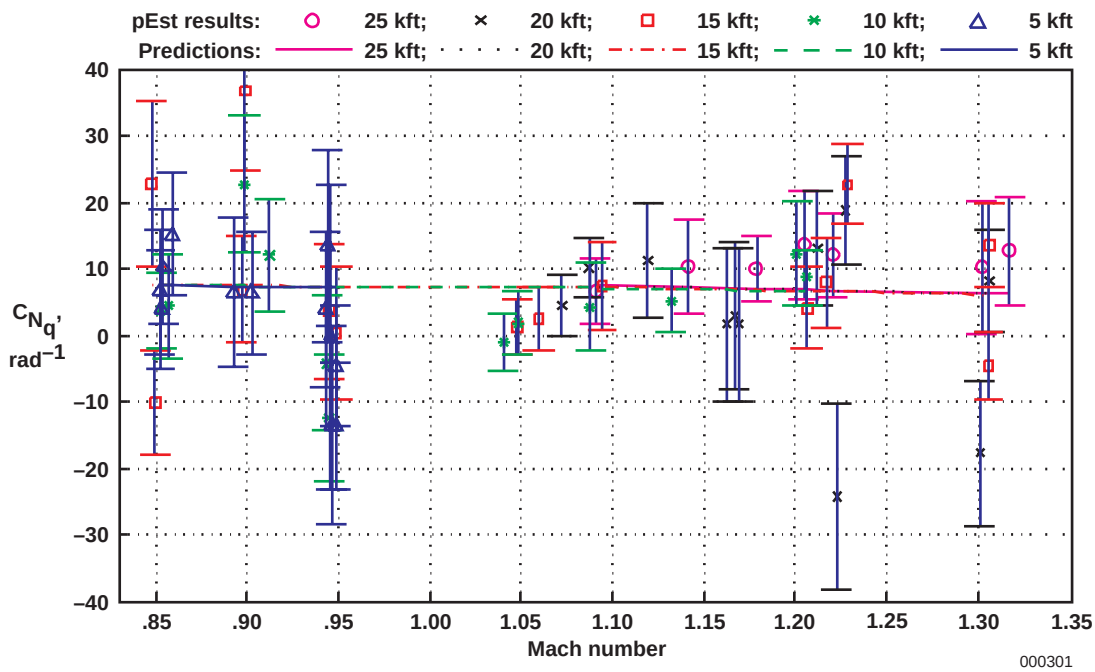

(a) C_{N_q}.

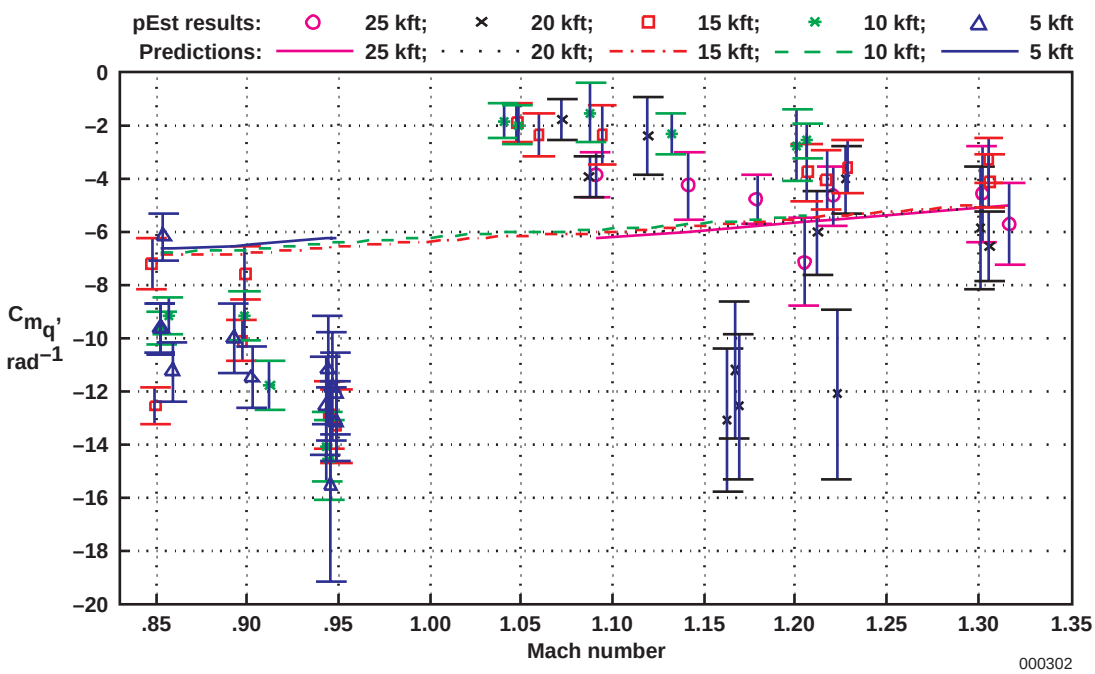

(b) C_{m_q} (moment reference at 0.25 c).

Figure 15. Predicted and flight-determined pitch-rate derivatives (pEst program analysis using CPT measurements).

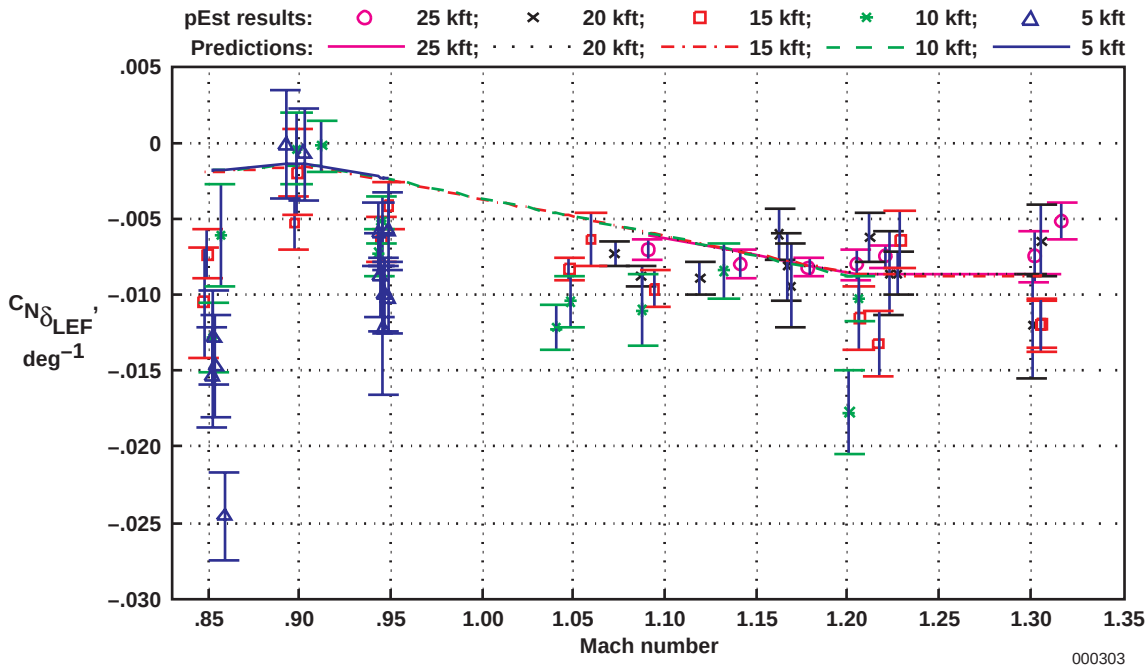

(a) $C_{N_{\delta_{LEF}}}$.

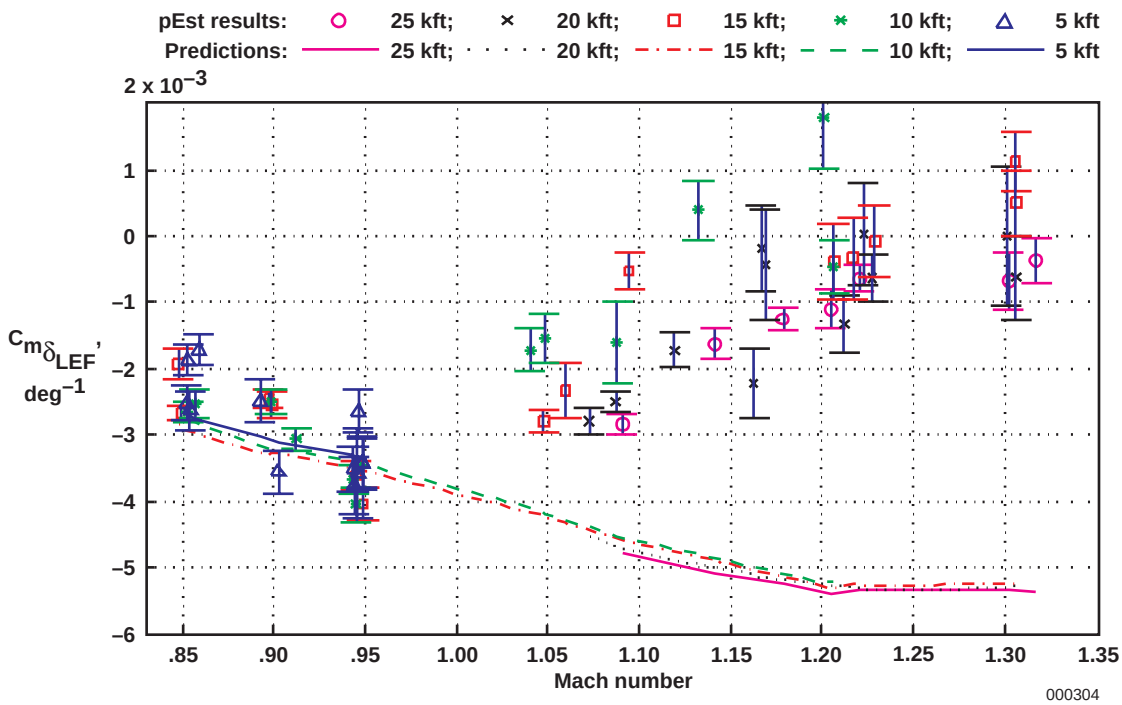

(b) $C_{m_{\delta_{LEF}}}$ (moment reference at 0.25 c).

Figure 16. Predicted and flight-determined symmetric LEF derivatives (pEst program analysis using CPT measurements).

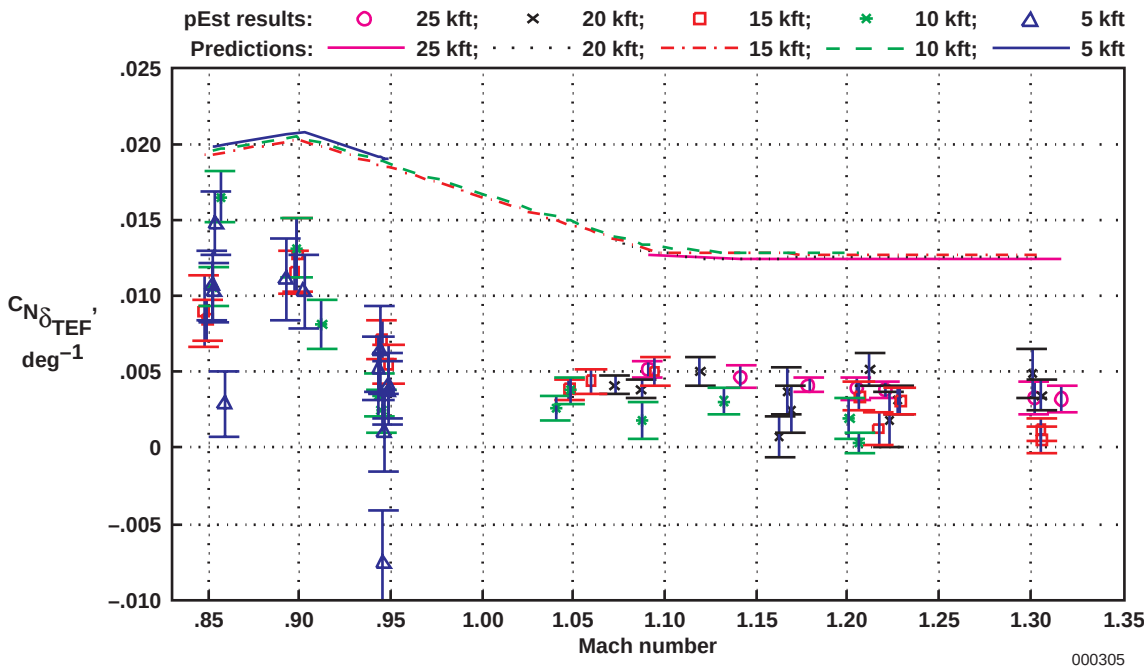

(a) $C_{N_{\delta_{TEF}}}$.

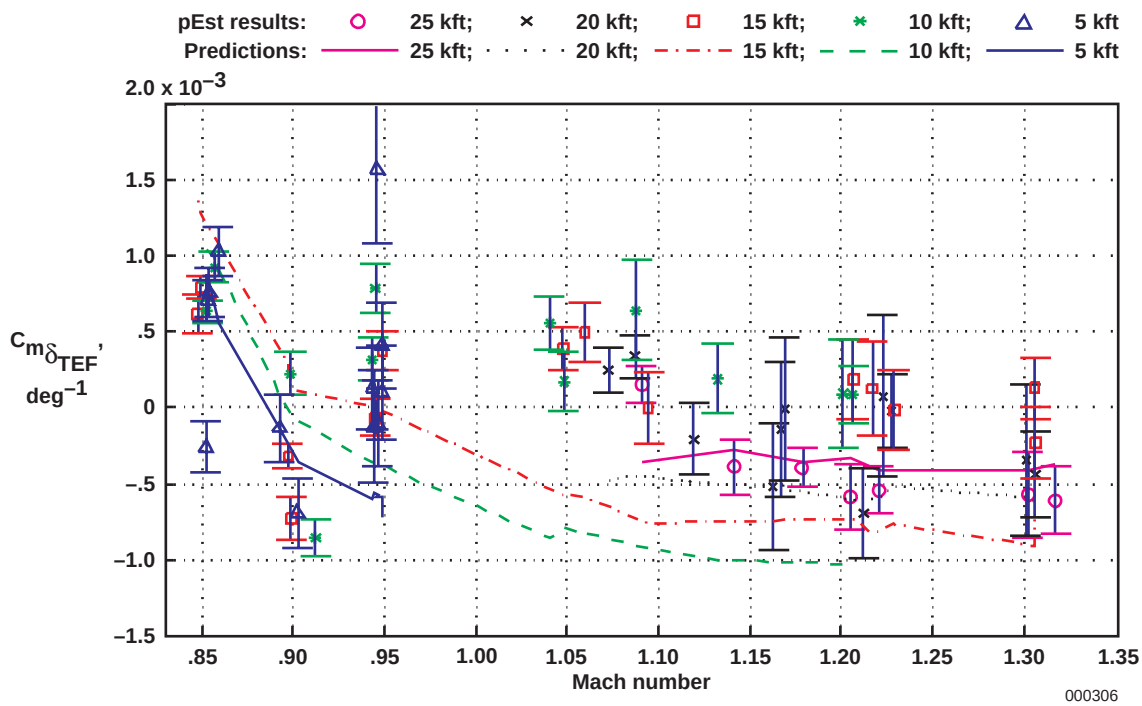

(b) $C_{m_{\delta_{TEF}}}$ (moment reference at 0.25 c).

Figure 17. Predicted and flight-determined symmetric TEF derivatives (pEst program analysis using CPT measurements).

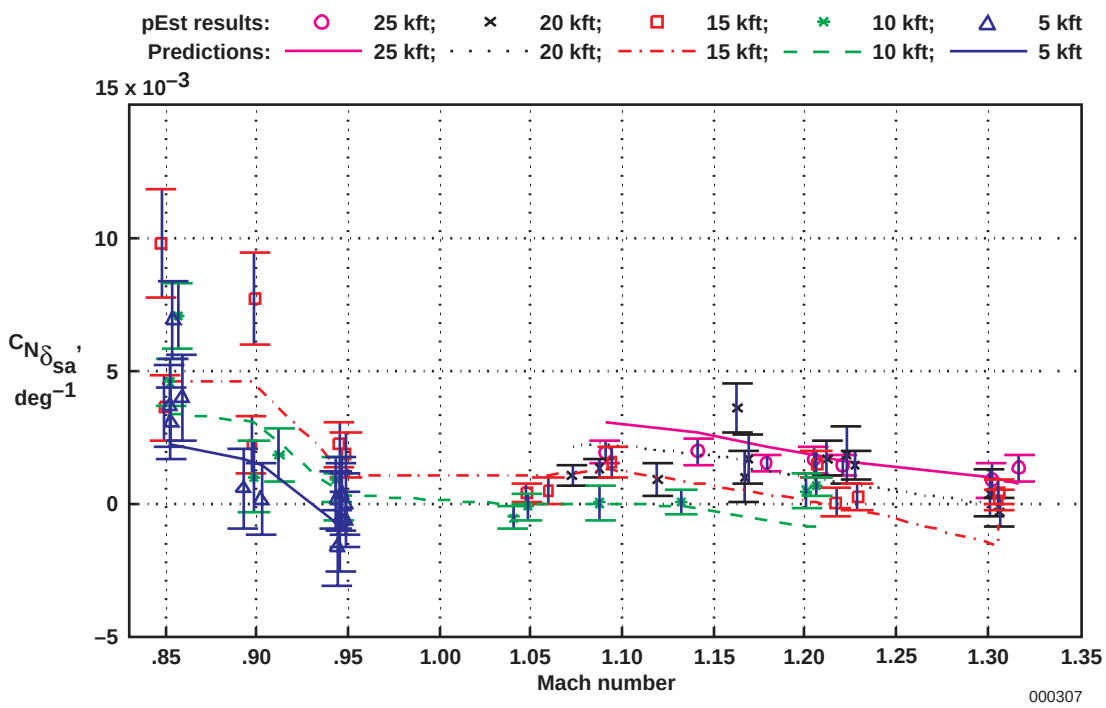

(a) $C_{N_{\delta_{sa}}}$.

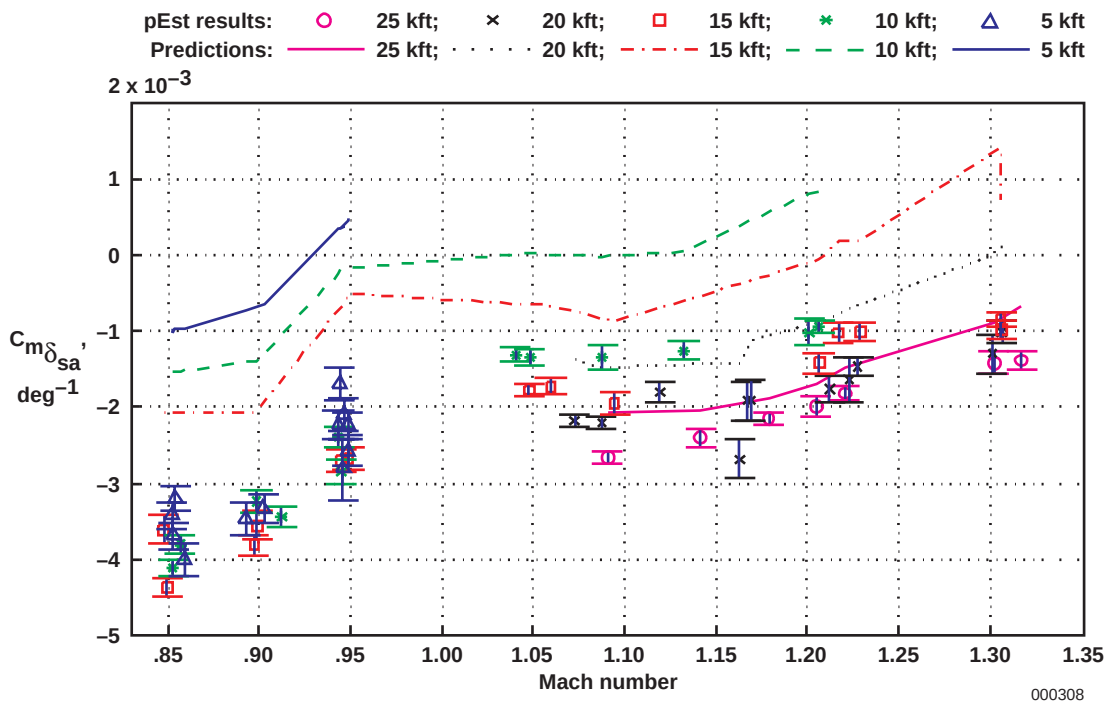

(b) $C_{m_{\delta_{sa}}}$ (moment reference at 0.25 c).

Figure 18. Predicted and flight-determined symmetric aileron derivatives (pEst program analysis using CPT measurements).

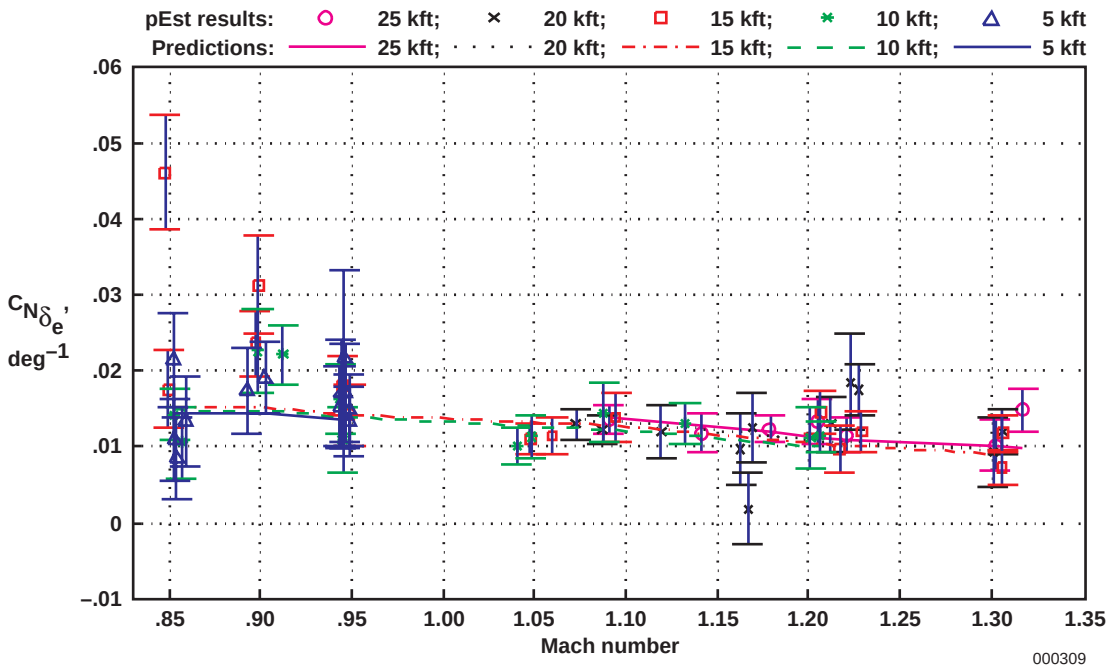

(a) $C_{N_{\delta_e}}$.

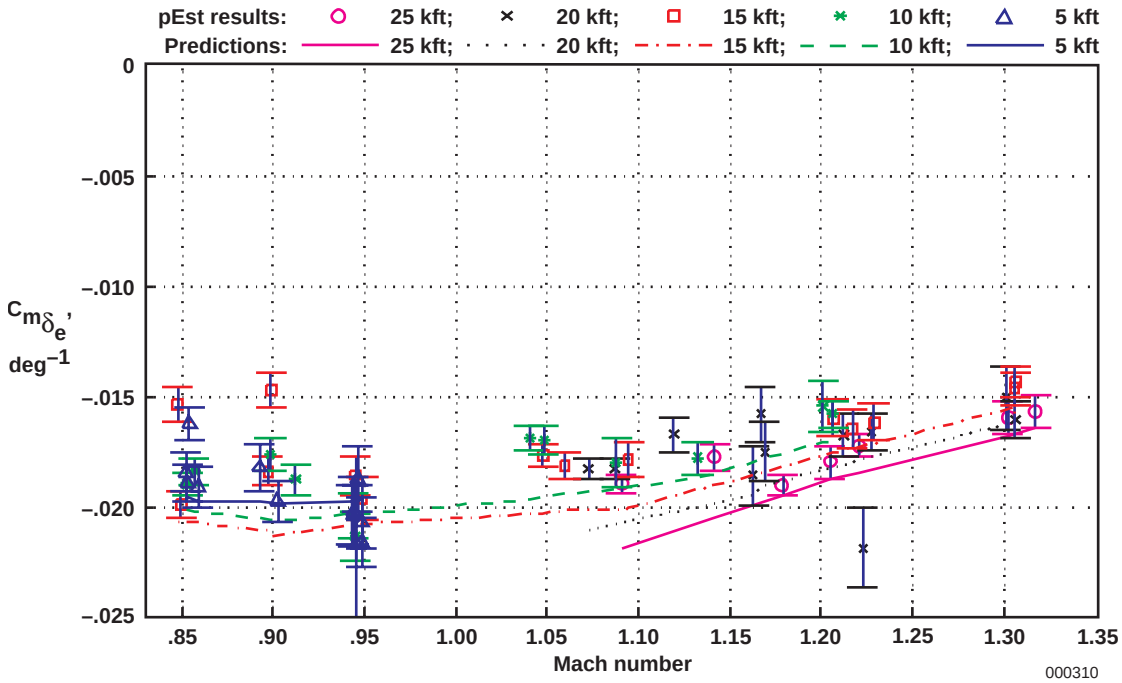

(b) $C_{m_{\delta_e}}$ (moment reference at 0.25 c).

Figure 19. Predicted and flight-determined elevator (symmetric stabilator) derivatives (pEst program analysis using CPT measurements).

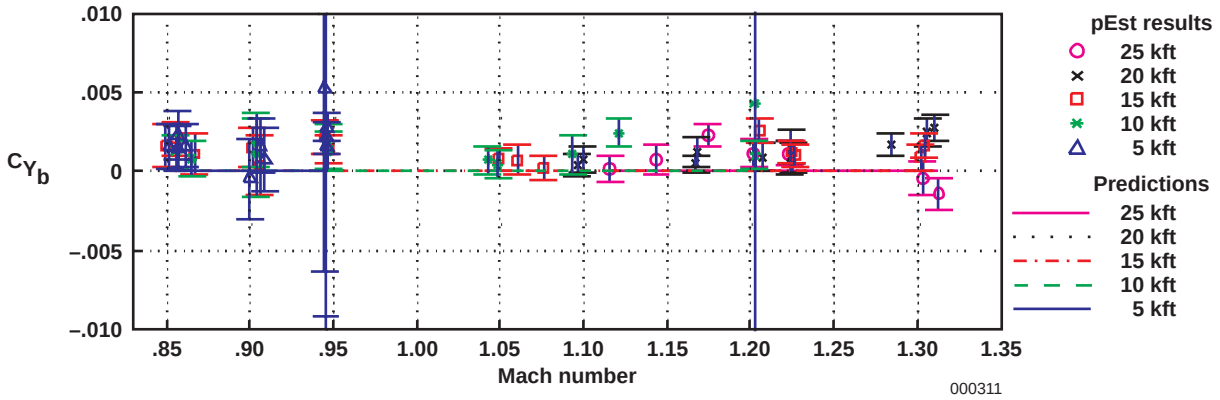

(a) C_{Y_b}.

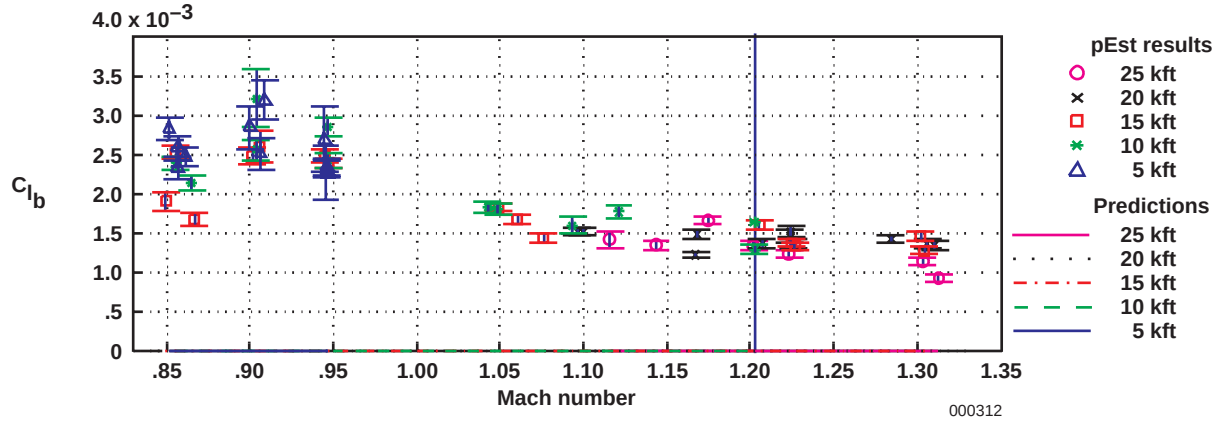

(b) C_{l_b}.

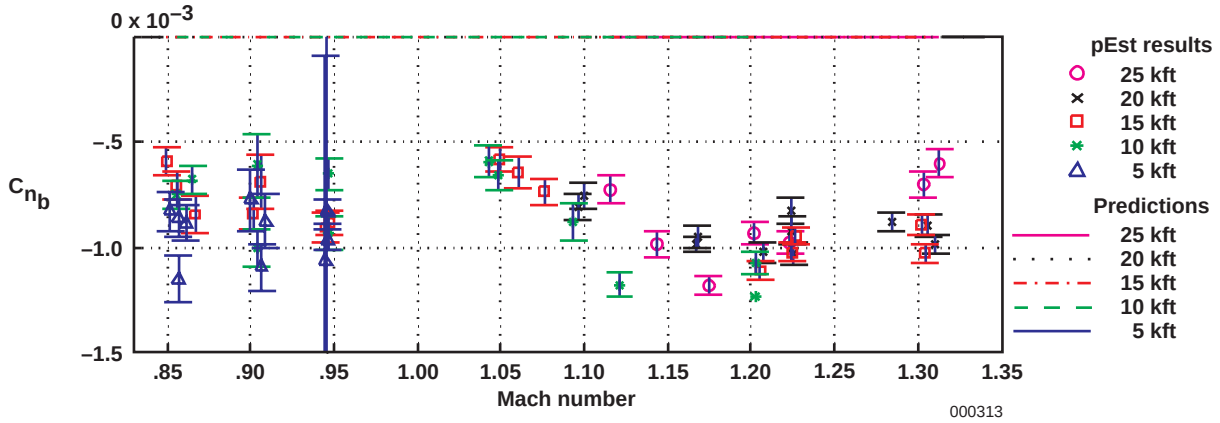

(c) C_{n_b}.

Figure 20. Predicted and flight-determined lateral-directional coefficient biases (pEst program analysis using CPT measurements).

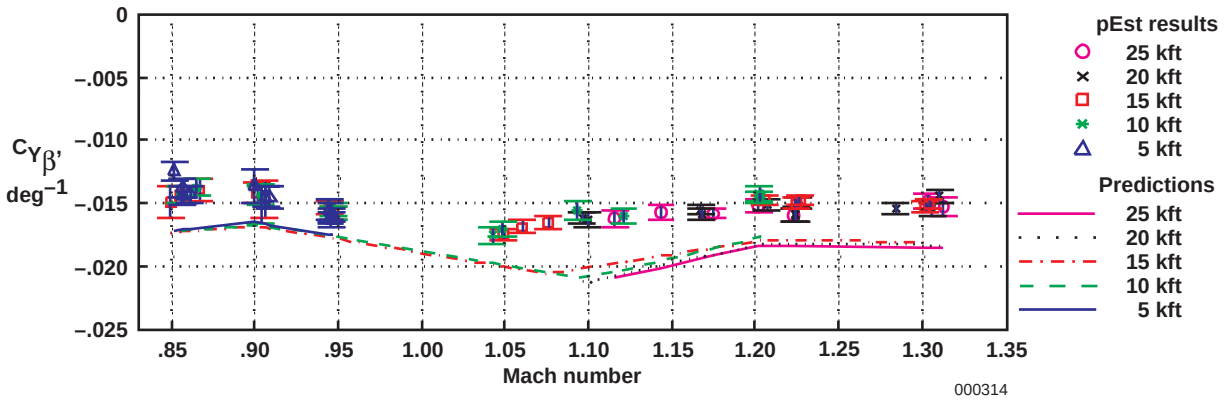

(a) C_{Y_β}.

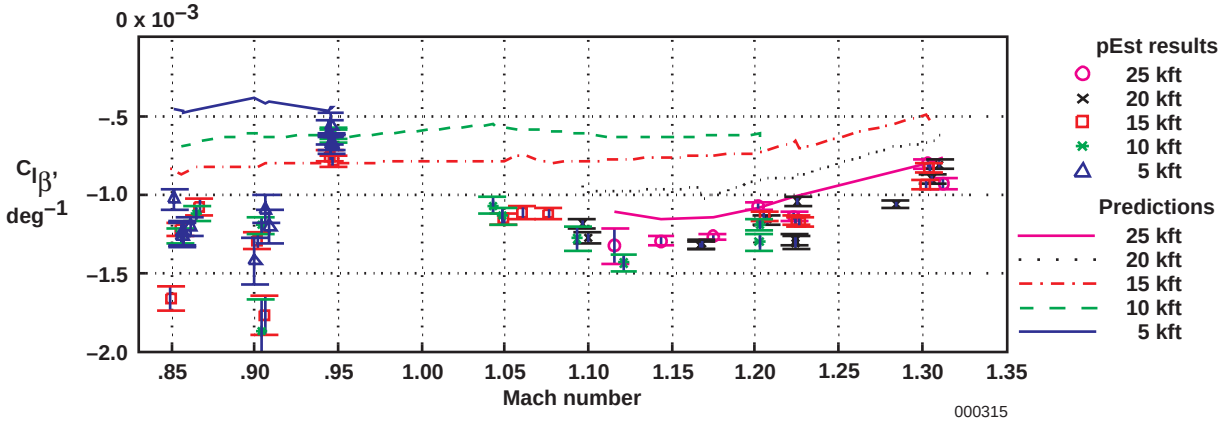

(b) C_{l_β} (vertical moment reference at *WL* 100).

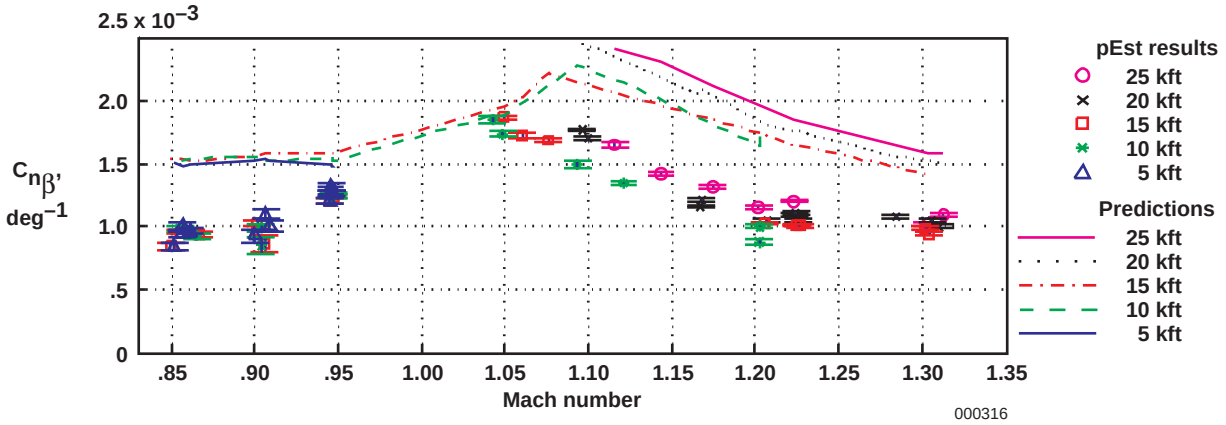

(c) C_{n_β} (moment reference at 0.25 *c*).

Figure 21. Predicted and flight-determined angle-of-sideslip derivatives (pEst program analysis using CPT measurements).

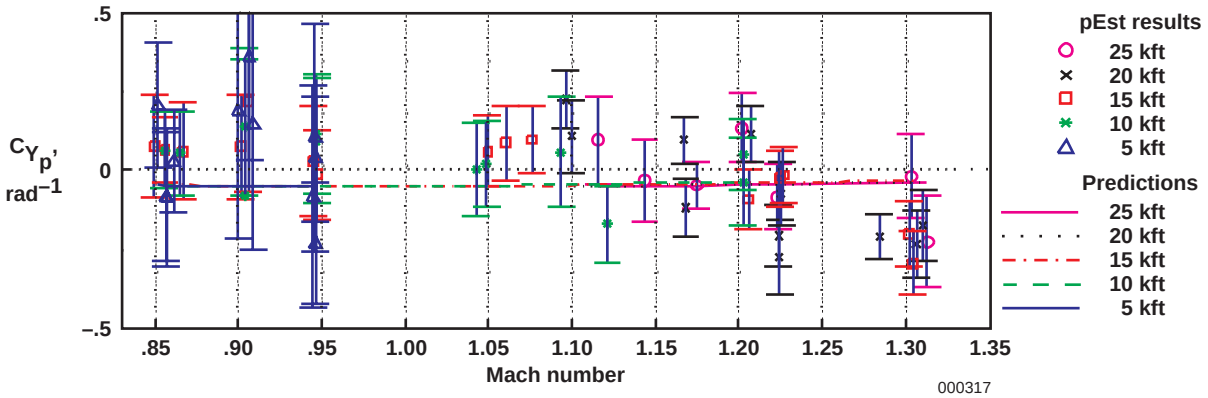

(a) C_{Y_p}.

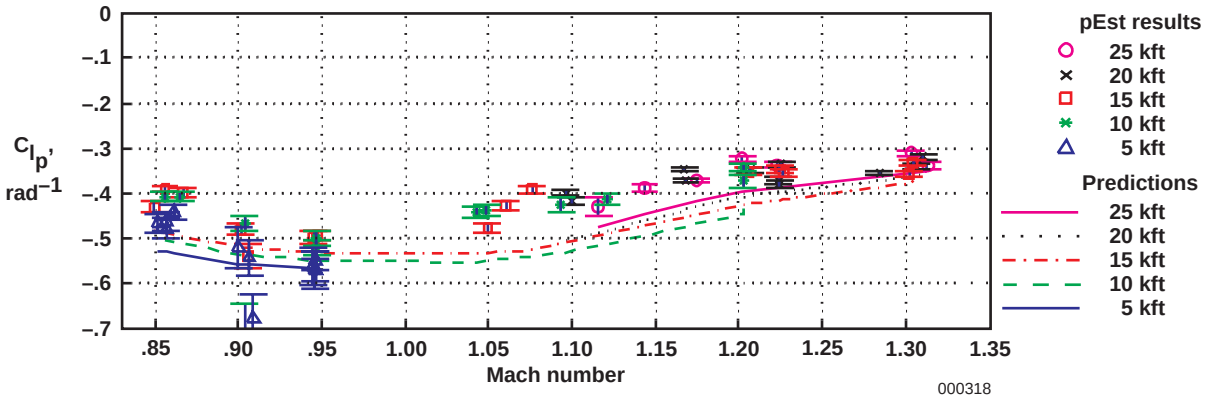

(b) C_{l_p} (vertical moment reference at *WL* 100).

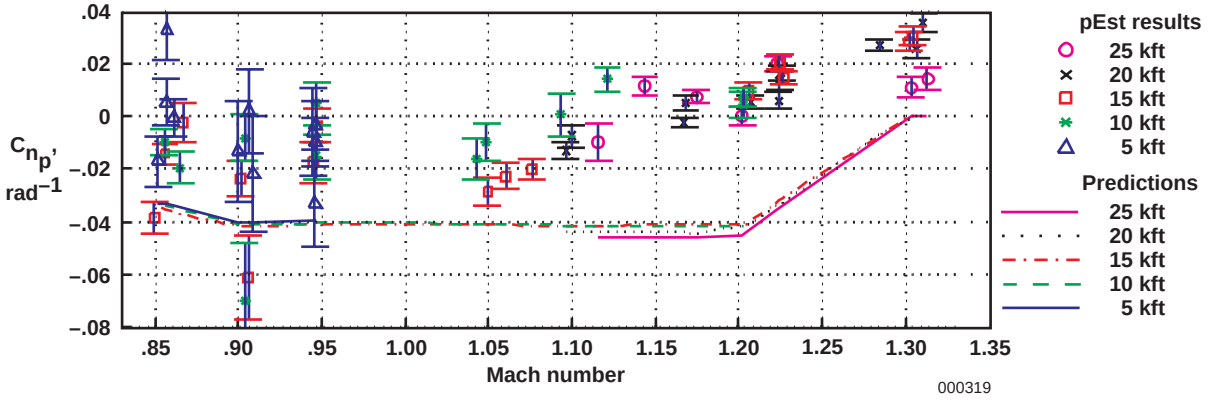

(c) C_{n_p} (moment reference at 0.25 *c*).

Figure 22. Predicted and flight-determined roll rate derivatives (pEst program analysis using CPT measurements).

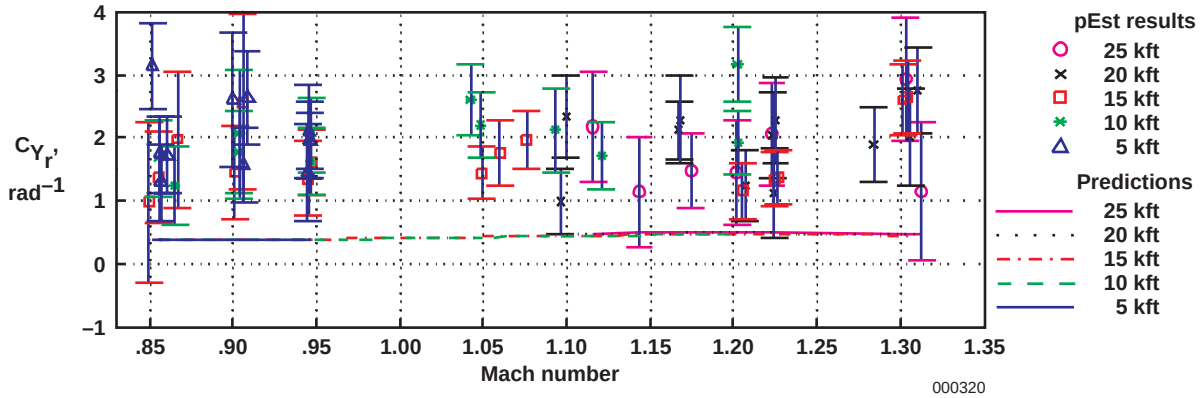

(a) C_{Y_r}.

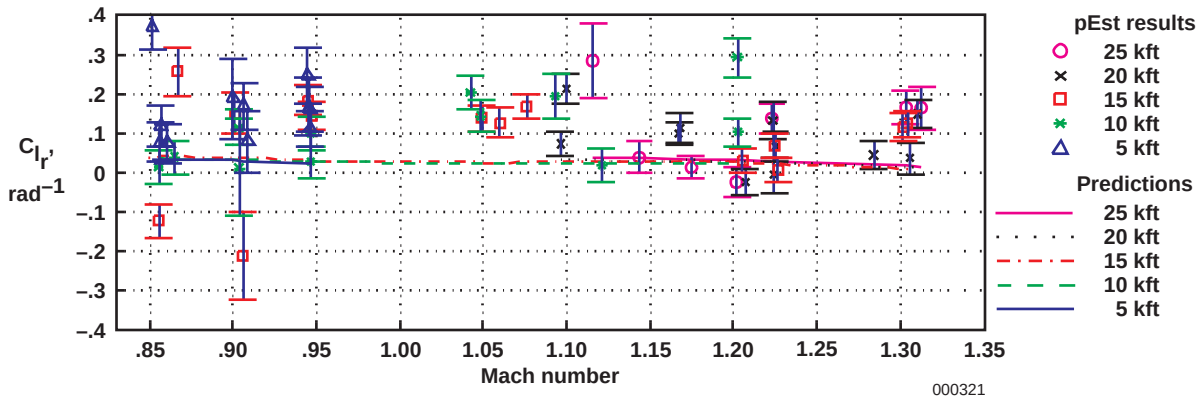

(b) C_{l_r} (vertical moment reference at *WL* 100).

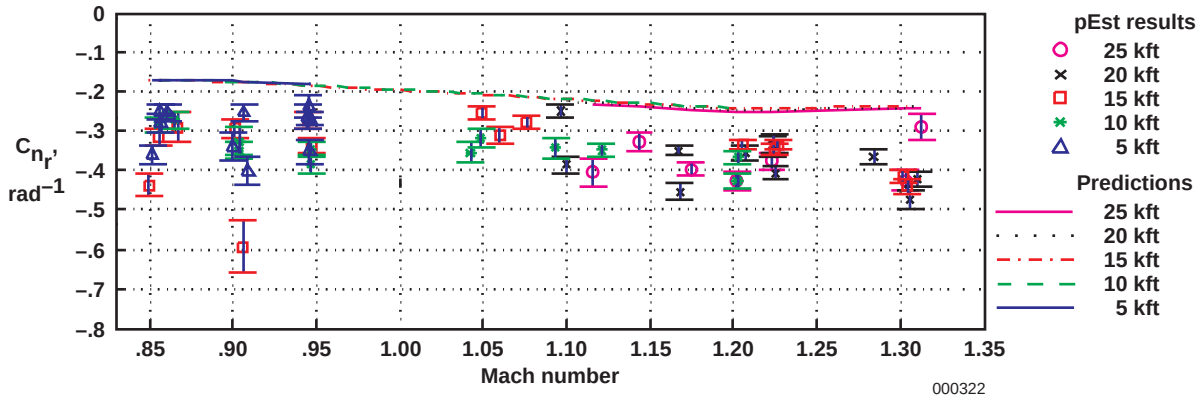

(c) C_{n_r} (moment reference at 0.25 *c*).

Figure 23. Predicted and flight-determined yaw rate derivatives (pEst program analysis using CPT measurements).

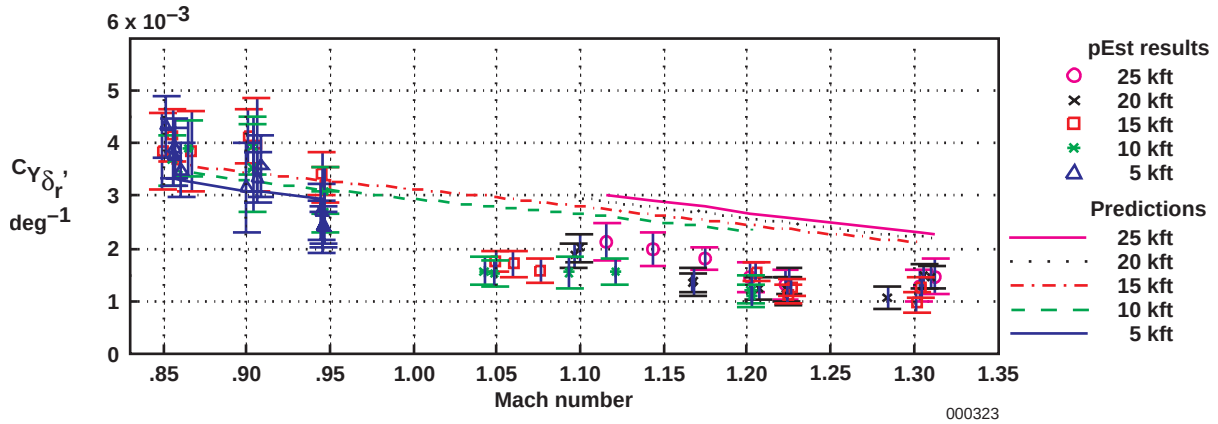

(a) $C_{Y_{\delta_r}}$.

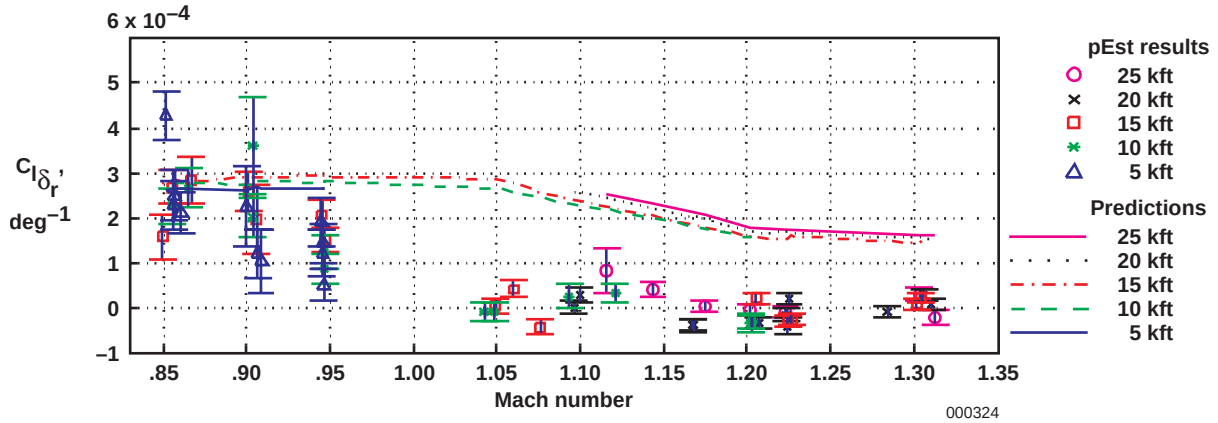

(b) $C_{l_{\delta_r}}$ (vertical moment reference at *WL* 100).

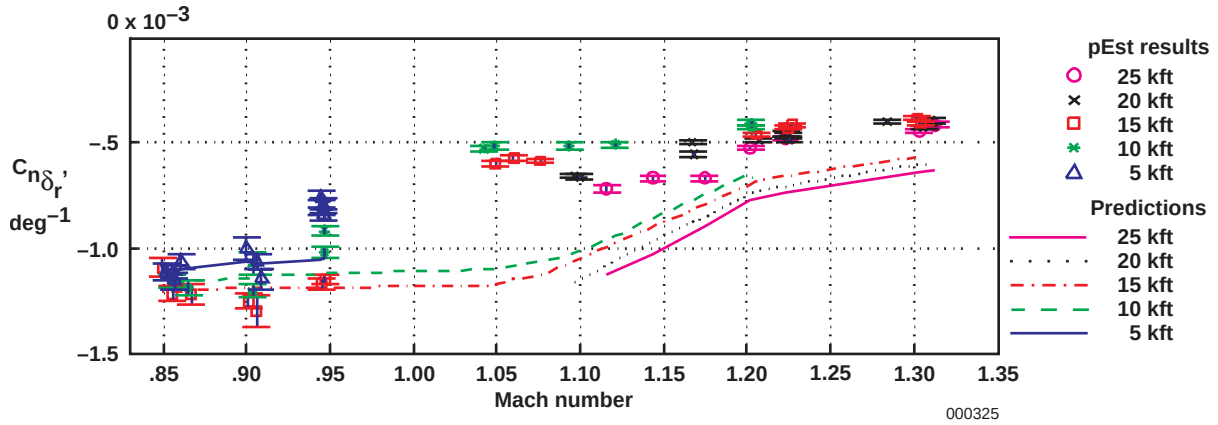

(c) $C_{n_{\delta_r}}$ (moment reference at 0.25 *c*).

Figure 24. Predicted and flight-determined rudder derivatives (pEst program analysis using CPT measurements).

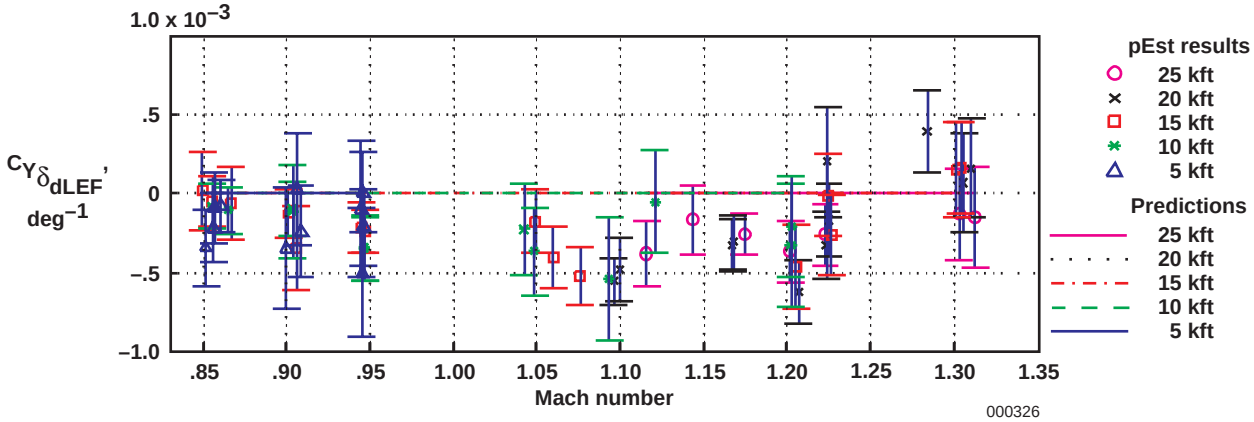

(a) $C_{Y_{\delta_{dLEF}}}$.

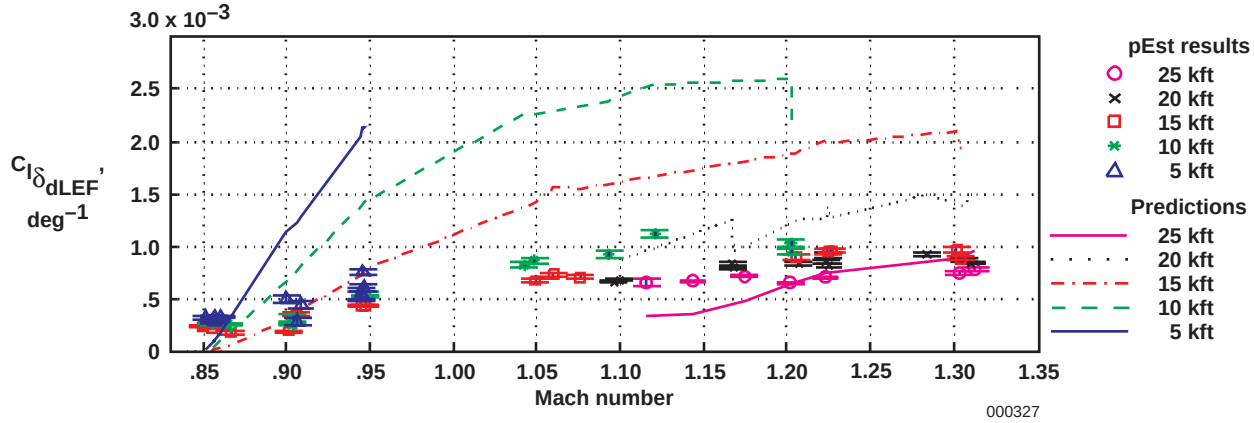

(b) $C_{l_{\delta_{dLEF}}}$ (vertical moment reference at *WL* 100).

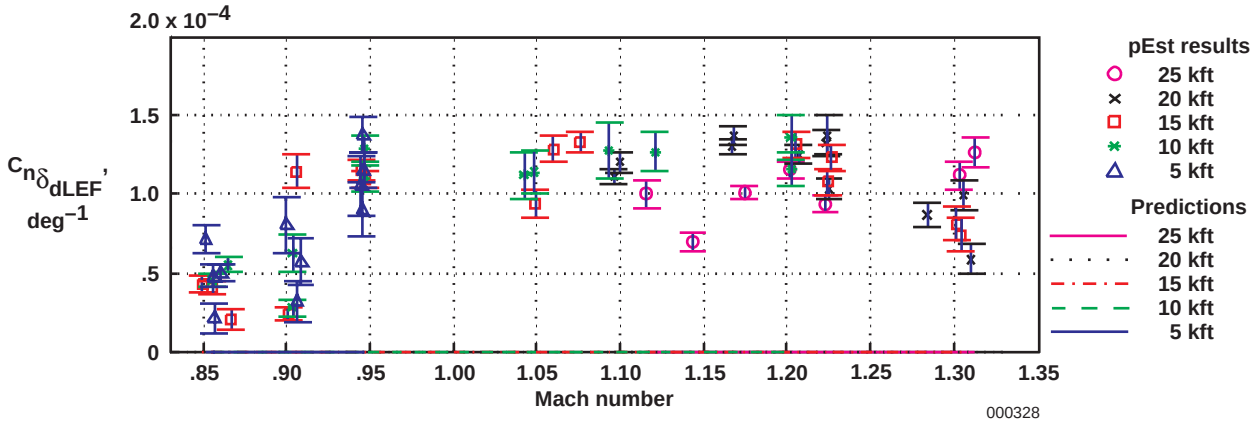

(c) $C_{n_{\delta_{dLEF}}}$ (moment reference at 0.25 *c*).

Figure 25. Predicted and flight-determined differential LEF derivatives (pEst program analysis using CPT measurements).

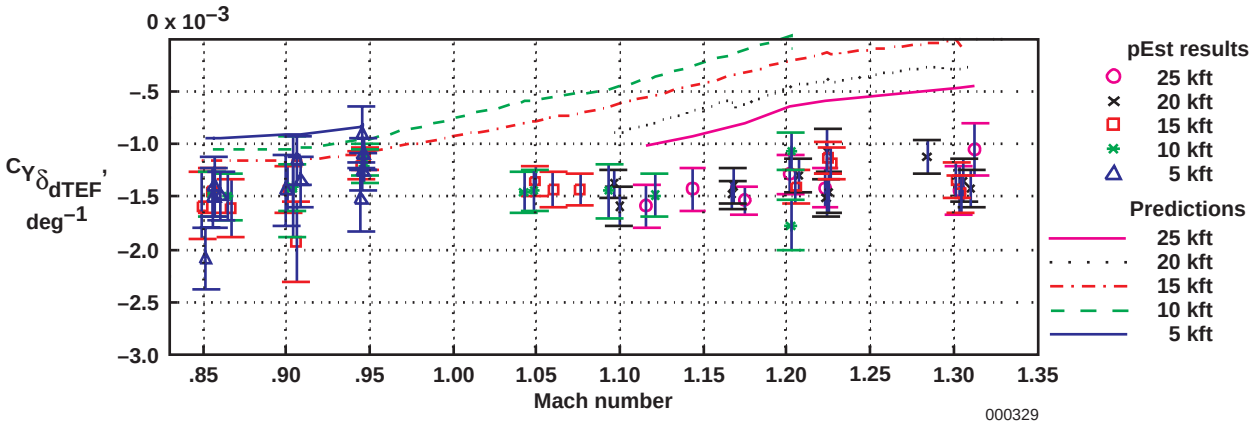

(a) $C_{Y_{\delta_{dTEF}}}$.

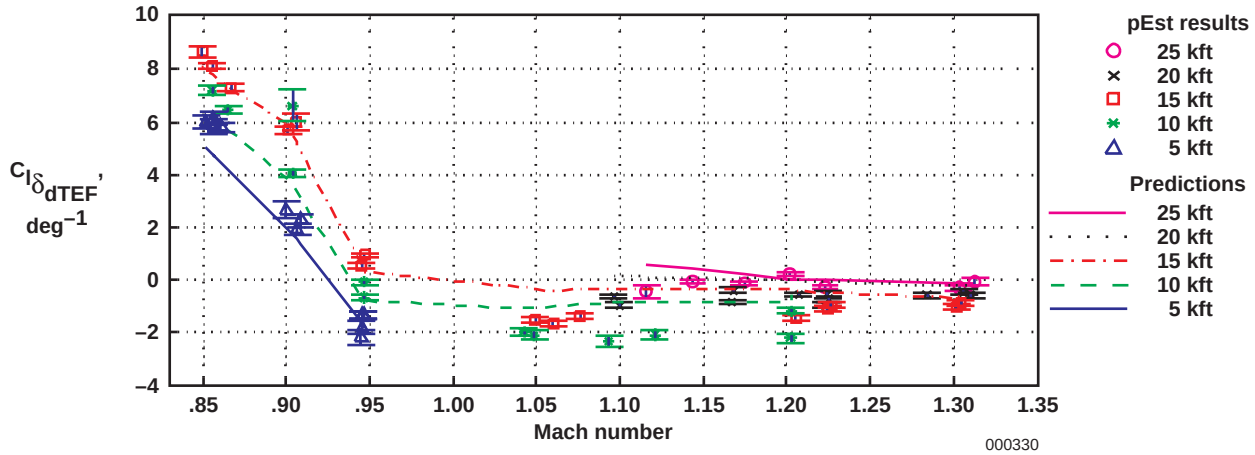

(b) $C_{l_{\delta_{dTEF}}}$ (vertical moment reference at *WL* 100).

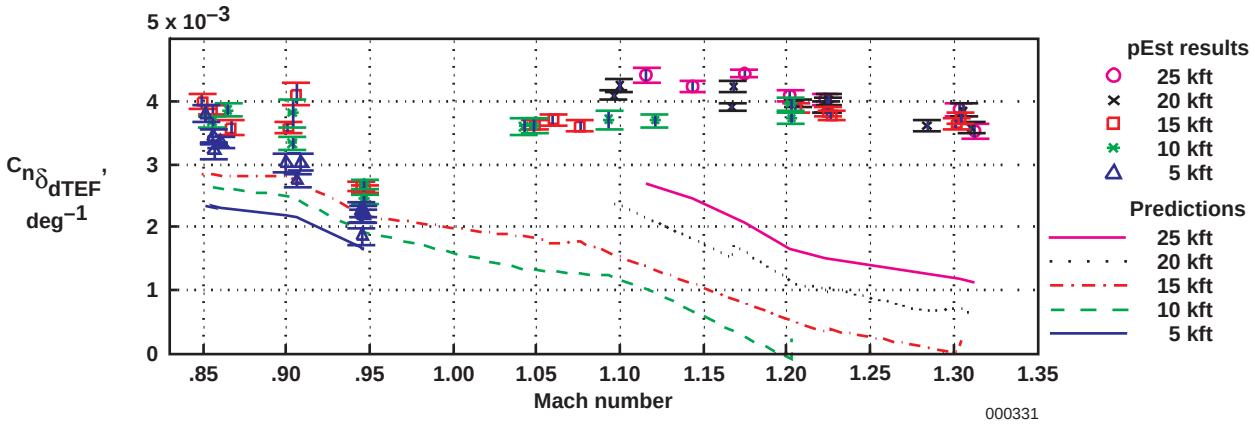

(c) $C_{n_{\delta_{dTEF}}}$ (moment reference at 0.25 *c*).

Figure 26. Predicted and flight-determined differential TEF derivatives (pEst program analysis using CPT measurements).

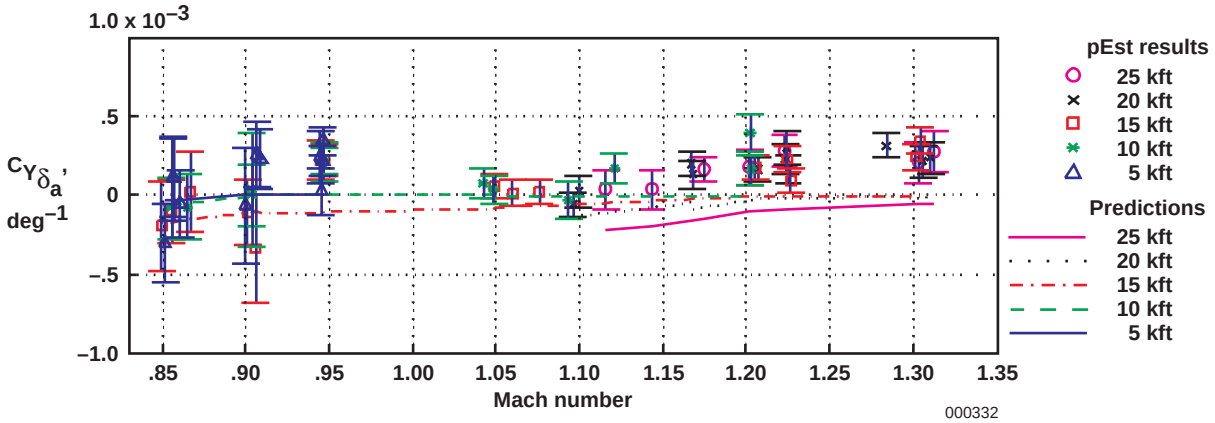

(a) $C_{Y_{\delta_a}}$.

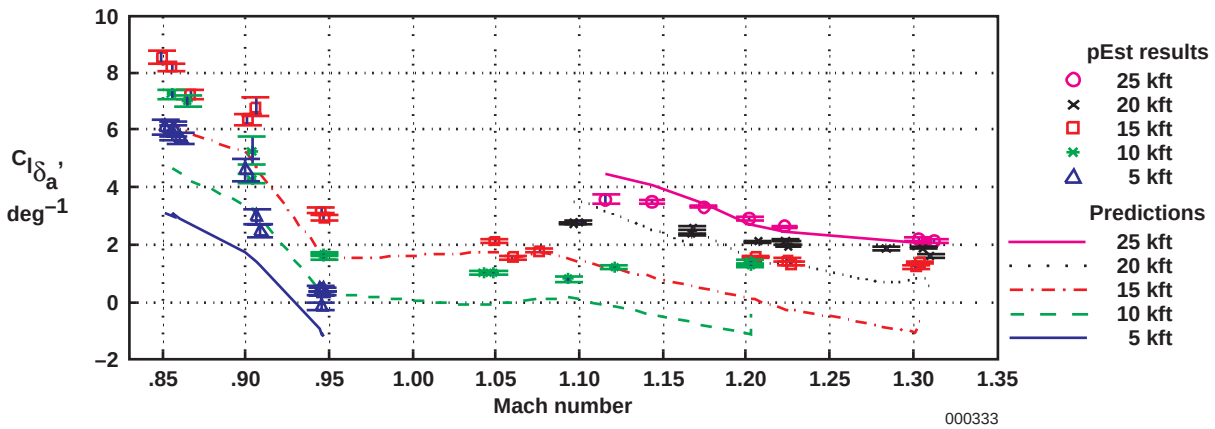

(b) $C_{l_{\delta_a}}$ (vertical moment reference at *WL* 100).

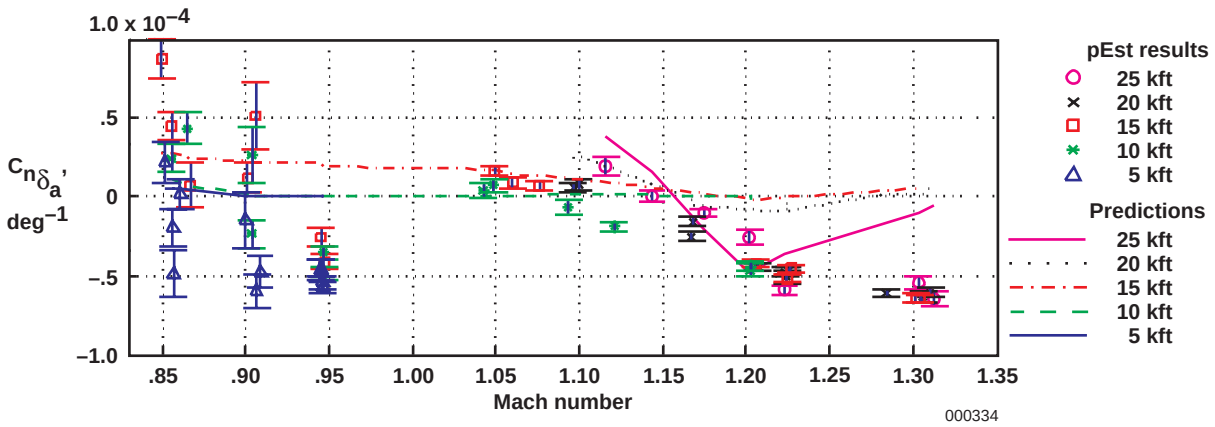

(c) $C_{n_{\delta_a}}$ (moment reference at 0.25 *c*).

Figure 27. Predicted and flight-determined aileron derivatives (pEst program analysis using CPT measurements).

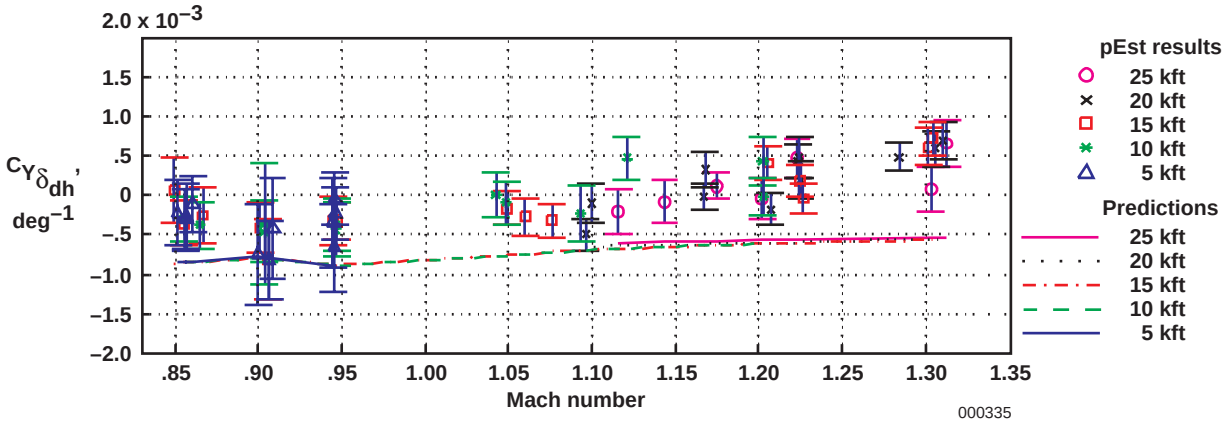

(a) $C_{Y_{\delta_{dh}}}$.

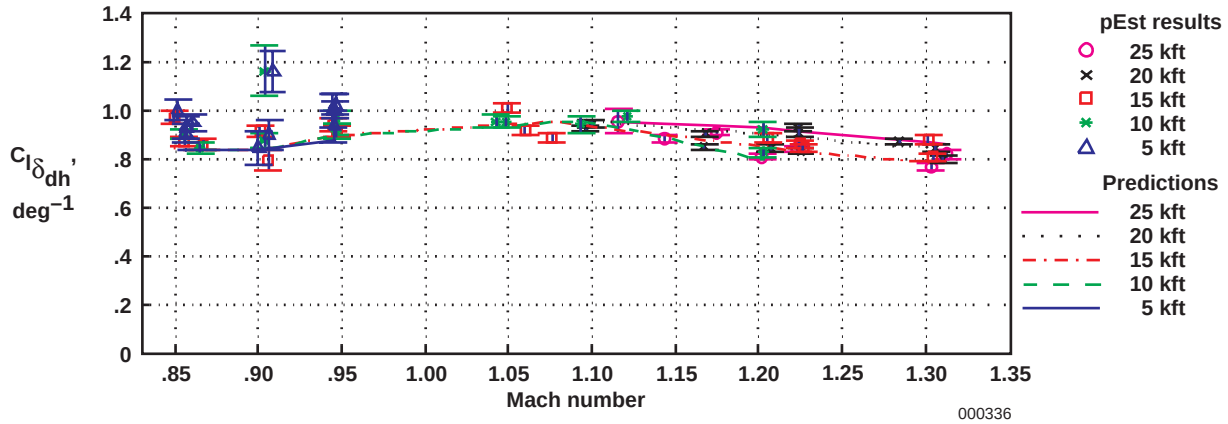

(b) $C_{l_{\delta_{dh}}}$ (vertical moment reference at *WL* 100).

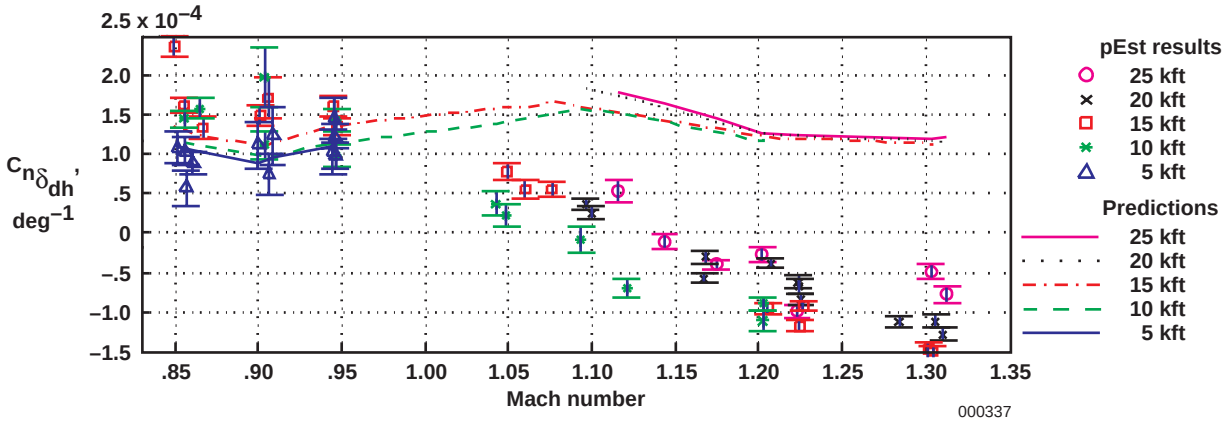

(c) $C_{n_{\delta_{dh}}}$ (moment reference at 0.25 *c*).

Figure 28. Predicted and flight-determined differential stabilator derivatives (pEst program analysis using CPT measurements).

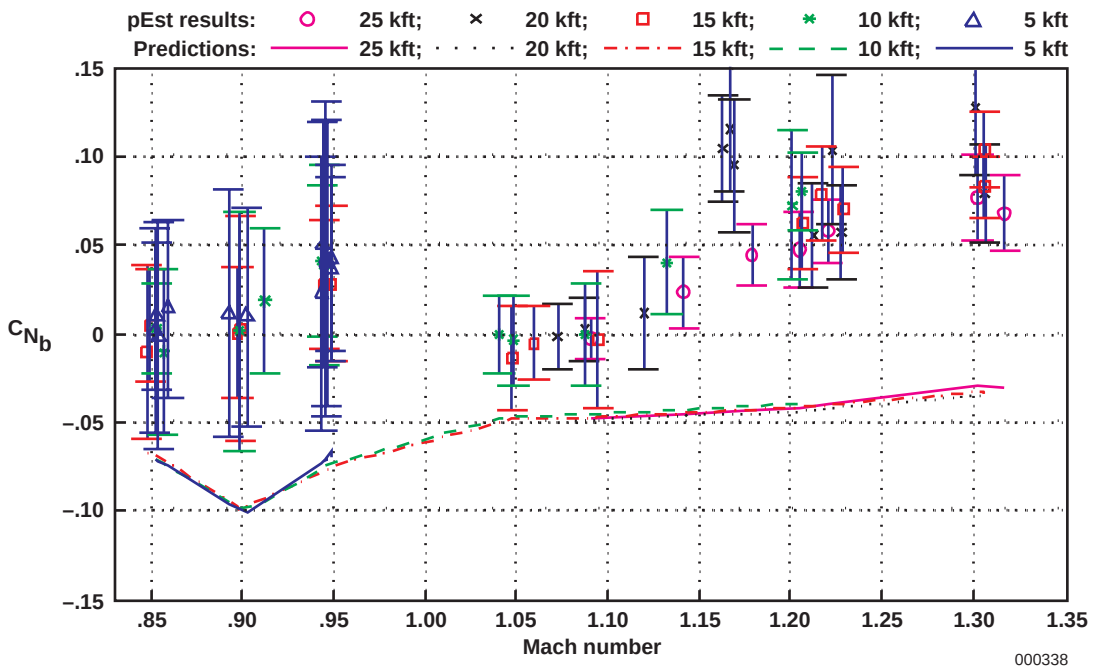

(a) C_{N_b}.

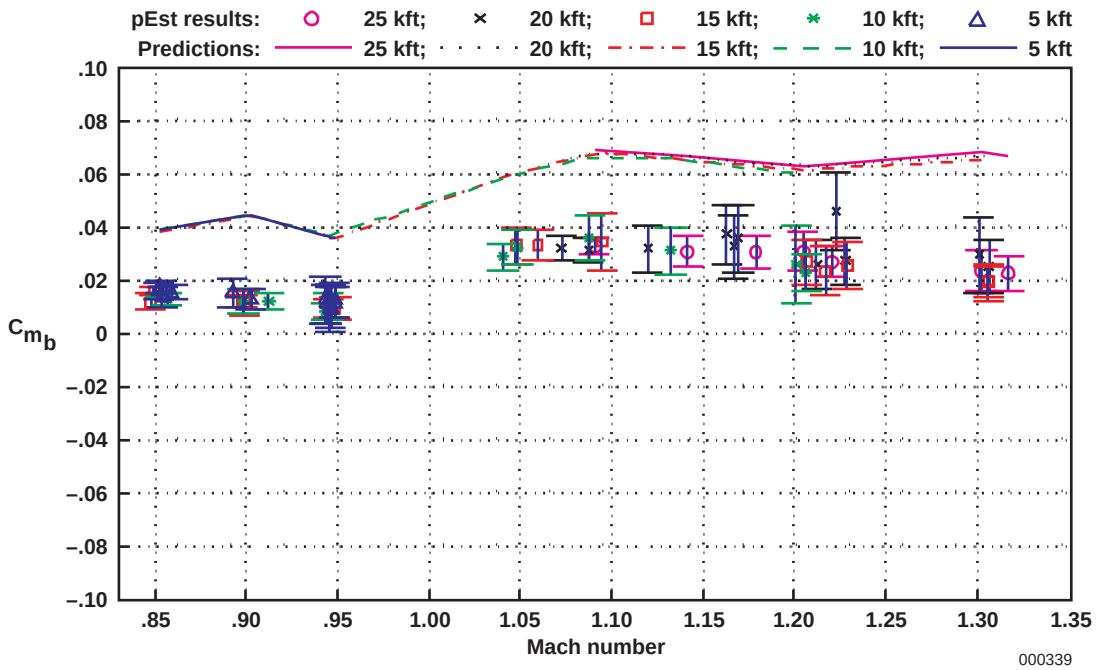

(b) C_{m_b}.

Figure 29. Predicted and flight-determined longitudinal coefficient biases (pEst program analysis using RVDT measurements).

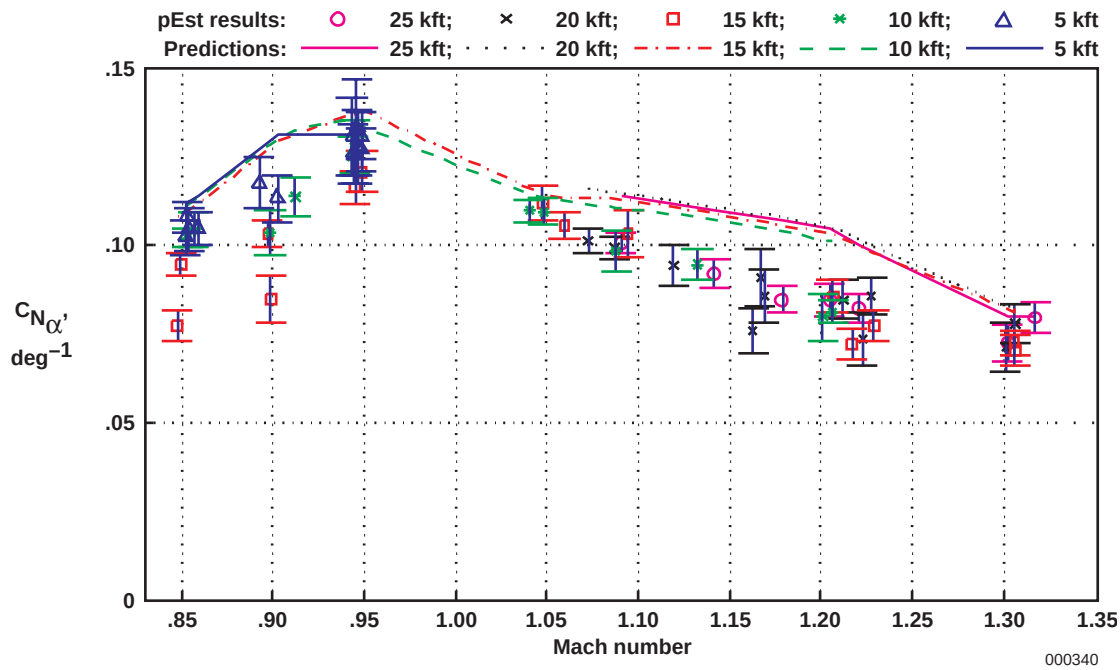

(a) C_{N_α}.

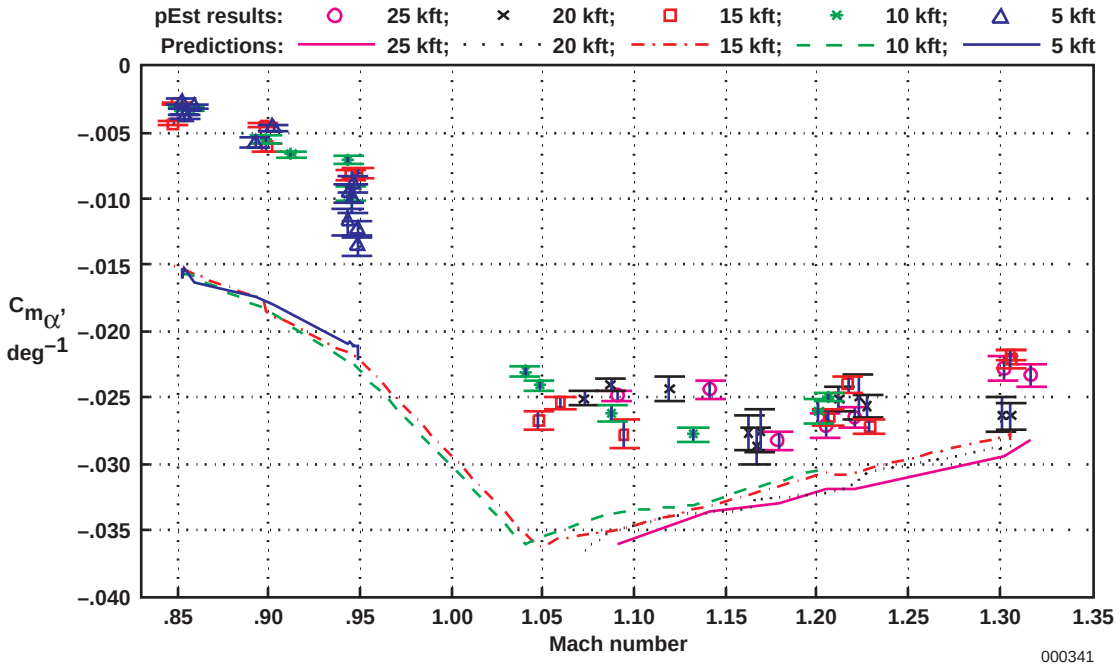

(b) C_{m_α} (moment reference at 0.25 c).

Figure 30. Predicted and flight-determined angle-of-attack derivatives (pEst program analysis using RVDT measurements).

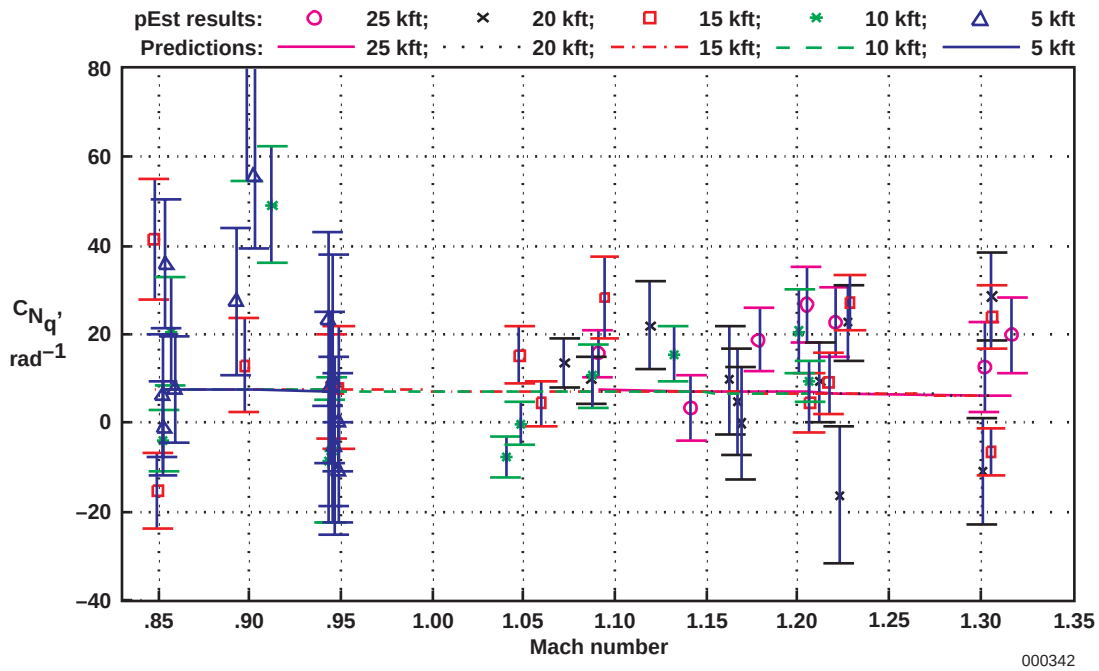

(a) C_{N_q}.

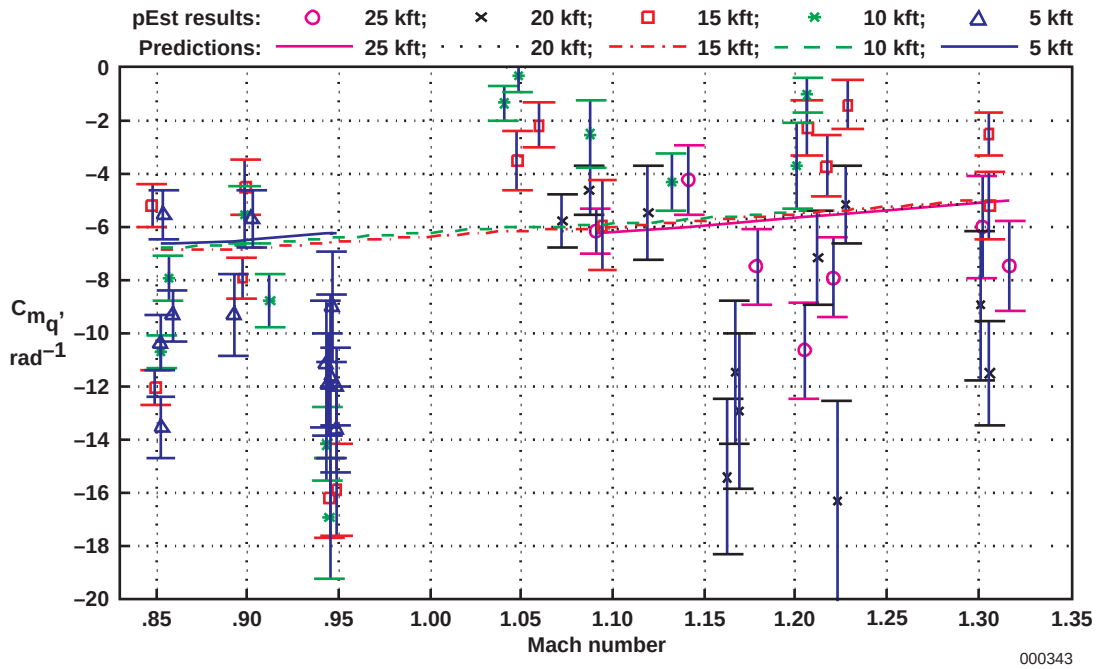

(b) C_{m_q} (moment reference at 0.25 c).

Figure 31. Predicted and flight-determined pitch-rate derivatives (pEst program analysis using RVDT measurements).

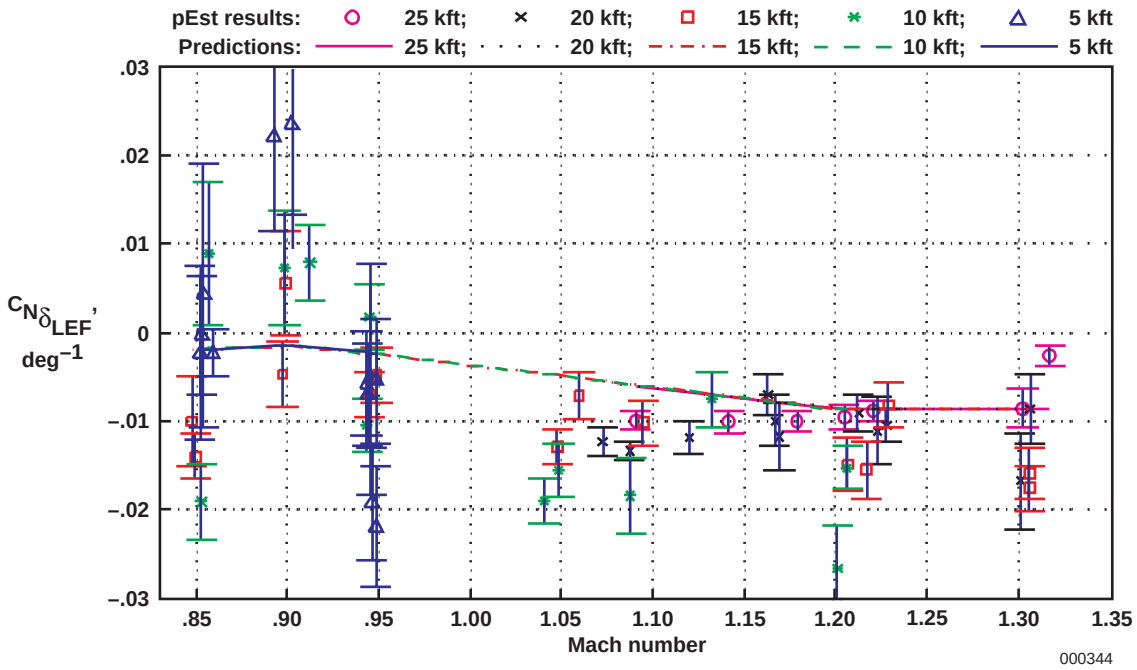

(a) $C_{N_{\delta_{LEF}}}$.

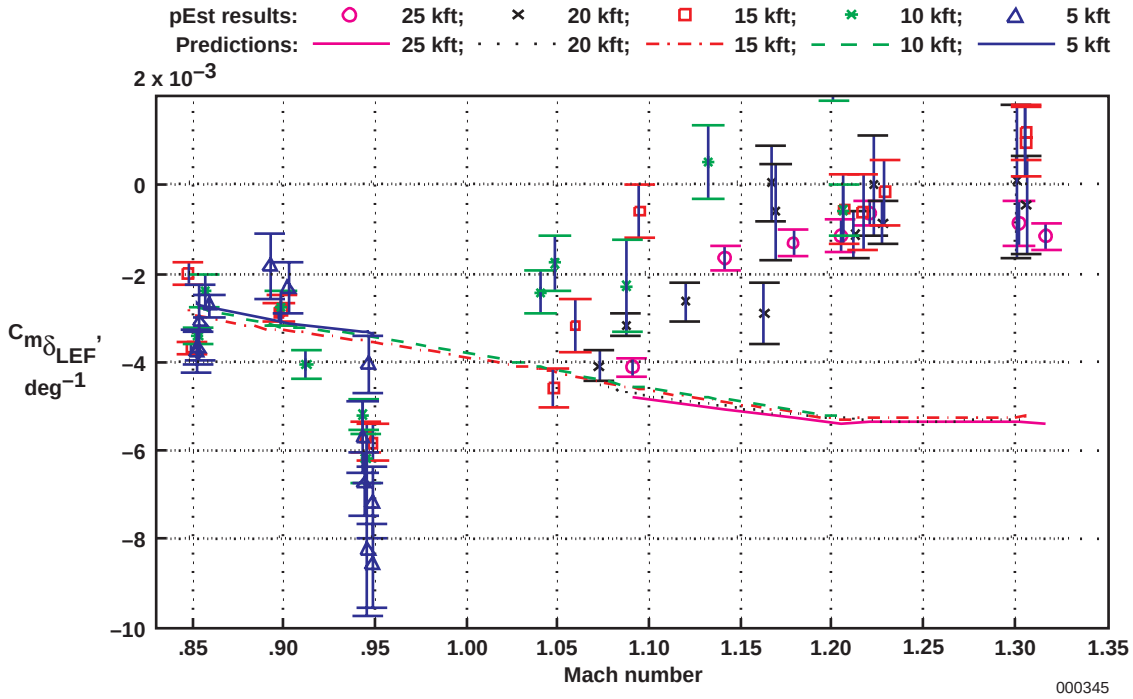

(b) $C_{m_{\delta_{LEF}}}$ (moment reference at 0.25 c).

Figure 32. Predicted and flight-determined symmetric LEF derivatives (pEst program analysis using RVDT measurements).

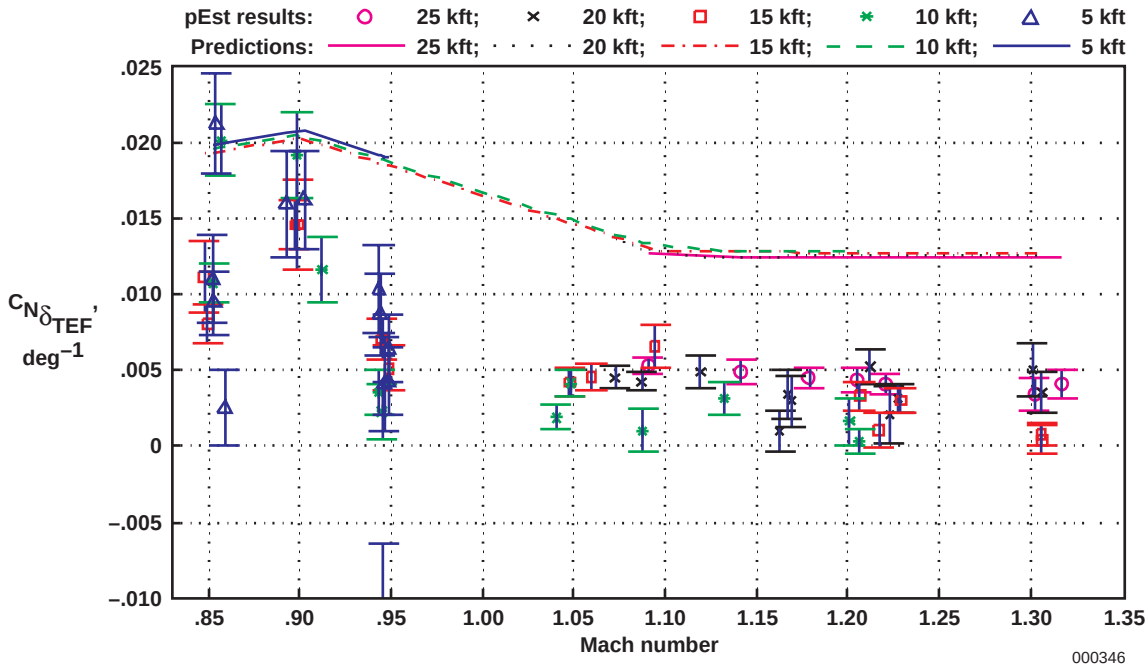

(a) $C_{N_{\delta_{TEF}}}$.

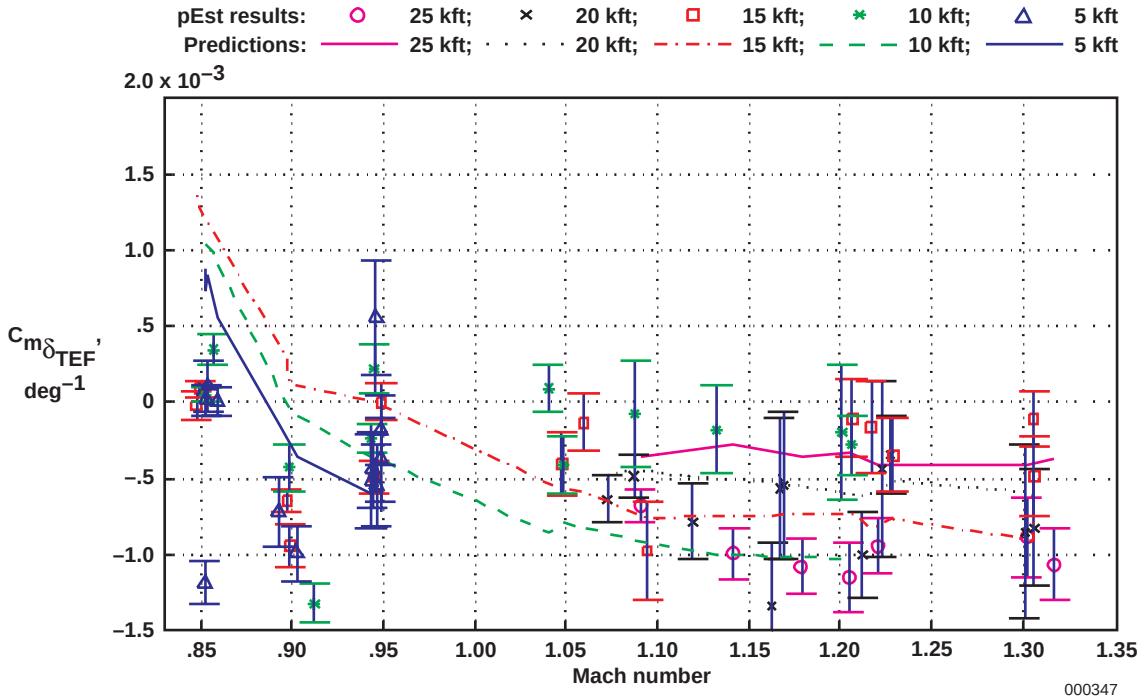

(b) $C_{m_{\delta_{TEF}}}$ (moment reference at 0.25 c).

Figure 33. Predicted and flight-determined symmetric TEF derivatives (pEst program analysis using RVDT measurements).

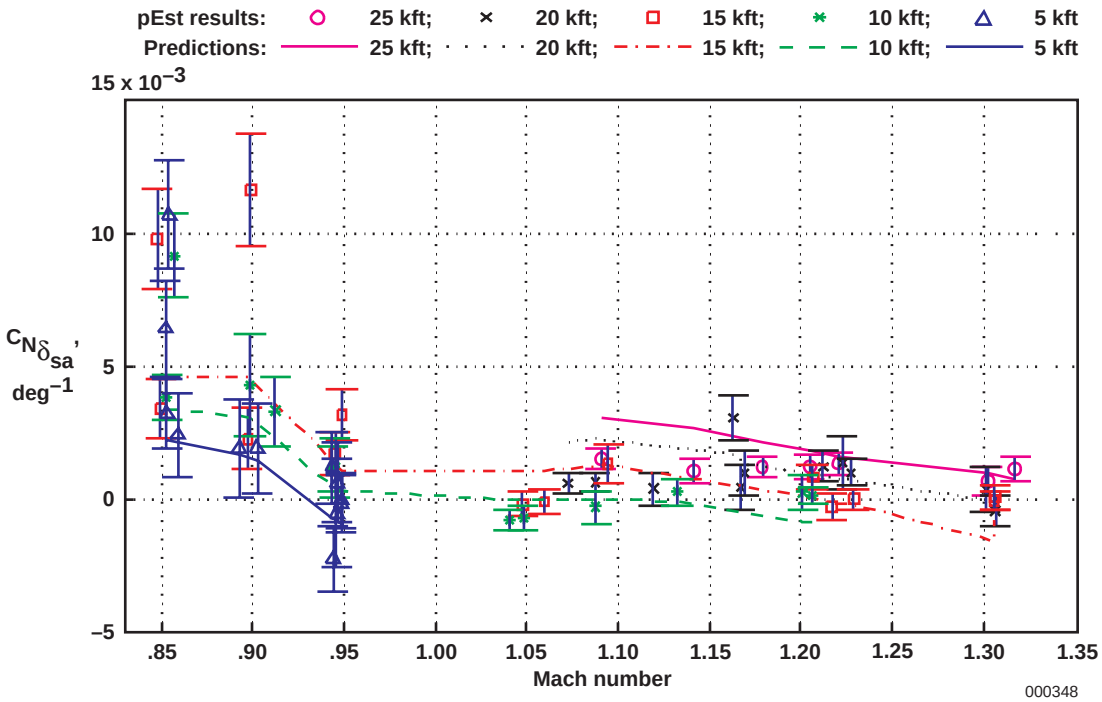

(a) $C_{N_{\delta_{sa}}}$.

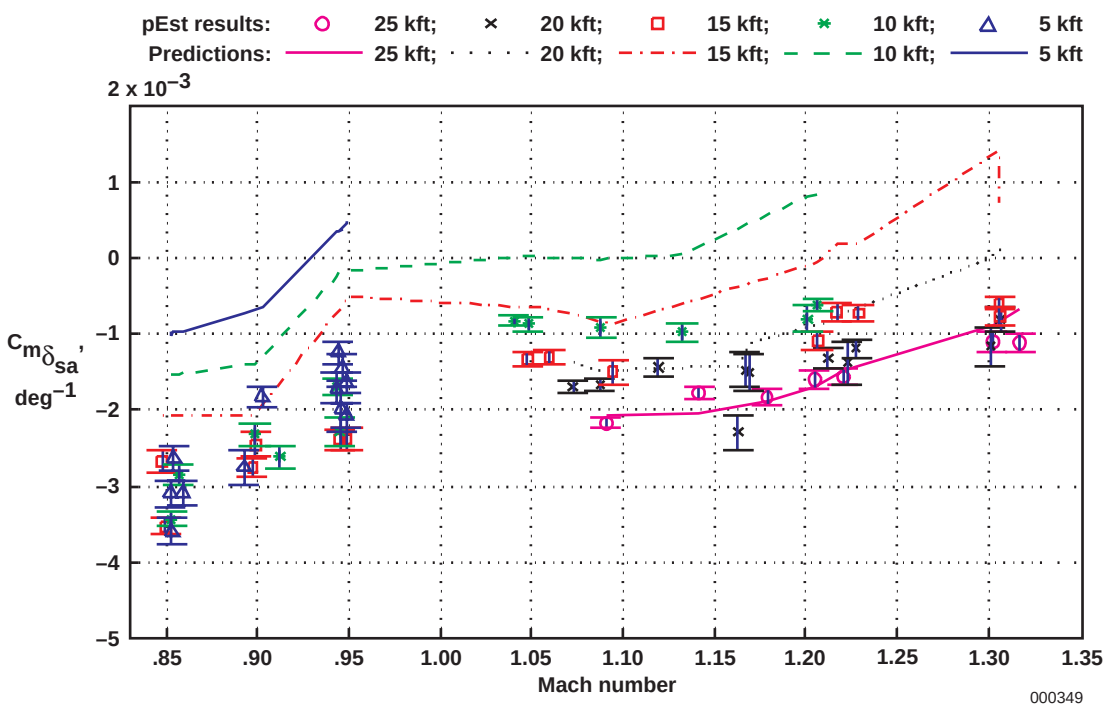

(b) $C_{m_{\delta_{sa}}}$ (moment reference at 0.25 c).

Figure 34. Predicted and flight-determined symmetric aileron derivatives (pEst program analysis using RVDT measurements).

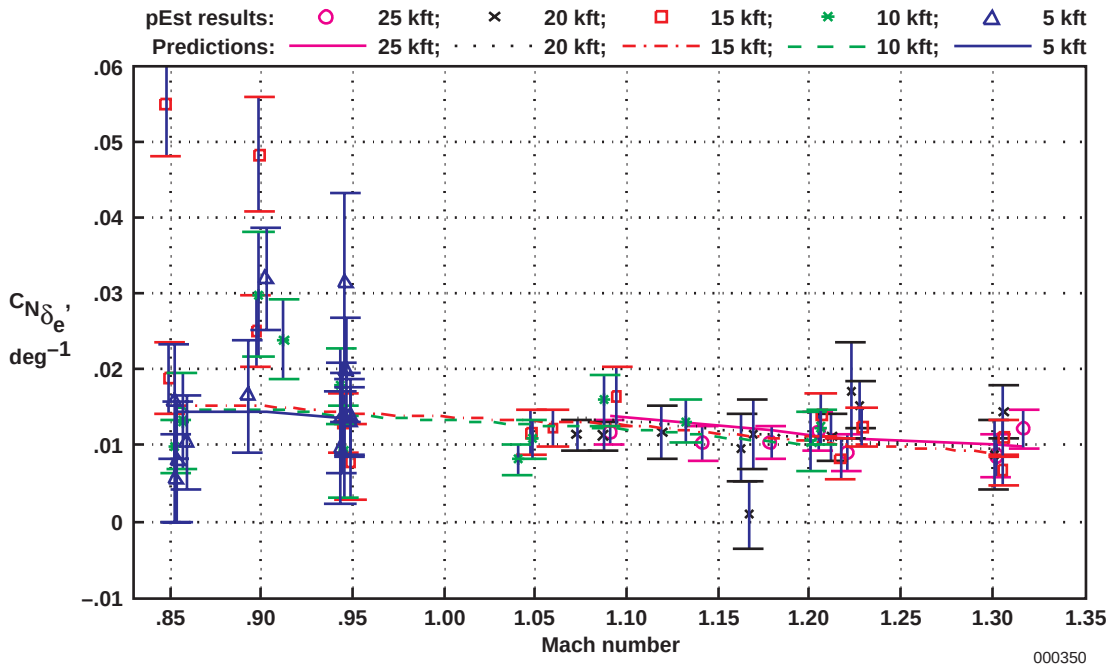

(a) $C_{N_{\delta_e}}$.

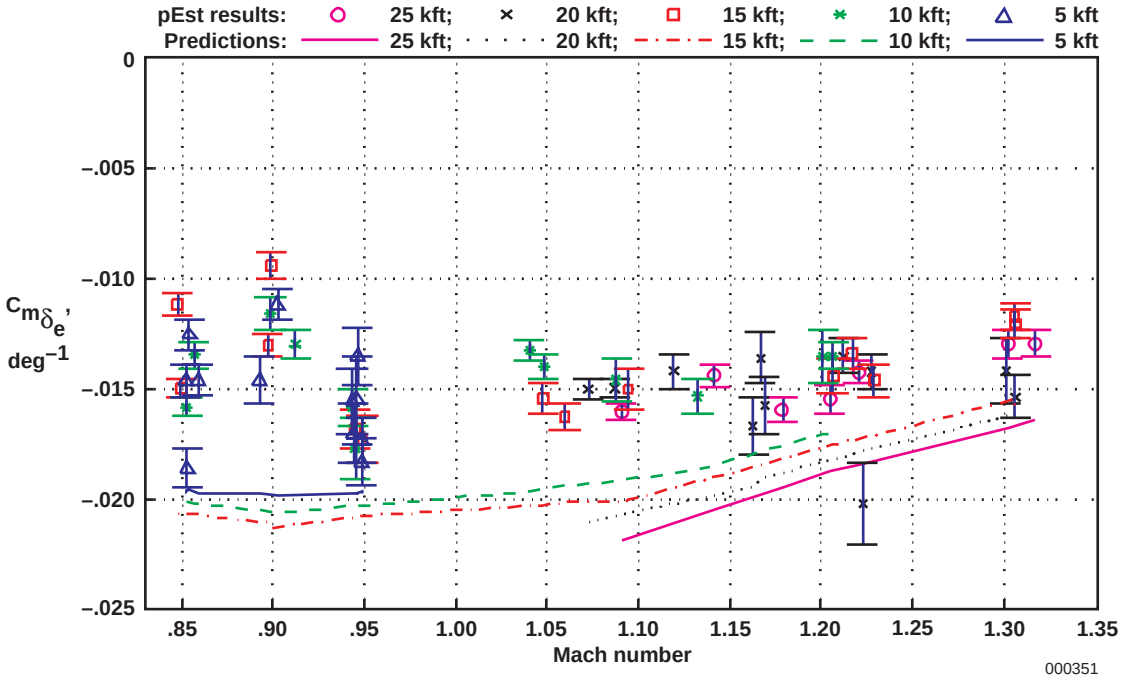

(b) $C_{m_{\delta_e}}$ (moment reference at 0.25 c).

Figure 35. Predicted and flight-determined elevator (symmetric stabilator) derivatives (pEst program analysis using RVDT measurements).

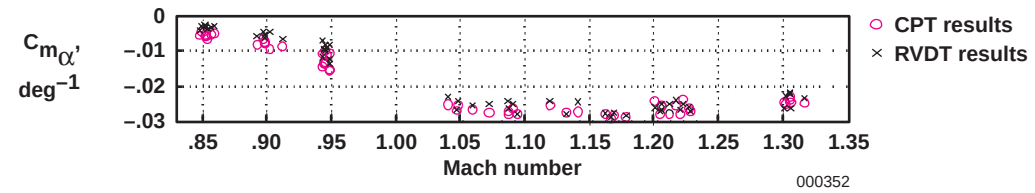

(a) C_{m_α}.

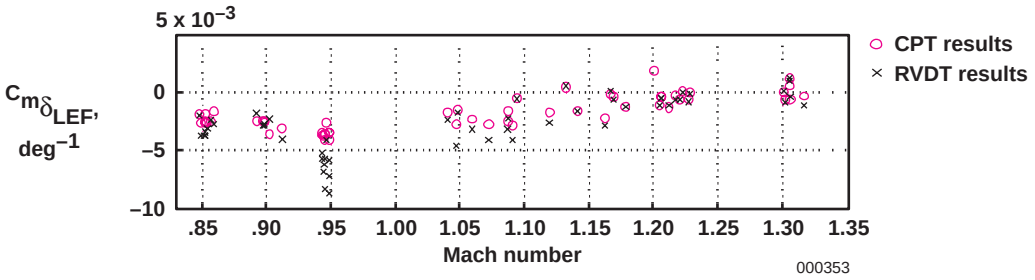

(b) $C_{m_{\delta_{LEF}}}$.

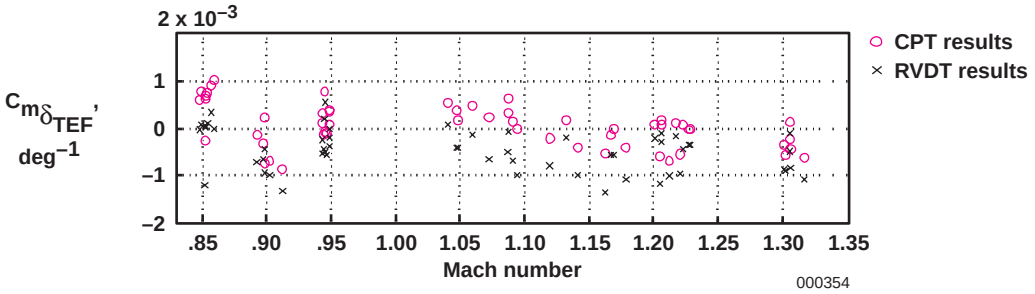

(c) $C_{m_{\delta_{TEF}}}$.

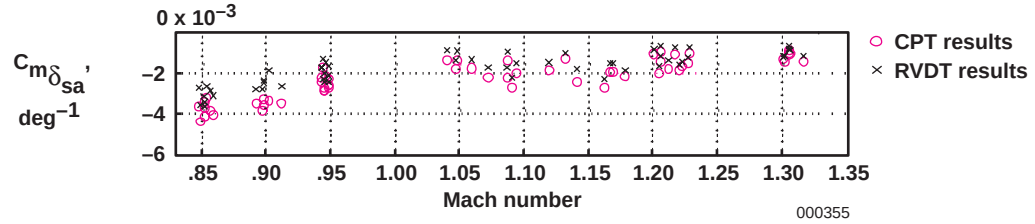

(d) $C_{m_{\delta_{sa}}}$.

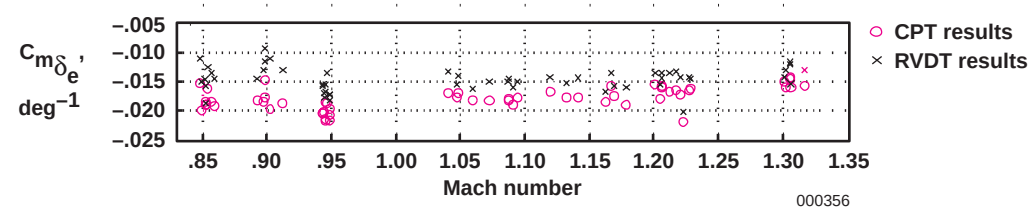

(e) $C_{m_{\delta_e}}$.

Figure 36. Comparison of pitching-moment derivatives measured using CPTs and RVDTs.

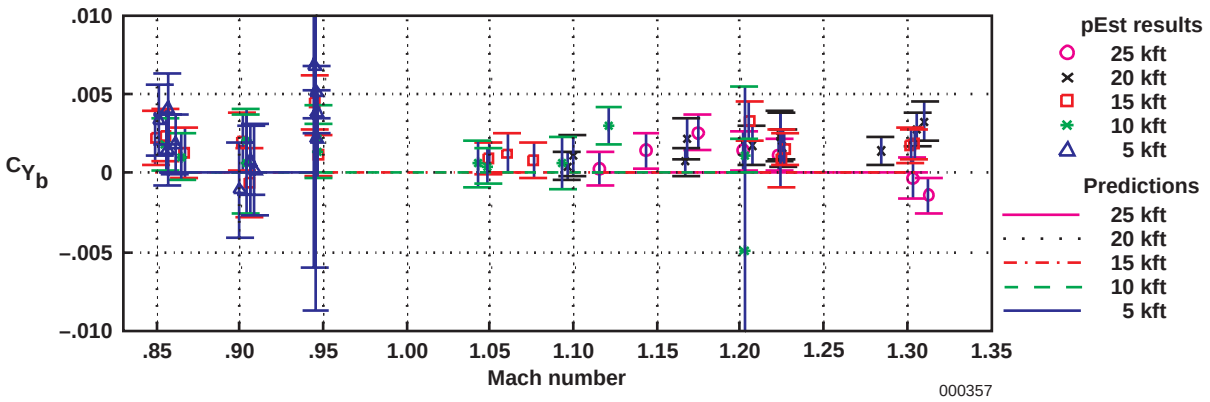

(a) C_{Y_b}.

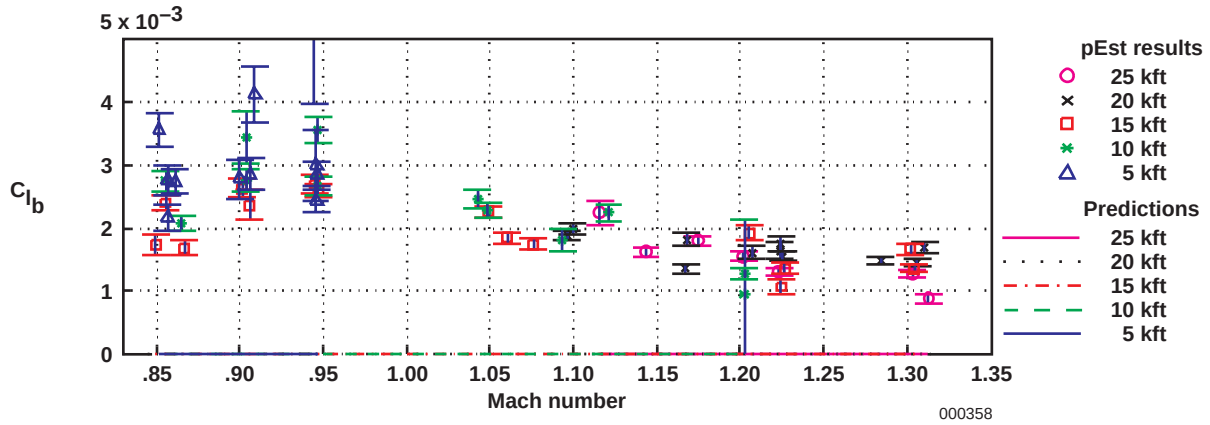

(b) C_{l_b}.

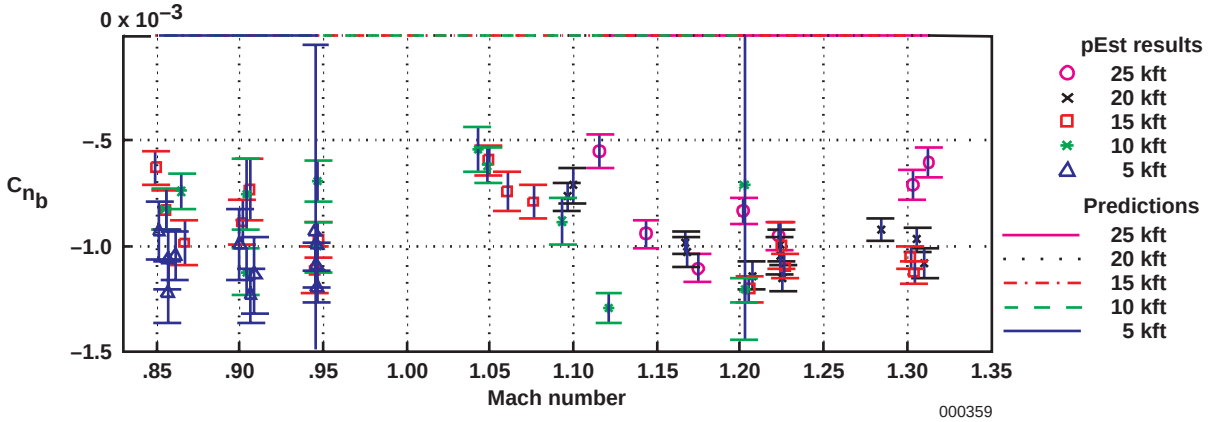

(c) C_{n_b}.

Figure 37. Predicted and flight-determined lateral-directional coefficient biases (pEst program analysis using RVDT measurements).

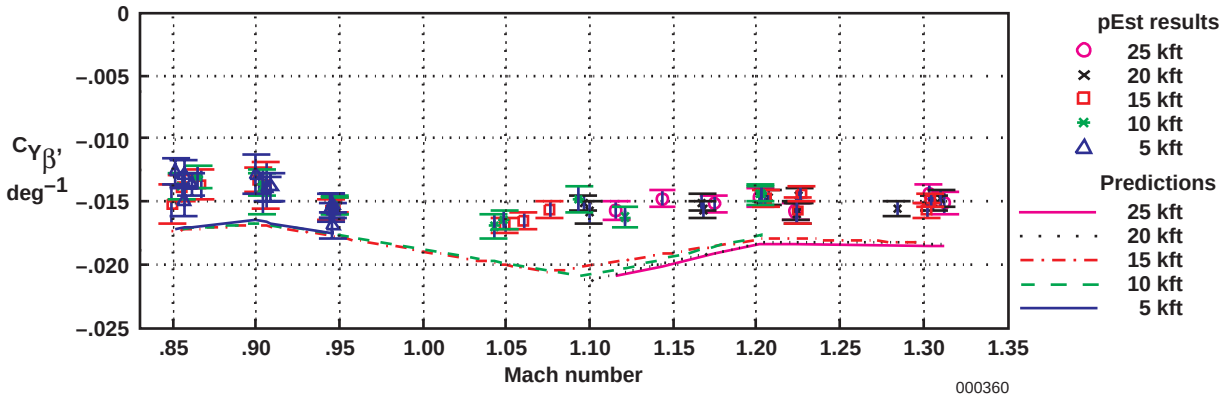

(a) C_{Y_β}.

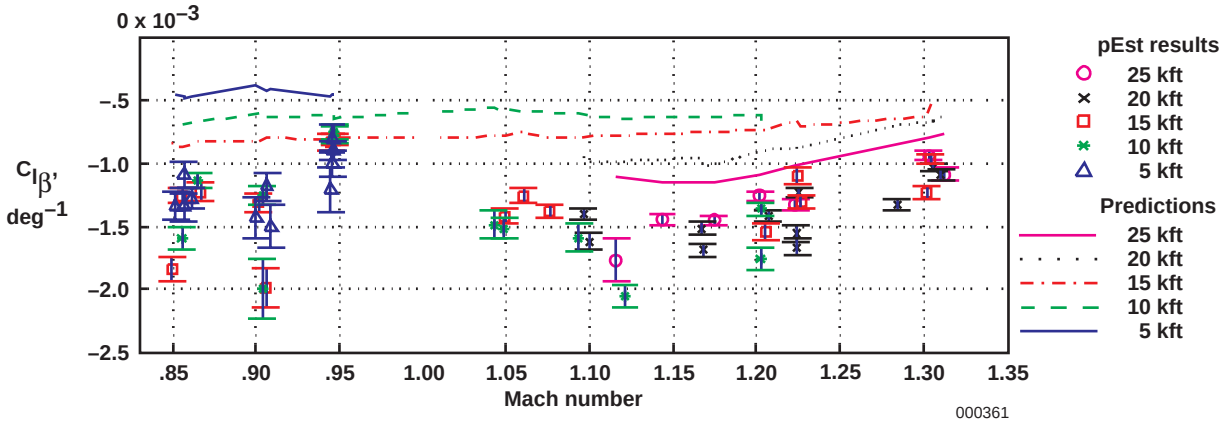

(b) C_{l_β} (vertical moment reference at *WL* 100).

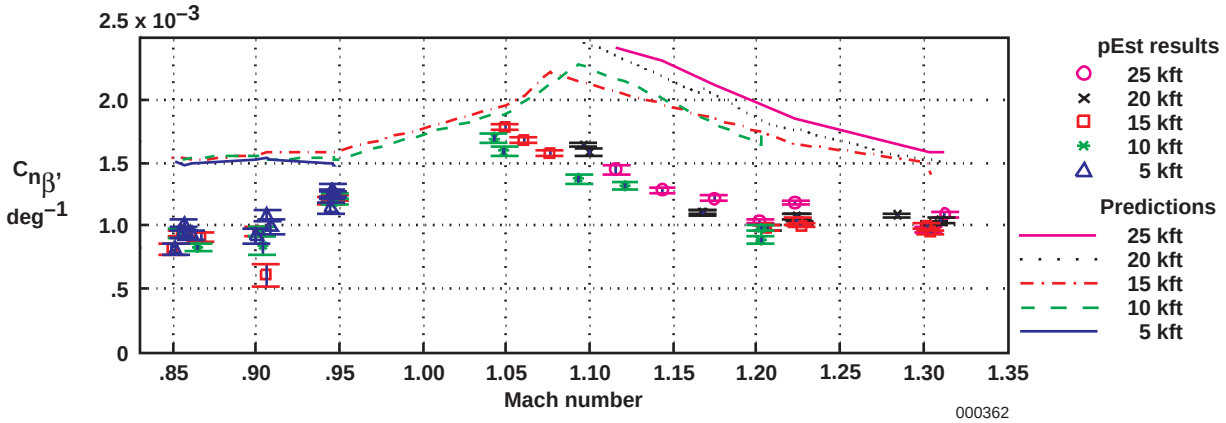

(c) C_{n_β} (moment reference at 0.25 *c*).

Figure 38. Predicted and flight-determined angle of sideslip derivatives (pEst program analysis using RVDT measurements).

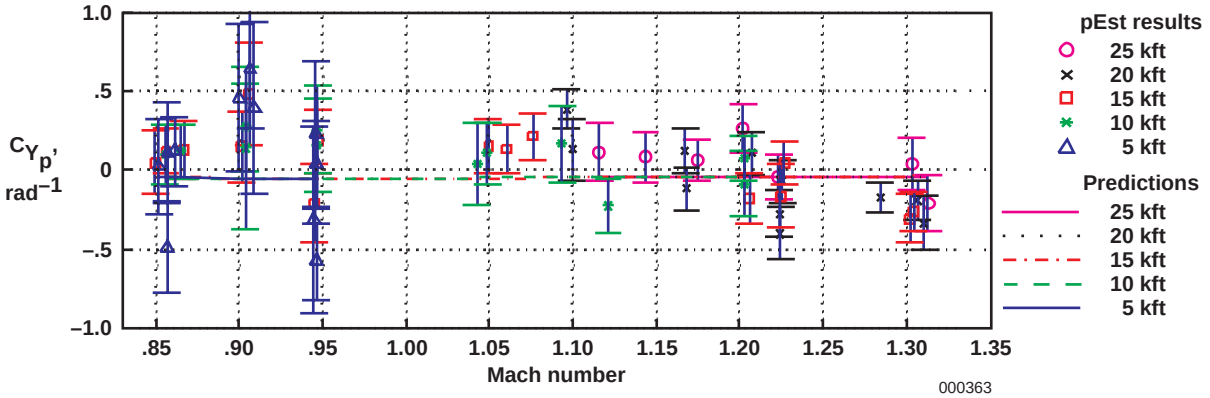

(a) C_{Y_p}.

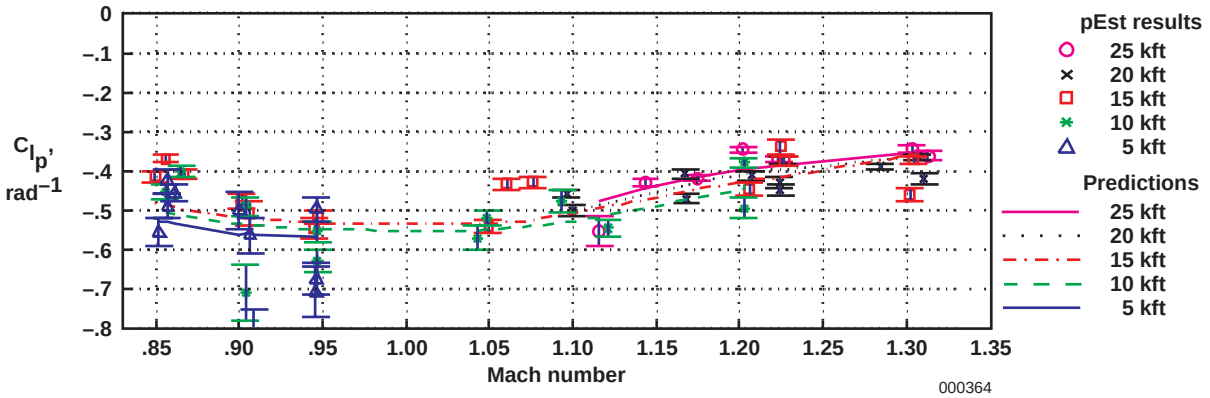

(b) C_{l_p} (vertical moment reference at *WL* 100).

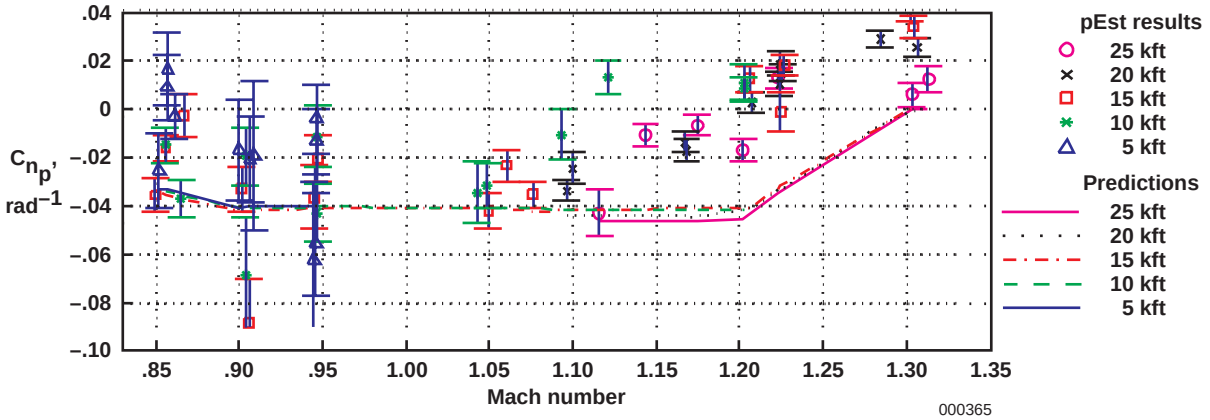

(c) C_{n_p} (moment reference at 0.25 *c*).

Figure 39. Predicted and flight-determined roll rate derivatives (pEst program analysis using RVDT measurements).

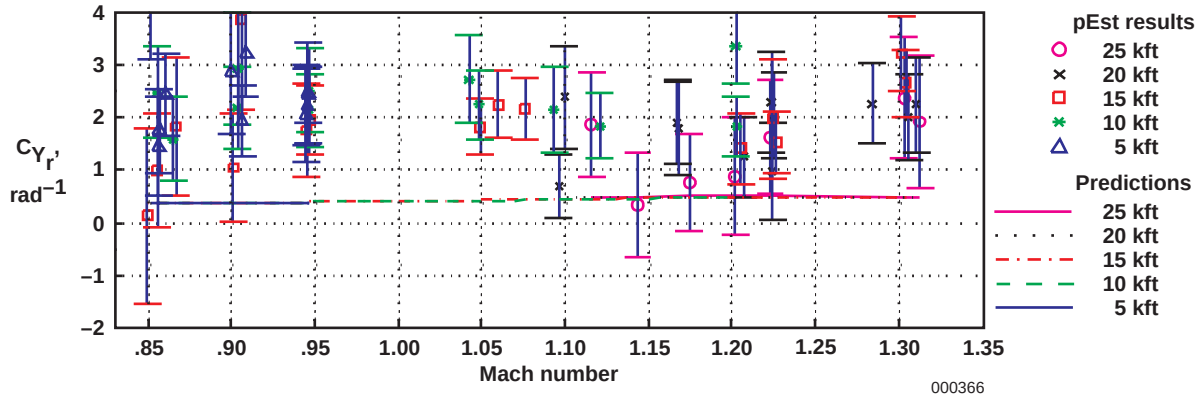

(a) C_{Y_r}.

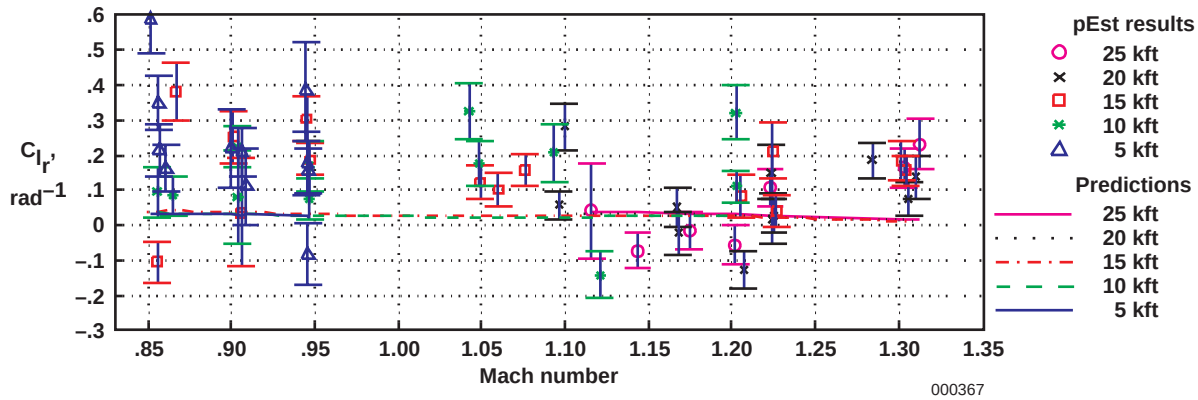

(b) C_{l_r} (vertical moment reference at *WL* 100).

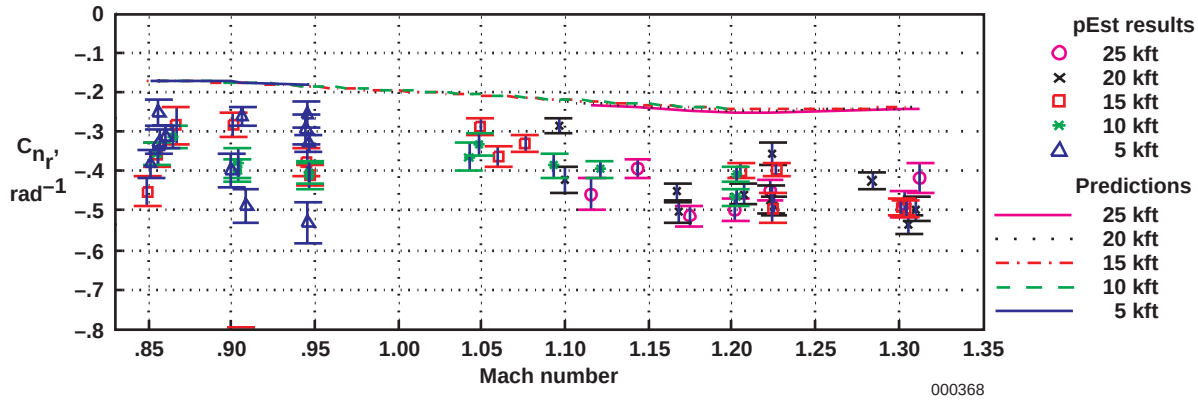

(c) C_{n_r} (moment reference at 0.25 *c*).

Figure 40. Predicted and flight-determined yaw rate derivatives (pEst program analysis using RVDT measurements).

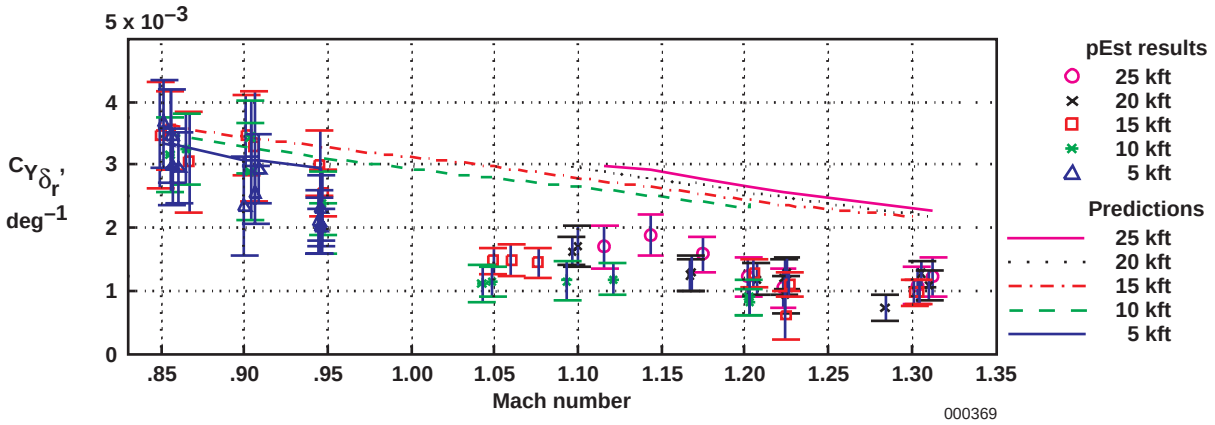

(a) $C_{Y_{\delta_r}}$.

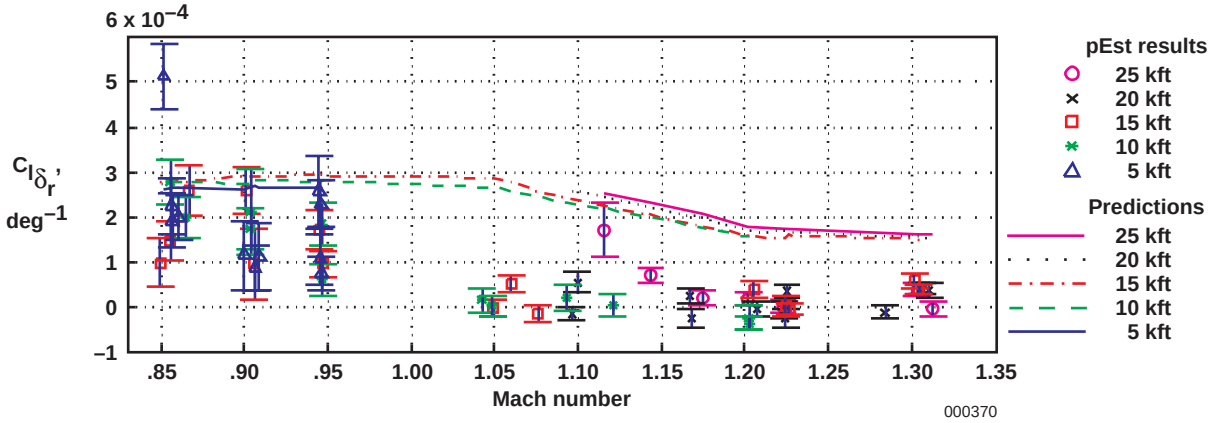

(b) $C_{l_{\delta_r}}$ (vertical moment reference at *WL* 100).

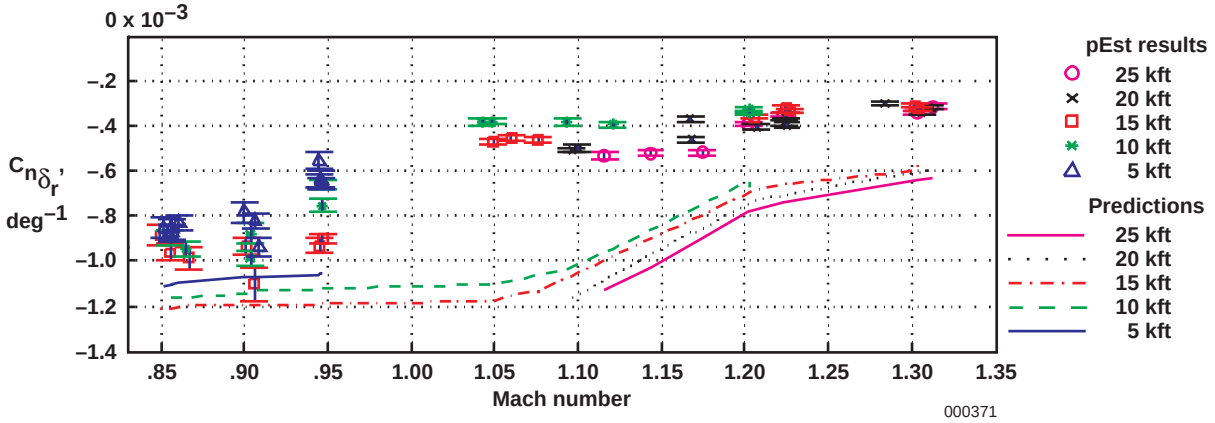

(c) $C_{n_{\delta_r}}$ (moment reference at 0.25 *c*).

Figure 41. Predicted and flight-determined rudder derivatives (pEst program analysis using RVDT measurements).

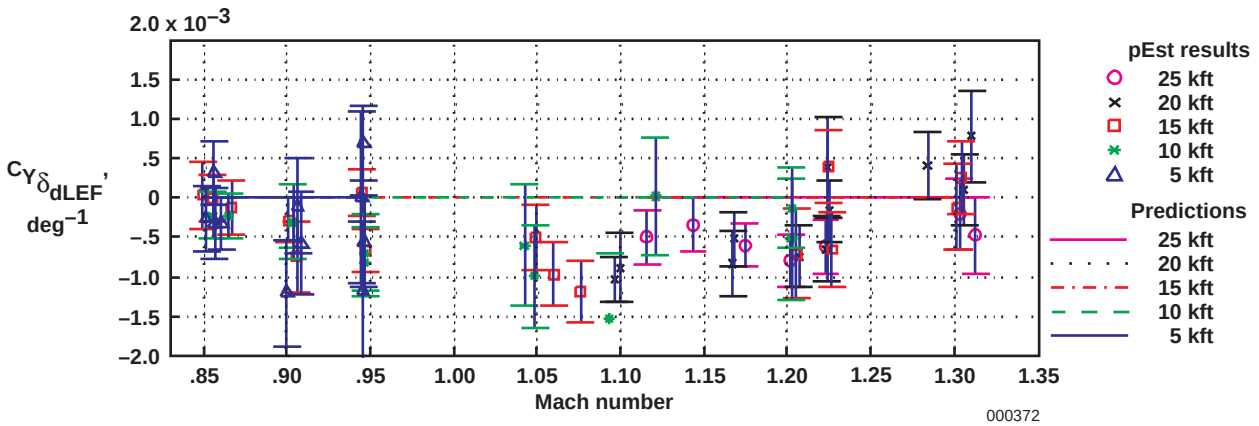

(a) $C_{Y_{\delta_{dLEF}}}$.

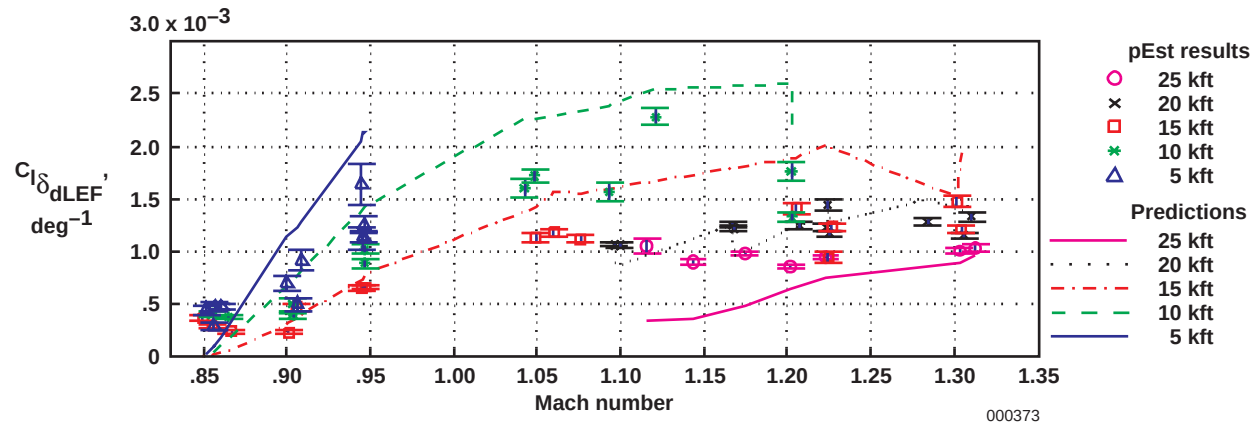

(b) $C_{l_{\delta_{dLEF}}}$ (vertical moment reference at *WL* 100).

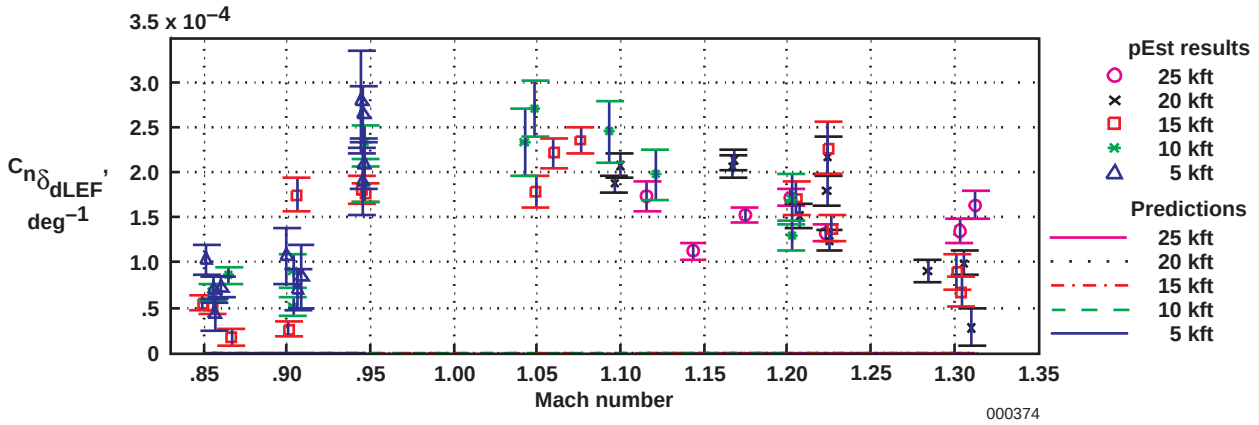

(c) $C_{n_{\delta_{dLEF}}}$ (moment reference at 0.25 *c*).

Figure 42. Predicted and flight-determined differential LEF derivatives (pEst program analysis using RVDT measurements).

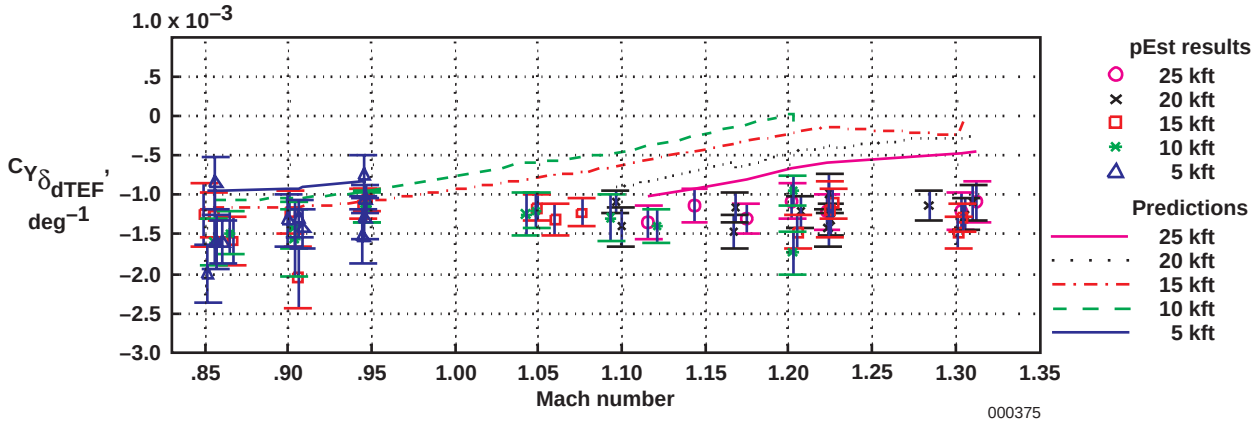

(a) $C_{Y_{\delta_{dTEF}}}$.

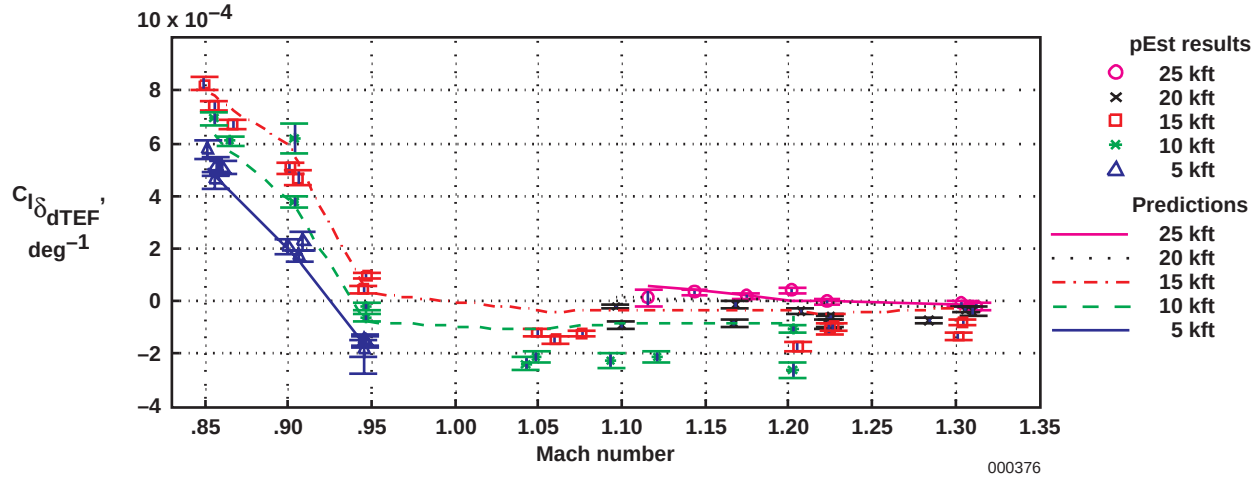

(b) $C_{l_{\delta_{dTEF}}}$ (vertical moment reference at *WL* 100).

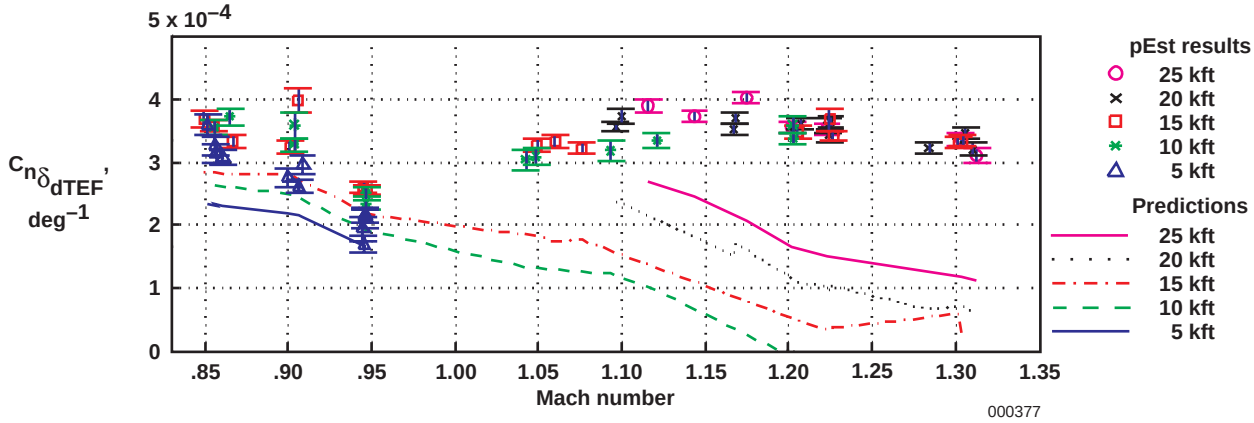

(c) $C_{n_{\delta_{dTEF}}}$ (moment reference at 0.25 *c*).

Figure 43. Predicted and flight-determined differential TEF derivatives (pEst program analysis using RVDT measurements).

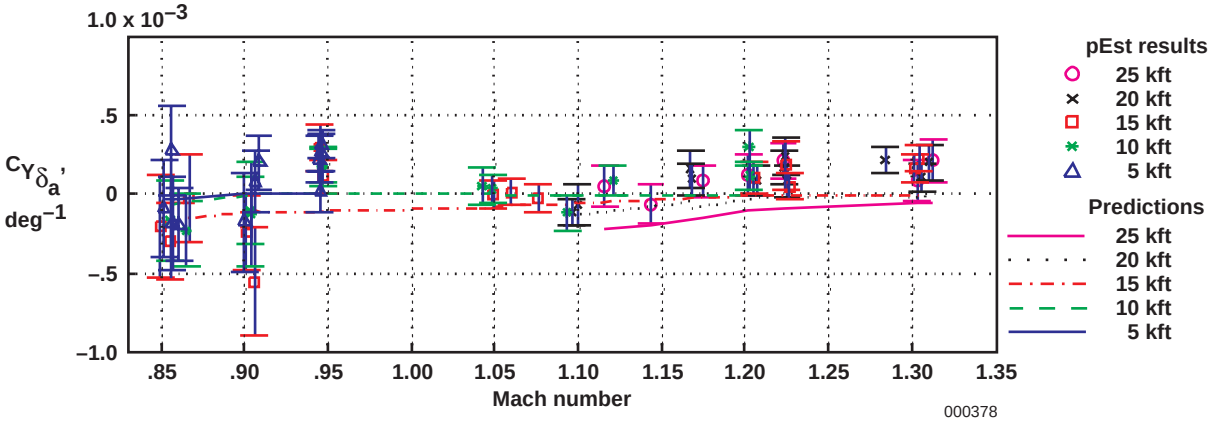

(a) $C_{Y_{\delta_a}}$.

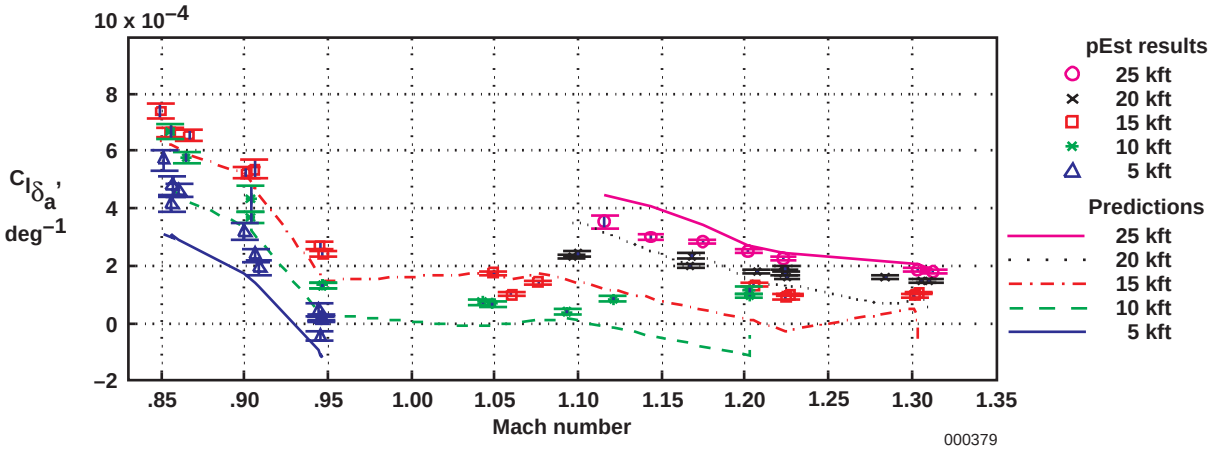

(b) $C_{l_{\delta_a}}$ (vertical moment reference at *WL* 100).

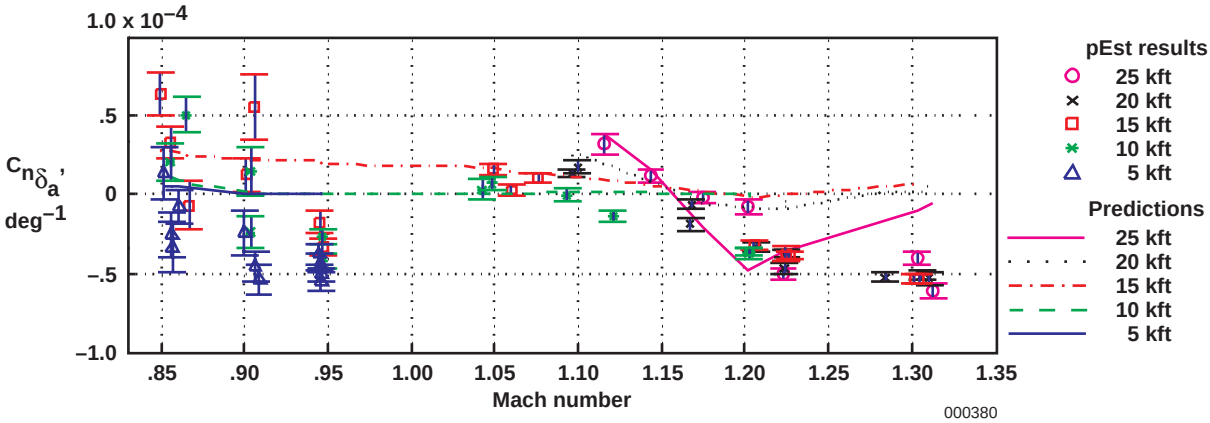

(c) $C_{n_{\delta_a}}$ (moment reference at 0.25 *c*).

Figure 44. Predicted and flight-determined aileron derivatives (pEst program analysis using RVDT measurements).

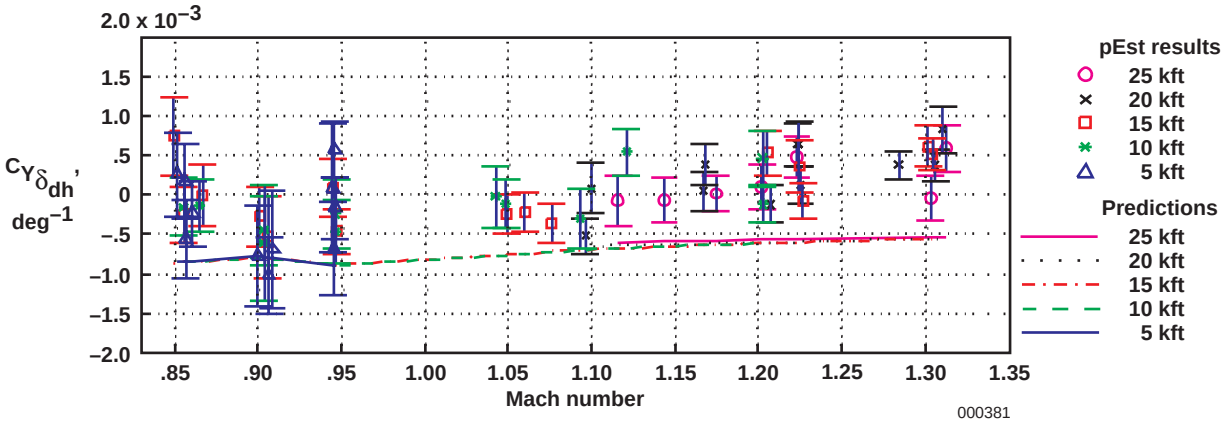

(a) $C_{Y_{\delta_{dh}}}$.

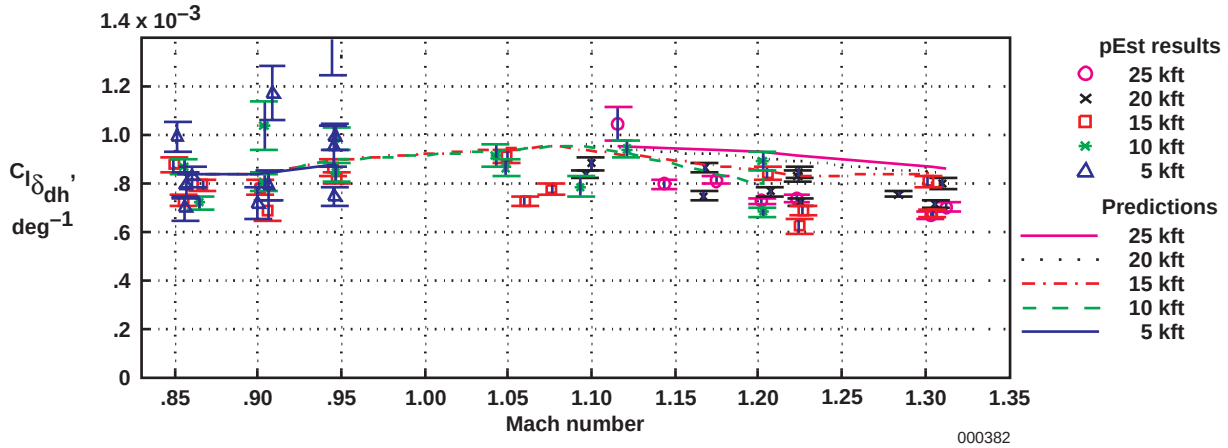

(b) $C_{l_{\delta_{dh}}}$ (vertical moment reference at *WL* 100).

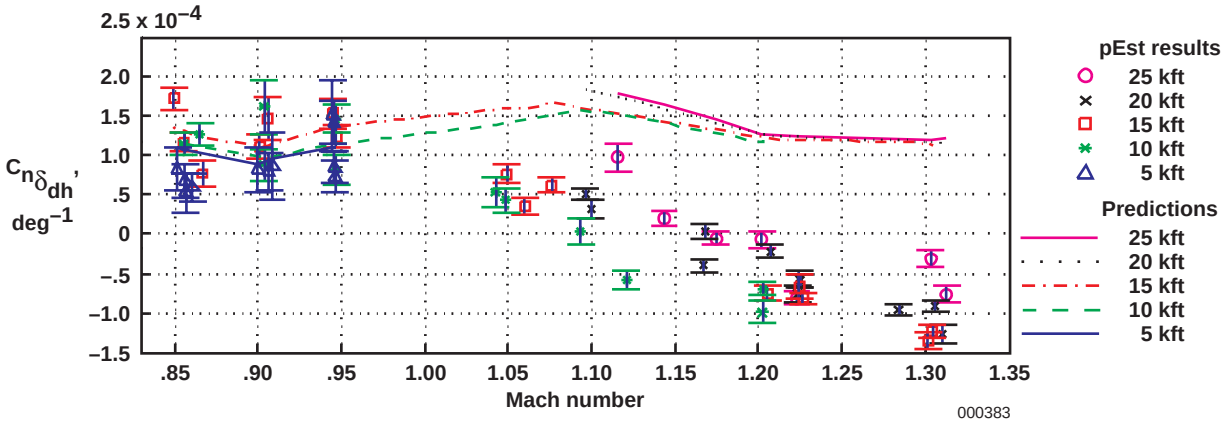

(c) $C_{n_{\delta_{dh}}}$ (moment reference at 0.25 *c*).

Figure 45. Predicted and flight-determined differential stabilator derivatives (pEst program analysis using RVDT measurements).

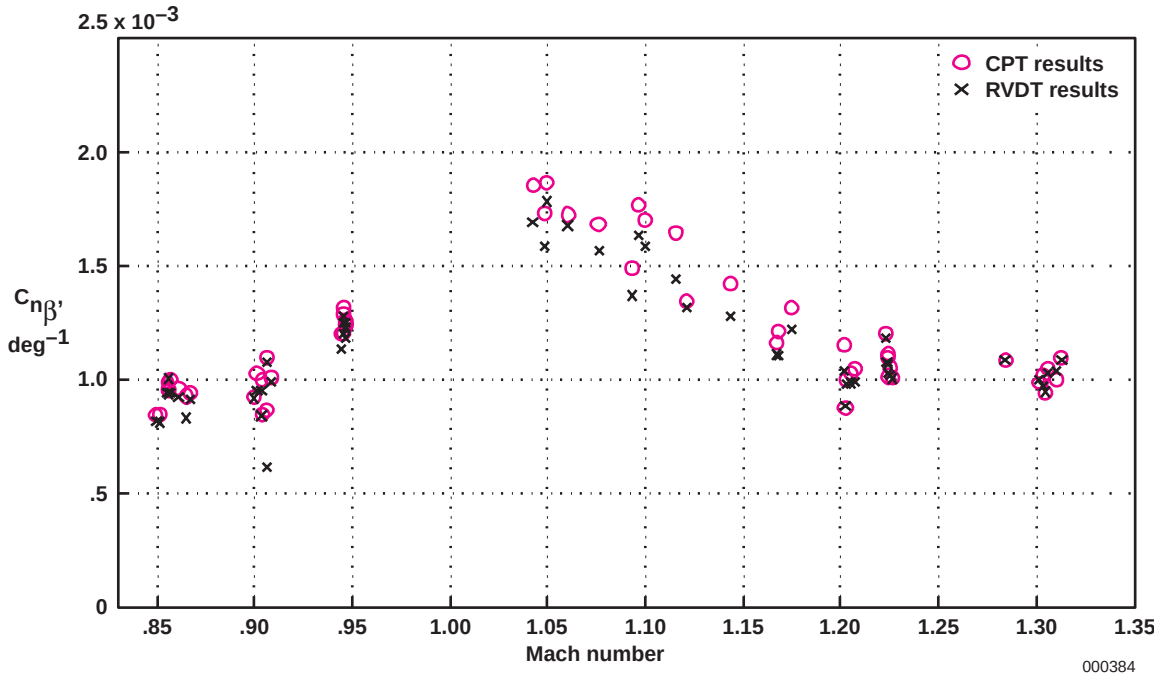

(a) C_{n_β}.

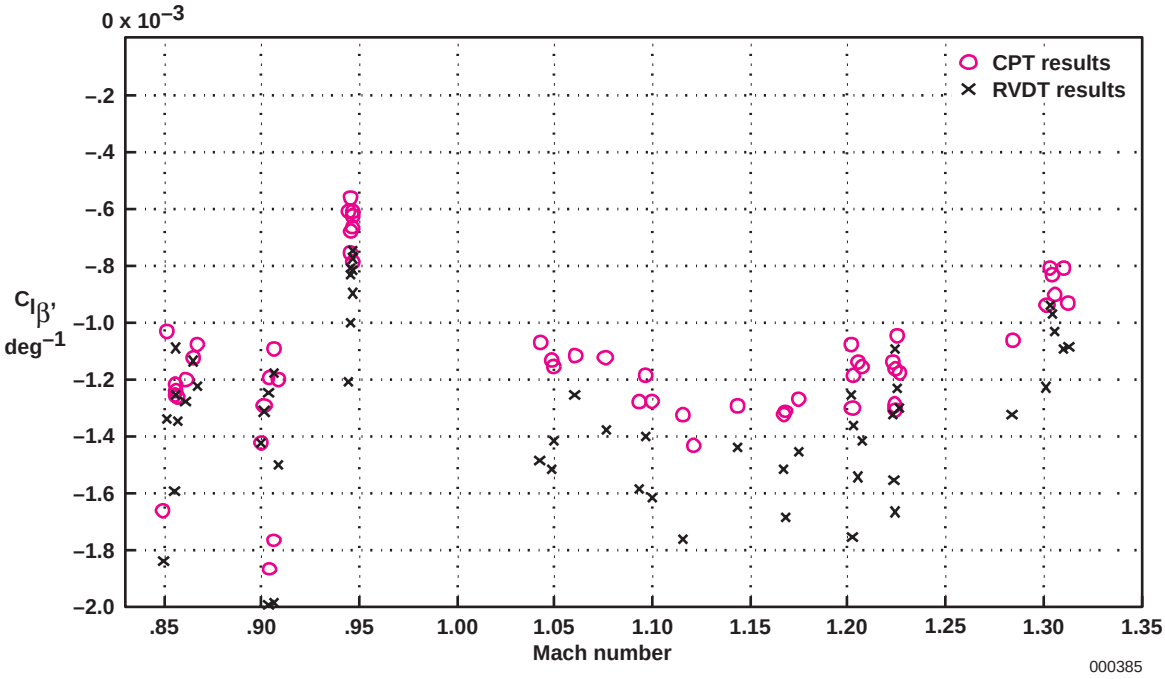

(b) C_{l_β}.

Figure 46. Comparison of sideslip derivatives using CPT and RVDT measurements.

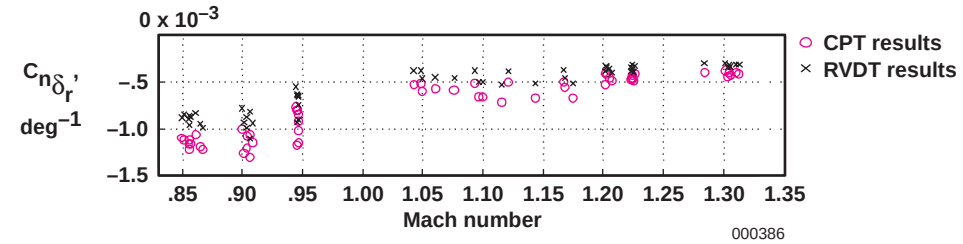

(a) $C_{n_{\delta_r}}$.

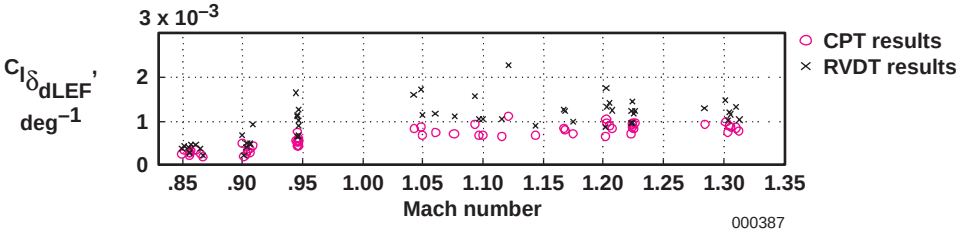

(b) $C_{l_{\delta_{dLEF}}}$.

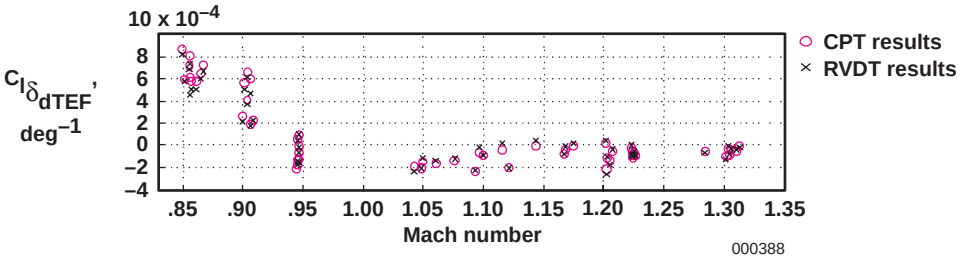

(c) $C_{l_{\delta_{dTEF}}}$.

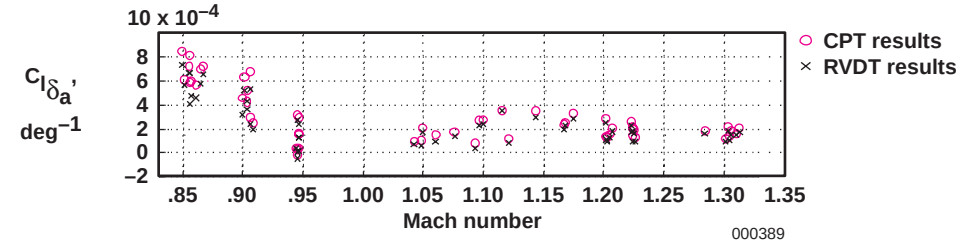

(d) $C_{n_{\delta_a}}$.

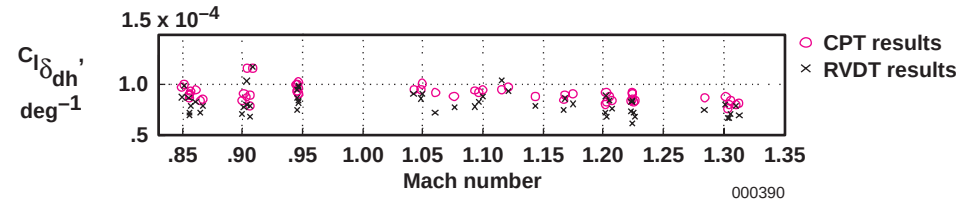

(e) $C_{n_{\delta_{dh}}}$.

Figure 47. Comparison of control derivatives using CPT and RVDT measurements.

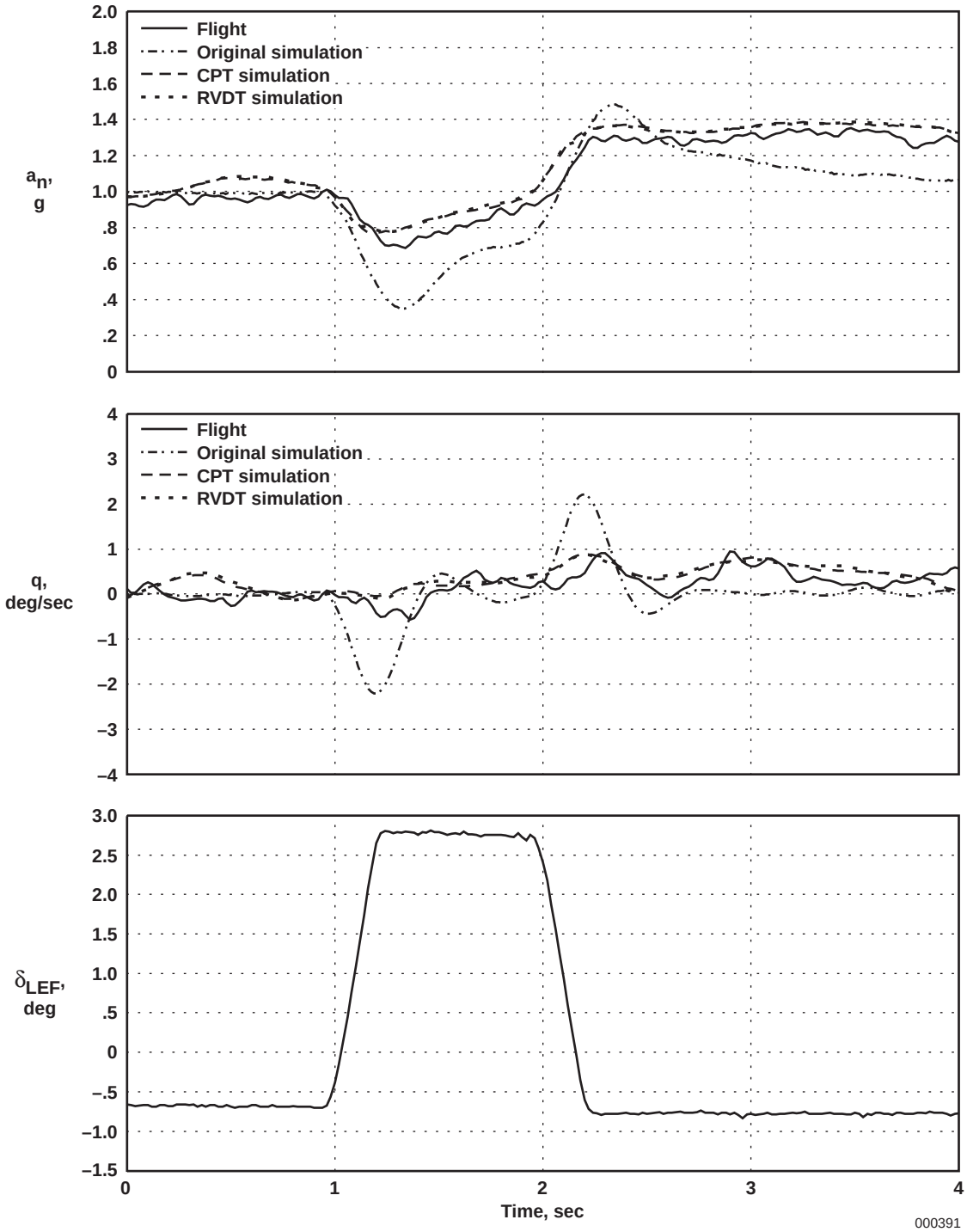

Figure 48. Symmetric LEF SSI (Mach 1.2 at 25,000 ft).

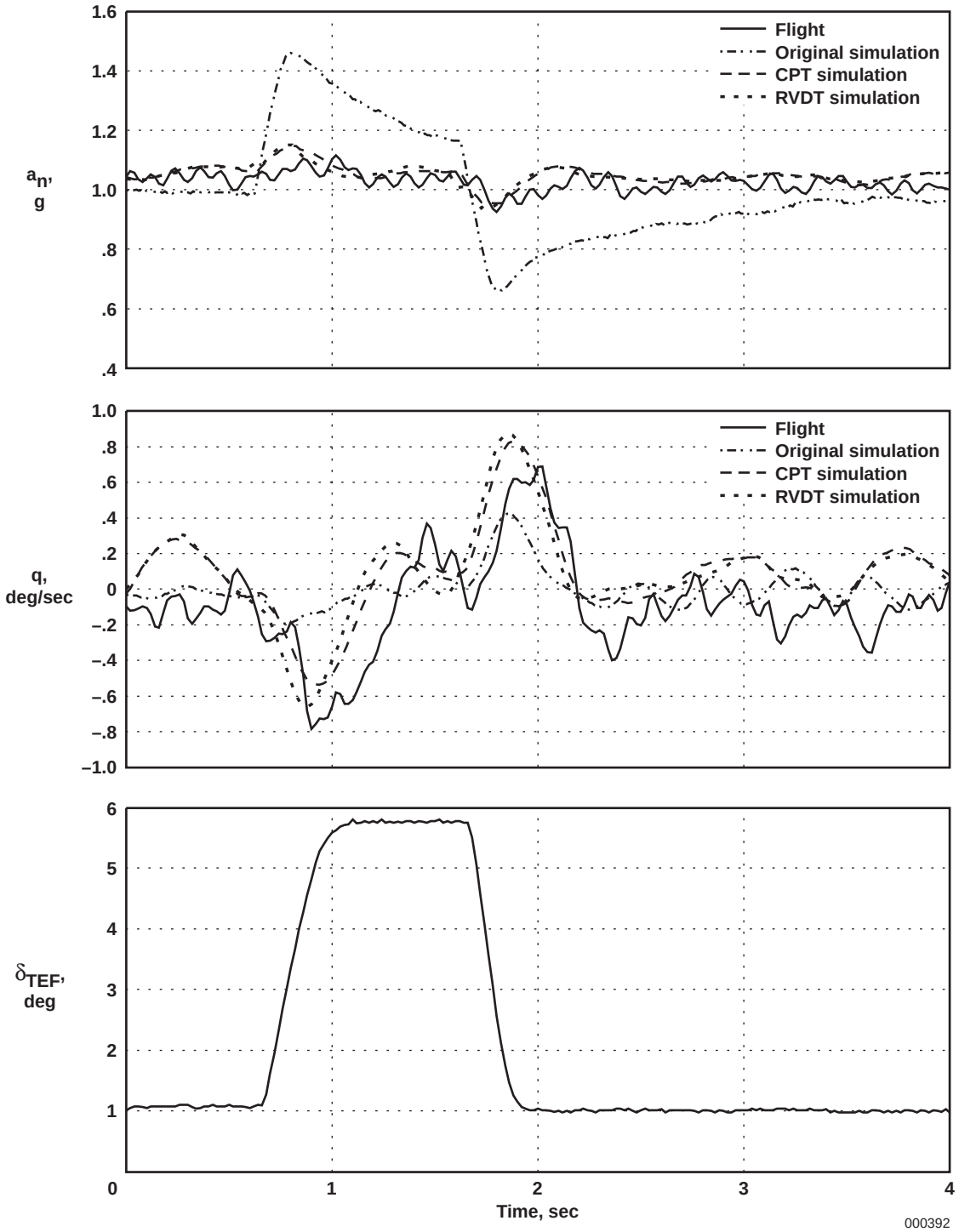

Figure 49. Symmetric TEF SSI (Mach 1.2 at 25,000 ft).

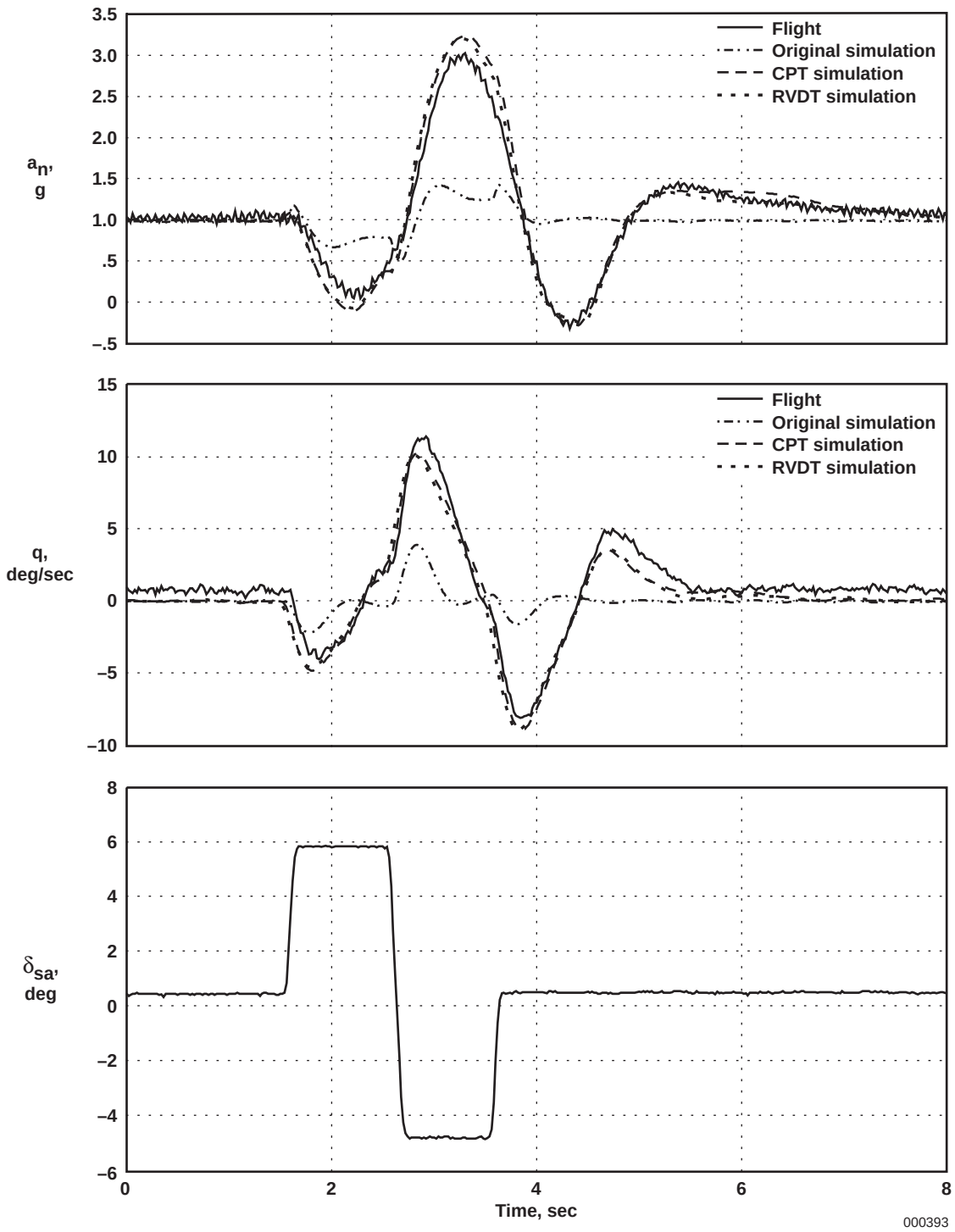

Figure 50. Symmetric aileron doublet (Mach 0.85 at 15,000 ft).

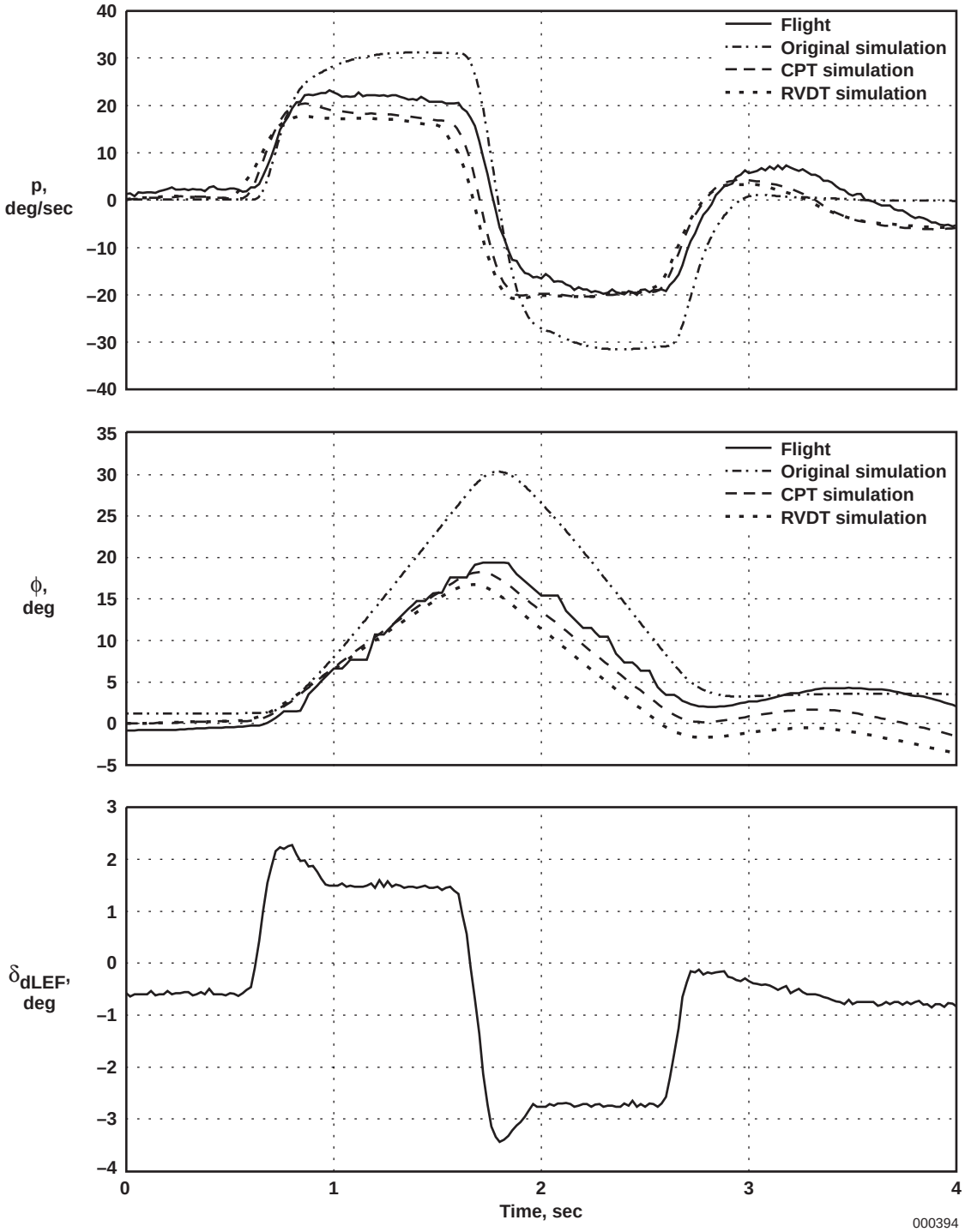

Figure 51. Differential LEF doublet (Mach 1.2 at 15,000 ft).

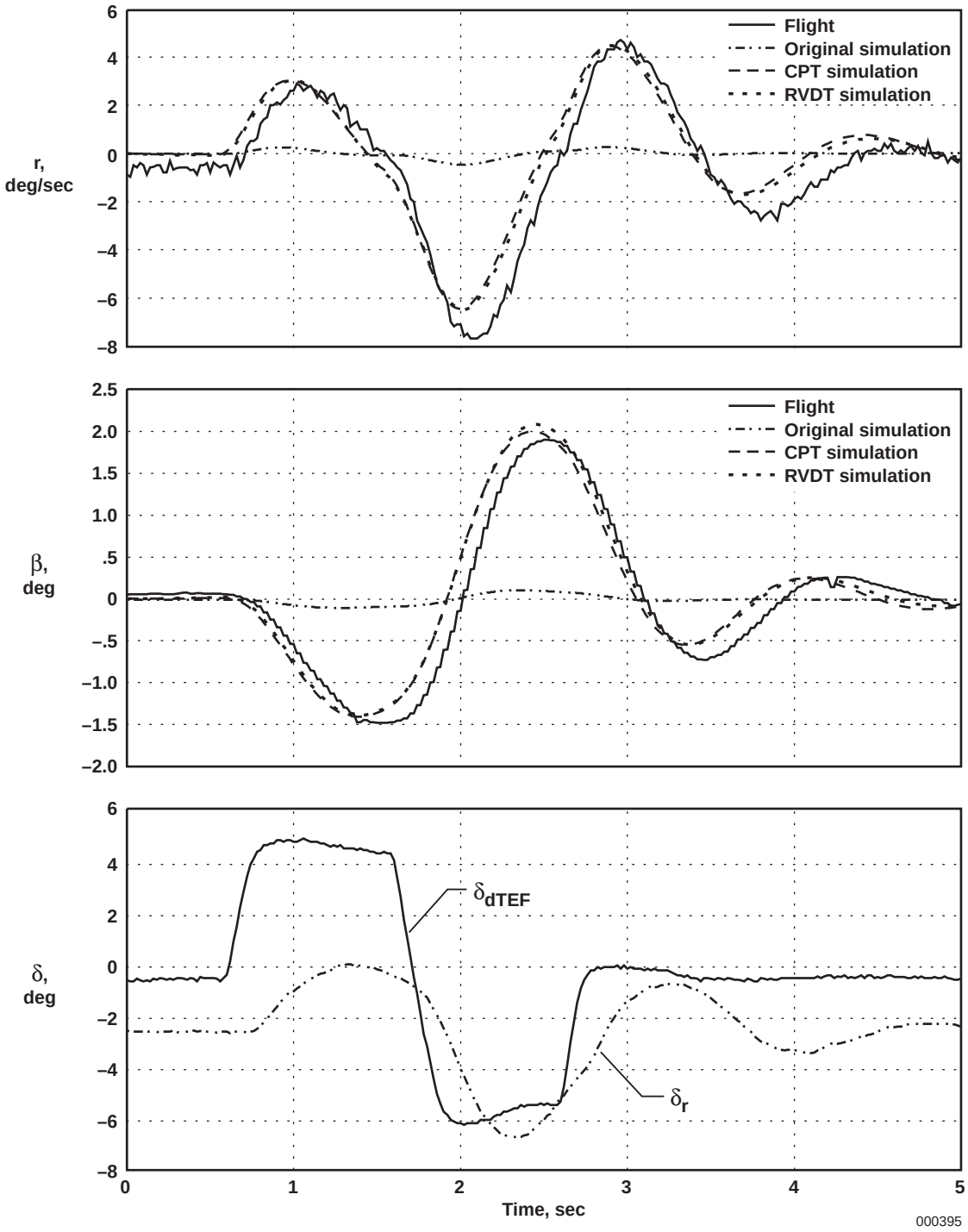

Figure 52. Differential TEF doublet (Mach 1.2 at 15,000 ft).

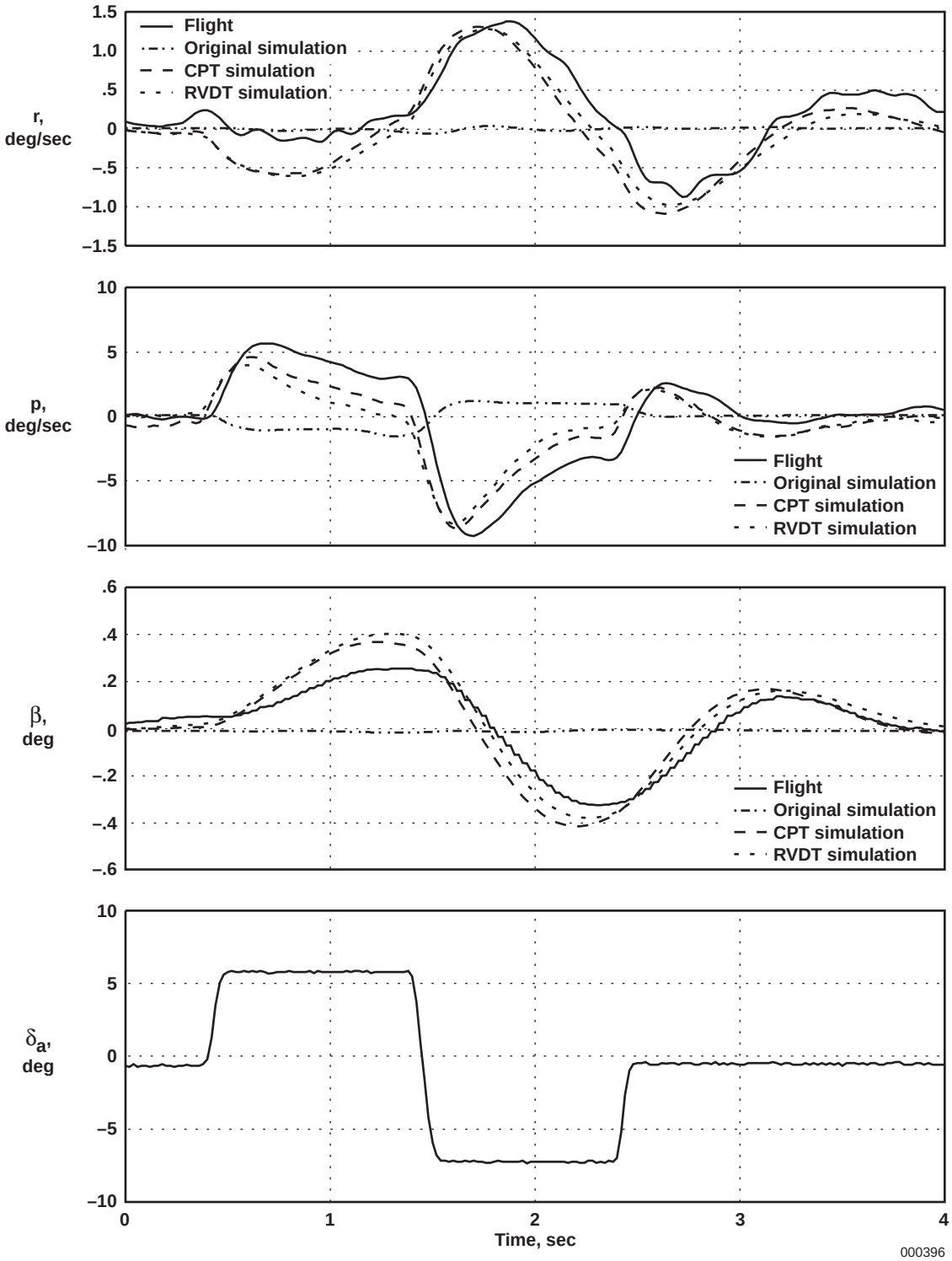

Figure 53. Aileron doublet (Mach 1.2 at 15,000 ft).

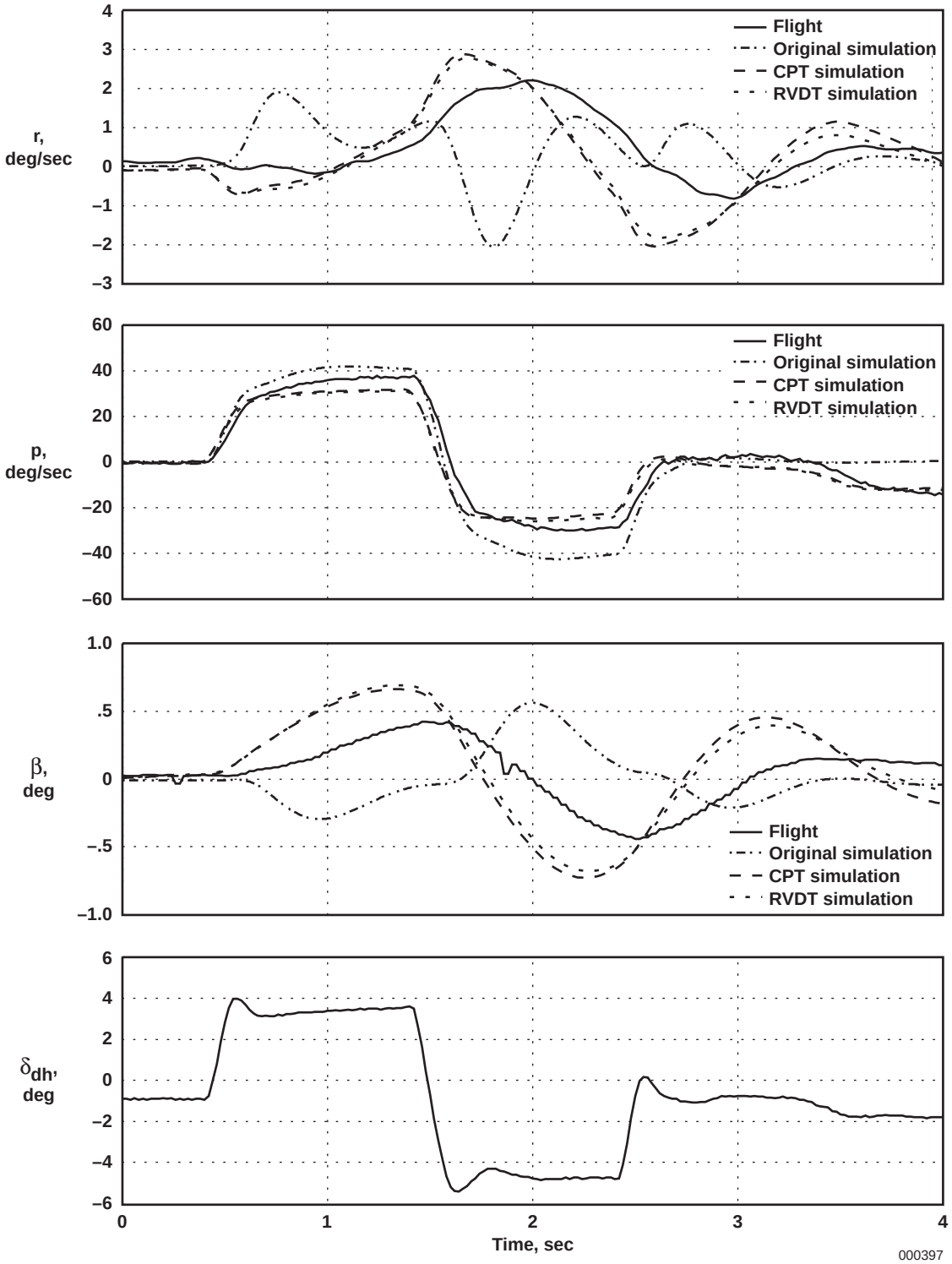

Figure 54. Differential stabilator doublet (Mach 1.2 at 15,000 ft).

APPENDIX A

LONGITUDINAL MANEUVER TIME HISTORIES

Figures A-1–A-20 show time histories of longitudinal doublet sequences. A typical time history is shown for each of the 20 flight test conditions. This appendix shows actual aircraft responses to the four longitudinal single-surface inputs (SSIs) and qualitatively shows how well the parameter estimation program, pEst (ref. 1), was able to match the actual response time histories. Aircraft response parameters include angle of attack, pitch rate, pitch attitude, and normal acceleration. The solid line is the response parameter measured from flight data. The dashed line is the pEst program–estimated response at convergence obtained by integrating the equations of motion using the pEst program estimates of the stability and control derivatives.

Only selected windows of data were used in the pEst program analysis. Some of the data between subsequent SSI inputs were removed from the pEst program analysis to minimize integration drift. The data removed were from times when the aircraft was no longer responding to the previous SSI input. The time history points not used in the integration are indicated by the step discontinuities in the dashed line.

The control-surface positions measured by the control-surface position transducers are also plotted. For the longitudinal sequences, the SSIs were done in the following order: symmetric leading-edge flap, symmetric trailing-edge flap, symmetric aileron, and elevator (stabilator). A 5-sec delay was built in between each SSI.

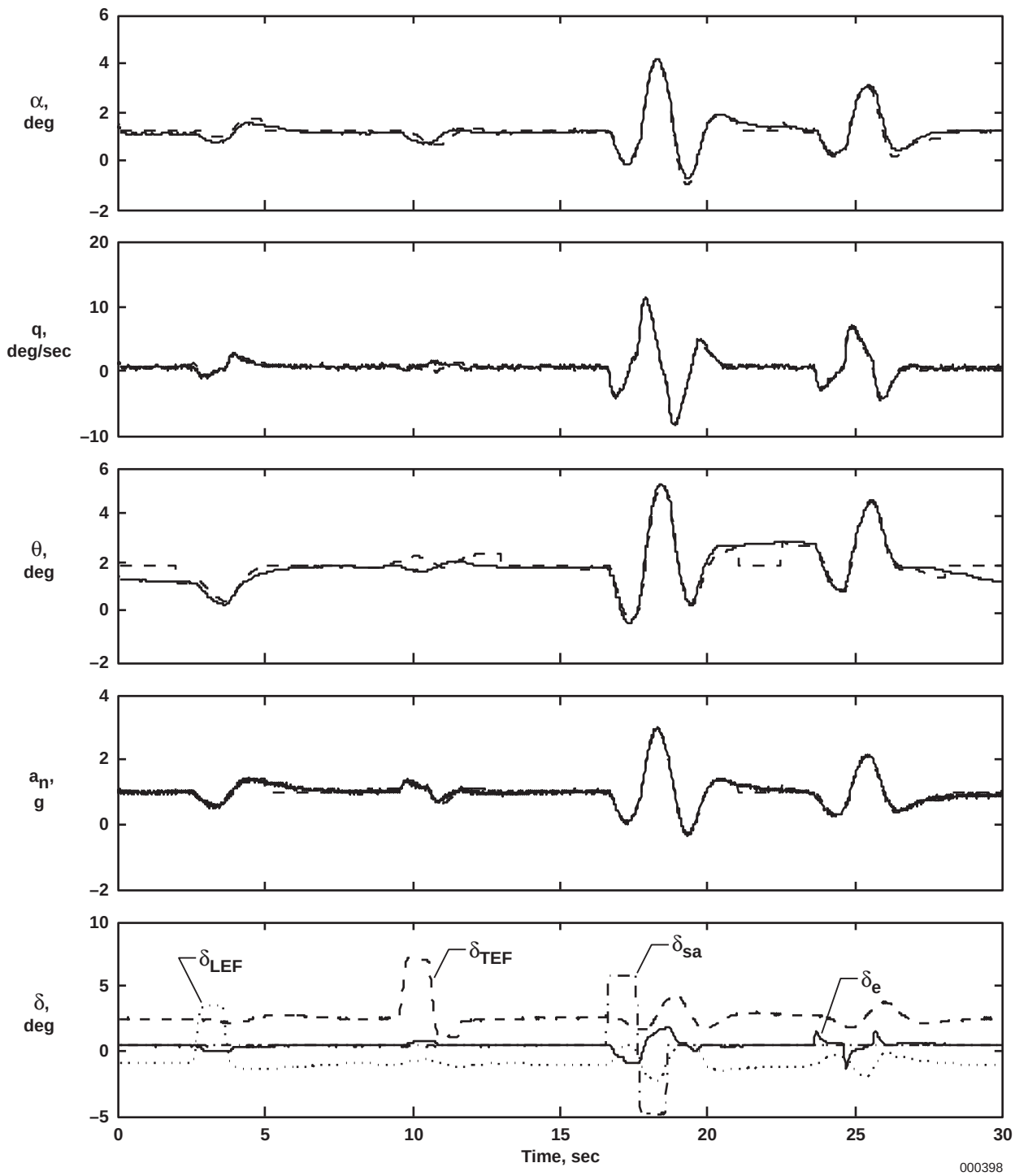

Figure A-1. Large doublet sequence (Mach 0.85 at 15,000 ft).

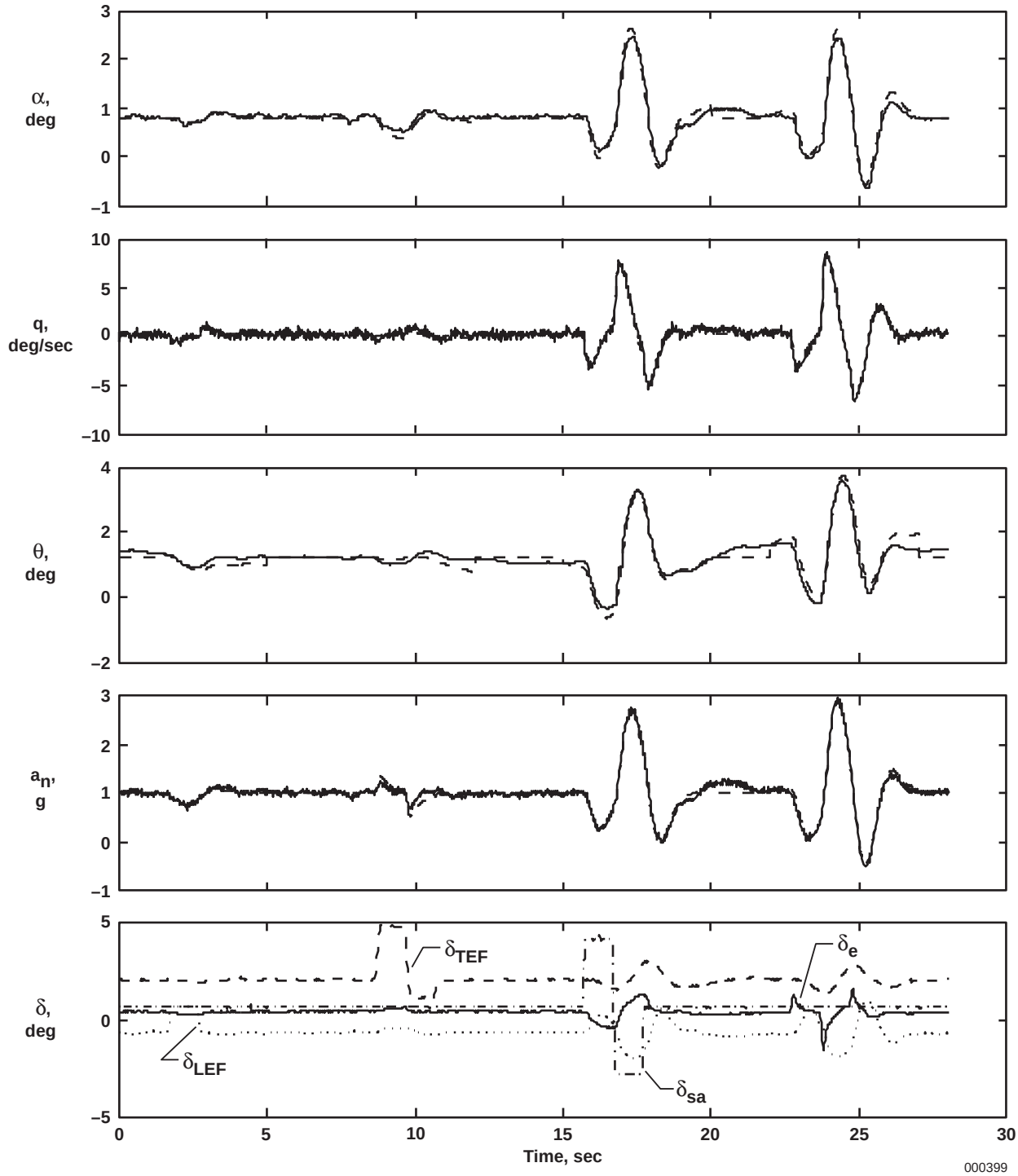

Figure A-2. Small doublet sequence (Mach 0.85 at 10,000 ft).

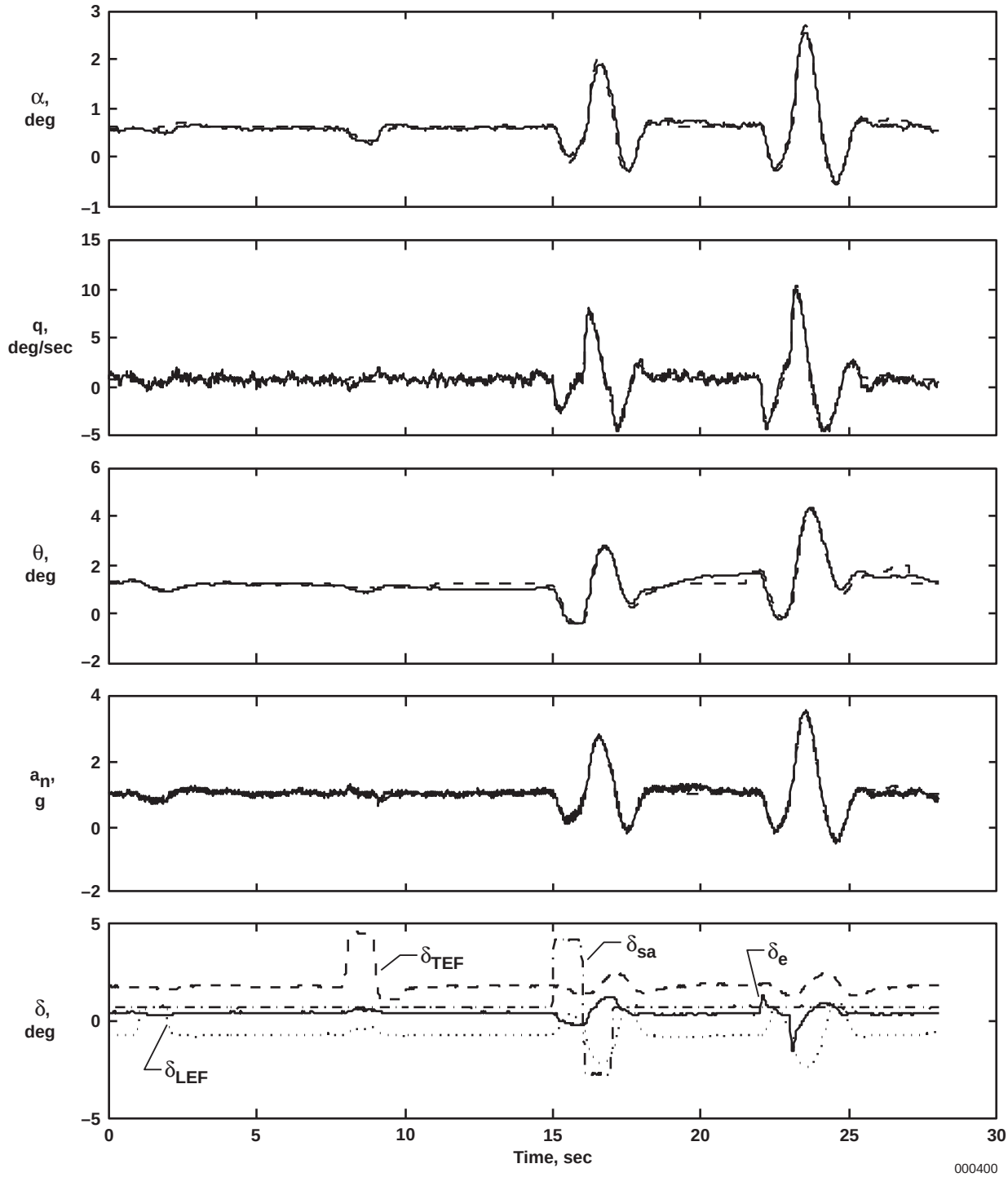

Figure A-3. Small doublet sequence (Mach 0.85 at 5,000 ft).

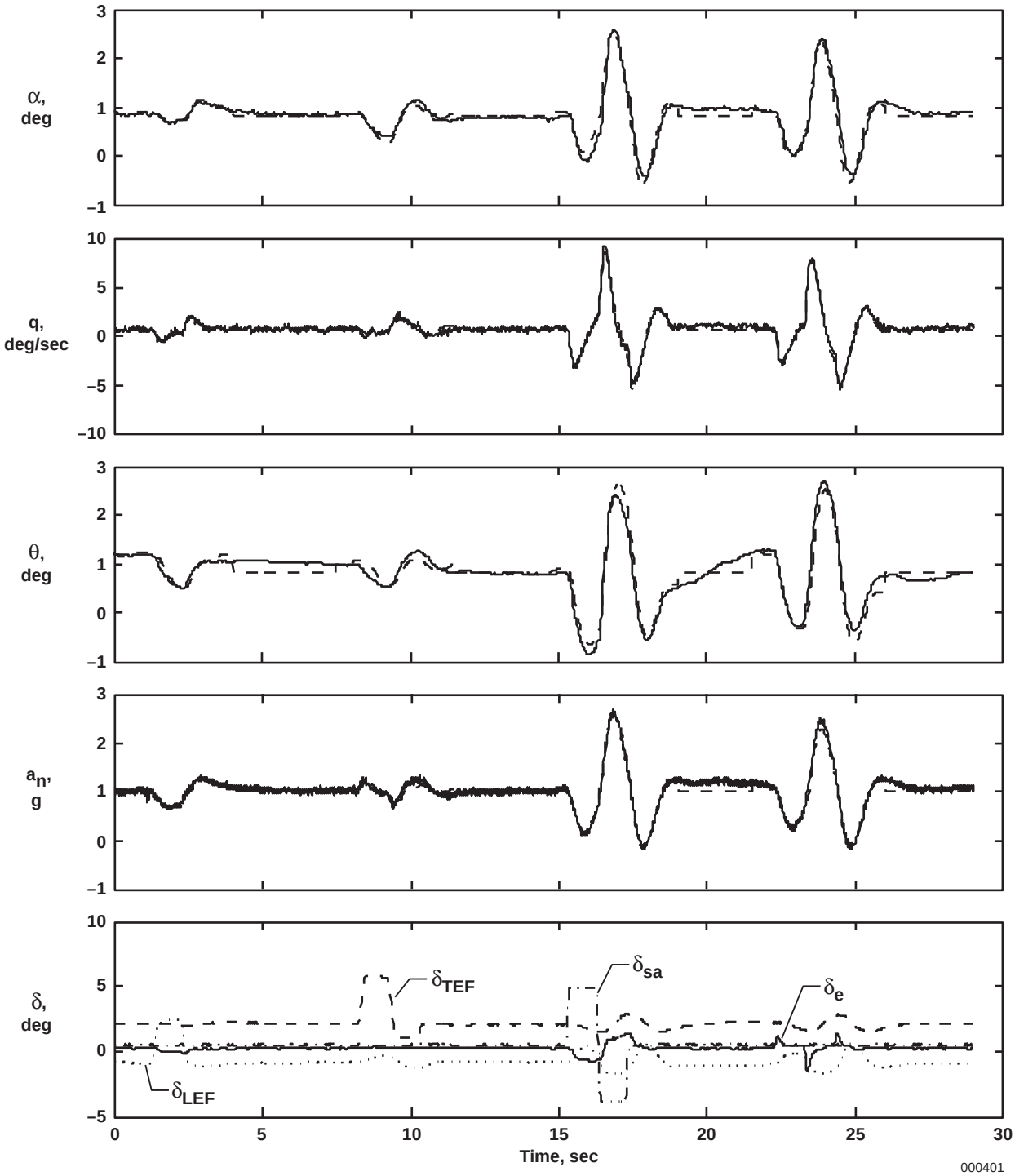

Figure A-4. Medium doublet sequence (Mach 0.9 at 15,000 ft).

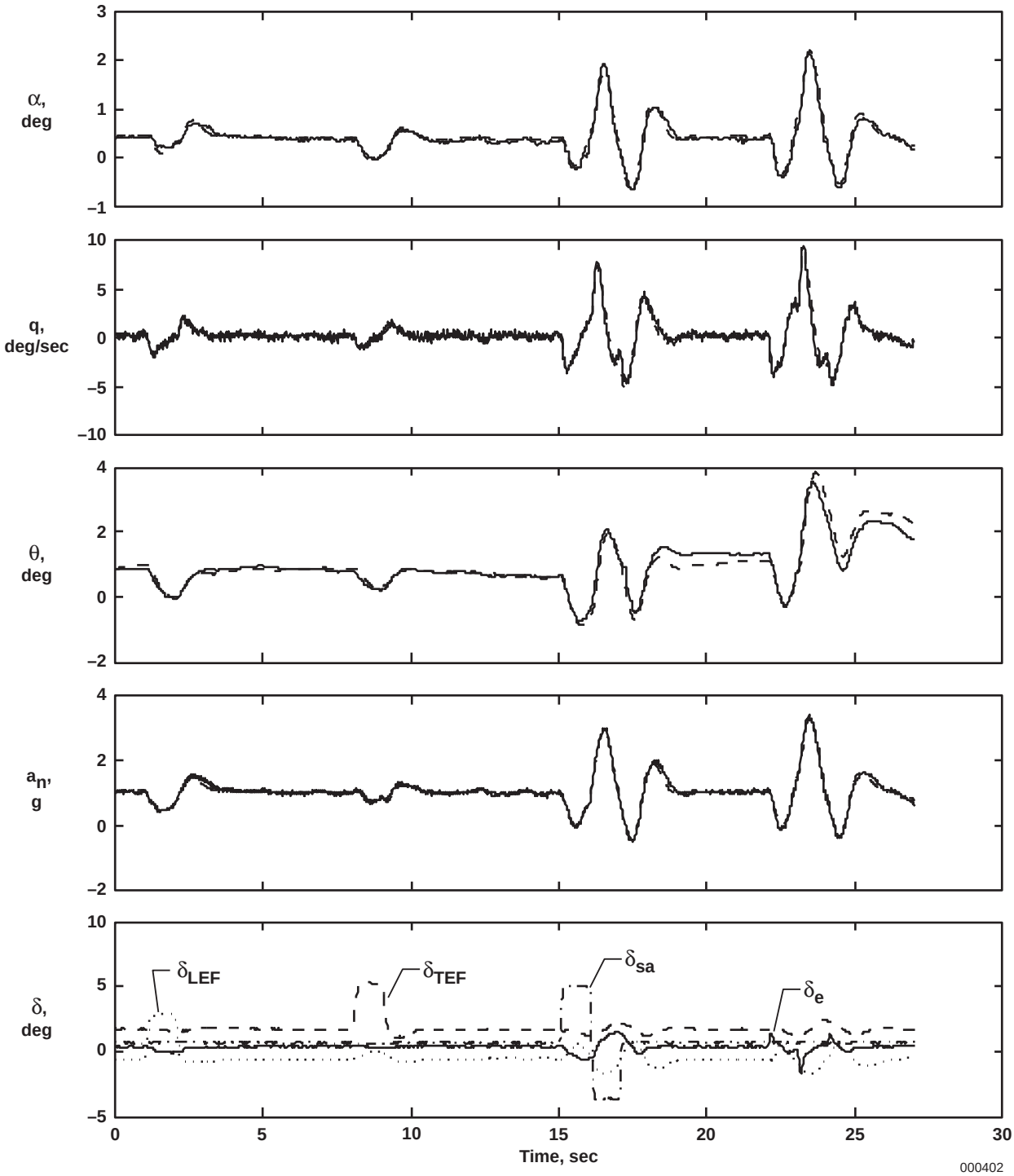

Figure A-5. Medium doublet sequence (Mach 0.9 at 10,000 ft).

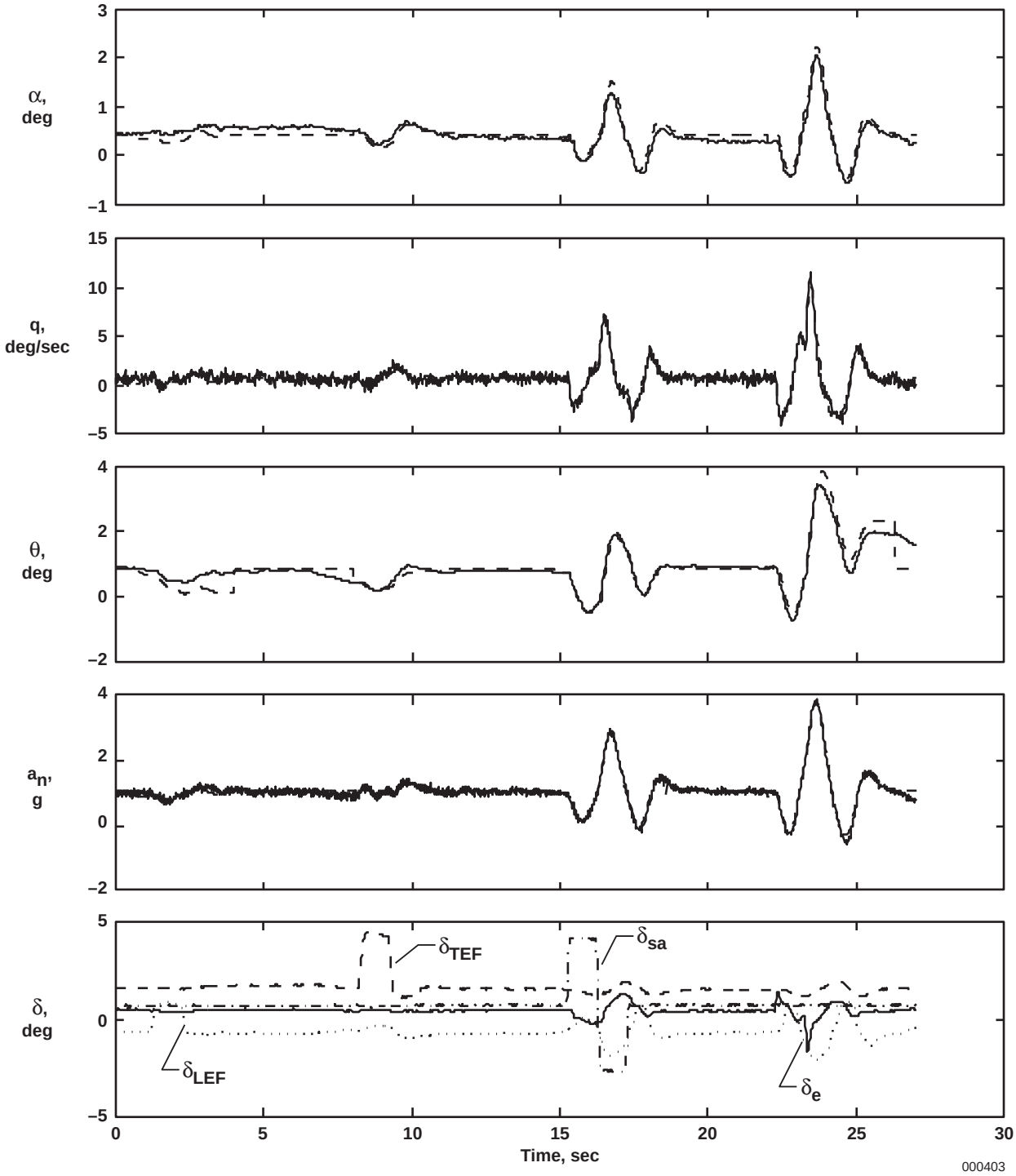

Figure A-6. Small doublet sequence (Mach 0.9 at 5,000 ft).

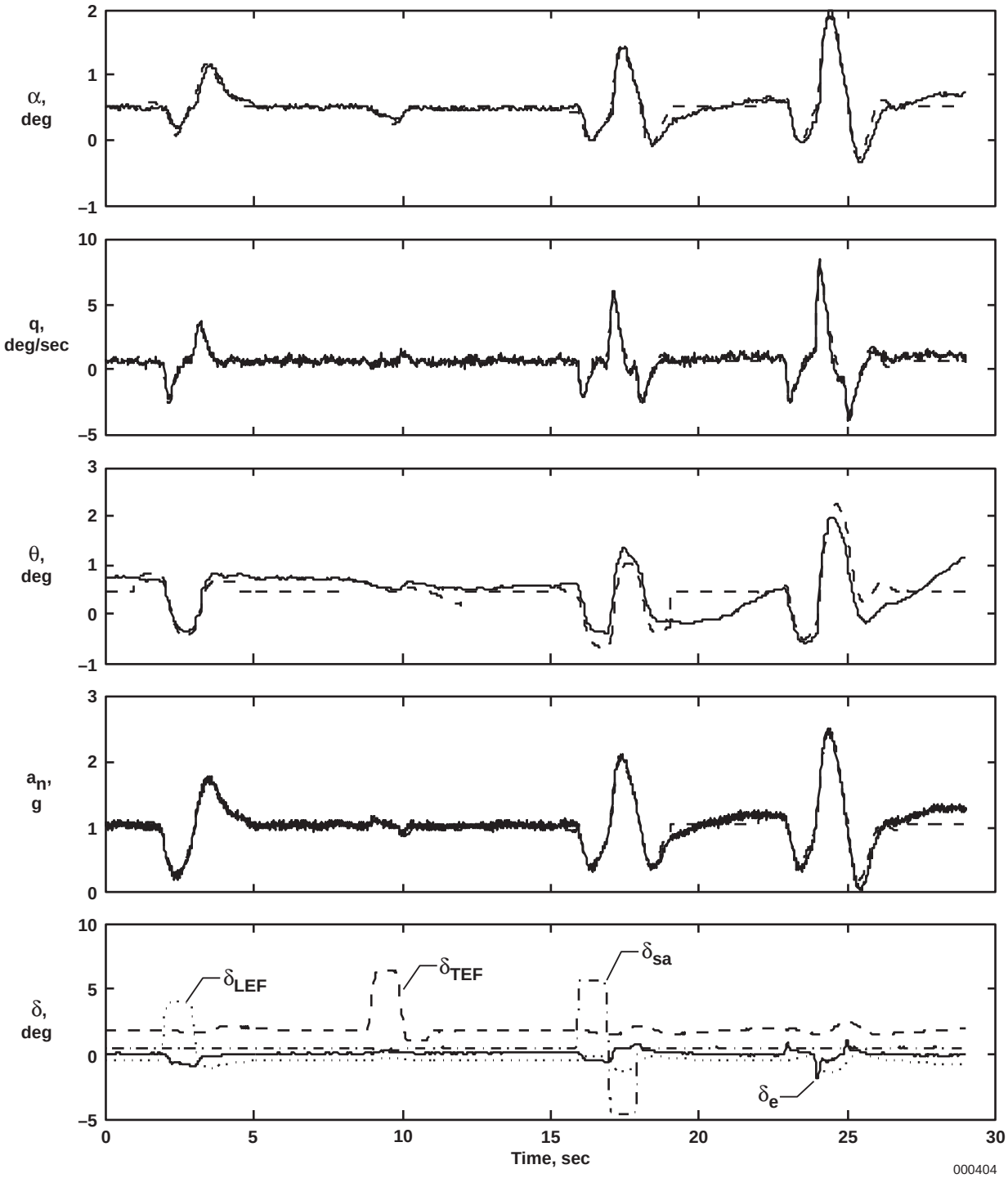

Figure A-7. Large doublet sequence (Mach 0.95 at 15,000 ft).

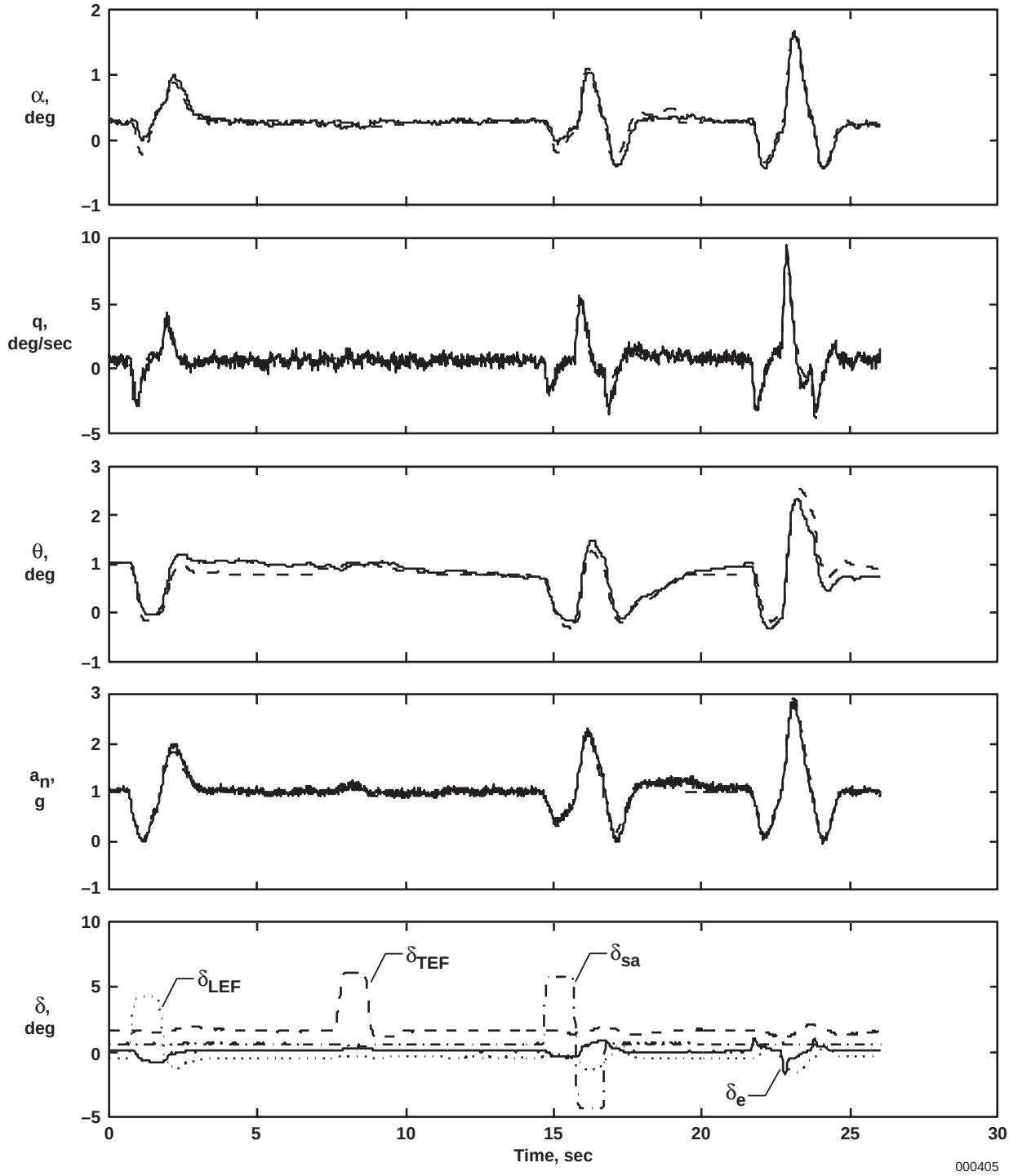

Figure A-8. Large doublet sequence (Mach 0.95 at 10,000 ft).

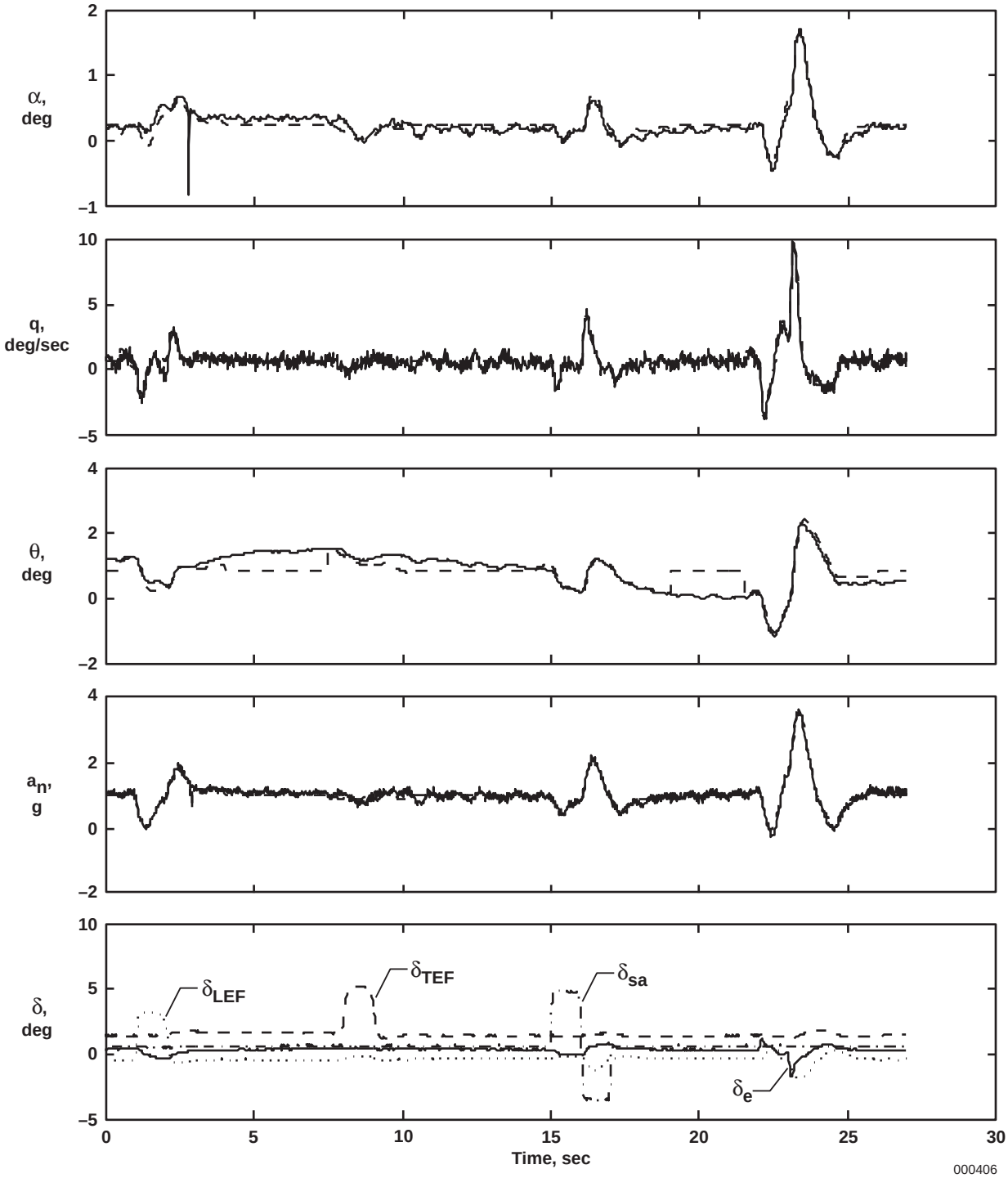

Figure A-9. Medium doublet sequence (Mach 0.95 at 5,000 ft).

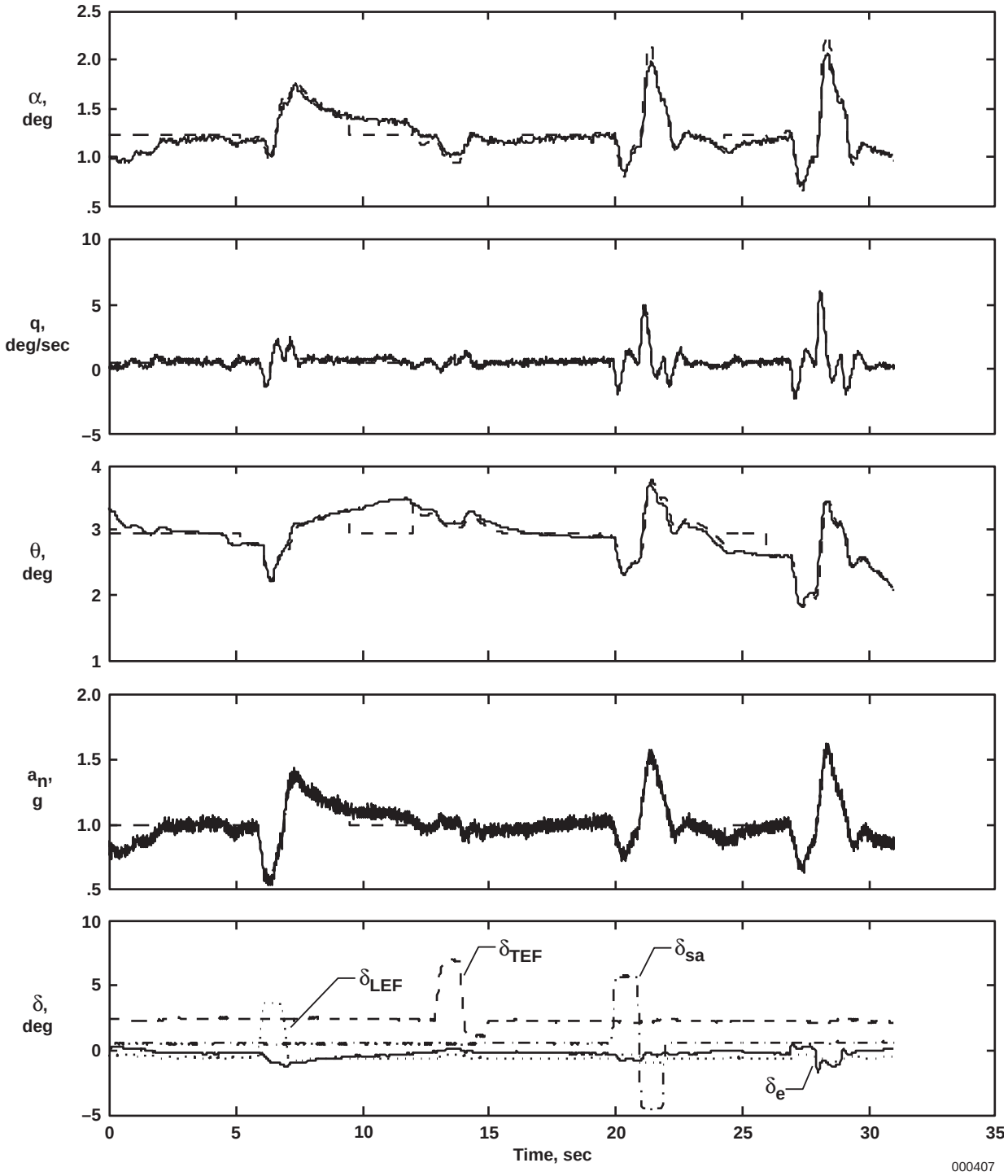

Figure A-10. Large doublet sequence (Mach 1.1 at 25,000 ft).

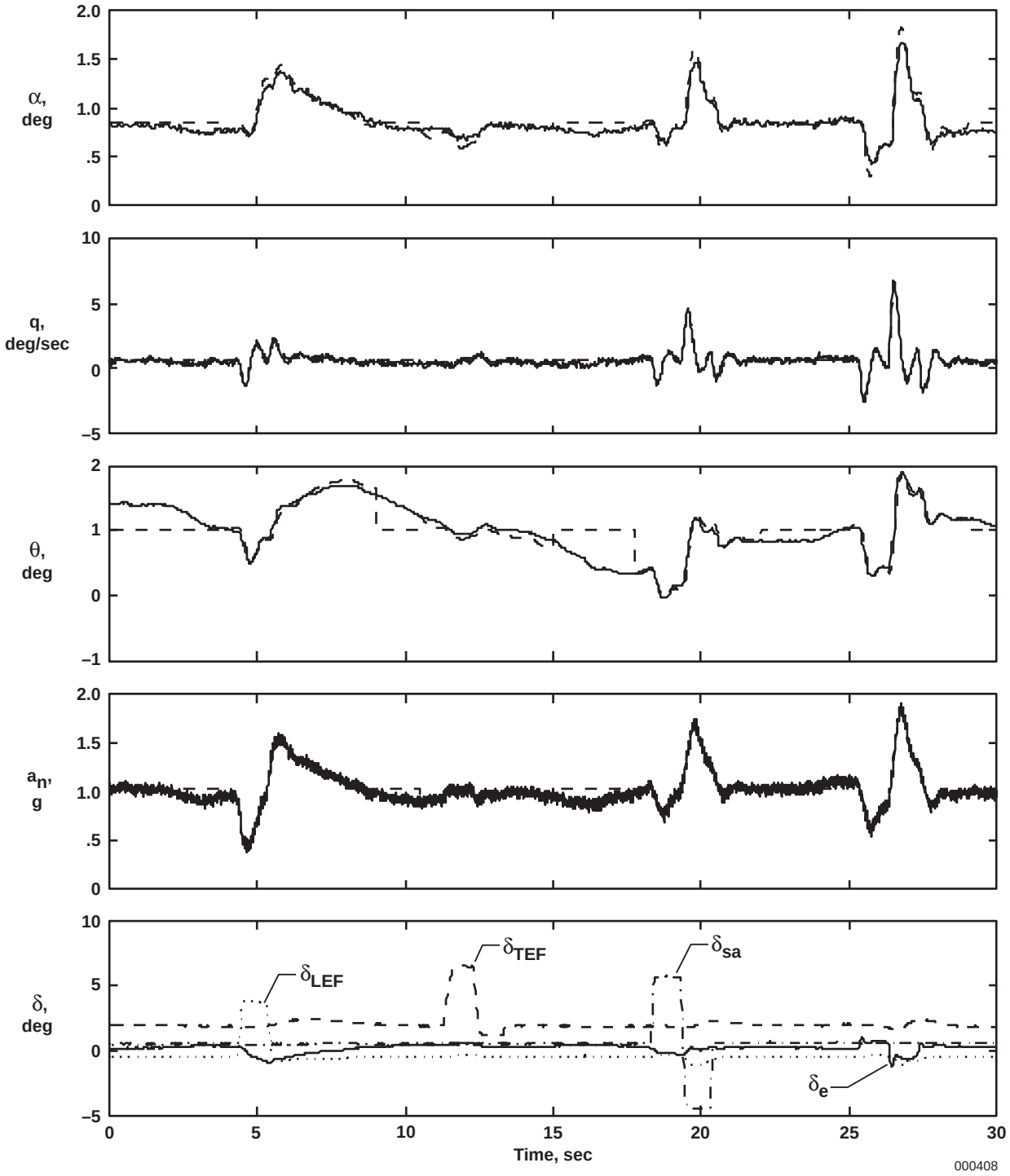

Figure A-11. Large doublet sequence (Mach 1.1 at 20,000 ft).

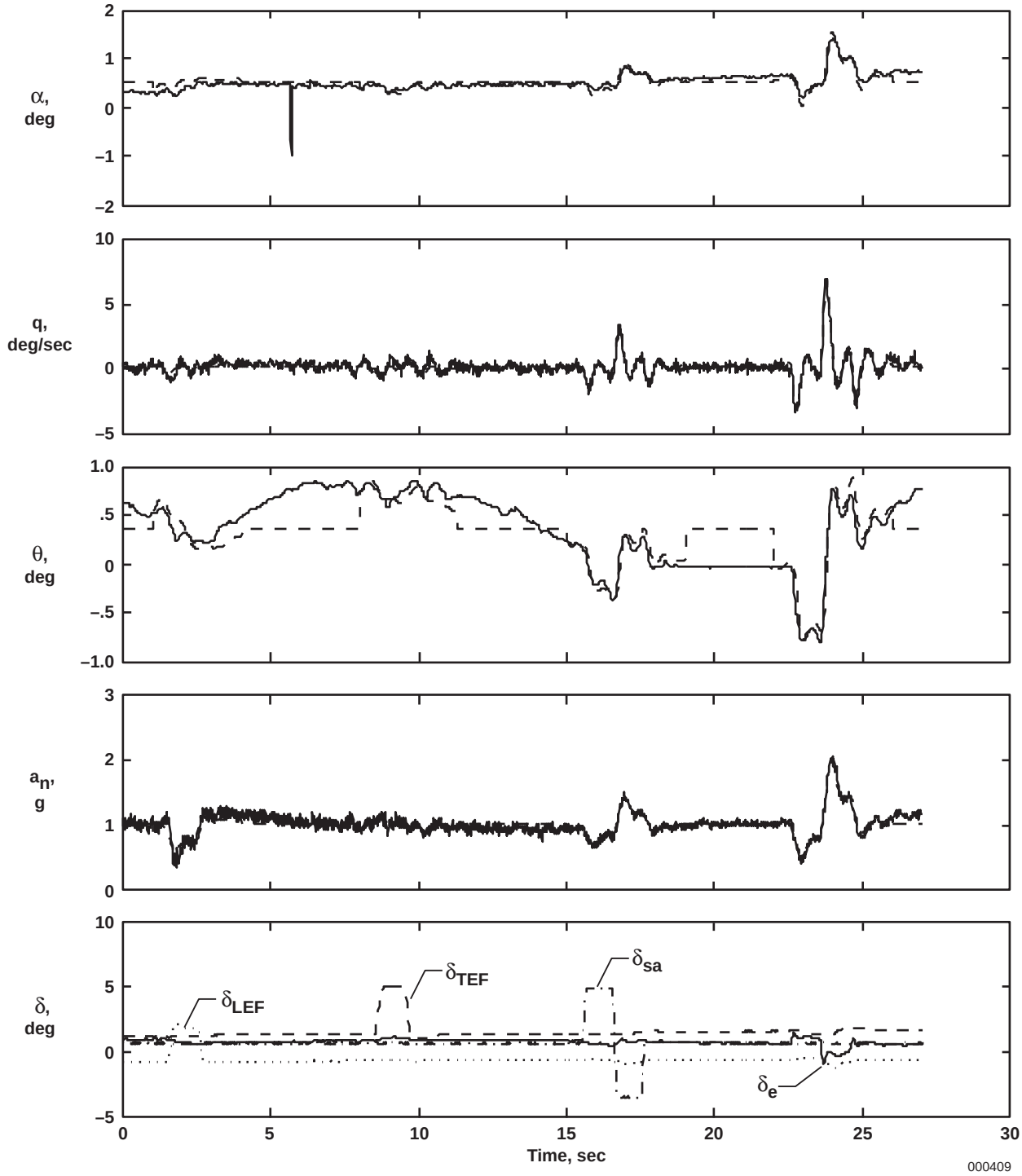

Figure A-12. Medium doublet sequence (Mach 1.1 at 15,000 ft).

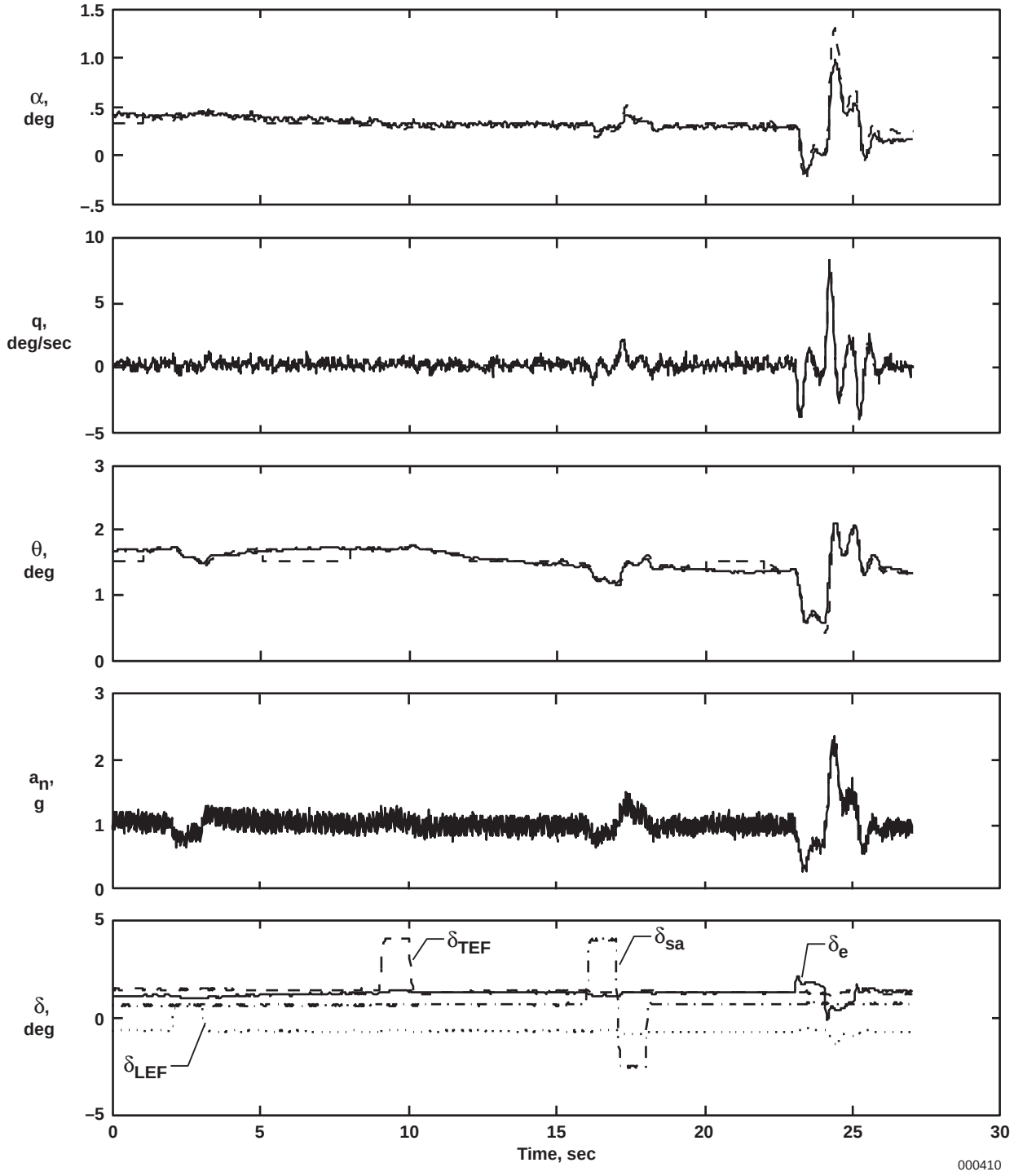

Figure A-13. Small doublet sequence (Mach 1.1 at 10,000 ft).

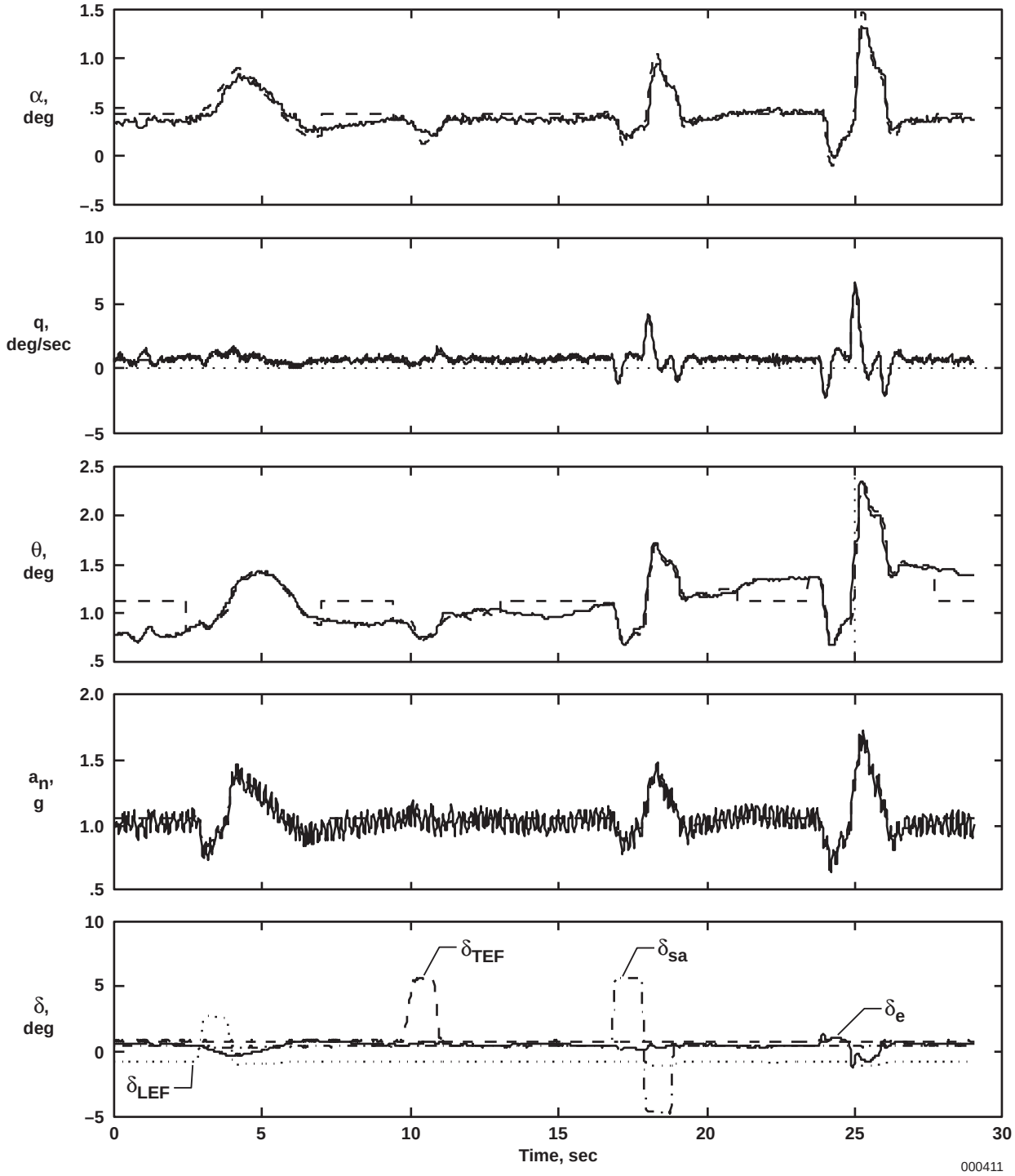

Figure A-14. Large doublet sequence (Mach 1.2 at 25,000 ft).

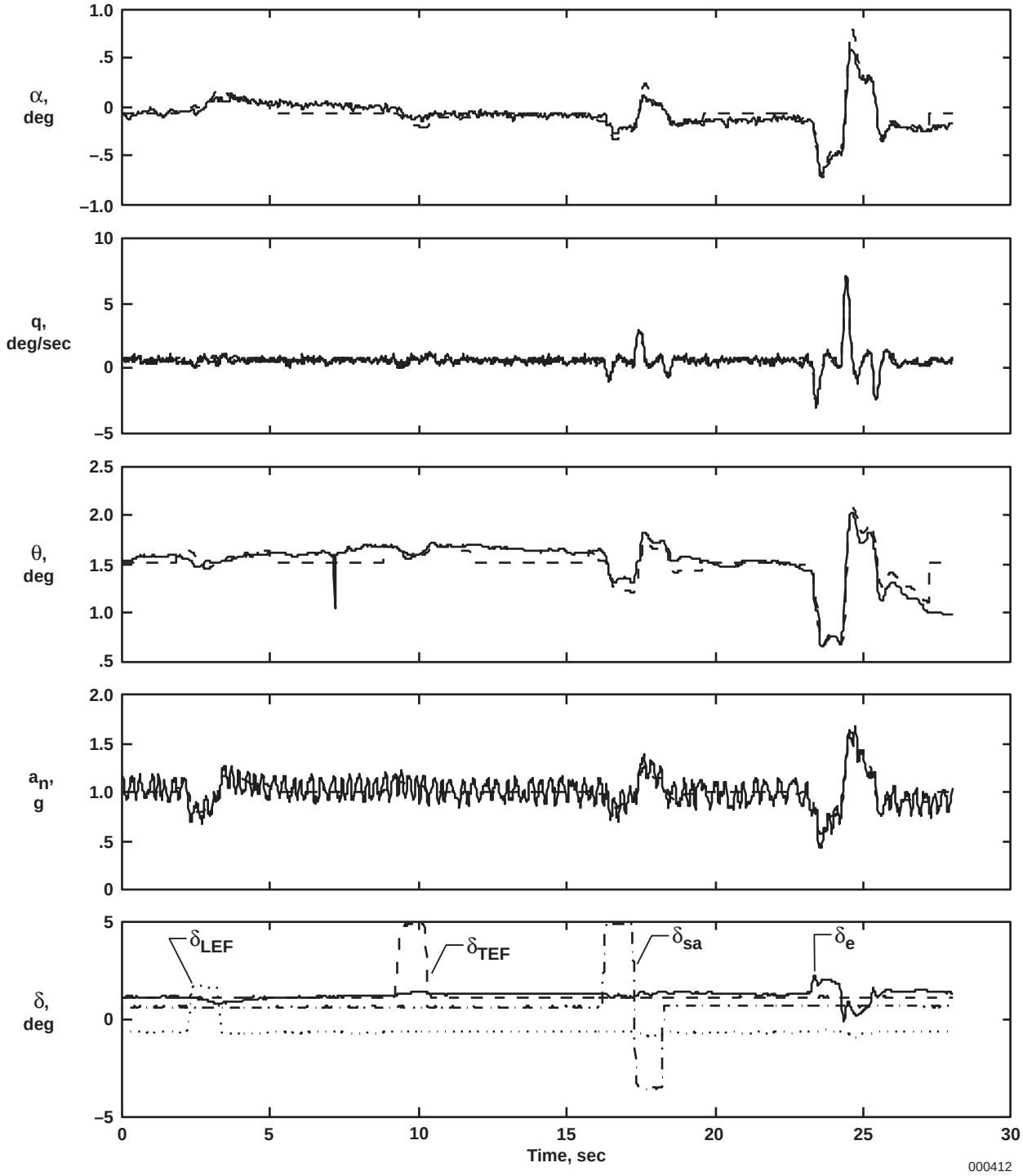

Figure A-15. Medium doublet sequence (Mach 1.2 at 20,000 ft).

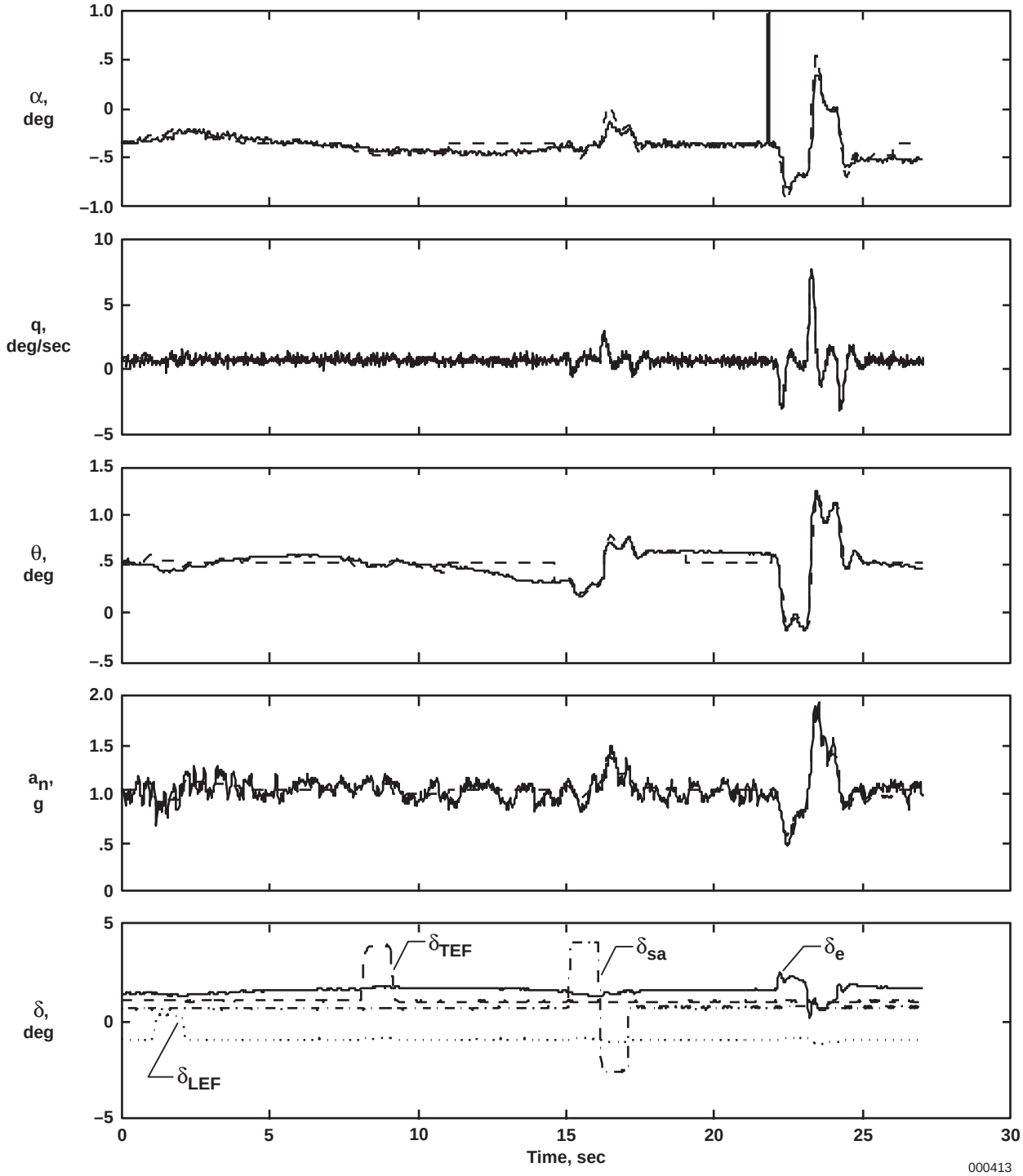

Figure A-16. Small doublet sequence (Mach 1.2 at 15,000 ft).

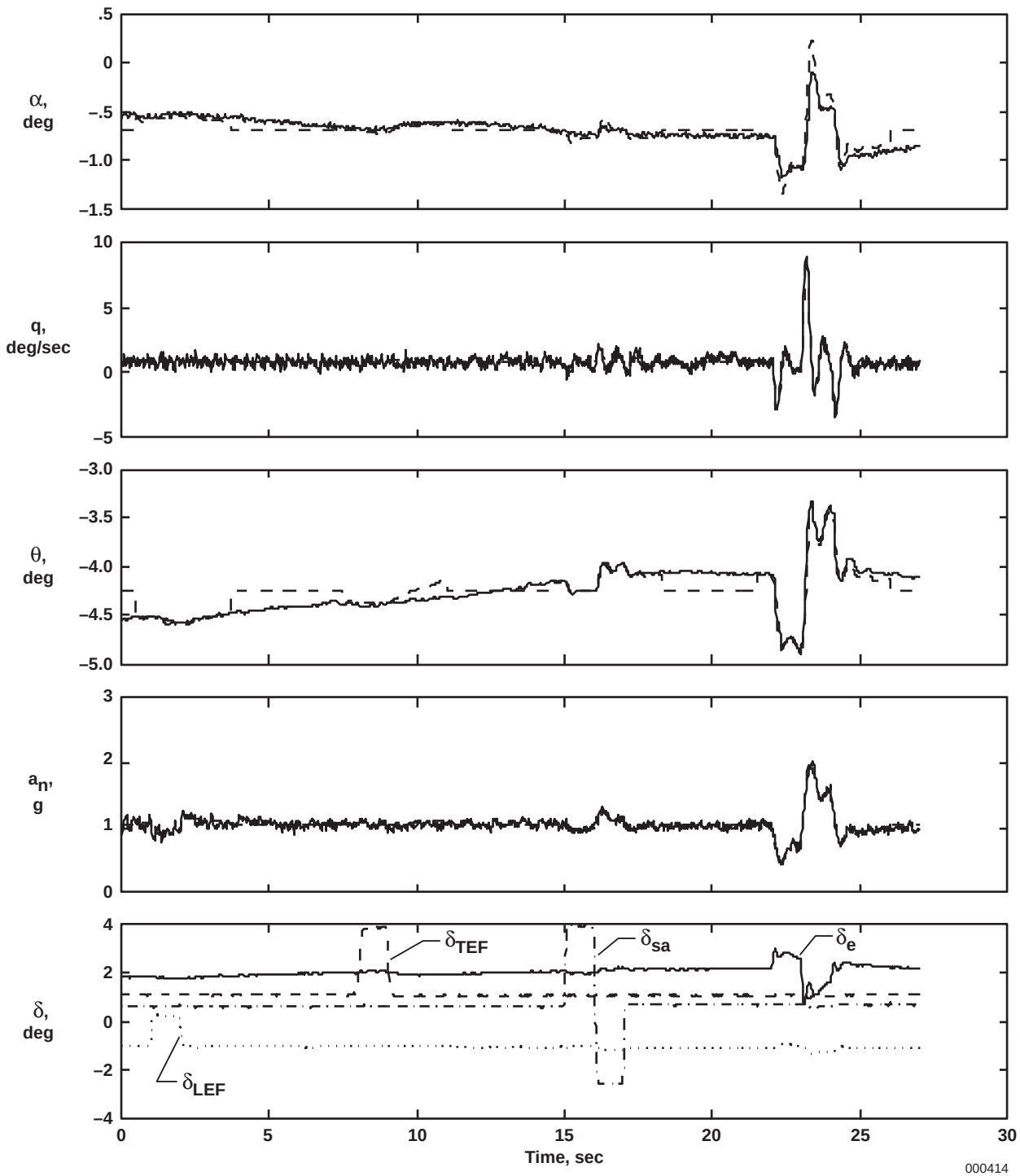

Figure A-17. Small doublet sequence (Mach 1.2 at 10,000 ft).

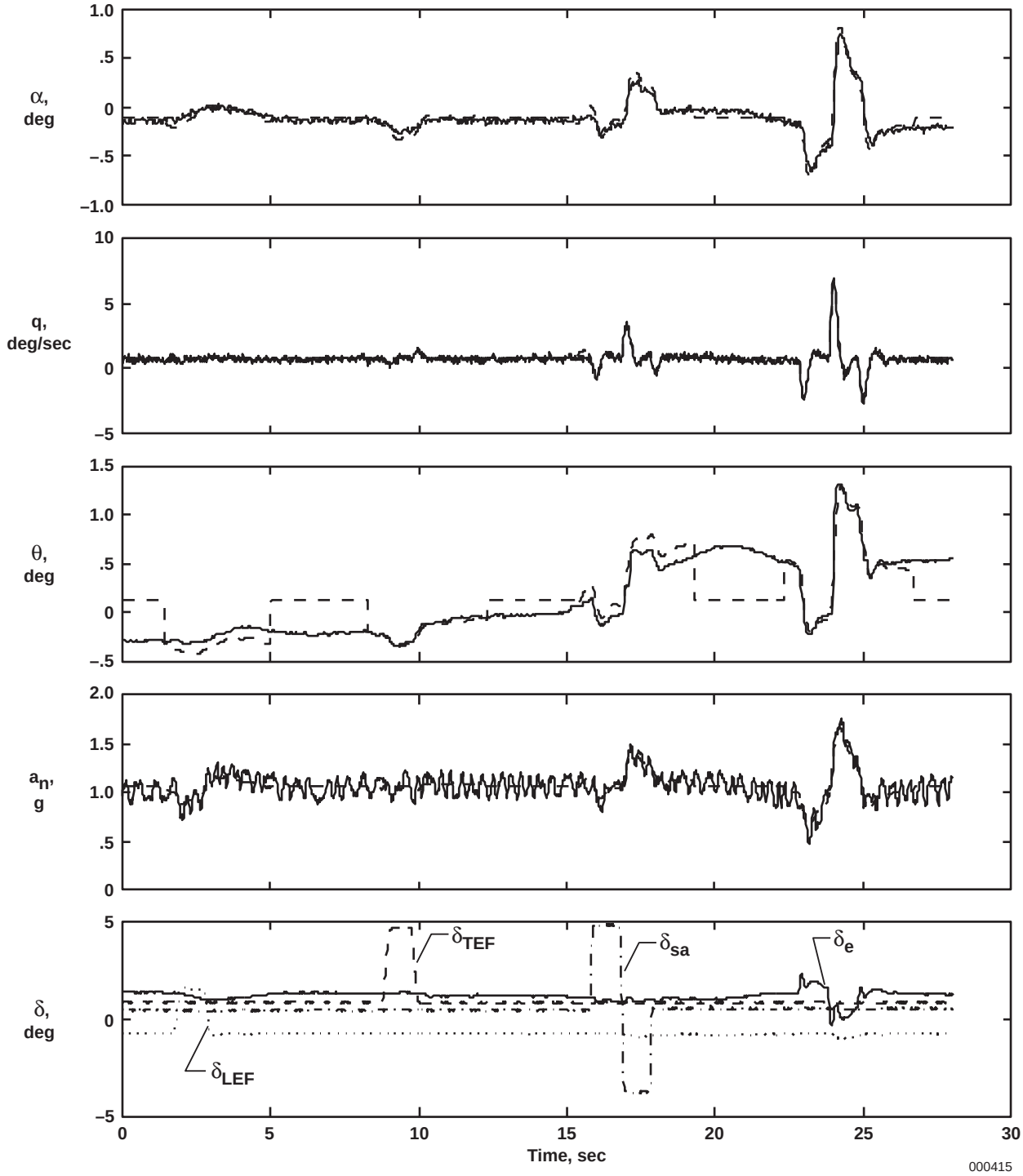

Figure A-18. Medium doublet sequence (Mach 1.3 at 25,000 ft).

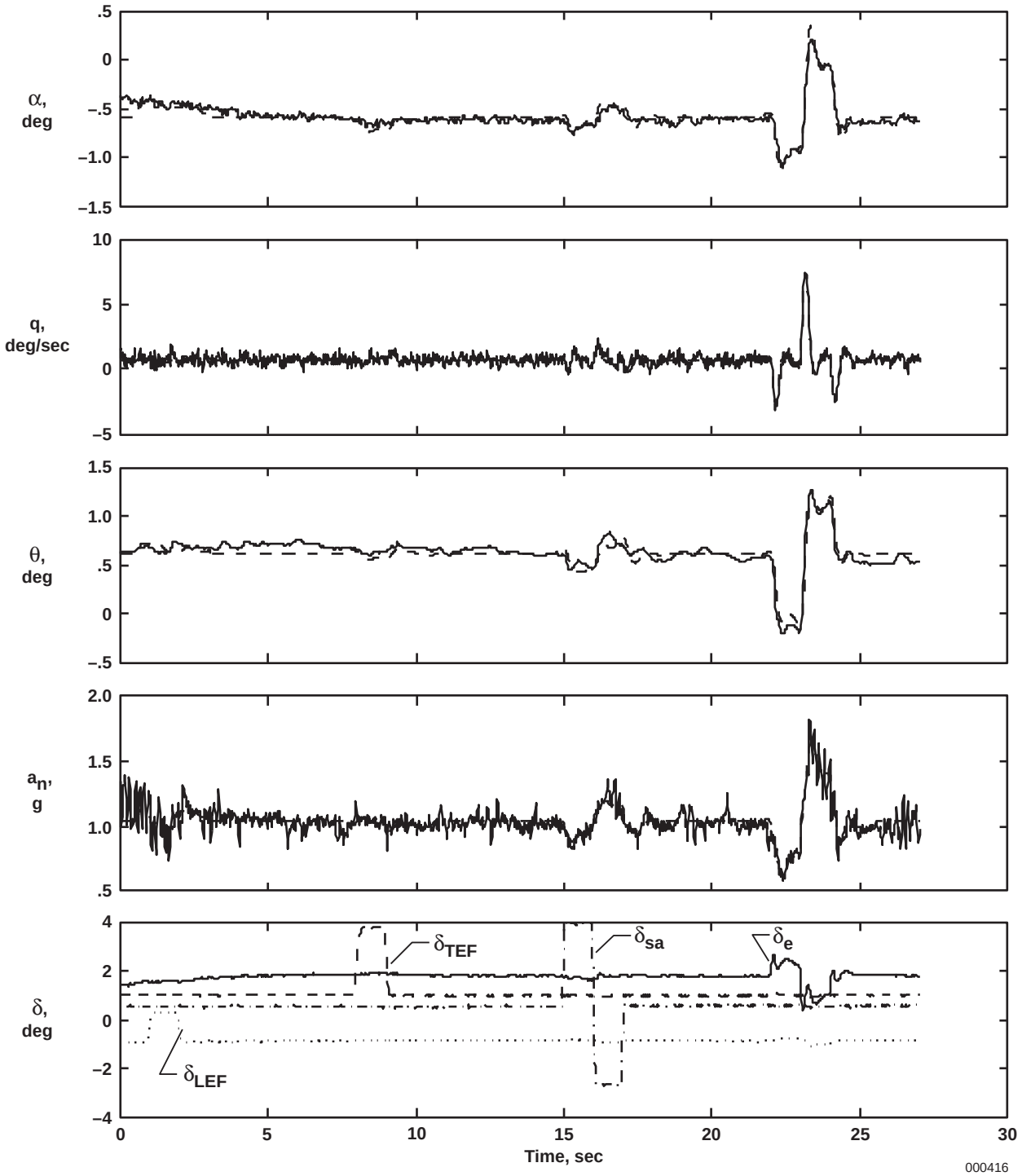

Figure A-19. Small doublet sequence (Mach 1.3 at 20,000 ft).

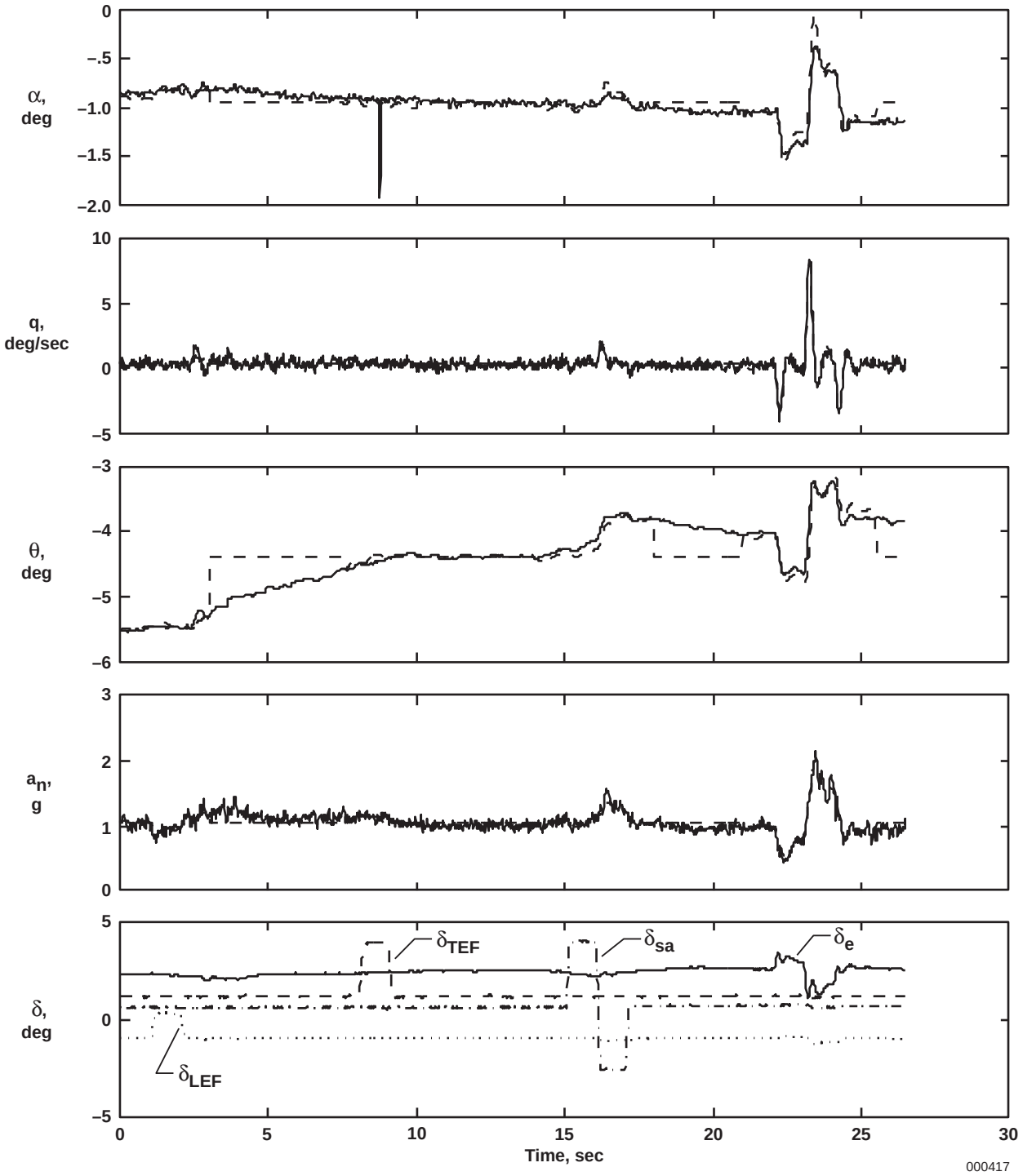

Figure A-20. Small doublet sequence (Mach 1.3 at 15,000 ft).

APPENDIX B

LATERAL-DIRECTIONAL MANEUVER TIME HISTORIES

Figures B-1–B-20 show time histories of lateral-directional doublet sequences. A typical time history is shown for each of the 20 flight test conditions. This appendix shows actual aircraft responses to the five lateral-directional single-surface inputs (SSIs) and qualitatively shows how well the parameter estimation program, pEst (ref. 1), was able to match the actual response time histories. Aircraft response parameters include angle of sideslip, roll rate, yaw rate, bank angle, and lateral acceleration. The solid line is the response parameter measured from flight data. The dashed line is the pEst program–estimated response at convergence obtained by integrating the equations of motion using the pEst program estimates of the stability and control derivatives. Note that in figure B-5, no measured angle of sideslip exists. In this case, the flush airdata sensing angle-of-sideslip measurement was not available; therefore, the angle-of-sideslip response parameter was weighted low in the pEst program.

Only selected windows of data were used in the pEst program analysis. Some of the data between subsequent SSI inputs were removed from the pEst program analysis to minimize integration drift. The data removed were from times when the aircraft was no longer responding to the previous SSI input. The time history points not used in the integration are indicated by the step discontinuities in the dashed line.

The control-surface positions measured by the control-surface position transducers are also plotted. For the lateral-directional sequences, the SSIs were done in the following order: rudder, differential leading-edge flap, differential trailing-edge flap, aileron, and differential stabilator. A 5-sec delay was built in between each SSI.

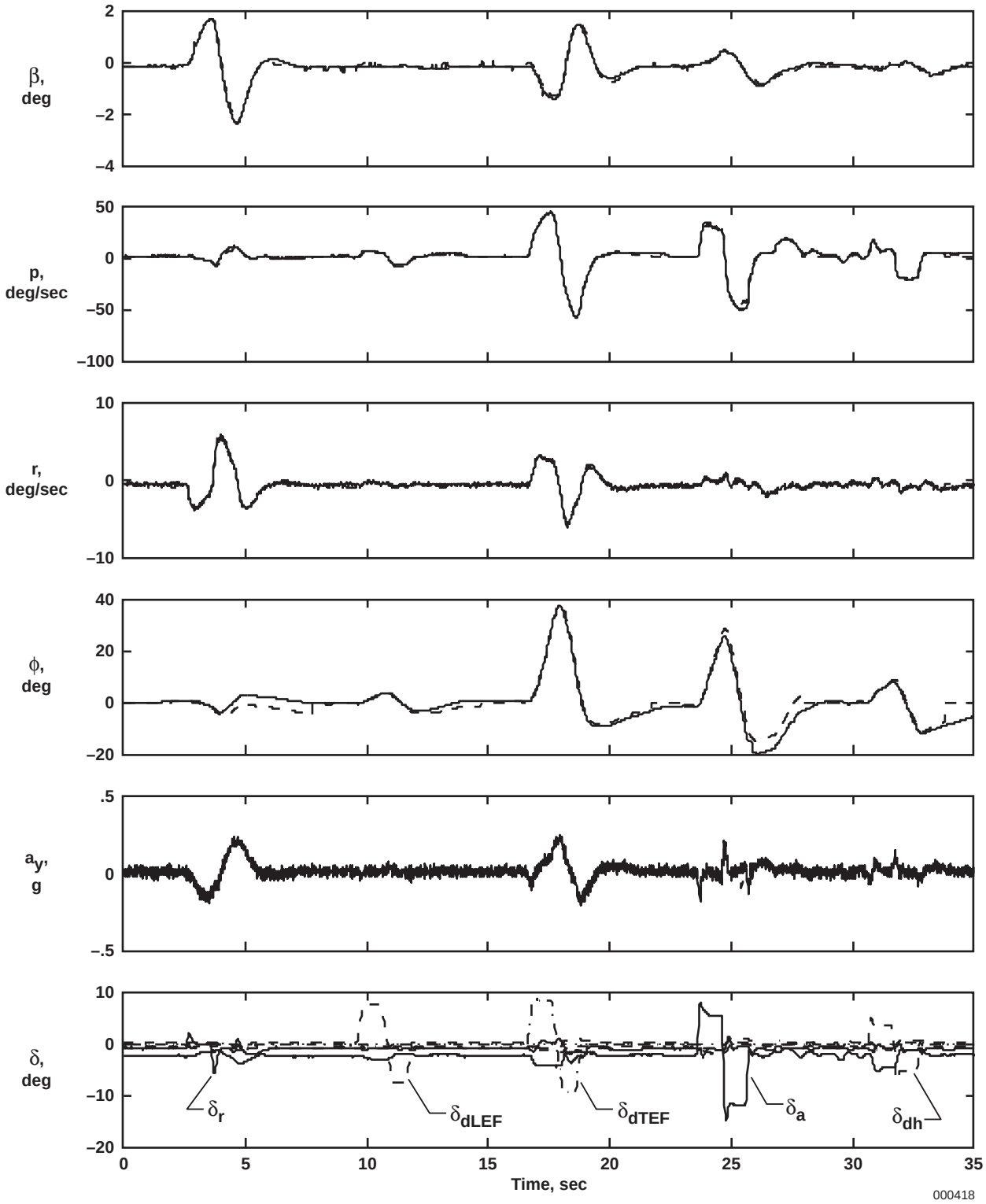

Figure B-1. Large doublet sequence (Mach 0.85 at 15,000 ft).

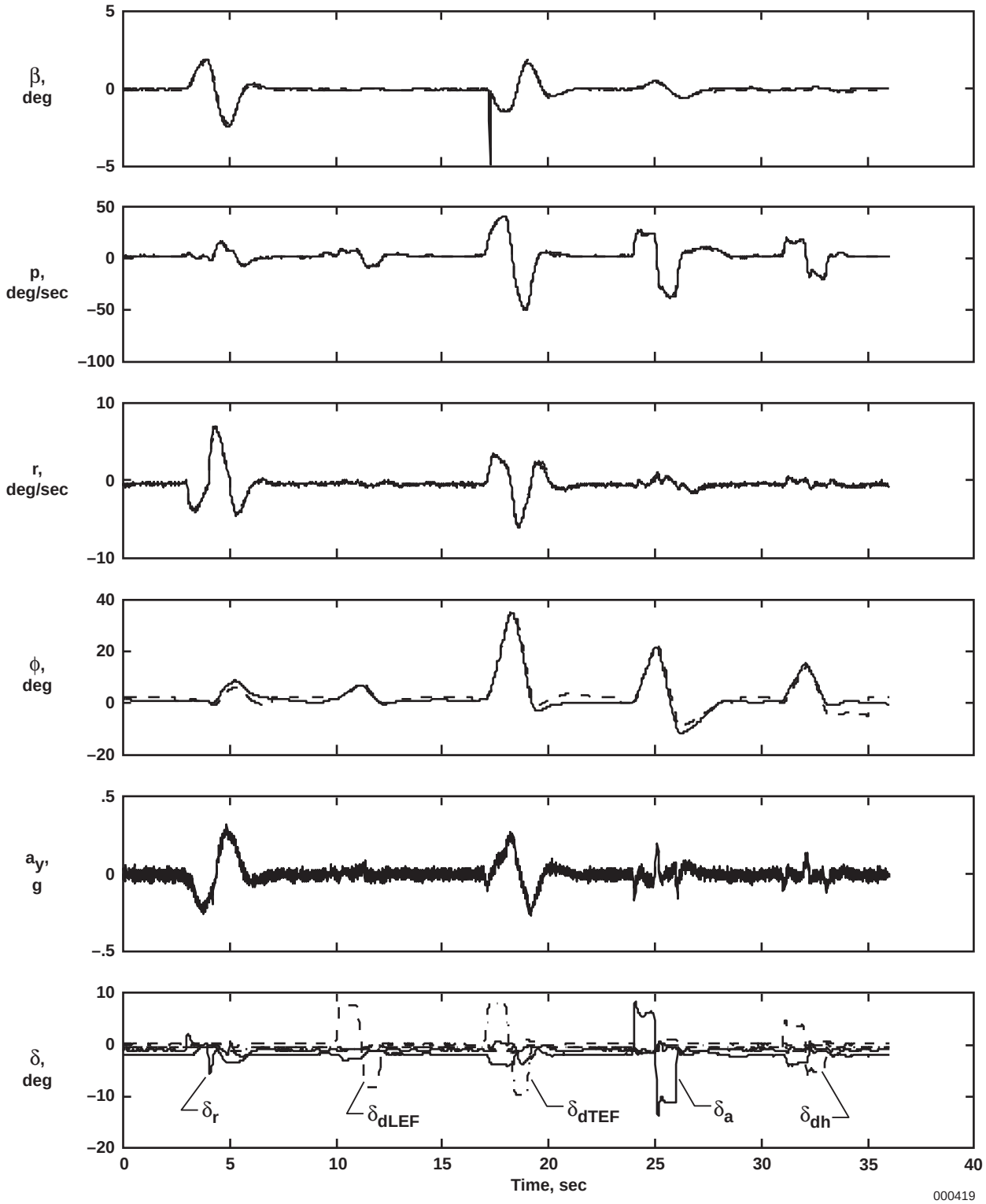

Figure B-2. Large doublet sequence (Mach 0.85 at 10,000 ft).

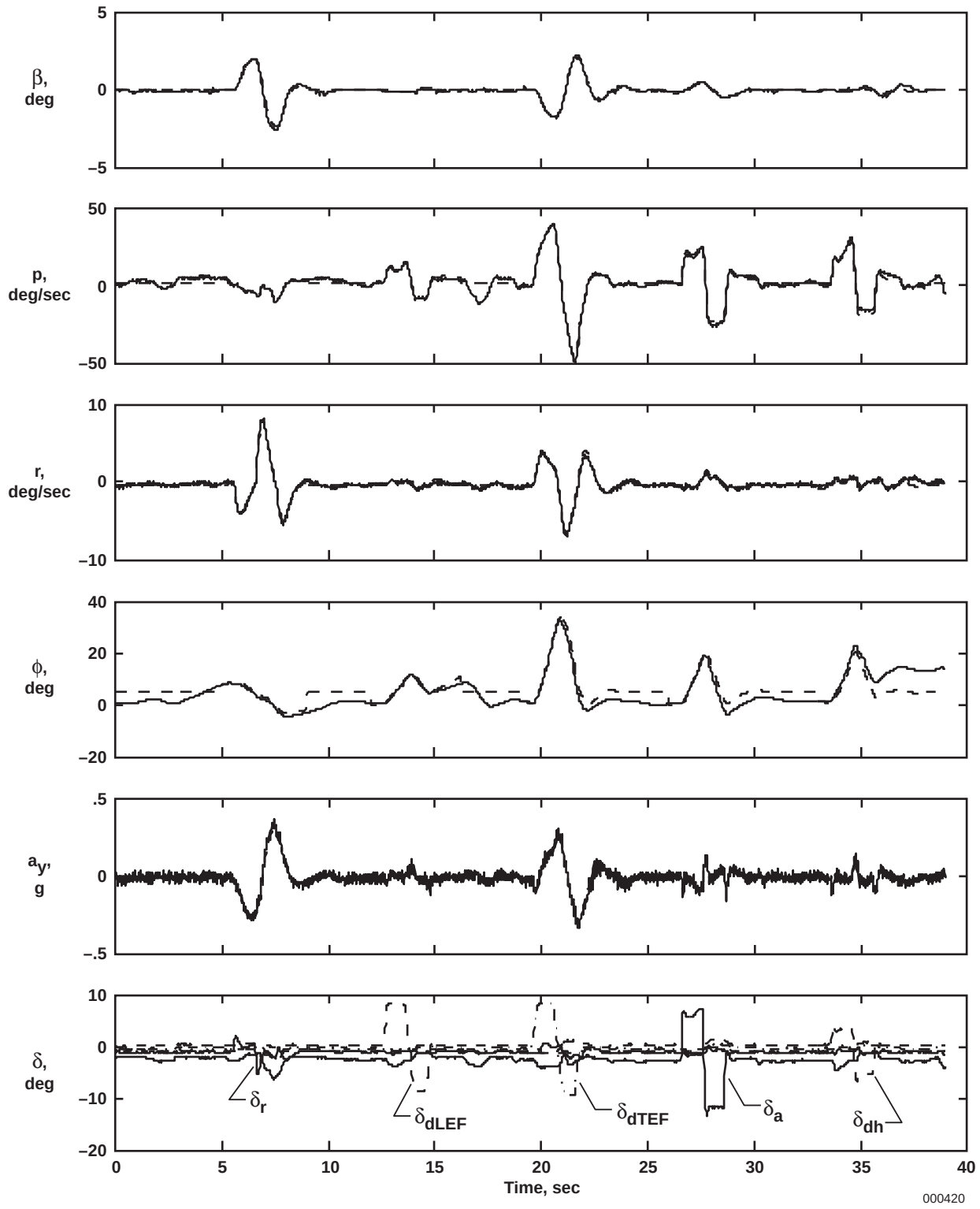

Figure B-3. Large doublet sequence (Mach 0.85 at 5,000 ft).

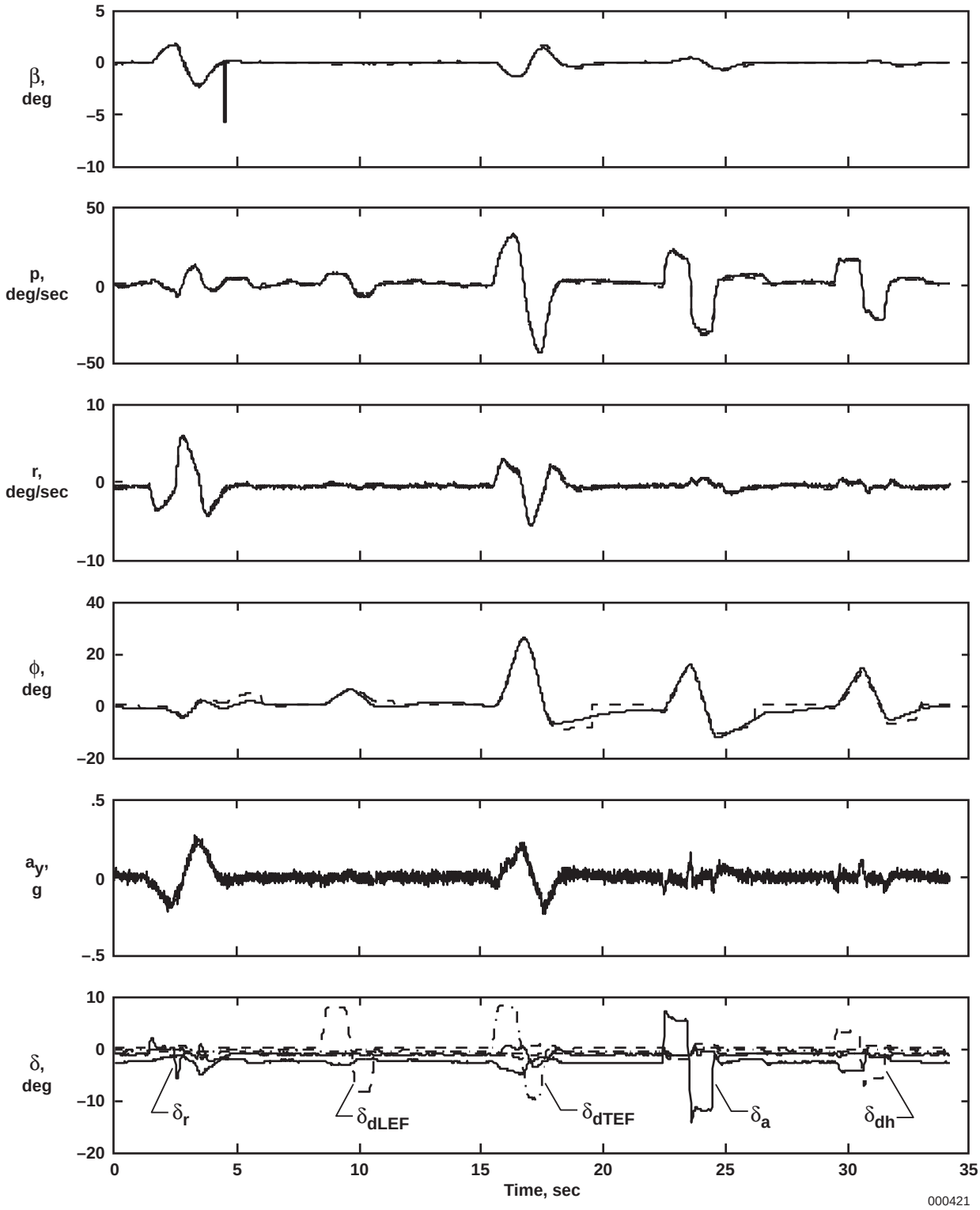

Figure B-4. Large doublet sequence (Mach 0.9 at 15,000 ft).

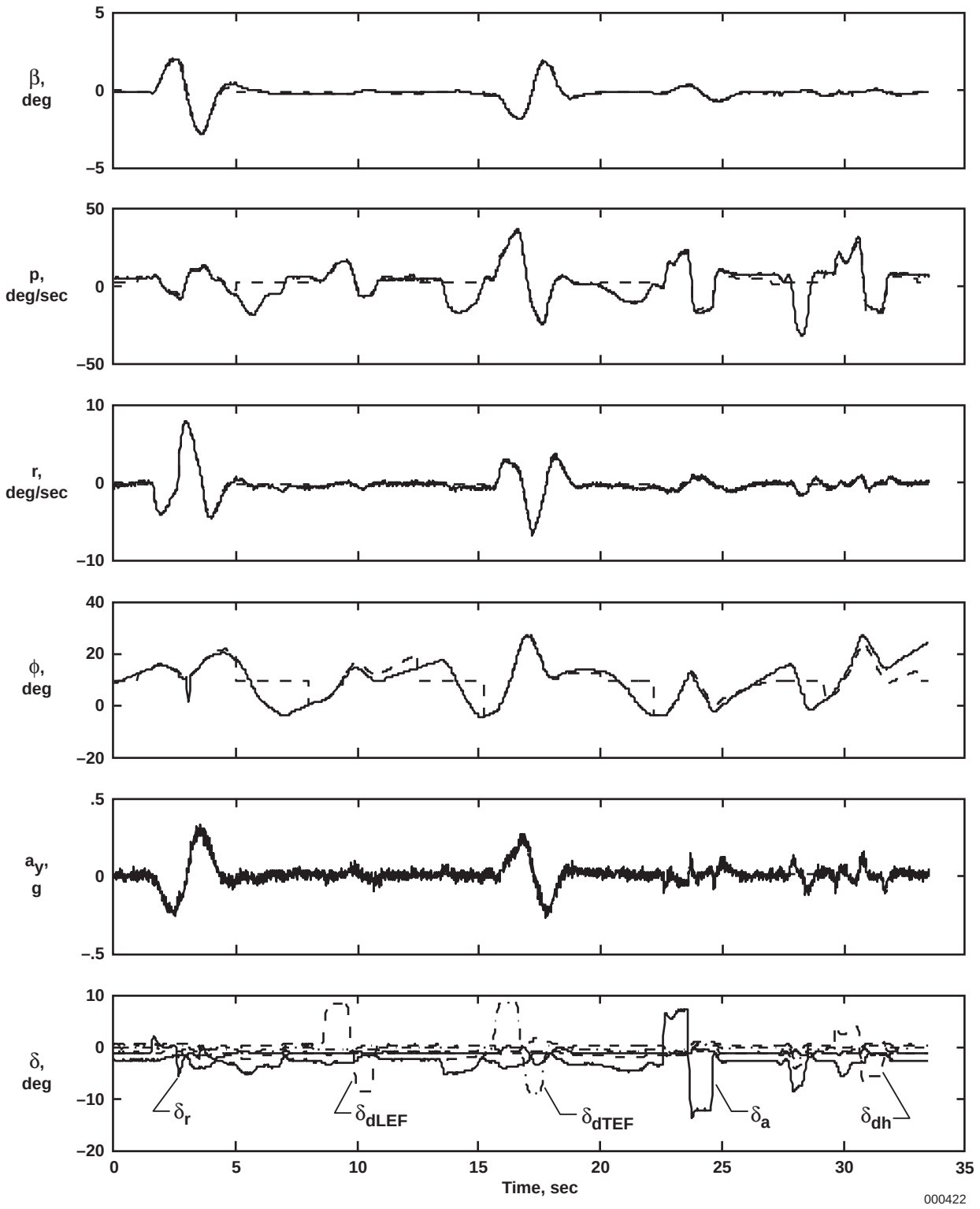

Figure B-5. Large doublet sequence (Mach 0.9 at 10,000 ft).

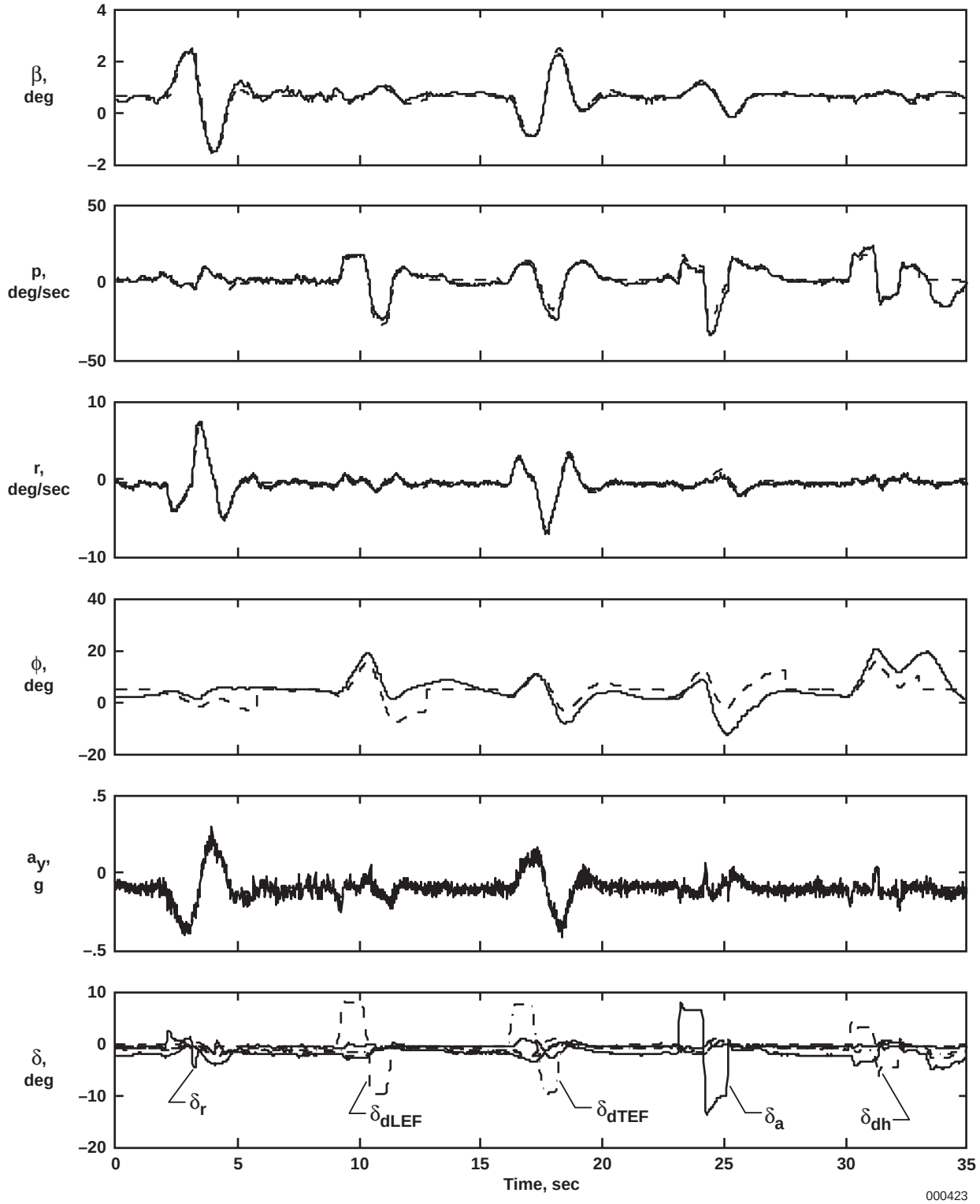

Figure B-6. Large doublet sequence (Mach 0.9 at 5,000 ft).

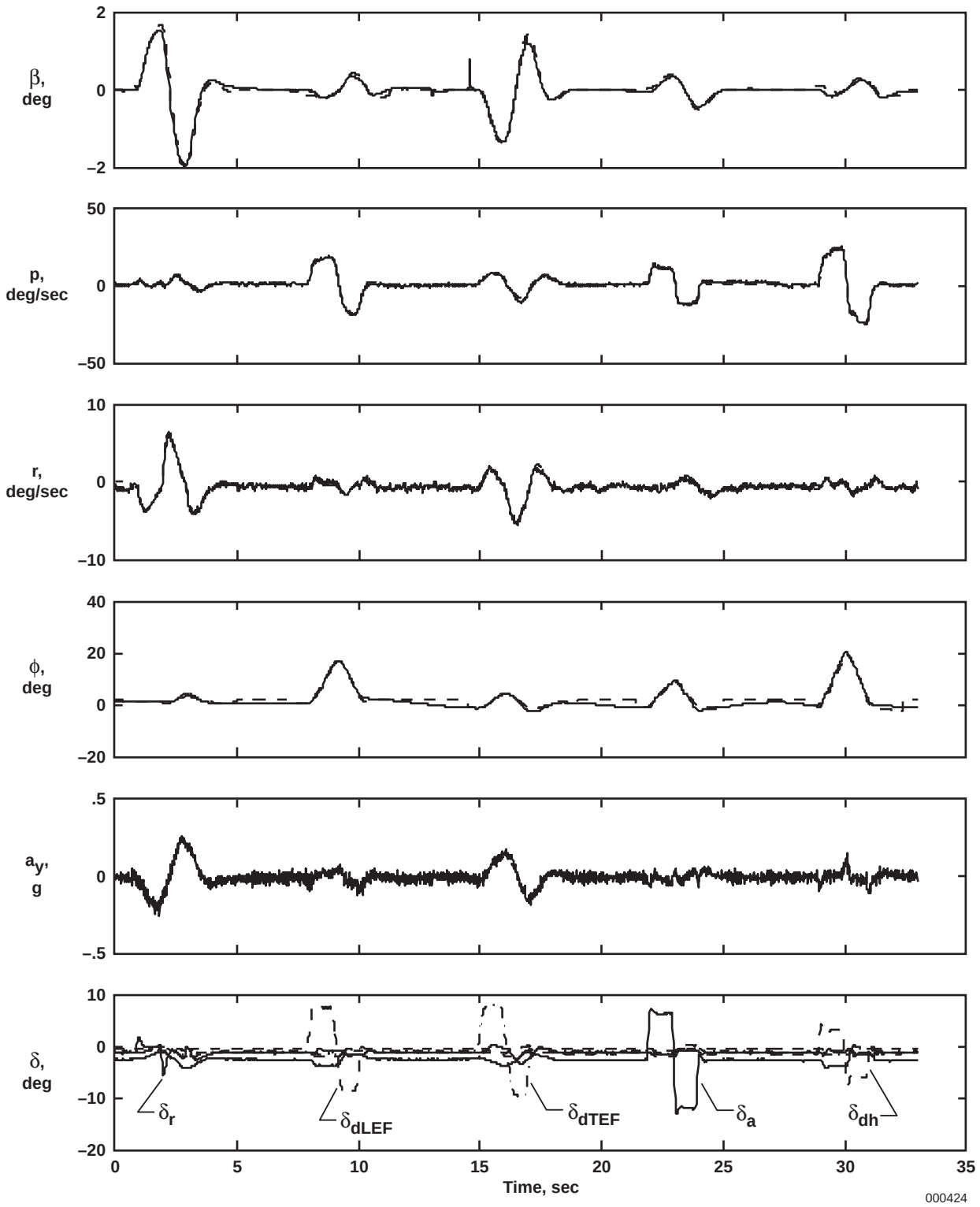

Figure B-7. Large doublet sequence (Mach 0.95 at 15,000 ft).

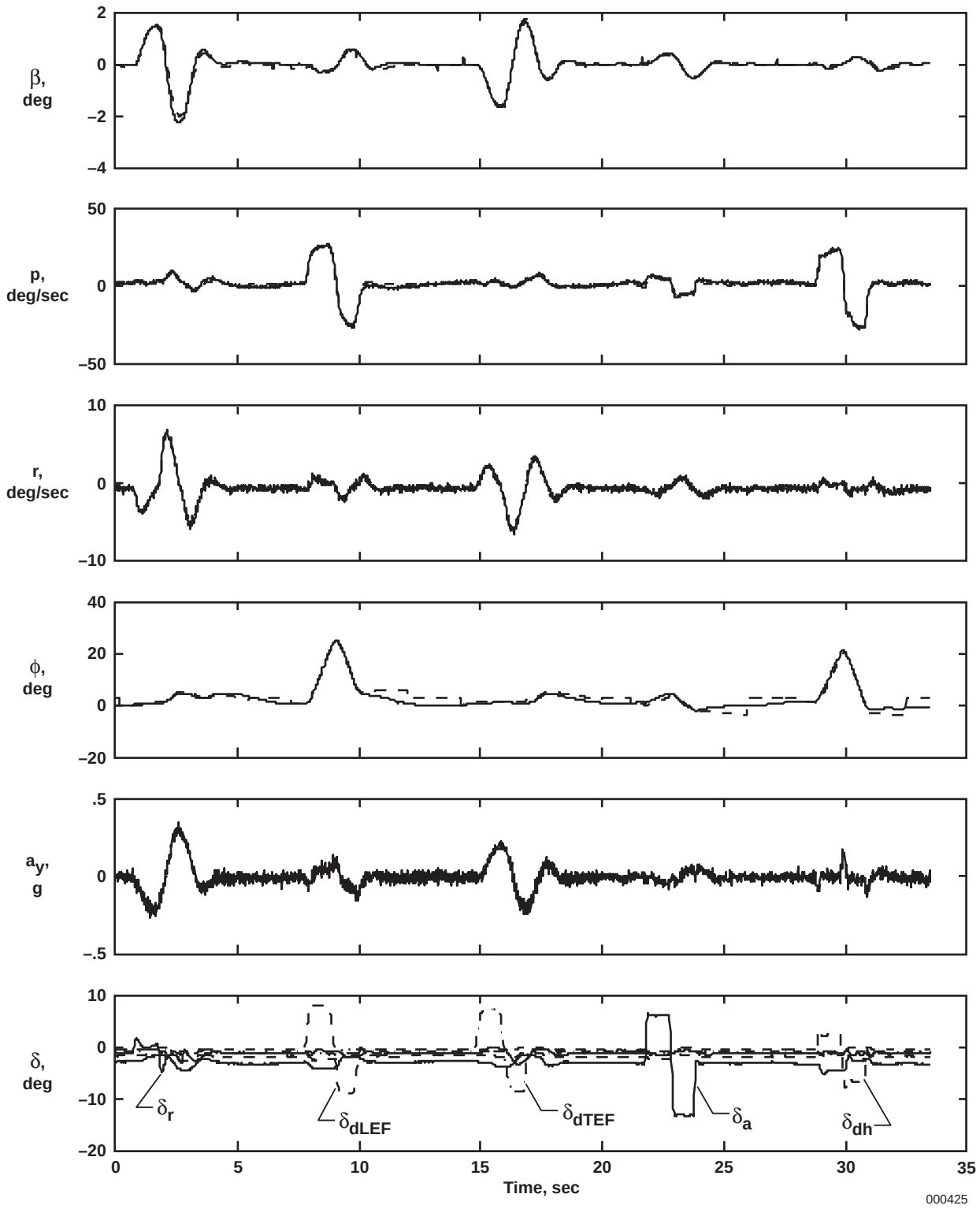

Figure B-8. Large doublet sequence (Mach 0.95 at 10,000 ft).

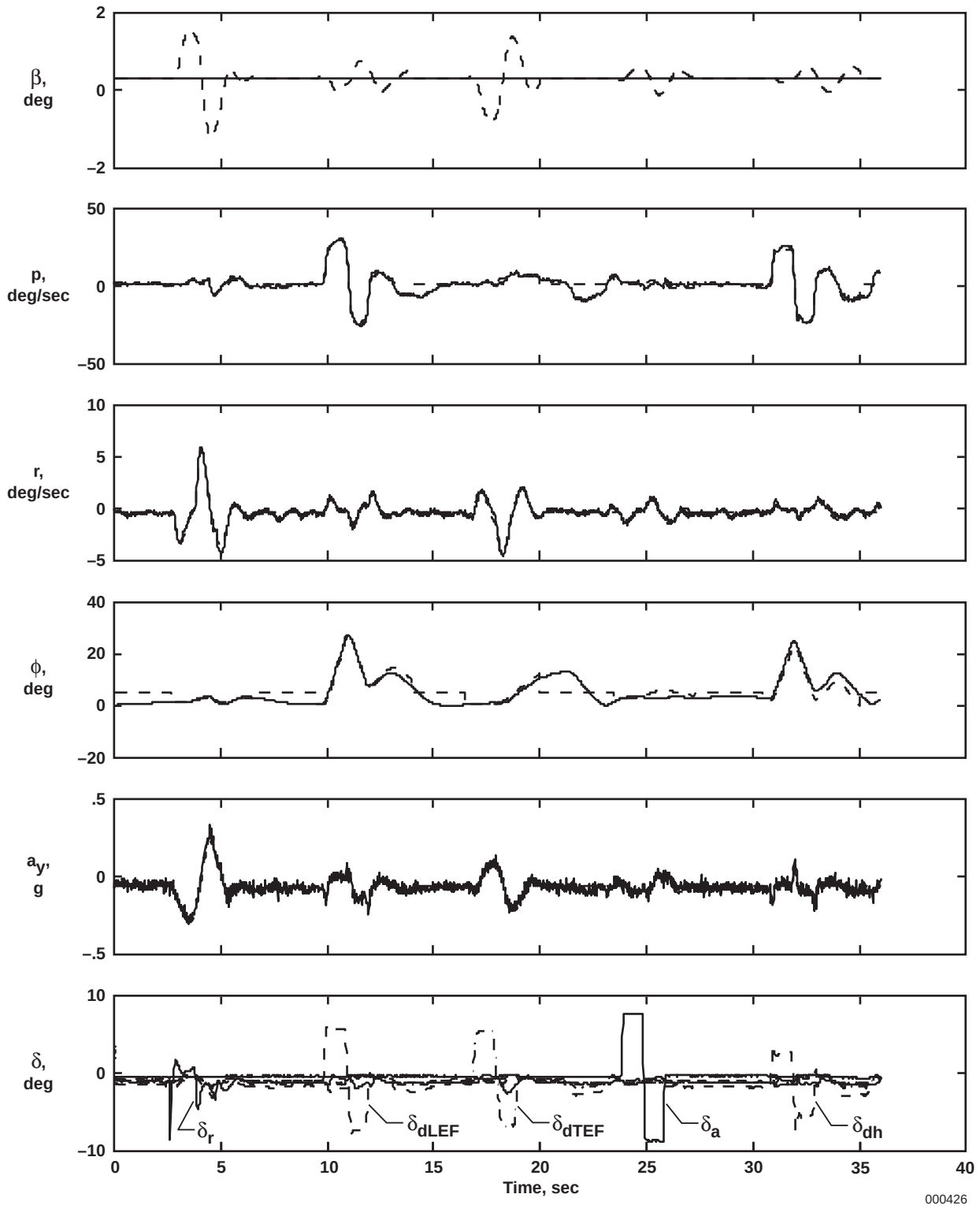

Figure B-9. Medium doublet sequence (Mach 0.95 at 5,000 ft).

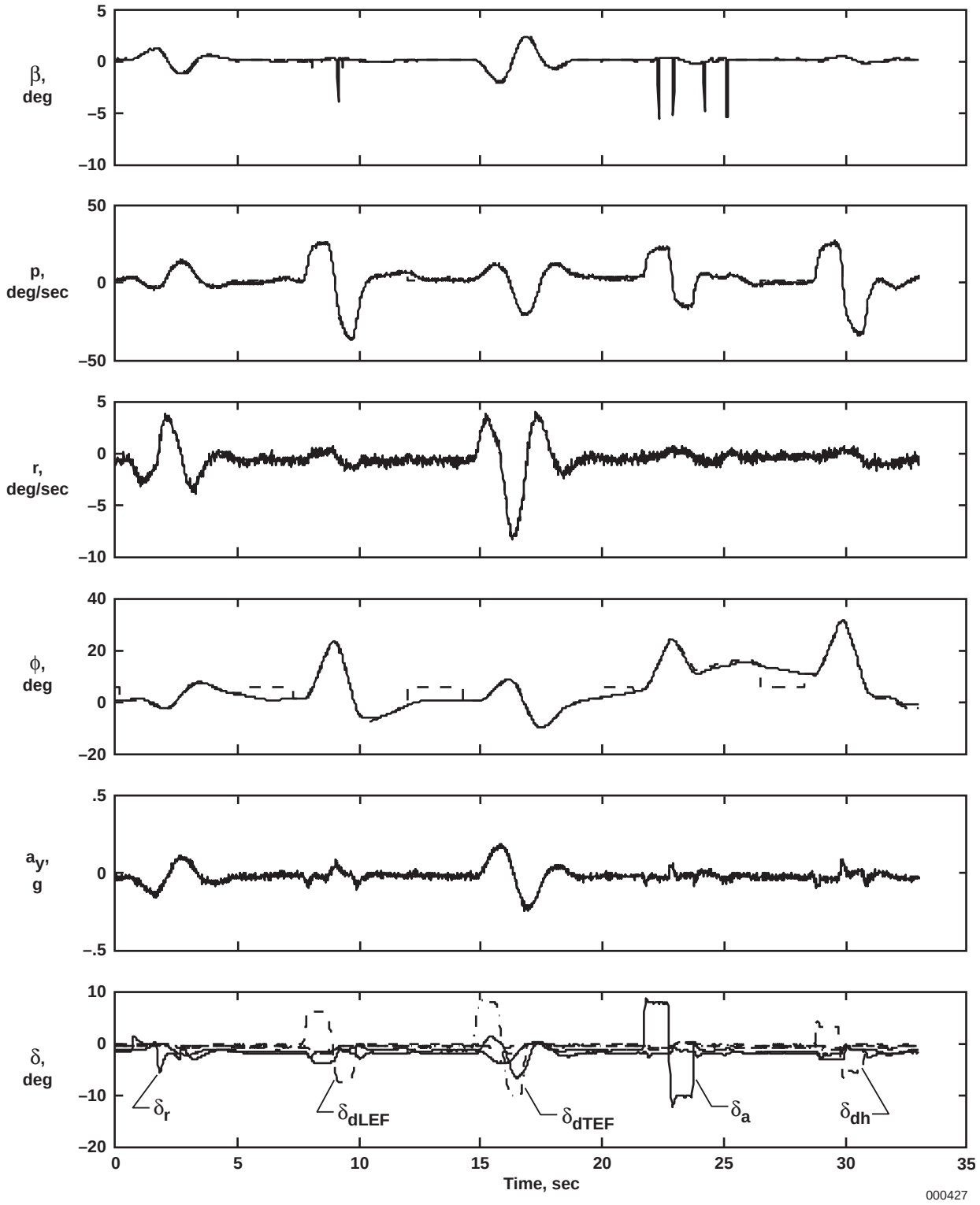

Figure B-10. Large doublet sequence (Mach 1.1 at 25,000 ft).

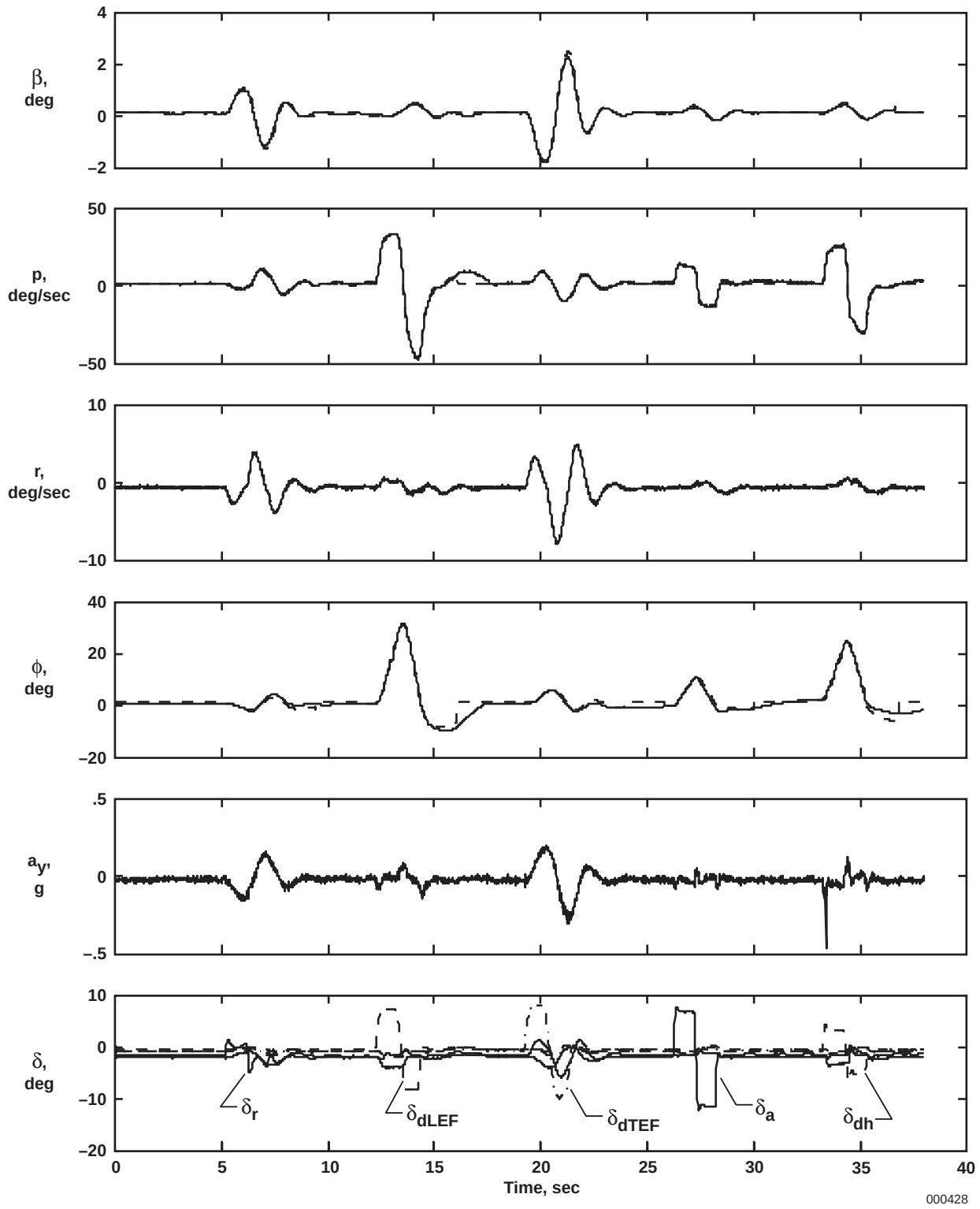

Figure B-11. Large doublet sequence (Mach 1.1 at 20,000 ft).

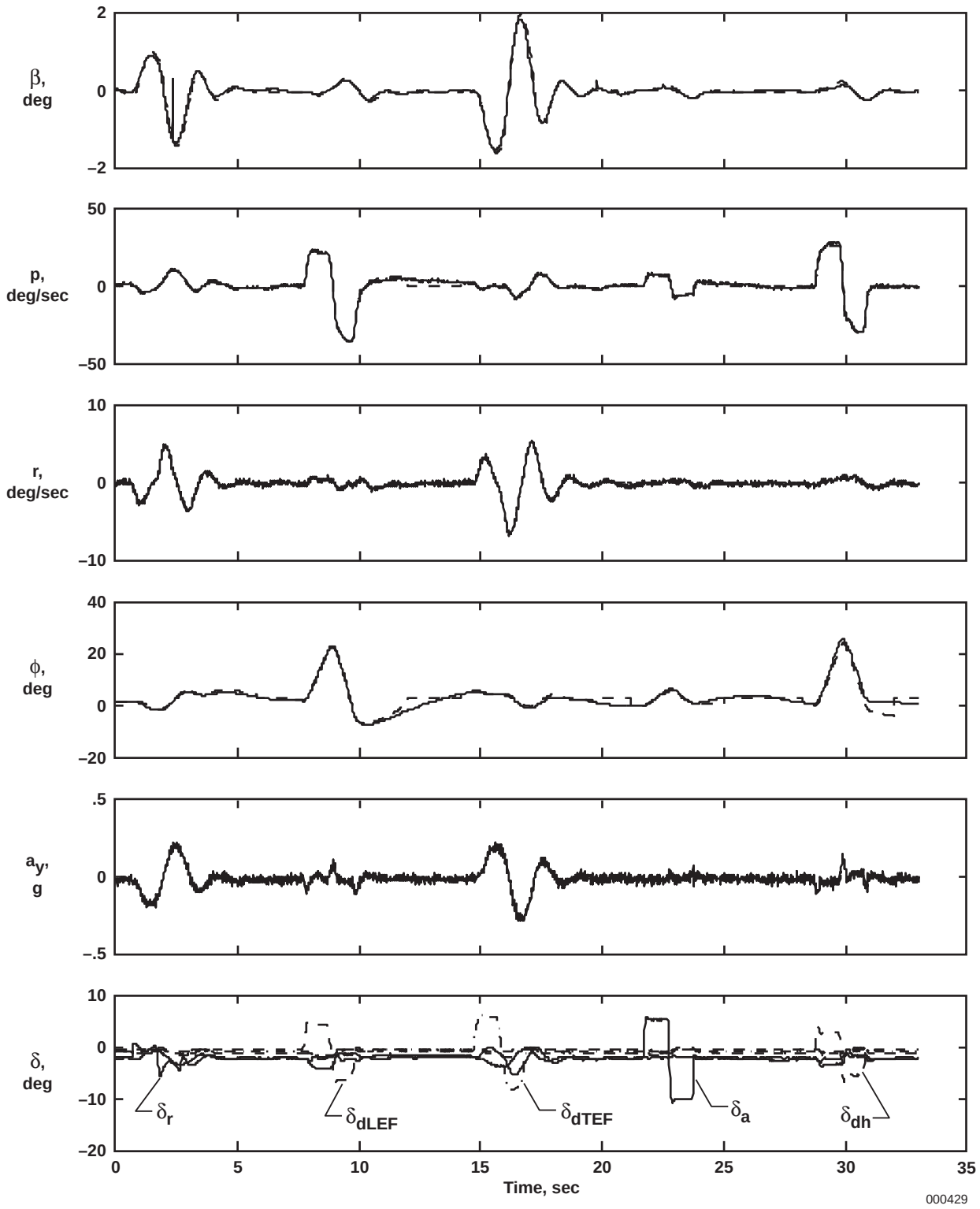

Figure B-12. Medium doublet sequence (Mach 1.1 at 15,000 ft).

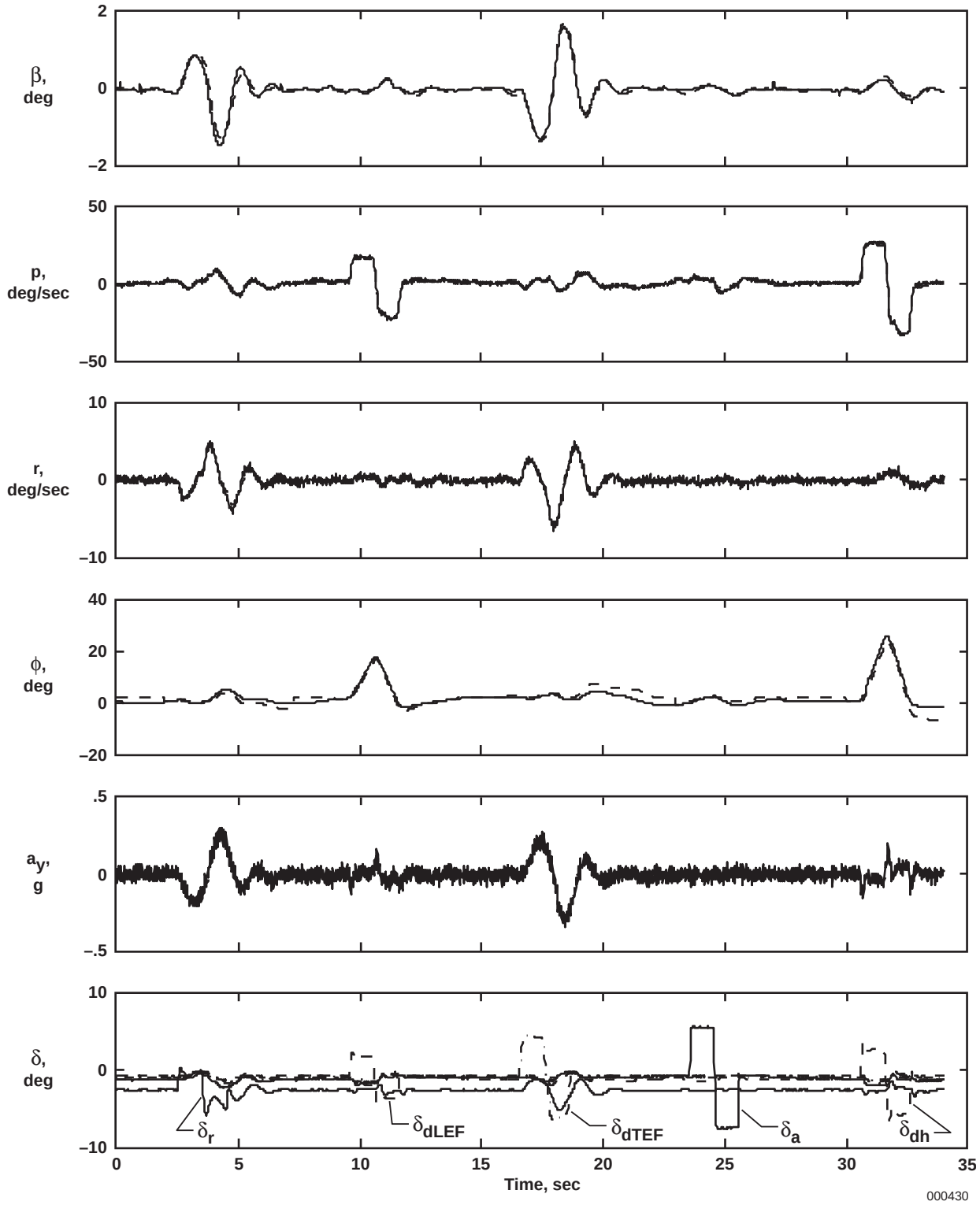

Figure B-13. Small doublet sequence (Mach 1.1 at 10,000 ft).

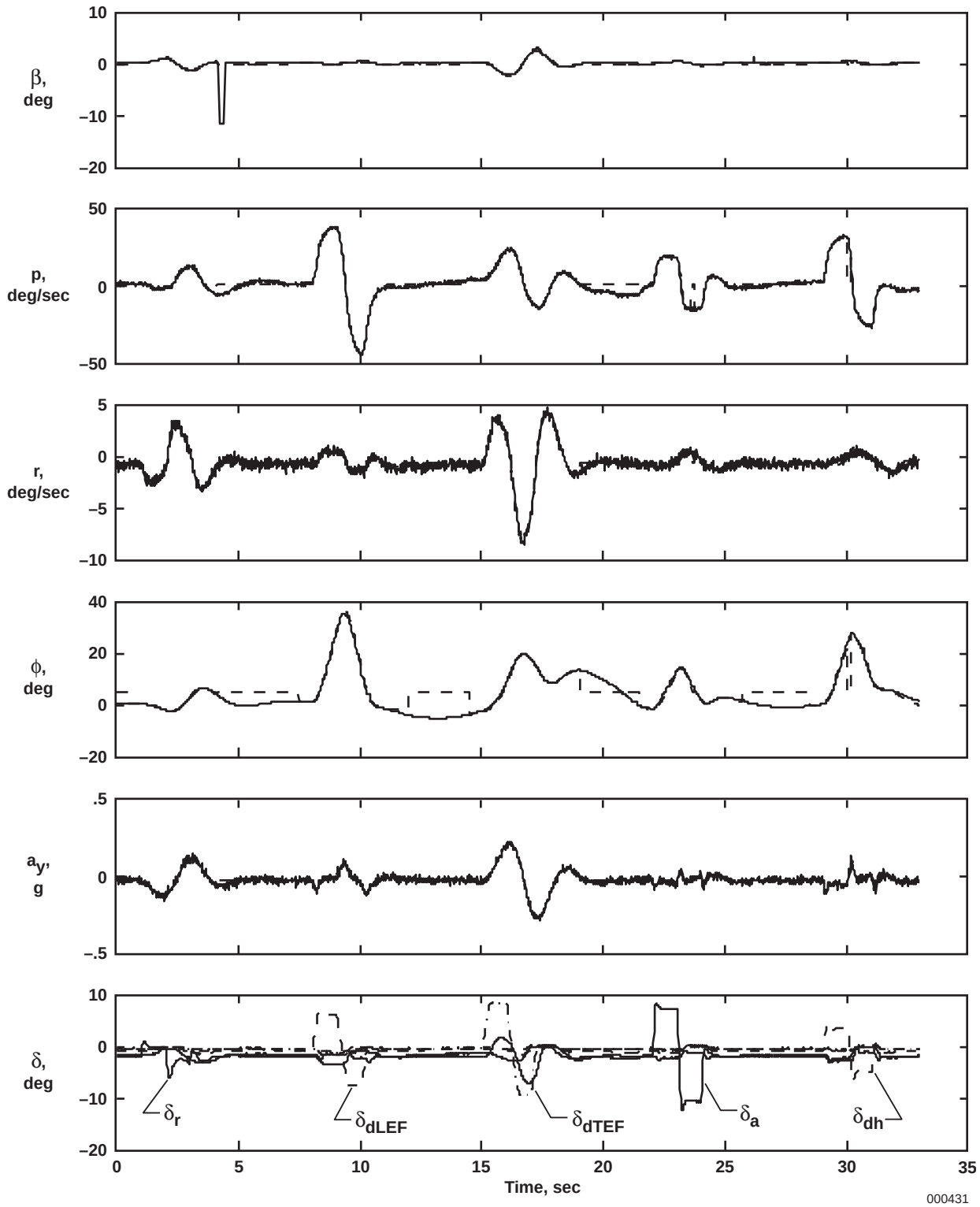

Figure B-14. Large doublet sequence (Mach 1.2 at 25,000 ft).

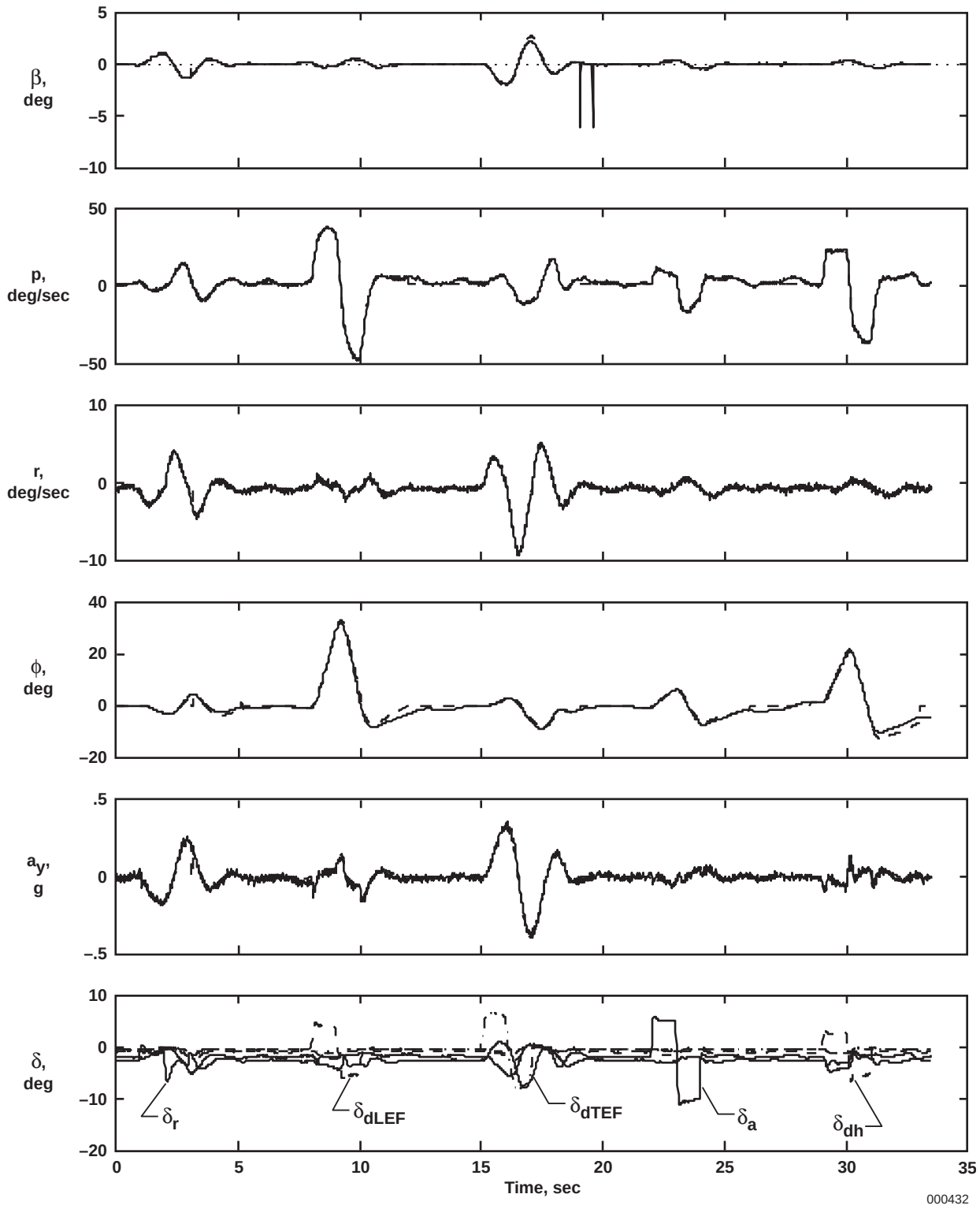

Figure B-15. Medium doublet sequence (Mach 1.2 at 20,000 ft).

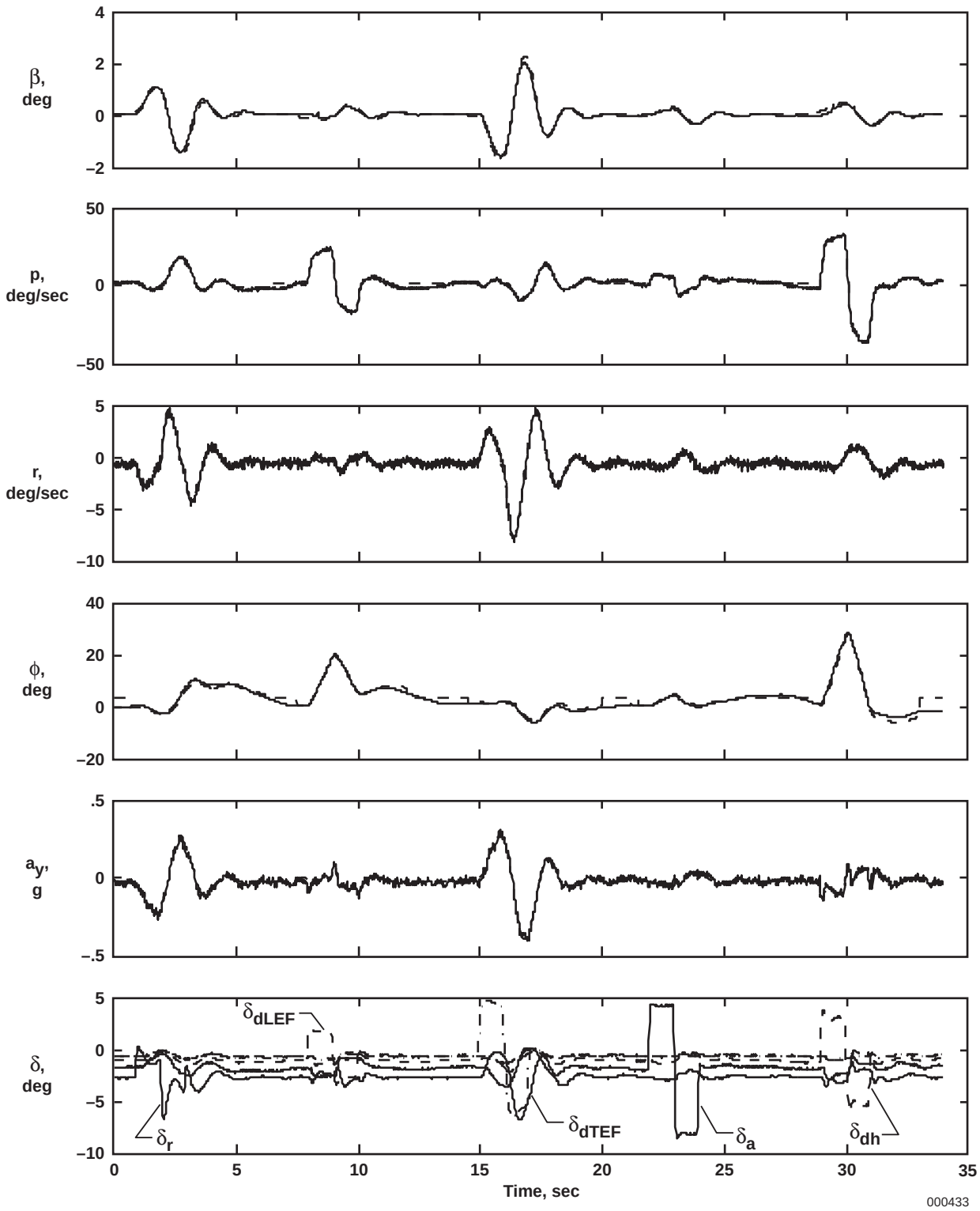

Figure B-16. Small doublet sequence (Mach 1.2 at 15,000 ft).

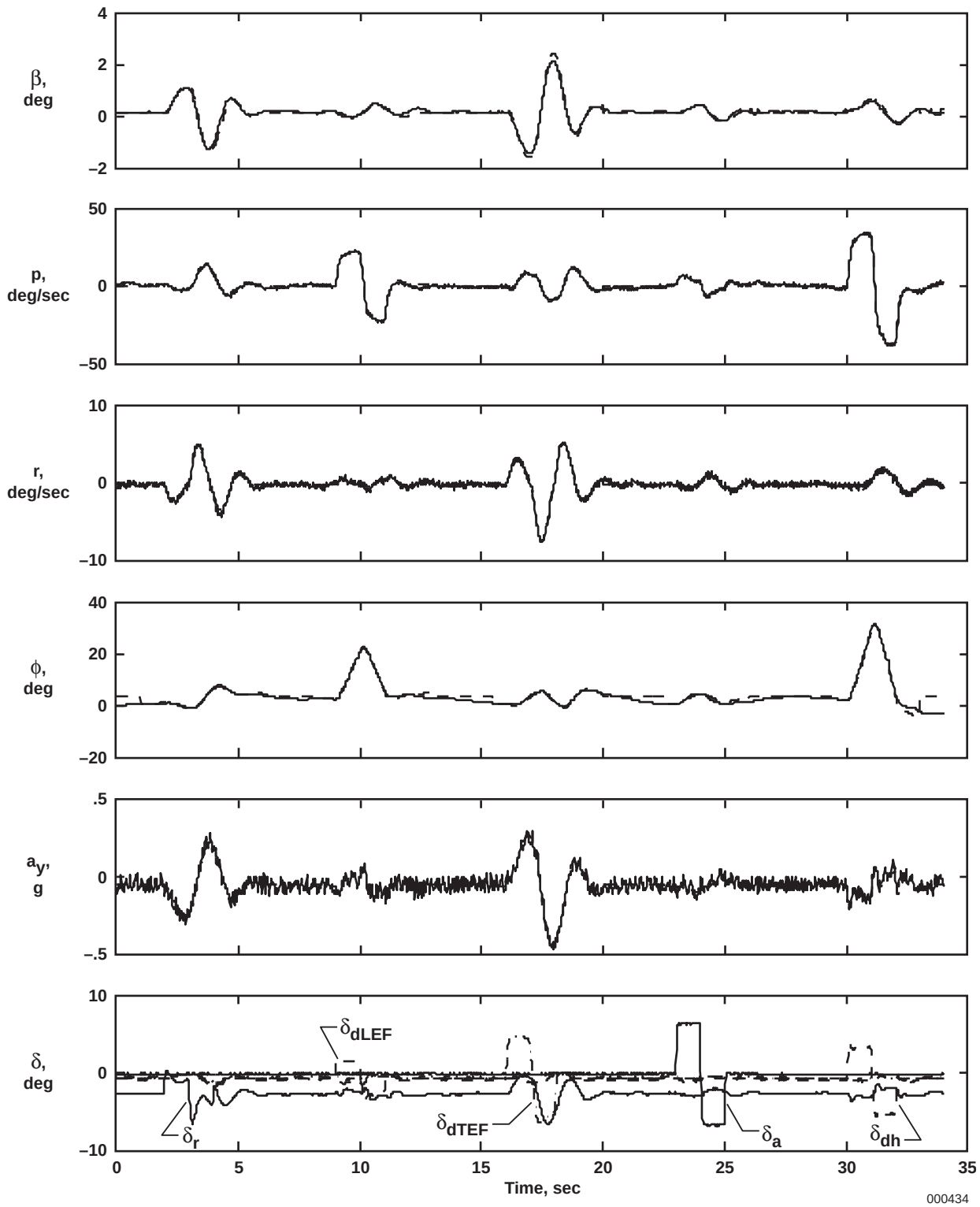

Figure B-17. Small doublet sequence (Mach 1.2 at 10,000 ft).

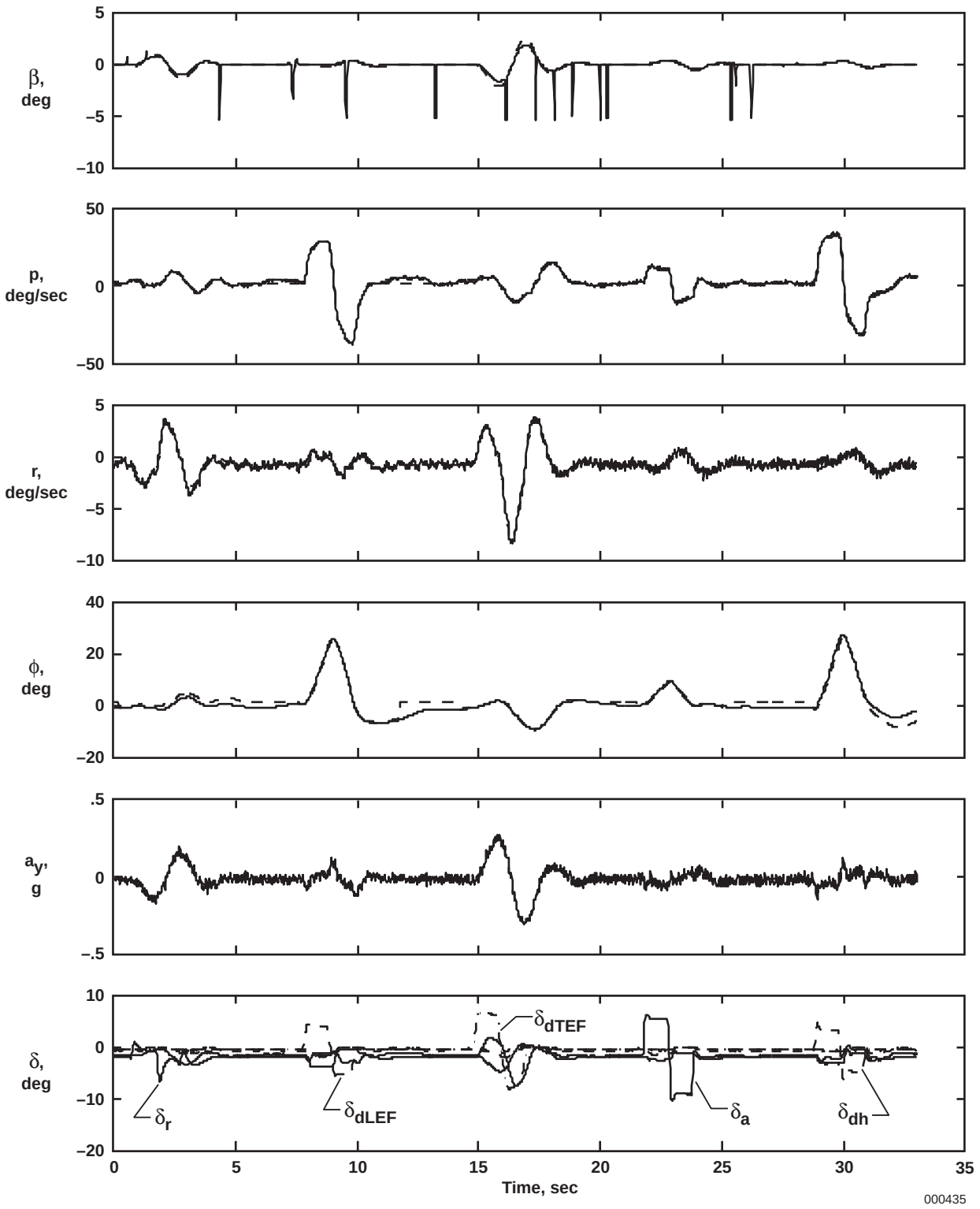

Figure B-18. Medium doublet sequence (Mach 1.3 at 25,000 ft).

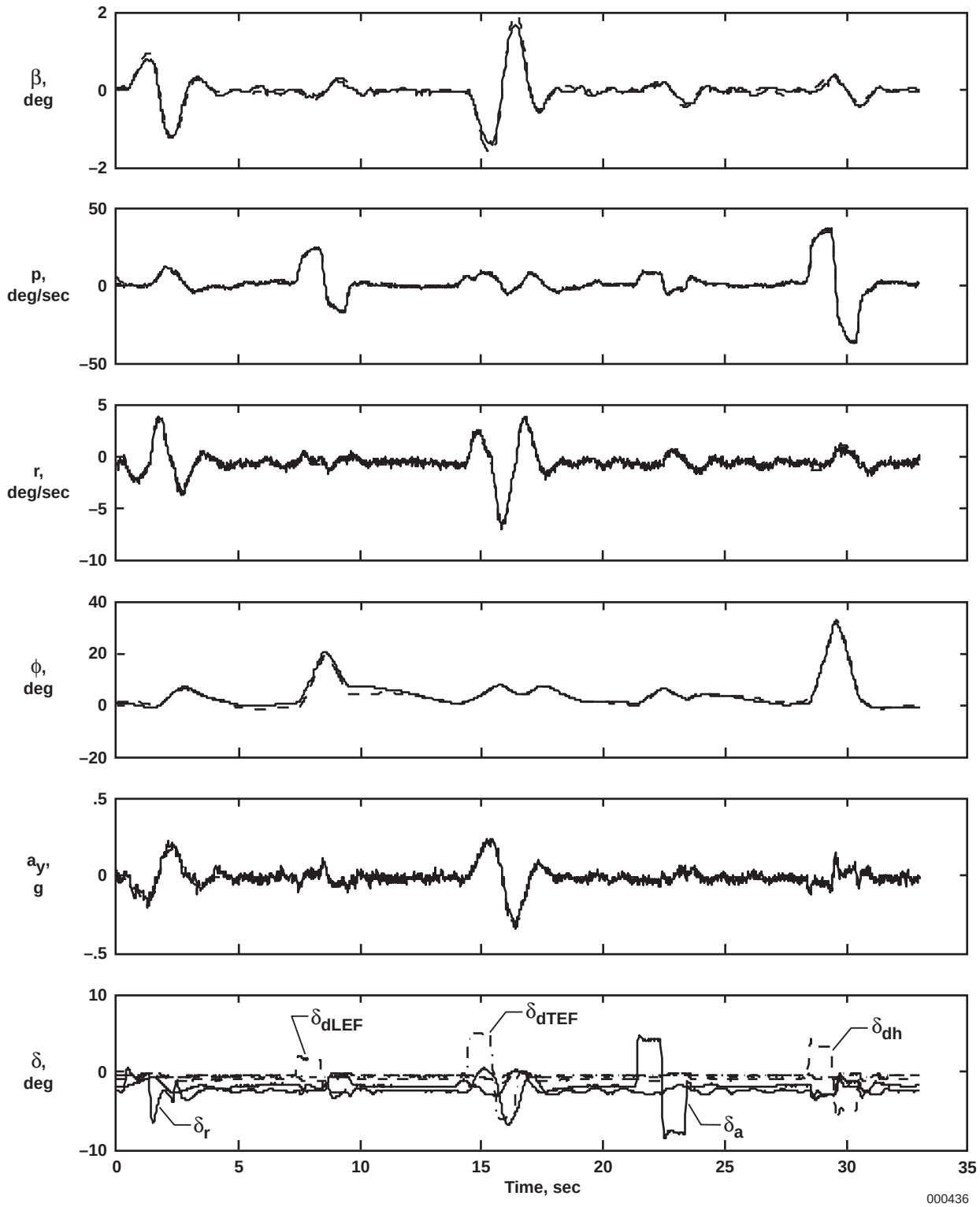

Figure B-19. Small doublet sequence (Mach 1.3 at 20,000 ft).

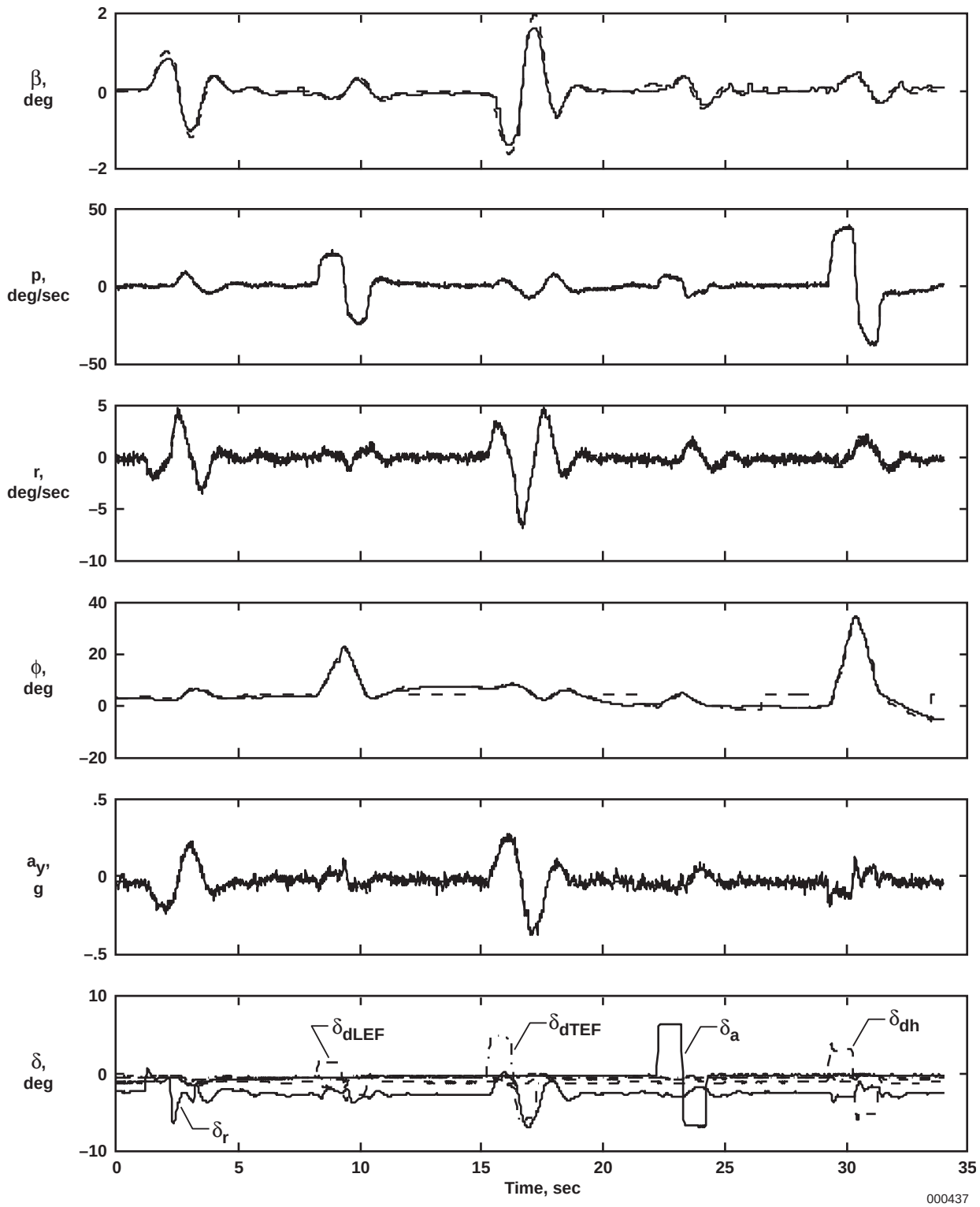

Figure B-20. Small doublet sequence (Mach 1.3 at 15,000 ft).

APPENDIX C

STABILITY AND CONTROL DERIVATIVE INCREMENTS OBTAINED FROM PARAMETER IDENTIFICATION ANALYSIS USING CONTROL-SURFACE POSITION TRANSDUCER MEASUREMENTS

Tables C-1–C-5 show tabulated stability and control derivative increments as defined in equations (26)–(30). These increments were obtained from the parameter estimation program, pEst (ref. 1), analysis that used the control-surface position transducer (CPT) measurements. Increments are defined by subtracting the simulation-predicted derivative from the flight-determined derivative and averaging the results from multiple maneuvers at each flight condition. The increments are separated into Mach number and altitude breakpoints. In some cases at Mach 1.05 and Mach 1.15, fight data were nonexistent, and interpolation or “hold last value” were used to complete the tables.

Table C-1. Normal-force coefficient derivative increments as a function of Mach number and altitude (pEst program analysis with CPT surface positions).

Derivative increment	Altitude, kft	Mach number 0.85	0.90	0.95	1.05	1.10	1.15	1.20	1.30
ΔC_{N_b}	5	0.06979	0.10511	0.11234					
	10	0.05551	0.10475	0.11663	0.04612	0.05003	0.08459	0.11127	
	15	0.06213	0.09266	0.09976	0.03911	0.04582	0.07782	0.10983	0.12842
	20				0.04476	0.05243	0.14339	0.09625	0.12896
	25				0.04476	0.04255	0.10496	0.08776	0.09853
ΔC_{N_α}	5	–0.02561	–0.00946	–0.01352					
	10	–0.01667	–0.01694	–0.01819	–0.01027	–0.01382	–0.01688	–0.02451	
	15	–0.01614	–0.02590	–0.02641	–0.00823	–0.01305	–0.01867	–0.02429	–0.01023
	20				–0.01622	–0.01915	–0.02130	–0.01651	–0.01248
	25				–0.01622	–0.01640	–0.02592	–0.02085	–0.00373
ΔC_{N_q}	5	1.44609	–0.88377	–9.66942					
	10	–3.56552	9.97219	–15.63990	–6.73941	–2.85784	–1.82020	3.82213	
	15	–17.78343	–0.63701	–5.46427	–5.36077	0.15169	2.53439	4.91708	–10.73700
	20				–2.89814	3.46065	–4.72085	9.26574	–4.92922
	25				–2.89814	–0.87555	–1.10987	4.99502	5.22792
$\Delta C_{N_{\delta_{LEF}}}$	5	–0.01505	0.00100	–0.00655					
	10	–0.00764	0.00122	–0.00390	–0.00662	–0.00519	–0.00148	–0.00526	
	15	–0.00536	–0.00376	–0.00285	–0.00242	–0.00365	–0.00266	–0.00167	–0.00321
	20				–0.00178	–0.00259	–0.00091	0.00127	–0.00149
	25				–0.00178	–0.00099	0.00048	0.00055	0.00232
$\Delta C_{N_{\delta_{TEF}}}$	5	–0.01020	–0.01002	–0.01697					
	10	–0.00604	–0.00962	–0.01594	–0.01186	–0.01156	–0.00980	–0.01177	
	15	–0.01090	–0.00866	–0.01222	–0.01038	–0.00789	–0.00902	–0.01015	–0.01156
	20				–0.00953	–0.00833	–0.00942	–0.00839	–0.00965
	25				–0.00953	–0.00756	–0.00974	–0.00845	–0.00916
$\Delta C_{N_{\delta_{sa}}}$	5	0.00221	–0.00118	0.00045					
	10	0.00243	–0.00128	0.00016	–0.00028	0.00000	0.00016	0.00143	
	15	–0.00094	–0.00237	0.00084	–0.00061	0.00028	0.00049	0.00070	0.00169
	20				–0.00111	–0.00104	–0.00009	0.00078	0.00047
	25				–0.00111	–0.00115	0.00060	–0.00029	0.00023
$\Delta C_{N_{\delta_e}}$	5	–0.00091	0.00391	0.00297					
	10	–0.00239	0.00767	–0.00033	–0.00213	0.00221	0.00146	0.00128	
	15	0.00248	0.00840	0.00181	–0.00200	0.00102	0.00143	0.00185	–0.00173
	20				–0.00063	–0.00100	–0.00451	0.00460	0.00154
	25				–0.00063	–0.00032	–0.00161	0.00101	0.00263

Table C-2. Pitching-moment coefficient derivative increments as a function of Mach number and altitude (pEst program analysis with CPT surface positions).

Derivative increment	Altitude, kft	Mach number 0.85	0.90	0.95	1.05	1.10	1.15	1.20	1.30
ΔC_{m_b}	5	–0.02569	–0.02804	–0.02636					
	10	–0.02702	–0.03087	–0.03054	–0.03110	–0.03501	–0.04122	–0.04251	
	15	–0.02291	–0.03043	–0.02895	–0.03334	–0.03816	–0.04185	–0.04554	–0.05075
	20			–0.02895	–0.03558	–0.03928	–0.03554	–0.04253	–0.04872
	25			–0.02895	–0.03558	–0.03941	–0.03684	–0.04000	–0.04767
ΔC_{m_α}	5	0.01002	0.00897	0.00736					
	10	0.01013	0.01078	0.01016	0.01054	0.00571	0.00577	0.00559	
	15	0.01062	0.01112	0.01163	0.00921	0.00696	0.00577	0.00458	0.00389
	20				0.00902	0.00830	0.00397	0.00424	0.00449
	25				0.00902	0.00977	0.00595	0.00401	0.00383
ΔC_{m_q}	5	–2.54772	–4.26513	–6.46124					
	10	–2.63694	–3.83941	–7.90439	4.12364	4.40901	3.45007	2.74548	
	15	–5.69810	–3.29697	–6.54682	4.01878	3.67101	2.64762	1.62424	1.65979
	20				4.42074	2.91068	–6.14382	0.42716	–0.48362
	25				4.42074	2.36339	–2.78240	0.10917	–0.09082
$\Delta C_{m_{\delta_{LEF}}}$	5	0.00053	0.00005	–0.00006					
	10	0.00020	0.00043	–0.00046	0.00250	0.00292	0.00517	0.00587	
	15	0.00024	0.00085	–0.00030	0.00172	0.00407	0.00454	0.00500	0.00634
	20				0.00172	0.00267	0.00484	0.00432	0.00523
	25				0.00172	0.00195	0.00317	0.00431	0.00483
$\Delta C_{m_{\delta_{TEF}}}$	5	–0.00019	–0.00016	0.00094					
	10	–0.00023	–0.00021	0.00091	0.00119	0.00155	0.00119	0.00112	
	15	–0.00049	–0.00061	0.00016	0.00102	0.00075	0.00082	0.00088	0.00104
	20				0.00073	0.00053	0.00043	0.00021	0.00031
	25				0.00073	0.00051	–0.00006	–0.00014	–0.00020
$\Delta C_{m_{\delta_{sa}}}$	5	–0.00260	–0.00271	–0.00267					
	10	–0.00244	–0.00212	–0.00242	–0.00135	–0.00133	–0.00130	–0.00179	
	15	–0.00229	–0.00176	–0.00212	–0.00110	–0.00109	–0.00117	–0.00125	–0.00227
	20				–0.00080	–0.00054	–0.00072	–0.00087	–0.00137
	25				–0.00080	–0.00060	–0.00082	–0.00030	–0.00062
$\Delta C_{m_{\delta_e}}$	5	0.00144	0.00083	–0.00083					
	10	0.00148	0.00236	–0.00054	0.00262	0.00120	0.00091	0.00139	
	15	0.00073	0.00267	0.00170	0.00231	0.00224	0.00169	0.00114	0.00082
	20				0.00276	0.00298	0.00244	0.00122	0.00093
	25				0.00276	0.00296	0.00180	0.00083	0.00078

Table C-3. Side-force coefficient derivative as a function of Mach number and altitude (pEst program analysis with CPT surface positions).

Derivative increment	Altitude, kft	Mach number 0.85	0.90	0.95	1.05	1.10	1.15	1.20	1.30
ΔC_{Y_b}	5	0.00173	0.00062	0.00293					
	10	0.00103	0.00143	0.00141	0.00058	0.00175	0.00301	0.00427	
	15	0.00158	0.00096	0.00178	0.00074	0.00022	0.00084	0.00146	0.00126
	20				0.00074	0.00058	0.00049	0.00104	0.00228
	25				0.00074	0.00017	0.00140	0.00113	–0.00096
ΔC_{Y_β}	5	0.00335	0.00242	0.00156					
	10	0.00310	0.00196	0.00201	0.00245	0.00480	0.00410	0.00340	
	15	0.00288	0.00241	0.00215	0.00295	0.00402	0.00357	0.00312	0.00293
	20				0.00295	0.00501	0.00362	0.00274	0.00318
	25				0.00295	0.00471	0.00373	0.00285	0.00339
ΔC_{Y_p}	5	0.06451	0.27906	0.00729					
	10	0.10673	0.07833	0.15440	0.06123	–0.01400	–0.00799	–0.00197	
	15	0.11420	0.19665	0.05983	0.12477	0.14625	0.08136	0.01648	–0.21429
	20				0.12477	0.21426	0.14234	–0.06754	–0.16882
	25				0.12477	0.14287	–0.01868	0.06878	–0.08240
ΔC_{Y_r}	5	1.59471	1.89223	1.47315					
	10	1.08063	1.53549	1.44936	1.98186	1.47642	2.07620	2.67598	
	15	1.05871	1.62551	1.08966	1.16967	1.52738	1.24590	0.96441	2.17252
	20				1.16967	1.20035	1.63484	1.17422	1.75038
	25				1.16967	1.69706	1.13978	1.24084	1.56621
$\Delta C_{Y_{\delta_r}}$	5	0.00054	0.00028	–0.00046					
	10	0.00032	0.00046	–0.00023	–0.00125	–0.00108	–0.00110	–0.00112	
	15	0.00032	0.00062	0.00003	–0.00122	–0.00131	–0.00122	–0.00112	–0.00102
	20				–0.00122	–0.00103	–0.00135	–0.00123	–0.00089
	25				–0.00122	–0.00088	–0.00109	–0.00123	–0.00091
$\Delta C_{Y_{\delta_{dLEF}}}$	5	–0.00018	–0.00019	–0.00020					
	10	–0.00009	–0.00011	–0.00034	–0.00030	–0.00030	–0.00031	–0.00032	
	15	–0.00003	–0.00024	–0.00023	–0.00029	–0.00052	–0.00038	–0.00024	0.00016
	20				–0.00029	–0.00052	–0.00032	–0.00023	0.00021
	25				–0.00029	–0.00038	–0.00024	–0.00031	–0.00014
$\Delta C_{Y_{\delta_{dTEF}}}$	5	–0.00068	–0.00041	–0.00037					
	10	–0.00043	–0.00037	–0.00021	–0.00086	–0.00105	–0.00143	–0.00181	
	15	–0.00039	–0.00052	–0.00008	–0.00063	–0.00071	–0.00088	–0.00105	–0.00136
	20				–0.00063	–0.00059	–0.00090	–0.00093	–0.00103
	25				–0.00063	–0.00058	–0.00066	–0.00073	–0.00079
$\Delta C_{Y_{\delta_a}}$	5	0.00000	0.00014	0.00021					
	10	–0.00002	0.00002	0.00021	0.00006	0.00008	0.00024	0.00040	
	15	0.00008	–0.00011	0.00033	0.00011	0.00009	0.00013	0.00017	0.00030
	20				0.00011	0.00011	0.00024	0.00024	0.00026
	25				0.00011	0.00026	0.00026	0.00032	0.00030
$\Delta C_{Y_{\delta_{dh}}}$	5	0.00062	0.00013	0.00057					
	10	0.00051	0.00038	0.00049	0.00073	0.00080	0.00092	0.00103	
	15	0.00067	0.00020	0.00056	0.00053	0.00039	0.00056	0.00073	0.00124
	20				0.00053	0.00035	0.00061	0.00082	0.00115
	25				0.00053	0.00040	0.00071	0.00078	0.00090

Table C-4. Rolling-moment coefficient derivative increments as a function of Mach number and altitude (pEst program analysis with CPT surface positions).

Derivative increment	Altitude, kft	Mach number 0.85	0.90	0.95	1.05	1.10	1.15	1.20	1.30
ΔC_{l_b}	5	0.00255	0.00284	0.00240					
	10	0.00227	0.00289	0.00264	0.00181	0.00168	0.00166	0.00165	
	15	0.00204	0.00254	0.00244	0.00175	0.00143	0.00142	0.00141	0.00138
	20				0.00175	0.00153	0.00123	0.00143	0.00138
	25				0.00175	0.00142	0.00150	0.00129	0.00104
ΔC_{l_β}	5	–0.00071	–0.00083	–0.00017					
	10	–0.00051	–0.00091	0.00001	–0.00054	–0.00073	–0.00071	–0.00068	
	15	–0.00048	–0.00072	0.00003	–0.00037	–0.00033	–0.00039	–0.00046	–0.00037
	20				–0.00037	–0.00026	–0.00037	–0.00032	–0.00026
	25				–0.00037	–0.00022	–0.00018	–0.00006	–0.00009
ΔC_{l_p}	5	0.06601	–0.02057	0.00743					
	10	0.10004	–0.05228	0.03795	0.11243	0.10277	0.08755	0.07232	
	15	0.08280	0.00995	0.03442	0.07916	0.13382	0.10325	0.07268	0.03075
	20				0.07916	0.09547	0.09121	0.04021	0.02686
	25				0.07916	0.04632	0.05471	0.06143	0.02816
ΔC_{l_r}	5	0.12767	0.11411	0.14699					
	10	–0.00724	0.02933	0.03625	0.15072	0.08140	0.17372	0.26603	
	15	–0.16914	–0.06754	0.13239	0.10671	0.13990	0.08385	0.02779	0.10871
	20				0.10671	0.11046	0.07153	0.01493	0.06237
	25				0.10671	0.24774	0.02164	0.02590	0.14876
$\Delta C_{l_{\delta_r}}$	5	0.00001	–0.00012	–0.00014					
	10	–0.00003	0.00000	–0.00017	–0.00027	–0.00019	–0.00019	–0.00019	
	15	–0.00004	–0.00006	–0.00011	–0.00026	–0.00030	–0.00024	–0.00017	–0.00013
	20				–0.00026	–0.00024	–0.00024	–0.00018	–0.00014
	25				–0.00026	–0.00017	–0.00021	–0.00018	–0.00016
$\Delta C_{l_{\delta_{dLEF}}}$	5	0.00022	–0.00080	–0.00149					
	10	0.00016	–0.00044	–0.00088	–0.00141	–0.00144	–0.00150	–0.00156	
	15	0.00019	–0.00007	–0.00031	–0.00079	–0.00084	–0.00096	–0.00108	–0.00109
	20				–0.00079	–0.00021	–0.00042	–0.00044	–0.00058
	25				–0.00079	0.00031	0.00013	–0.00001	–0.00016
$\Delta C_{l_{\delta_{dTEF}}}$	5	0.00012	0.00007	0.00000					
	10	0.00008	0.00017	0.00004	–0.00010	–0.00014	–0.00014	–0.00014	
	15	0.00003	0.00003	0.00003	–0.00012	–0.00010	–0.00009	–0.00007	–0.00003
	20				–0.00012	–0.00010	–0.00009	–0.00007	–0.00003
	25				–0.00012	–0.00010	–0.00004	0.00000	–0.00001
$\Delta C_{l_{\delta_a}}$	5	0.00029	0.00019	0.00013					
	10	0.00027	0.00015	0.00013	0.00011	0.00010	0.00018	0.00025	
	15	0.00018	0.00016	0.00015	0.00002	0.00001	0.00008	0.00016	0.00021
	20				0.00002	–0.00007	0.00004	0.00008	0.00011
	25				0.00002	–0.00009	–0.00002	0.00002	0.00002
$\Delta C_{l_{\delta_{dh}}}$	5	0.00011	0.00013	0.00012					
	10	0.00004	0.00018	0.00004	0.00002	0.00002	0.00007	0.00013	
	15	0.00006	0.00001	0.00003	0.00002	–0.00007	–0.00002	0.00002	0.00005
	20				0.00002	–0.00002	–0.00007	–0.00001	–0.00001
	25				0.00002	0.00000	–0.00004	–0.00009	–0.00007

Table C-5. Yawing-moment coefficient derivative increments as a function of Mach number and altitude (pEst program analysis with CPT surface positions).

Derivative increment	Altitude, kft	Mach number 0.85	0.90	0.95	1.05	1.10	1.15	1.20	1.30
ΔC_{n_b}	5	–0.00093	–0.00092	–0.00092					
	10	–0.00072	–0.00081	–0.00079	–0.00063	–0.00103	–0.00113	–0.00124	
	15	–0.00072	–0.00077	–0.00090	–0.00061	–0.00074	–0.00089	–0.00104	–0.00096
	20				–0.00061	–0.00078	–0.00098	–0.00095	–0.00092
	25				–0.00061	–0.00073	–0.00104	–0.00096	–0.00065
ΔC_{n_β}	5	–0.00055	–0.00052	–0.00022					
	10	–0.00058	–0.00061	–0.00029	–0.00009	–0.00080	–0.00078	–0.00076	
	15	–0.00061	–0.00063	–0.00036	–0.00019	–0.00053	–0.00060	–0.00067	–0.00045
	20				–0.00019	–0.00071	–0.00088	–0.00069	–0.00048
	25				–0.00019	–0.00076	–0.00086	–0.00073	–0.00053
ΔC_{n_p}	5	0.03857	0.02943	0.02655					
	10	0.02005	0.00187	0.03523	0.02757	0.04900	0.04749	0.04598	
	15	0.01695	–0.00060	0.03056	0.01556	0.02198	0.03568	0.04938	0.02957
	20				0.01556	0.03388	0.04157	0.04543	0.03165
	25				0.01556	0.03649	0.05389	0.05040	0.01259
ΔC_{n_r}	5	–0.11558	–0.15808	–0.09831					
	10	–0.10645	–0.16395	–0.18070	–0.13104	–0.12559	–0.15489	–0.18419	
	15	–0.17609	–0.26857	–0.11925	–0.07472	–0.06409	–0.08337	–0.10265	–0.19113
	20				–0.07472	–0.09351	–0.11078	–0.11250	–0.18217
	25				–0.07472	–0.17234	–0.15027	–0.14854	–0.11559
$\Delta C_{n_{\delta_r}}$	5	–0.00001	0.00000	0.00025					
	10	–0.00001	–0.00001	0.00015	0.00058	0.00048	0.00036	0.00024	
	15	0.00003	–0.00008	0.00003	0.00058	0.00055	0.00039	0.00023	0.00017
	20				0.00058	0.00049	0.00037	0.00023	0.00020
	25				0.00058	0.00041	0.00030	0.00026	0.00020
$\Delta C_{n_{\delta_{dLEF}}}$	5	0.00005	0.00006	0.00011					
	10	0.00005	0.00005	0.00012	0.00011	0.00013	0.00013	0.00014	
	15	0.00003	0.00007	0.00011	0.00011	0.00013	0.00013	0.00012	0.00008
	20				0.00011	0.00012	0.00013	0.00012	0.00008
	25				0.00011	0.00010	0.00010	0.00010	0.00012
$\Delta C_{n_{\delta_{dTEF}}}$	5	0.00011	0.00008	0.00005					
	10	0.00012	0.00011	0.00006	0.00023	0.00026	0.00033	0.00040	
	15	0.00010	0.00011	0.00004	0.00019	0.00018	0.00026	0.00034	0.00036
	20				0.00019	0.00018	0.00024	0.00029	0.00030
	25				0.00019	0.00017	0.00022	0.00025	0.00025
$\Delta C_{n_{\delta_a}}$	5	–0.00002	–0.00004	–0.00005					
	10	0.00003	0.00000	–0.00004	0.00001	–0.00001	–0.00003	–0.00005	
	15	0.00002	0.00001	–0.00005	0.00000	–0.00001	–0.00003	–0.00005	–0.00007
	20				0.00000	–0.00002	–0.00002	–0.00004	–0.00007
	25				0.00000	–0.00002	–0.00001	0.00000	–0.00005
$\Delta C_{n_{\delta_{dh}}}$	5	–0.00002	0.00001	0.00001					
	10	0.00004	0.00006	0.00001	–0.00011	–0.00019	–0.00021	–0.00023	
	15	0.00005	0.00005	0.00001	–0.00009	–0.00011	–0.00017	–0.00022	–0.00026
	20				–0.00009	–0.00015	–0.00020	–0.00019	–0.00023
	25				–0.00009	–0.00013	–0.00018	–0.00019	–0.00018

APPENDIX D

STABILITY AND CONTROL DERIVATIVE INCREMENTS OBTAINED FROM PARAMETER IDENTIFICATION ANALYSIS USING ROTARY VARIABLE DIFFERENTIAL TRANSFORMER MEASUREMENTS

Tables D-1–D-5 show tabulated stability and control derivative increments as defined in equations (26)–(30). These increments were obtained from the parameter estimation program, pEst (ref. 1), analysis that used the rotary variable differential transducer (RVDT) measurements. Increments are defined by subtracting the simulation-predicted derivative from the flight-determined derivative and averaging the results from multiple maneuvers at each flight condition. The increments are separated into Mach number and altitude breakpoints. In some cases at Mach 1.05 and Mach 1.15, fight data were nonexistent, and interpolation or “hold last value” were used to complete the tables.

Table D-1. Normal-force coefficient derivative increments as a function of Mach number and altitude (pEst program analysis with RVDT surface positions).

Derivative increment	Altitude, kft	Mach number 0.85	0.90	0.95	1.05	1.10	1.15	1.20	1.30
ΔC_{N_b}	5	0.07809	0.10914	0.10919					
	10	0.06830	0.10718	0.11536	0.04568	0.04449	0.08381	0.11574	
	15	0.07070	0.09748	0.10378	0.03827	0.04401	0.07744	0.11088	0.13640
	20				0.04756	0.05518	0.15042	0.09891	0.13077
	25				0.04756	0.04487	0.10897	0.09163	0.10244
ΔC_{N_α}	5	–0.00728	–0.01387	–0.00236					
	10	–0.00858	–0.02191	–0.00885	–0.00414	–0.01226	–0.01370	–0.02097	
	15	–0.01349	–0.02377	–0.01936	–0.00506	–0.00991	–0.01608	–0.02225	–0.00856
	20				–0.01476	–0.01698	–0.02070	–0.01672	–0.00916
	25				–0.01476	–0.01338	–0.02561	–0.02017	–0.00391
ΔC_{N_q}	5	4.51911	34.07513	–3.07418					
	10	0.73089	52.93171	–14.75774	1.11457	3.47850	8.48389	8.33281	
	15	–23.01455	5.46610	0.68781	2.58764	21.08836	13.95645	6.82453	–12.85931
	20				5.99556	8.52812	–4.66909	9.22458	7.61891
	25				5.99556	8.24887	–0.61660	15.81876	9.91289
$\Delta C_{N_{\delta_{LEF}}}$	5	0.00166	0.02428	–0.00847					
	10	–0.00325	0.00913	–0.00210	–0.01255	–0.01261	–0.00059	–0.01224	
	15	–0.01199	–0.00318	–0.00352	–0.00507	–0.00418	–0.00416	–0.00414	–0.00888
	20				–0.00678	–0.00632	–0.00294	–0.00116	–0.00510
	25				–0.00678	–0.00392	–0.00101	–0.00096	0.00309
$\Delta C_{N_{\delta_{TEF}}}$	5	–0.00881	–0.00463	–0.01523					
	10	–0.00416	–0.00487	–0.01598	–0.01207	–0.01233	–0.00973	–0.01191	
	15	–0.01124	–0.00568	–0.01246	–0.01010	–0.00631	–0.00829	–0.01026	–0.01193
	20				–0.00913	–0.00821	–0.00936	–0.00834	–0.00958
	25				–0.00913	–0.00740	–0.00948	–0.00807	–0.00863
$\Delta C_{N_{\delta_{sa}}}$	5	0.00350	0.00034	0.00064					
	10	0.00311	0.00112	0.00075	–0.00073	–0.00031	0.00035	0.00104	
	15	–0.00117	–0.00233	0.00124	–0.00122	0.00007	0.00018	0.00029	0.00150
	20				–0.00155	–0.00162	–0.00070	0.00032	0.00030
	25				–0.00155	–0.00159	–0.00011	–0.00058	0.00004
$\Delta C_{N_{\delta_e}}$	5	–0.00452	0.00992	0.00335					
	10	–0.00331	0.01215	–0.00041	–0.00333	0.00364	0.00153	0.00146	
	15	0.00371	0.00981	–0.00399	–0.00125	0.00354	0.00242	0.00131	–0.00235
	20				–0.00226	–0.00162	–0.00548	0.00251	0.00197
	25				–0.00226	–0.00229	–0.00242	–0.00099	0.00050

Table D-2. Pitching-moment coefficient derivative increments as a function of Mach number and altitude (pEst program analysis with RVDT surface positions).

Derivative increment	Altitude, kft	Mach number 0.85	0.90	0.95	1.05	1.10	1.15	1.20	1.30
ΔC_{m_b}	5	–0.02366	–0.02982	–0.02506					
	10	–0.02554	–0.03175	–0.02787	–0.02852	–0.03026	–0.03489	–0.03600	
	15	–0.02204	–0.03159	–0.02693	–0.02836	–0.03375	–0.03526	–0.03677	–0.04625
	20				–0.03303	–0.03591	–0.03018	–0.03663	–0.04162
	25				–0.03303	–0.03633	–0.03219	–0.03426	–0.04425
ΔC_{m_α}	5	0.01243	0.01251	0.01023					
	10	0.01263	0.01280	0.01386	0.01222	0.00748	0.00530	0.00501	
	15	0.01232	0.01310	0.01366	0.00989	0.00711	0.00590	0.00470	0.00595
	20				0.01140	0.01030	0.00448	0.00592	0.00354
	25				0.01140	0.01122	0.00749	0.00495	0.00575
ΔC_{m_q}	5	–3.06823	0.98749	–5.29898					
	10	–2.54572	–0.51536	–9.14333	5.20828	3.41662	1.45447	3.02996	
	15	–5.21019	1.10825	–9.48105	3.29556	0.08441	1.51519	2.94598	2.45931
	20				0.41598	1.01649	–6.46238	–0.69409	–3.53175
	25				0.41598	0.06170	–3.94509	–3.06909	–1.67706
$\Delta C_{m_{\delta_{LEF}}}$	5	–0.00061	0.00099	–0.00343					
	10	–0.00012	–0.00020	–0.00228	0.00204	0.00224	0.00529	0.00655	
	15	–0.00078	0.00043	–0.00223	0.00039	0.00401	0.00442	0.00483	0.00640
	20				0.00043	0.00188	0.00487	0.00432	0.00548
	25				0.00043	0.00067	0.00283	0.00428	0.00434
$\Delta C_{m_{\delta_{TEF}}}$	5	–0.00101	–0.00061	0.00036					
	10	–0.00081	–0.00078	0.00035	0.00066	0.00084	0.00082	0.00079	
	15	–0.00119	–0.00094	–0.00024	0.00031	–0.00022	0.00018	0.00057	0.00080
	20				–0.00015	–0.00017	–0.00005	–0.00011	–0.00007
	25				–0.00015	–0.00032	–0.00077	–0.00069	–0.00059
$\Delta C_{m_{\delta_{sa}}}$	5	–0.00212	–0.00160	–0.00209					
	10	–0.00163	–0.00125	–0.00179	–0.00087	–0.00090	–0.00103	–0.00153	
	15	–0.00145	–0.00070	–0.00181	–0.00067	–0.00063	–0.00079	–0.00095	–0.00202
	20				–0.00032	–0.00009	–0.00029	–0.00051	–0.00120
	25				–0.00032	–0.00011	–0.00031	0.00002	–0.00033
$\Delta C_{m_{\delta_e}}$	5	0.00448	0.00690	0.00349					
	10	0.00550	0.00821	0.00353	0.00592	0.00456	0.00333	0.00346	
	15	0.00563	0.00801	0.00371	0.00432	0.00503	0.00410	0.00318	0.00373
	20				0.00600	0.00588	0.00438	0.00399	0.00218
	25				0.00600	0.00584	0.00439	0.00366	0.00364

Table D-3. Side-force coefficient derivative increments as a function of Mach number and altitude (pEst program analysis with RVDT surface positions).

Derivative increment	Altitude, kft	Mach number 0.85	0.90	0.95	1.05	1.10	1.15	1.20	1.30
ΔC_{Y_b}	5	0.00265	–0.00005	0.00447					
	10	0.00138	0.00132	0.00177	0.00050	0.00183	–0.00153	–0.00489	
	15	0.00196	0.00069	0.00283	0.00105	0.00078	0.00123	0.00168	0.00180
	20				0.00105	0.00078	0.00071	0.00201	0.00247
	25				0.00105	0.00025	0.00205	0.00127	–0.00089
ΔC_{Y_β}	5	0.00357	0.00307	0.00161					
	10	0.00369	0.00277	0.00228	0.00306	0.00503	0.00416	0.00330	
	15	0.00300	0.00336	0.00229	0.00343	0.00487	0.00397	0.00307	0.00289
	20				0.00343	0.00578	0.00409	0.00296	0.00315
	25				0.00343	0.00521	0.00433	0.00317	0.00375
ΔC_{Y_p}	5	–0.01047	0.54748	–0.10553					
	10	0.15762	0.25652	0.25682	0.12048	0.01360	–0.01863	–0.05085	
	15	0.14575	0.36796	0.03738	0.19439	0.26463	0.12335	–0.01793	–0.24676
	20				0.19439	0.30710	0.16524	–0.11841	–0.19469
	25				0.19439	0.16126	0.05737	0.15680	–0.04527
ΔC_{Y_r}	5	2.03979	2.29597	1.90942					
	10	1.64535	2.16166	1.92500	2.06169	1.54622	2.20620	2.86617	
	15	0.60019	2.07808	1.45936	1.60374	1.73333	1.46482	1.19632	2.47005
	20				1.60374	1.07318	1.41458	1.14416	1.70608
	25				1.60374	1.39307	0.46331	0.74092	1.67241
$\Delta C_{Y_{\delta_r}}$	5	–0.00006	–0.00047	–0.00082					
	10	–0.00026	–0.00011	–0.00093	–0.00166	–0.00146	–0.00144	–0.00142	
	15	–0.00026	–0.00005	–0.00051	–0.00146	–0.00143	–0.00143	–0.00142	–0.00117
	20				–0.00146	–0.00130	–0.00144	–0.00134	–0.00119
	25				–0.00146	–0.00130	–0.00122	–0.00147	–0.00112
$\Delta C_{Y_{\delta_{dLEF}}}$	5	–0.00015	–0.00063	–0.00025					
	10	–0.00023	–0.00031	–0.00075	–0.00079	–0.00076	–0.00064	–0.00052	
	15	–0.00003	–0.00051	–0.00030	–0.00073	–0.00119	–0.00073	–0.00027	0.00007
	20				–0.00073	–0.00096	–0.00083	–0.00029	0.00043
	25				–0.00073	–0.00050	–0.00049	–0.00070	–0.00034
$\Delta C_{Y_{\delta_{dTEF}}}$	5	–0.00057	–0.00044	–0.00033					
	10	–0.00048	–0.00044	–0.00019	–0.00063	–0.00092	–0.00134	–0.00177	
	15	–0.00021	–0.00047	0.00000	–0.00048	–0.00051	–0.00078	–0.00104	–0.00122
	20				–0.00048	–0.00036	–0.00088	–0.00082	–0.00089
	25				–0.00048	–0.00034	–0.00040	–0.00052	–0.00069
$\Delta C_{Y_{\delta_a}}$	5	–0.00002	0.00003	0.00020					
	10	–0.00014	–0.00011	0.00018	0.00004	0.00000	0.00015	0.00030	
	15	–0.00001	–0.00029	0.00032	0.00008	0.00004	0.00008	0.00012	0.00020
	20				0.00008	0.00004	0.00021	0.00017	0.00019
	25				0.00008	0.00027	0.00018	0.00026	0.00020
$\Delta C_{Y_{\delta_{dh}}}$	5	0.00076	–0.00003	0.00085					
	10	0.00070	0.00026	0.00053	0.00070	0.00081	0.00094	0.00108	
	15	0.00102	0.00040	0.00070	0.00052	0.00036	0.00056	0.00077	0.00112
	20				0.00052	0.00043	0.00067	0.00091	0.00108
	25				0.00052	0.00053	0.00070	0.00085	0.00081

Table D-4. Rolling-moment coefficient derivative increments as a function of Mach number and altitude (pEst program analysis with RVDT surface positions).

Derivative increment	Altitude, kft	Mach number 0.85	0.90	0.95	1.05	1.10	1.15	1.20	1.30
ΔC_{l_b}	5	0.00281	0.00325	0.00333					
	10	0.00242	0.00310	0.00311	0.00237	0.00203	0.00150	0.00096	
	15	0.00194	0.00250	0.00265	0.00206	0.00175	0.00158	0.00141	0.00152
	20				0.00206	0.00194	0.00136	0.00164	0.00155
	25				0.00206	0.00225	0.00175	0.00144	0.00109
ΔC_{l_β}	5	–0.00079	–0.00096	–0.00052					
	10	–0.00068	–0.00100	–0.00013	–0.00093	–0.00119	–0.00117	–0.00114	
	15	–0.00060	–0.00084	–0.00002	–0.00057	–0.00058	–0.00060	–0.00062	–0.00052
	20				–0.00057	–0.00054	–0.00056	–0.00059	–0.00049
	25				–0.00057	–0.00066	–0.00042	–0.00024	–0.00023
ΔC_{l_p}	5	0.04713	–0.07282	–0.14428					
	10	0.07963	–0.06273	–0.04300	0.00651	0.01161	–0.01882	–0.04925	
	15	0.09243	0.02729	–0.00118	0.04349	0.09590	0.06625	0.03661	–0.04897
	20				0.04349	0.02379	0.03129	–0.01717	–0.02633
	25				0.04349	–0.07799	–0.00805	0.03298	0.00016
ΔC_{l_r}	5	0.29574	0.14842	0.13387					
	10	0.05536	0.11723	0.09417	0.22771	0.00858	0.15274	0.29691	
	15	–0.13846	0.10623	0.21498	0.08709	0.13068	0.10934	0.08799	0.15764
	20				0.08709	0.13782	0.02241	–0.00901	0.11797
	25				0.08709	0.00515	–0.07076	–0.00445	0.18159
$\Delta C_{l_{\delta_r}}$	5	0.00002	–0.00016	–0.00010					
	10	–0.00004	–0.00009	–0.00016	–0.00026	–0.00021	–0.00020	–0.00018	
	15	–0.00011	–0.00011	–0.00016	–0.00026	–0.00027	–0.00021	–0.00016	–0.00010
	20				–0.00026	–0.00024	–0.00017	–0.00017	–0.00013
	25				–0.00026	–0.00008	–0.00019	–0.00017	–0.00014
$\Delta C_{l_{\delta_{dLEF}}}$	5	0.00032	–0.00051	–0.00082					
	10	0.00029	–0.00029	–0.00047	–0.00060	–0.00054	–0.00069	–0.00083	
	15	0.00027	0.00000	–0.00010	–0.00034	–0.00044	–0.00062	–0.00080	–0.00038
	20				–0.00034	0.00018	0.00000	–0.00002	–0.00021
	25				–0.00034	0.00071	0.00043	0.00021	0.00010
$\Delta C_{l_{\delta_{dTEF}}}$	5	0.00004	0.00004	–0.00003					
	10	0.00005	0.00013	0.00003	–0.00012	–0.00013	–0.00016	–0.00018	
	15	–0.00003	–0.00007	0.00002	–0.00010	–0.00009	–0.00008	–0.00007	–0.00007
	20				–0.00010	–0.00007	–0.00009	–0.00006	–0.00003
	25				–0.00010	–0.00004	–0.00001	0.00002	0.00000
$\Delta C_{l_{\delta_a}}$	5	0.00018	0.00010	0.00012					
	10	0.00018	0.00007	0.00010	0.00008	0.00006	0.00014	0.00023	
	15	0.00007	0.00004	0.00010	–0.00003	–0.00003	0.00005	0.00013	0.00011
	20				–0.00003	–0.00011	0.00000	0.00005	0.00008
	25				–0.00003	–0.00009	–0.00006	–0.00002	–0.00002
$\Delta C_{l_{\delta_{dh}}}$	5	–0.00001	0.00005	0.00015					
	10	–0.00004	0.00008	0.00002	–0.00005	–0.00008	0.00001	0.00009	
	15	–0.00004	–0.00011	–0.00005	–0.00013	–0.00018	–0.00015	–0.00013	–0.00008
	20				–0.00013	–0.00010	–0.00017	–0.00010	–0.00009
	25				–0.00013	0.00009	–0.00011	–0.00019	–0.00018

Table D-5. Yawing-moment coefficient derivative increments as a function of Mach number and altitude (pEst program analysis with RVDT surface positions).

Derivative increment	Altitude, kft	Mach number 0.85	0.90	0.95	1.05	1.10	1.15	1.20	1.30
ΔC_{n_b}	5	–0.00107	–0.00112	–0.00106					
	10	–0.00079	–0.00094	–0.00085	–0.00058	–0.00109	–0.00090	–0.00071	
	15	–0.00082	–0.00081	–0.00104	–0.00067	–0.00079	–0.00096	–0.00113	–0.00109
	20				–0.00067	–0.00074	–0.00099	–0.00109	–0.00099
	25				–0.00067	–0.00055	–0.00103	–0.00089	–0.00066
ΔC_{n_β}	5	–0.00057	–0.00054	–0.00026					
	10	–0.00065	–0.00064	–0.00032	–0.00024	–0.00087	–0.00081	–0.00076	
	15	–0.00064	–0.00079	–0.00037	–0.00026	–0.00065	–0.00066	–0.00068	–0.00048
	20				–0.00026	–0.00083	–0.00093	–0.00073	–0.00048
	25				–0.00026	–0.00097	–0.00097	–0.00079	–0.00056
ΔC_{n_p}	5	0.03266	0.02126	0.00569					
	10	0.00872	–0.00292	0.01324	0.00747	0.04265	0.04765	0.05264	
	15	0.01713	–0.01846	0.01258	0.00839	0.00685	0.02623	0.04561	0.03788
	20				0.00839	0.01497	0.03027	0.04652	0.03668
	25				0.00839	0.00346	0.03422	0.03814	0.00903
ΔC_{n_r}	5	–0.14721	–0.20850	–0.17061					
	10	–0.16353	–0.21550	–0.22506	–0.14360	–0.16997	–0.19693	–0.22389	
	15	–0.19311	–0.40989	–0.20990	–0.11683	–0.11609	–0.14923	–0.18237	–0.25447
	20				–0.11683	–0.12992	–0.21220	–0.19752	–0.24631
	25				–0.11683	–0.22664	–0.22742	–0.22180	–0.20911
$\Delta C_{n_{\delta_r}}$	5	0.00025	0.00022	0.00043					
	10	0.00024	0.00020	0.00042	0.00072	0.00060	0.00046	0.00032	
	15	0.00026	0.00018	0.00027	0.00070	0.00067	0.00050	0.00033	0.00027
	20				0.00070	0.00065	0.00050	0.00032	0.00029
	25				0.00070	0.00059	0.00044	0.00039	0.00031
$\Delta C_{n_{\delta_{dLEF}}}$	5	0.00007	0.00009	0.00024					
	10	0.00008	0.00007	0.00021	0.00025	0.00022	0.00020	0.00017	
	15	0.00004	0.00010	0.00018	0.00020	0.00024	0.00020	0.00017	0.00008
	20				0.00020	0.00020	0.00021	0.00017	0.00007
	25				0.00020	0.00017	0.00016	0.00015	0.00015
$\Delta C_{n_{\delta_{dTEF}}}$	5	0.00009	0.00006	0.00003					
	10	0.00010	0.00010	0.00005	0.00017	0.00022	0.00029	0.00037	
	15	0.00007	0.00008	0.00004	0.00015	0.00014	0.00023	0.00031	0.00029
	20				0.00015	0.00013	0.00020	0.00025	0.00026
	25				0.00015	0.00012	0.00017	0.00019	0.00021
$\Delta C_{n_{\delta_a}}$	5	–0.00002	–0.00004	–0.00005					
	10	0.00003	–0.00001	–0.00003	0.00000	–0.00001	–0.00002	–0.00004	
	15	0.00000	0.00001	–0.00005	–0.00001	0.00000	–0.00002	–0.00004	–0.00006
	20				–0.00001	–0.00001	–0.00002	–0.00003	–0.00006
	25				–0.00001	–0.00001	0.00000	0.00001	–0.00004
$\Delta C_{n_{\delta_{dh}}}$	5	–0.00004	–0.00001	0.00000					
	10	0.00001	0.00003	0.00000	–0.00009	–0.00018	–0.00020	–0.00022	
	15	–0.00001	0.00002	0.00000	–0.00010	–0.00011	–0.00015	–0.00019	–0.00024
	20				–0.00010	–0.00014	–0.00019	–0.00018	–0.00022
	25				–0.00010	–0.00008	–0.00015	–0.00017	–0.00017

REFERENCES

1. Murray, James E. and Richard E. Maine, *pEst Version 2.1 User's Manual*, NASA TM-88280, 1987.

2. Maine, Richard E. and Kenneth W. Iliff, *Application of Parameter Estimation to Aircraft Stability and Control: the Output-Error Approach*, NASA RP-1168, 1986.

3. United States Naval Air Systems Command, *Preliminary NATOPS Flight Manual*: *Navy Model F/TF-18A*, A1-F18AA-NFM-000, Feb. 1980.

4. Carter, John F., *Production Support Flight Control Computers: Research Capability for F/A-18 Aircraft at Dryden Flight Research Center*, NASA TM-97-206233, 1997.

5. Whitmore, Stephen A., Roy J. Davis, and John Michael Fife, *In-Flight Demonstration of a Real-Time Flush Airdata Sensing (RT–FADS) System*, NASA TM-104314, 1995.

6. Maine, R. E. and K. W. Iliff, *Identification of Dynamic Systems*, AGARD-AG-300, vol. 2, Jan. 1985. (Also available as NASA RP-1138, 1985).

7. Gainer, Thomas G. and Sherwood Hoffman, *Summary of Transformation Equations and Equations of Motion Used in Free-Flight and Wind-Tunnel Data Reduction and Analysis*, NASA SP-3070, 1972.

8. Iliff, Kenneth W. and Richard E. Maine, *Practical Aspects of Using a Maximum Likelihood Estimation Method to Extract Stability and Control Derivatives From Flight Data*, NASA TN-D-8209, 1976.

REPORT DOCUMENTATION PAGE

Form Approved
OMB No. 0704-0188

Public reporting burden for this collection of information is estimated to average 1 hour per response, including the time for reviewing instructions, searching existing data sources, gathering and maintaining the data needed, and completing and reviewing the collection of information. Send comments regarding this burden estimate or any other aspect of this collection of information, including suggestions for reducing this burden, to Washington Headquarters Services, Directorate for Information Operations and Reports, 1215 Jefferson Davis Highway, Suite 1204, Arlington, VA 22202-4302, and to the Office of Management and Budget, Paperwork Reduction Project (0704-0188), Washington, DC 20503.

1. AGENCY USE ONLY (Leave blank)

2. REPORT DATE
November 2000

3. REPORT TYPE AND DATES COVERED
Technical Publication

4. TITLE AND SUBTITLE
Results From F-18B Stability and Control Parameter Estimation Flight Tests at High Dynamic Pressures

5. FUNDING NUMBERS
WU 529-61-14-E8-14-00-SRA

6. AUTHOR(S)
Timothy R. Moes, Gregory K. Noffz, and Kenneth W. Iliff

7. PERFORMING ORGANIZATION NAME(S) AND ADDRESS(ES)
NASA Dryden Flight Research Center
P.O. Box 273
Edwards, California 93523-0273

8. PERFORMING ORGANIZATION REPORT NUMBER
H-2424

9. SPONSORING/MONITORING AGENCY NAME(S) AND ADDRESS(ES)
National Aeronautics and Space Administration
Washington, DC 20546-0001

10. SPONSORING/MONITORING AGENCY REPORT NUMBER
NASA/TP-2000-209033

11. SUPPLEMENTARY NOTES

12a. DISTRIBUTION/AVAILABILITY STATEMENT
Unclassified—Unlimited
Subject Category 08

This report is available at http://www.dfrc.nasa.gov/DTRS/

12b. DISTRIBUTION CODE

13. ABSTRACT (Maximum 200 words)

A maximum-likelihood output-error parameter estimation technique has been used to obtain stability and control derivatives for the NASA F-18B Systems Research Aircraft. This work has been performed to support flight testing of the active aeroelastic wing (AAW) F-18A project. The goal of this research is to obtain baseline F-18 stability and control derivatives that will form the foundation of the aerodynamic model for the AAW aircraft configuration. Flight data have been obtained at Mach numbers between 0.85 and 1.30 and at dynamic pressures ranging between 600 and 1500 lbf/ft^2. At each test condition, longitudinal and lateral-directional doublets have been performed using an automated onboard excitation system. The doublet maneuver consists of a series of single-surface inputs so that individual control-surface motions cannot be correlated with other control-surface motions. Flight test results have shown that several stability and control derivatives are significantly different than prescribed by the F-18B aerodynamic model. This report defines the parameter estimation technique used, presents stability and control derivative results, compares the results with predictions based on the current F-18B aerodynamic model, and shows improvements to the nonlinear simulation using updated derivatives from this research.

14. SUBJECT TERMS
Active aeroelastic wing, Control derivatives, Maximum likelihood estimates, Parameter identification, Stability derivatives

15. NUMBER OF PAGES
144

16. PRICE CODE
A07

17. SECURITY CLASSIFICATION OF REPORT
Unclassified

18. SECURITY CLASSIFICATION OF THIS PAGE
Unclassified

19. SECURITY CLASSIFICATION OF ABSTRACT
Unclassified

20. LIMITATION OF ABSTRACT
Unlimited